THE UNIVERSITY *of* EDINBURGH

Interactions between ice shelves and phytoplankton blooms in the Amundsen Sea, and their relevance to the Southern Ocean

Andrew G. Twelves

Doctor of Philosophy

THE UNIVERSITY OF EDINBURGH

2022

"It is advisable to look from the tide pool to the stars and then back to the tide pool again."

John Steinbeck

"This is a very complicated case, Maude. You know, a lotta ins, a lotta outs, a lotta what-have-yous."

Jeffrey "The Dude" Lebowski

Abstract

The coastal Southern Ocean is both highly sensitive to climate change and disproportionately important as a regulator of global carbon and nutrient fluxes. In particular, the polynyas which occur at many locations along the coastline host annual phytoplankton blooms which act as sinks of nutrients and carbon, whilst fueling the growth of higher trophic levels. Spring phytoplankton blooms in the Amundsen Sea are amongst the most intensely productive in the Southern Ocean and occur near some of the fastest melting ice shelves around Antarctica. In recent years both observations and modelling have been used to investigate the possible role of ice shelf melting in fuelling phytoplankton growth, with ice shelves implicated as sources of the dissolved iron whose scarcity would otherwise severely limit primary production. However there remains debate in the literature as to the importance of this iron limitation in comparison to light limitation, and as to the precise mechanism by which ice shelf melting enhances local iron concentrations. Meanwhile, expanded observations and advances in data assimilation have revealed pronounced zonal variation in both physical and biogeochemical aspects of oceanography near the Antarctic margin.

In this thesis, idealised and realistic models of the Amundsen Sea are combined to examine the role that ice shelves play in driving Net Primary Production (NPP) in ice-free polynyas on Antarctic continental shelves, and how this role is affected by climate-driven processes. Addtionally, the impact of phytoplankton blooms themselves on the physical components of the Antarctic margin – particularly ice shelf melting and sea ice cover – are investigated. The modelling is undertaken using the MIT General Circulation Model (MITgcm) to represent ocean physics and the Biology Light Iron Nutrients and Gases (BLING) to represent biogeochemistry. This is the same combination used for the Biological Southern Ocean State Estimate (BSOSE), here modified and repurposed to study coastal processes with an emphasis on how these processes impact the wider Southern Ocean.

In the first results chapter of this thesis, modelling using an idealised domain covering the Amundsen Sea Polynya (ASP) reveals transitions between light and iron limitation, with iron limitation shown to be more important a) later in the season, b) higher in the water column and c) further from the ice shelf, as compared to light limitation. Thus the categorization of the ASP as either iron or light limited is shown to be overly simplistic. Meanwhile, a significant driver of light limitation is shown to be the self-shading feedback by which surface phytoplankton reduce the light available to deeper phytoplankton. This result emphasizes the importance of including the self-shading feedback in BSOSE and in other ocean state estimates. In addition,

the use of a simple one-dimensional Lagrangian particle-tracking model demonstrates the importance of mixing and photo-adaptation timescales in modifying the light limitation of phytoplankton blooms such as that in the ASP, motivating further studies of how different phytoplankton species adapt to fluctuating light environments.

In the second results chapter, a different set of experiments on the same model setup is used to confirm that ice-shelf melting leads to greater upper ocean iron concentrations, both directly due to release of glacial iron, and indirectly via a buoyancy-driven overturning circulation which pulls iron from Circumpolar Deep Water to the surface. Both of these mechanisms drive increased NPP in front of Dotson Ice Shelf, and sensitivity experiments reveal further complexity in the coupled physical-biological system. Varying the level of shortwave radiation incident on the ocean leads to a moderate, linear response in NPP. However, varying the level of the thermocline gives a non-monotonic and counter-intuitive response. Despite increasing the amount of iron in the upper ocean, a warmer ocean does not necessarily lead to an increase in NPP, since the increased melt rate modifies coastal currents, potentially steering the iron away from where it is most limiting to phytoplankton growth.

In the third results chapter, the same basic setup of MITgcm-BLING is employed in a larger, more realistic domain covering the entire Amundsen Sea sector. Notably, the phytoplankton bloom in Pine Island Polynya is shown to modify basal melting underneath the adjacent Pine Island Glacier Ice Shelf. This surprising result follows from the increased shortwave attenuation arising from high chlorophyll concentrations in the euphotic zone, which warms the sea surface whilst cooling the sub-surface. Model outputs also show that high NPP reverses the sign of the annual air-sea carbon flux on the Amundsen Sea continental shelf, with regional variability in the annual flux driven by meltwater distributions, phytoplankton blooms, and the coupling between the two.

The results presented in this thesis have wider implications for studies of the Southern Ocean, including due to their novel implementation of self-shading and biophysical feedbacks within an ice-ocean model. In the final part of the thesis, a list of scenarios summarising possible future changes in the Amundsen Sea are described, encompassing changes to ice shelves, sea ice and cloud cover, as well as to the timing, magnitude and species composition of the phytoplankton bloom. Each of these scenarios has potential impacts for processes at lower latitudes, and each motivates further study of ice-ocean-biological interactions in other coastal polynyas around Antarctica.

Lay Summary

The seas around Antarctica are covered for much of the year with sea ice. When gaps (known as polynyas) develop, the exposed ocean surface can exchange carbon dioxide with the atmosphere. These polynyas often host large seasonal blooms of floating algae – phytoplankton – which take up carbon as they photosynthesise. The most intense blooms tend to form close to the floating ice shelves which form the margins of the West Antarctic Ice Sheet.

Over recent years these polynyas and the phytoplankton blooms within them have been extensively studied using ice-breaking ships, unmanned autonomous gliders and even sensors placed on seals. At the same time, they have been studied from space using satellite technology, as have nearby ice shelves. In this thesis, the interactions between ice shelves and phytoplankton blooms are instead investigated using computer models. This modelling is focused on the Amundsen Sea, in which both ice shelf melt rates and phytoplankton biomass concentrations are some of the highest anywhere around the Antarctic coastline.

Primarily, this thesis shows that ice shelves help to supply phytoplankton with the iron that they need to grow, allowing polynyas to take up more carbon from the atmosphere. This supply of iron is both from the ice itself and from the deep waters which are pulled towards the surface along with buoyant meltwater. On the other hand, the early growth of the bloom results in a progressive “greening” of the polynya, which prevents sufficient light from reaching deeper phytoplankton. This slows the development of the bloom and thus reduces overall carbon uptake within polynyas. Similarly, the uptake of iron by growing phytoplankton reduces the availability of iron at later times in the summer growing season. Suggestions are also given as to how other complicating factors – such as the ability of phytoplankton to adapt to changes in light availability – might be included in future modelling studies.

A set of model experiments with slightly different parameters is used to investigate how environmental variability affects phytoplankton blooms in the Amundsen Sea. This modelling demonstrates that ice shelves act to translate variations in the depth profile of ocean temperature into variations in the horizontal distribution of phytoplankton. Changes to this horizontal distribution impact Net Primary Production - the rate at which phytoplankton convert inorganic carbon to organic carbon – in complex ways. As a result, an increase in ice shelf melt rate, and accompanying increase in iron released to the ocean surface, does not always lead to a more productive phytoplankton bloom.

Ice shelves can also contribute more directly to polynya carbon fluxes, by bringing waters rich in inorganic carbon to the surface. This counteracts the tendency for the iron within these same waters to remove inorganic carbon via phytoplankton growth – a balance of processes which is also investigated in this thesis. When sea ice first retreats in spring, modelling shows

large quantities of carbon being released from polynya into the atmosphere; as the spring and summer progresses, this is reversed and the polynya becomes a strong sink for carbon. At the same time, the greening of the surface ocean described previously also causes more of the sun's heat to be trapped close to the surface. With less heat reaching greater depths, ice shelves are partially insulated from this warming by the sun, and thus melt at a slower rate.

.

Acknowledgements

Firstly, thank you to Dan and to Sian, the best supervisory team that anyone could wish for. Additionally to Dan, Paul and David at the British Antarctic Survey, who made my occasional trips down to Cambridge both enjoyable and productive. Thanks also to everyone who made me feel so welcome during my visits to sunny Scripps, especially Matt, Ariane, and everyone involved in the SOCCOM group there. The short time I spent at Scripps has massively shaped the development of this thesis.

I would also like to thank Anne Juel, who first got me interested in fluid dynamics, and to the rest of the Manchester Centre for Nonlinear Dynamics who taught me how to persevere with scientific research during my internship there several years ago. Similarly, thank you to Tobias Galla and all the other inspiring lecturers from my undergraduate studies at the University of Manchester.

During the second year of my PhD, it was a privilege to attend the Advanced Climate Dynamics Course (ACDC) in Finse, Norway. Thank you to all the ACDC organisers, and to Natalya, DC, Jess, Katie and Holly for being a great team as we worked on code in the cabin.

Also in second year I was lucky enough to spend time aboard the RSS James Clark Ross (JCR), on the repeat transect across the Drake Passage led by Yvonne Firing. This experience immeasurably improved my overall grasp of oceanography, and left with me some of the most unforgettable memories of my life. Many thanks to Yvonne, the crew and all the other scientists onboard. In particular thanks to Twm and Julia for being great fun both on the JCR and later at the Ocean Sciences conference in 2020.

Next, thank you to everyone in "St Kilda" office and elsewhere in Drummond Street: Alex for dragging me up and down Arthur's Seat, George and Marina for our tag-team teaching efforts, Justine for being a beacon of positivity in our office. Thanks to Emma, Will and Boris for making EGU 2020 one of the highlights of my PhD. Thanks to Aythya and Nick for, amongst other things, being great culinary hosts and ceilidh critics, and to Polly for always being a positive influence on Brass Monkey outings.

I don't think I would have got through late nights plotting graphs in Drummond Street without late night meals at Mosque Kitchen. Similarly, thanks to Aga at the ECCI cafe, and to Rowan, Lizzie and Rebecca for making coffee breaks there a welcome respite over the years. Thank you to Louis for being a consistent lunchtime companion, particularly for several recent burrito-based pep talks.

Thank you to Josh and Lou for introducing me to home brewing and for always being great hosts. Thanks to Michael for staying to the bitter end in Durham, and for tennis sessions of varying quality. Also to the rest of the team involved in organising Gradschool 2019, and particularly to Jonny for putting me on to the Meadowbank flat. In addition, a big thank you to Henry for being a great flatmate under circumstances more challenging than any of us could have imagined a couple of years ago.

Thank you to all my Manchester friends – especially Jack, David and Jack – and to my Yorkshire friends – especially Jonny and Marcus. I have always looked forward to welcoming you on visits to Edinburgh and look forward to seeing you all more often soon.

Finally, many thanks to my mum for her ceaseless support, my to sister for her understanding and solidarity, to my dad for his encouragement, to my brothers for keeping me on my toes with their questions, and all my other family and friends.

Declaration

I declare that this thesis has been composed solely by myself, and that it contains only my work except where otherwise specified, or where the work is explicitly indicated below to have formed part of a jointly-authored publication. This work has not been submitted for any other degree or professional qualification. The candidate confirms that appropriate credit has been given within the thesis where reference has been made to the work of others.

Chapters 4 & 5

Citation: Twelves, A. G., Goldberg, D. N., Henley, S. F., Mazloff, M., and Jones, D. (2020). Self-shading and meltwater spreading control the transition from light to iron limitation in an antarctic coastal polynya. *Journal of Geophysical Research: Oceans*, page e2020JC016636.

DOI: `https://doi.org/10.1029/2020JC016636`

Author contributions: AGT performed all of the modelling and analysis of model results. All authors contributed to the design of the study and the writing of the paper.

Andrew G. Twelves

January 2022

Contents

Figures and Tables

Figures

Tables

Nomenclature

ASL Amundsen Sea Low
ASP Amundsen Sea Polynya
ASW Antarctic Surface Water
$BLING$ Biology Light Iron Nutrients and Gases model
$BSOSE$ Biological Southern Ocean State Estimate
$CDOM$ Colored Dissolved Organic Matter
CDW Circumpolar Deep Water
CIS Crosson Ice Shelf
DCM Deep Chlorophyll Maximum
DFe Dissolved Iron
DIC Dissolved Inorganic Carbon
DIS Dotson Ice Shelf
DON Dissolved Organic Nitrogen
DOP Dissolved Organic Phosphorous
$ENSO$ El Niño Southern Oscillation
$IPCC$ Intergovernmental Panel on Climate Change
$ITGC$ International Thwaites Glacier Collaboration
KPP K-Profile Parameterization
$mCDW$ Modified Circumpolar Deep Water
$MISI$ Marine Ice Sheet Instability
$MITgcm$ Massachusetts Institute of Technology general circulation model
MLD Mixed Layer Depth
NCP Net Community Production
NPP Net Primary Production
PAR Photosynthetically Available Radiation
PIB Pine Island Bay
PIG Pine Island Glacier
$PIGIS$ Pine Island Glacier Ice Shelf
PIP Pine Island Polynya
SAM Southern Annular Mode
$SOCCOM$ Southern Ocean Carbon and Climate Observations and Modelling
SOI Southern Oscillation Index
$SROCC$ Special Report on the Ocean and Cryosphere in a Changing Climate
SST Sea Surface Temperature
$TDFe$ Total Dissolvable Iron

$TFIT$	Thwaites Fast Ice Tongue
TG	Thwaites Glacier
$WAIS$	West Antarctic Ice Sheet
WW	Winter Water

Chapter 1

Introduction

1.1 Motivation

West Antarctica is currently undergoing rapid change, largely driven by anthropogenic carbon emissions. Warming of the atmosphere and of coastal waters is driving accelerated melting of the floating ice shelves which form the boundary between the West Antarctic Ice Sheet (WAIS) and the Southern Ocean. Combined with the melting of ice sheets in East Antarctica and Greenland, this has the potential to increase global sea levels substantially in the future (Masson-Delmotte et al., 2019).

However the melting of ice sheets and glaciers has other impacts on the Earth system, less obvious but potentially more immediate. The loss of high altitude glaciers places a strain on global water security (Haeberli and Weingartner, 2020), whilst increased meltwater from Greenland may weaken the Atlantic Meridional Overturning Circulation (AMOC) which dominates global ocean circulation (Beaird et al., 2018). Finally, in both the seas around Greenland and those around Antarctica, changes driven by glacial meltwater may affect the seasonal blooms of phytoplankton which form the basis of polar marine ecosystems (Cape et al., 2019; Oliver et al., 2020). In the Amundsen Sea region of West Antarctica, which hosts some of the most intense phytoplankton blooms on the planet (Arrigo et al., 2012; Arrigo and van Dijken, 2003), there is increasing focus on how the occurrence of these blooms is tied to the dynamics of nearby ice shelves (St-Laurent et al., 2019).

In the Southern Ocean, and worldwide, phytoplankton play a dual role in the Earth system; on the one hand they constitute a food source for krill and other zooplankton, which in turn support larger marine life; at the same time they contribute to the exchange of carbon between the atmosphere, sea surface and deep ocean (Henley et al., 2020). In much of the global ocean the rate at which phytoplankton convert inorganic carbon to organic carbon, or Net Primary Production (NPP), is limited by scarcity of nitrate and/or phosphate – both nutrients vital for phytoplankton growth. However in the Southern Ocean NPP is instead generally dictated by availability of iron and/or light (Martin et al., 1990), each of which may be sensitive to changes in the cryosphere.

Of particular importance for Southern Ocean phytoplankton are the gaps in sea ice cover, or polynyas, which open seasonally both in the open ocean and along the Antarctic coastline. Whilst the Southern Ocean as a whole is an important sink for anthropogenic carbon, a large fraction of total carbon uptake is concentrated in the relatively small area occupied by coastal polynyas (Arrigo and van Dijken, 2003; Sarmiento et al., 2004). This thesis focuses on two such polynyas, both located within the Amundsen Sea, both sites of large phytoplankton blooms.

1.2 Research questions

In the Pine Island Polynya (PIP) peak summertime NPP has been estimated to reach up to 1.5 g C $m^{-2}day^{-1}$, whilst in the nearby Amundsen Sea Polynya (ASP) the peak is even higher at up to 2.5 g C $m^{-2}day^{-1}$ (Arrigo et al., 2012). The phytoplankton blooms in these two polynyas have been extensively studied from space using satellite measurements, and more recently investigated in-situ from research ships. Numerical modelling by St-Laurent et al. (2019) and Oliver et al. (2019) has replicated some of these observations and has deepened understanding of seasonal cycles in the ASP and PIP. However some key research questions remain unanswered:

- What factors drive the onset of phytoplankton blooms in the Amundsen Sea, and what factors drive their decline?
- How does the basal melting of nearby ice shelves impact the physics and biogeochemistry of coastal polynyas?
- How does ocean colour affect polynya physics and biogeochemistry?
- How does NPP vary in response to the variability currently observed in the Amundsen Sea, and how is it likely to respond to future climate change?

Numerical modelling is employed to investigate these research questions over the course of the three results chapters which make up the core of this thesis.

1.3 Structure of Thesis

Following this introduction, Chapter 2 reviews the current state of knowledge regarding ice-ocean interactions, phytoplankton blooms and carbon fluxes in the Southern Ocean. The results sections of this thesis are then structured as follows:

- In Chapter 4, a combination of one-dimensional and three-dimensional modelling is used to locate the transitions, in time and in space, between light and iron limitation within the Amundsen Sea.

- In Chapter 5, it is demonstrated that the spatial heterogeneity in iron limitation, combined with a buoyancy-dependent distribution of meltwater, leads to a complex relationship between melt rates beneath Dotson Ice Shelf (DIS) and primary production in the ASP.
- In Chapter 6, the large phytoplankton bloom in the PIP is revealed to in turn impact melt rates beneath Pine Island Glacier Ice Shelf (PIGIS). The result is an intricate coupling between biology, the cryosphere and carbon fluxes.

The synthesis in Chapter 7 brings together results from across all three research chapters to make an assessment on likely scenarios for the future of biogeochemical cycles in the Amundsen Sea. At the same time, the broader relevance of these results to other coastal polynyas, and to the wider Southern Ocean, is reviewed in some detail. Finally in Chapter 8 the key outcomes of this thesis are summarised in the context of ongoing efforts to model the changing Southern Ocean.

Chapter 2

Literature Review

2.1 Introduction

This literature review is structured as follows: first (2.2) the key physical and biogeochemical mechanisms relevant to this thesis are outlined; next (2.3) the different ways in which these mechanisms interact and compete in different regions are described; then (2.4) a review of current observations and state estimation is presented. Section 2.5 is an overview of past, current, and future trends in important aspects of the Southern Ocean system. Finally, in Section 2.6, the focus of this thesis on the Amundsen Sea polynyas (location shown in Figure 2.1) is justified, based on their relevance to the Southern Ocean as a whole.

2.2 Key Physical and Biogeochemical Mechanisms

2.2.1 Ice-ocean interactions

Intrusion of Circumpolar Deep Water

The Southern Ocean borders three ocean basins to its north, but forms a unique system due to due to the absence of any western boundary halting zonal circulation. The Antarctic Circumpolar Current (ACC), though partially impeded by the narrow Drake Passage between South America and the West Antarctic Peninsula (WAP), stretches around the entire Antarctic continent (Xu et al., 2020). Along the way it entrains water from the Atlantic, Pacific and Indian Oceans. The Circumpolar Deep Water (CDW) which dominates ACC dynamics is a warm, highly saline water mass rich in macronutrients from the northerly basins. Where it moves onto the Antarctic continental shelf, CDW becomes a key driver of coastal processes (Heywood et al., 2016).

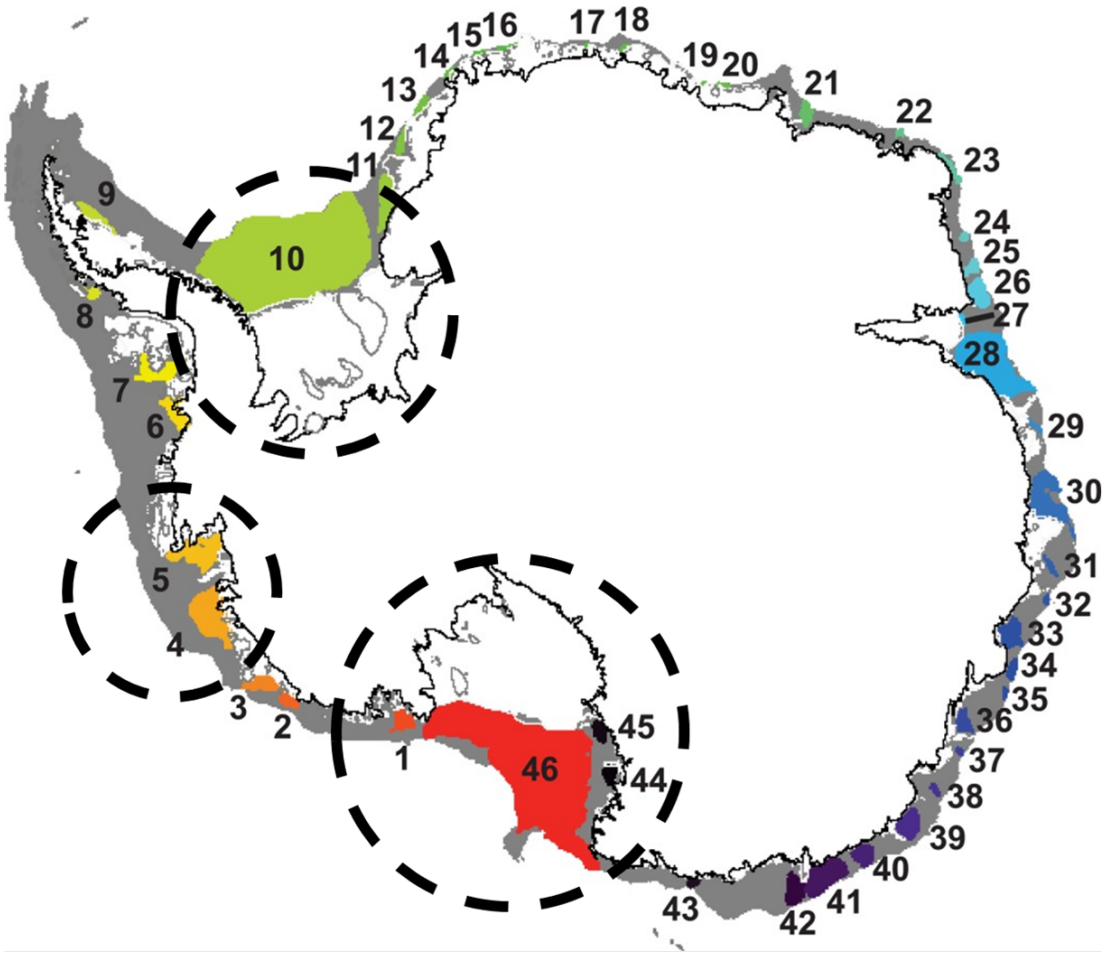

Figure 2.1: Location of important polynyas along the Antarctic coastline. Reproduced from Arrigo et al. (2015) with dashed circles added to emphasize regions of particular interest for this literature review. The Amundsen Sea Polynya and Pine Island Polynya are labelled numbers 4 and 5 respectively. The Weddell Sea Polynya is labelled number 10 and the Ross Sea Polynya is labelled number 46.

The location and timing of CDW intrusions onto the continental shelf is a primarily a product of bathymetry (Goldberg et al., 2020) and winds (Petty et al., 2013). Deep troughs in the continental shelf can extend below the CDW thermocline, providing a route for warm, saline waters to move towards the continent. Meanwhile the thermocline depth varies as a function of upper ocean – wind-driven – processes. Ekman pumping, forced by westerly winds at the sea edge, can move the position of the thermocline, and thus modulate the passage of CDW onto the continental shelf (Dutrieux et al., 2014).

As CDW moves closer to the coastline it undergoes a degree of mixing with other water masses, after which it is sometimes referred to as modified CDW (mCDW). Whether this mCDW ultimately comes into contact with the Antarctic Ice Sheet is, once again, dictated by bathymetry and by the overlying water masses (Silvano et al., 2018; St-Laurent et al., 2015). Where mCDW is able to flow into an ice shelf cavity, it can cause strong basal melting, and leaves the cavity itself substantially freshened by the input of glacial meltwater.

Holland and Jenkins (1999) arrived at a mathematical formulation to describe the relationship between the rate at which an ice shelf melts and the properties of the oceanic boundary layer adjacent to the ice shelf. This formulation describes the way that mCDW drives strong basal melting via the transfer of latent heat at the ice-ocean interface. Since the latent heat available is a function of mCDW properties, the basal melt rate is a function of the processes dictating CDW intrusions at the continental shelf break, as well as those dictating the degree of mixing it undergoes before reaching the cavity.

Formation of Dense Shelf Water

The wintertime freezing of seawater which forms sea ice across much of the Southern Ocean leaves behind an excess of salt in the surface ocean. This brine rejection increases the density at the top of the water column and thus has a destabilizing effect on the upper ocean (Petty et al., 2014). Where this leads to vertical mixing, the effect is to deepen the base of the mixed layer. Along with the degree of wind-driven mixing that the ocean is exposed to, the degree of brine rejection determines the depth of the wintertime mixed layer (St-Laurent et al., 2015; Venables et al., 2013).

Where brine rejection is strong, it can impact dynamics below the mixed layer by exporting relatively cool, saline water to depth (Haumann et al., 2020b). In the northern Atlantic this same mechanism underpins the Atlantic Meridional Overturning Circulation (AMOC); around Antarctica it leads to the formation of Antarctic Bottom Water (ABW). Exactly where and when this ABW formation occurs depends on the competition between downwards export of dense shelf water and intrusions of mCDW (Silvano et al., 2020).

The freezing point of seawater is pressure dependent, and thus with increasing depth the water temperature needed to melt ice shelves decreases. As dense shelf water is mixed downwards, it may eventually reach a point where its temperature lies above the local freezing temperature, thus allowing for basal melting even in the absence of mCDW (Jacobs et al., 1992).

Solar heating

In summer, surface waters are warmed by shortwave radiation from the sun, even in the cold, salinity-stratified polar oceans. A portion of shortwave radiation is reflected at the surface due to albedo, while the rest either contributes to ocean heating or is released back to the atmosphere via sensible, latent, and longwave heat fluxes. Solar heating is generally confined to the upper 50m of the ocean, but the autumnal deepening of the mixed layer – associated with wind-driven mixing and brine rejection – transports some of the sun's heat to greater depths.

If some of this heat is transported below ice shelves, then it may affect basal melt rates. Even when this near-surface melting is outweighed by high melt rates at depth, it may still have an important impact if it weakens the ice shelf at locations important for overall buttressing (Stewart et al., 2019).

2.2.2 Polynyas

Latent Heat Polynyas

Latent heat polynyas form wherever wind-driven export of sea ice exceeds wind-driven import of sea ice. This can occur if there is an upstream barrier which prevents sea ice being advected into the polynya, such as a land mass protruding into the ice floe.

Away from the polynya, where export and import are in balance, the annual freezing and melting of sea ice must also be in balance to maintain a consistent year-on-year ice cover. However within the polynya, where export is greater than import, a consistent seasonal cycle implies that each year more seawater is frozen into sea ice than is melted away. Accordingly, latent heat polynyas favor strong local brine rejection and, in some cases, formation of dense shelf-waters (Jacobs et al., 1992; St-Laurent et al., 2015).

At the same time, export of sea ice contributes to a net surface freshening away from polynyas as the exported sea ice melts. This can contribute to increased stratification and thus influence the upwelling of heat from depth (Haumann et al., 2020a).

Sensible Heat Polynyas

Sensible heat polynyas form because of convective heating of the surface ocean from depth. This heating may be steered by bathymetry, which can promoting upwelling of warm waters to the surface (Prend et al., 2019). The formation of sensible heat polynyas is highly unpredictable, and can have substantial impacts on exchanges of carbon and heat between the atmosphere and ocean (Bernardello et al., 2014). Both sensible heat and latent heat polynyas are poorly represented in the current generation of earth system models (Mohrmann et al., 2021).

2.2.3 Iron Supply

Atmospheric deposition and sea ice

The majority of worldwide iron supply to the ocean comes from the land, via the atmosphere, in the form of dust (Maher et al., 2010). In the Southern Ocean, deposition of iron-enriched dust is modulated by the presence of sea ice (Lannuzel et al., 2010). When sea ice melts, any dissolved iron which had been deposited on top of the ice floe is released into the water column, where it may help to initiate phytoplankton blooms. Conversely, when seawater freezes to form new sea ice, dissolved iron can be incorporated into the ice.

Iron within sea ice is generally found to be bound into long-lifetime organic ligands, as are other trace metals (Lannuzel et al., 2011). The transport of sea ice, and the seasonal nature of melting, means that sea ice can constitute a non-negligible source of iron even when atmospheric deposition rates are themselves low (Dinniman et al., 2020).

Circumpolar Deep Water, Sediments and the Meltwater Pump

Unlike macronutrients such as nitrate and phosphate, iron does not accumulate continuously with depth. This is due to the strong tendency for iron to be adsorbed onto sinking particles, ultimately becoming trapped in sediments. Nevertheless, CDW is in general richer in iron than overlying water masses, whilst iron captured in sediments at the seafloor may eventually be released back into the water column (Dinniman et al., 2020).

In order to transport this iron-enriched deep water to the surface, extensive upwelling or convective mixing must occur. In the vicinity of fast-melting ice shelves, this can be facilitated by a buoyancy-driven overturning circulation (St-Laurent et al., 2017), as has also been observed – for macronutrient supply – in Greenland (Cape et al., 2019; Oliver et al., 2020). This buoyancy-driven transport of nutrients and carbon is known as the meltwater pump. In sensible heat polynyas this upwelling of nutrients may instead be driven by bathymetric features (Prend et al., 2019).

Basal melting, subglacial runoff and iceberg calving

Atmospheric deposition of iron may also occur over the Antarctic Ice Sheet, whereupon the hydrological routing of surface meltwater to the base of the ice sheet can result in iron being incorporated into the ice. At the same time, the scouring of the Antarctic land mass entrains large quantities of iron-rich sediment at the glacial bed (Wadham et al., 2013).

Where the Antarctic Ice Sheet terminates in ice shelves, mass is lost by basal melting and iceberg calving, whilst liquid water at the glacial bed can also form a subglacial runoff into the ocean. All these three processes have the potential to carry both particulate and dissolved iron into coastal waters (Gerringa et al., 2012; Hopwood et al., 2018; Wadham et al., 2013)

2.2.4 Factors limiting phytoplankton growth

Iron Limitation

Phytoplankton require iron to maintain healthy photosynthetic apparatus and for uptake of nitrogen (Geider et al., 1997). Macronutrients such as nitrate and phosphate are replete in most of the Southern Ocean, due to the plentiful supply from the northerly ocean basins. Therefore it is the deficit of micronutrients, especially iron, which constrains growth rates and primary production.

The iron available to phytoplankton is a function of the wintertime iron inventory (Hopkinson et al., 2013) – before the onset of the bloom – as well as the rate at which iron is depleted and replenished during the bloom. The rate at which iron is depleted by phytoplankton is generally not in direct proportion to the phytoplankton growth rate, due to differing iron requirements under different light limitations (Geider et al., 1997), and the capacity of some phytoplankton species for intracellular storage (Borowitzka et al., 2016).

In addition to phytoplankton uptake, iron is lost from the mixed layer via scavenging by sinking particles. These losses are mitigated by recycling of dissolved iron and by remineralisation of particulate iron. Resupply of iron to the mixed layer can be from any of the sources detailed previously, and can occur via a combination of lateral and vertical transport (St-Laurent et al., 2017). At the end of the growth season these transport processes, coupled to the sea ice driven deepening of the mixed layer, control how much iron is available to phytoplankton at the start of the next growth season (Hopkinson et al., 2013).

Limitation by other Micronutrients

The mathematical basis of colimitation in phytoplankton was examined by Saito et al. (2008), with three distinct forms of colimitation identified:

- Independent
- Biochemically dependent
- Biochemical substitution

Independent colimitation refers to requirements for micronutrients which do not impact each other, in contrast to biochemically dependent colimitation. Biochemical substitution occurs where phytoplankton can adjust the micronutrient they utilise based on environmental availability (Robbins et al., 2016).

Although iron is the most widely limiting micronutrient across the Southern Ocean, observations do indicate instances where manganese (Middag et al., 2013) and vitamin B12 (Bertrand et al., 2007) colimit production alongside iron.

Light Limitation

The quantity of light available to phytoplankton is a function of surface irradiance, vertical mixing, and water column opacity. In turn, the surface irradiance is a function of solar angle, cloud cover and sea ice cover, whilst vertical mixing is a function of sea ice cover and winds (Venables et al., 2013).

The opacity of the water column is a function of its optically active constituents. Photosynthetically available radiation (PAR), the portion(s) of the visible light spectrum accessible to phytoplankton growth, is weakly attenuated by water molecules. Stronger attenuation can result from the presence of chlorophyll, coloured dissolved organic matter (CDOM) and particulate organic carbon (POC) detritus – all of which are biogeochemically coupled to the presence of phytoplankton (Dutkiewicz et al., 2015).

The two-way coupling between phytoplankton and the underwater light spectrum manifests as a negative “self-shading” feedback on further phytoplankton growth (Manizza et al., 2005; Schofield et al., 2015; Vernet et al., 2008). This is analogous to the process by which canopy cover in a forest restricts light available to tree saplings. Water column turbidity in some regions of Antarctica is also influenced by sediments sourced from glacial meltwater, potentially exacerbating light limitation (Pan et al., 2019).

2.2.5 Phytoplankton community composition

Succession

The factors limiting phytoplankton growth vary not only by location but by species; in general, different phytoplankton classes have different nutrient requirements. At the most basic level, this can be linked to the different sizes of cells from different species. Whilst the nutrient requirement scales with the volume of the cell – and therefore the cube of the radius – the capacity for uptake scales with the surface area – and therefore the square of the radius. As a result, smaller phytoplankton are in general better adapted to low nutrient environments compared to larger species (Borowitzka et al., 2016). The size spectrum of a phytoplankton bloom also influences its sinking speed, and thus its tendency to export carbon (Ducklow et al., 2015; Dunne et al., 2005; Henley et al., 2020). Finally, grazing by higher trophic levels tends to vary based on size and species of phytoplankton (Ducklow et al., 2015; Wilson et al., 2015)

In general, different species also have different light requirements. Phytoplankton are exposed to a fluctuating light environment (Carranza et al., 2018), and different species have evolved different strategies to cope with this. Idealised modelling by Burson et al. (2019) demonstrated gleaner-opportunist differentiation arising between species competing in a fluctuating light field. When combined with the effects of self-shading, this has the potential to lead to complex dynamics within intense phytoplankton blooms (Lee et al., 2021; Schofield et al., 2015; Vernet et al., 2008).

In general, natural phytoplankton communities exhibit a succession from one species to one or more others over the course of the growing season, linked to the succession from light limitation to micronutrient limitation (Arrigo et al., 2017; von Berg et al., 2020).

Silicification

Several classes of phytoplankton can incorporate silica into their internal or external structures, but silicon is only thought to be essential for diatoms. The diatom shell is formed from a combination of silicon with various carbohydrates and proteins (Borowitzka et al., 2016), and is in general well preserved in the fossil record (Konfirst et al., 2012; Smetacek, 1985). The necessary silicon is derived from seawater in the form of silicic acid, a process of active transport against a concentration gradient which implies significant metabolic cost (Borowitzka et al., 2016).

To justify this metabolic cost, there must be substantial benefits to diatoms in maintaining a silica shell. Borowitzka et al. (2016) summarise these benefits as

- Protection against attack by grazers (Pondaven et al., 2007), viruses (Biggs et al., 2021) or parasites;

- Protection against exposure to high levels of light (Lee et al., 2021) or toxic metals (Koppel et al., 2021);
- Faster sinking speeds (Raven and Waite, 2004; Smetacek, 1985), leading to increasing access to nutrients at depth.

Diatom silica requirement increases under iron limited conditions (Borowitzka et al., 2016), potentially leading to iron-silica colimitation in some Southern Ocean diatom communities.

Calcification

Natural seawater is abundant in calcium and carbonate ions, but the precipitation of calcium carbonate in the absence of biology is kintetically unfavourable, so spontaneous mineralisation is rare (Borowitzka et al., 2016). Analogous to silicic acid uptake in diatoms, the active transport of calcium ions across calcifying phytoplankton membranes is energetically expensive. The potential benefits of forming calcium carbonate structures are similar to those of forming a silica shell (Borowitzka et al., 2016), including the ability to modify the light field within the cell.

Around 50% of the burial flux of calcium carbonate worldwide originates from the coccolithophore class of phytoplankton, which take up bicarbonate from seawater and precipitate calcite within intracellular compartments (Borowitzka et al., 2016). The smaller size, and thus lower nutrient requirement, of coccolithophores can allow them to outcompete larger species such as diatoms in areas of the Southern Ocean (Nissen et al., 2018). However coccolithophores are uniquely vulnerable to climate change in the form of ocean acidification. Field observations and modelling indicate an ongoing threat to calcifying phytoplankton (Freeman and Lovenduski, 2015), though laboratory studies have been less conclusive (Borowitzka et al., 2016).

2.2.6 Phytoplankton in the ecosystem

Grazing

Phytoplankton are grazed by predators including copepods and krill, which in some regions can be the primary control on bloom termination (Kauko et al., 2021). Krill support a large part of the Southern Ocean ecosystem (Henley et al., 2020), as well as being a commercially important fishery themselves. Krill are prey for species of fish and seals, as well as seabirds (McClymont et al., 2021). Studies including Carvalho et al. (2020) have shown that localised relief from iron or light limitation can lead to phytoplankton blooms which in turn lead to hotspots of activity for higher trophic levels.

Different phytoplankton groups exhibit different levels of palatability to grazers (Ducklow et al., 2015; Wilson et al., 2015). Whilst diatoms and coccolithophores form silica and calcium carbonate shells respectively, haptophytes such as *Phaeocystis Antarctica* can agglomerate into large colonies that are harder for grazers to digest. On a large scale, modelling indicates that grazing is a major control on the competition between coccolithophores, diatoms and phaeocystis antarctica (Nissen and Vogt, 2021; Nissen et al., 2018). Grazing impacts carbon export both by this regulation of phytoplankton cell size and by providing an additional means of downwards transport through the water column (Ducklow et al., 2015; Smetacek, 1985; Wilson et al., 2015).

Viral lysis

The extent of viral infection in both lakes and oceans is a fast developing area of research, with viral lysis increasingly implicated as a first-order control on phytoplankton bloom demise (Biggs et al., 2021; Evans et al., 2021). The dead phytoplankton matter resulting from viral lysis can in some cases be a source of food for bacteria, thus reducing the food available to organic matter; in other cases the infected phytoplankton cells can agglomerate into larger particles which sink quickly through the water column. These two mechanisms are known respectively as the viral shunt and the viral shuttle and have opposite effects on overall carbon export, and it has been suggested that the strongly carbon-exporting shuttle may gain an advantage over the shunt in iron-limited regions (Kranzler et al., 2021).

Viral lysis can sometimes provide a source of dissolved organic matter to bacteria as part of the microbial loop (Williams et al., 2016), though bacteria themselves are also subject to viral infection. Succession from a microbial loop to a viral shunt has been shown by Evans et al. (2021), mirroring the tendency for a succession from light to micronutrient limitation of phytoplankton growth rate (Arrigo et al., 2017; von Berg et al., 2020).

2.2.7 Carbon fluxes

The Solubility Pump

The rate of exchange of carbon between the atmosphere and ocean increases as a function of the discrepancy in partial pressure at the air-ocean boundary. Thus any process which brings Dissolved Inorganic Carbon (DIC) to the surface favors outgassing, whilst any process which removes DIC from the surface favors uptake (Gupta et al., 2020).

In the vicinity of ice shelves, the same buoyancy-driven circulation which pulls iron to the surface may also pull DIC to the surface (Mu et al., 2014). On a larger scale, the upwelling of DIC-rich water masses at fronts in the Southern Ocean can lead to intense outgassing, particularly in sensible heat polynyas (Bernardello et al., 2014).

The solubility of carbon dioxide in seawater increases with decreasing temperature, so that cold waters tend to take up carbon from the atmosphere whilst warm waters release it. As well as temperature, carbon dioxide solubility is influenced by salinity and by alkalinity, although generally to a lesser extent (Follows et al., 2006).

The Biological Pump

Phytoplankton growth converts DIC to organic carbon, and thus depletes the pool of DIC close to the ocean surface. Depending on processes occurring at depth in the water column (Dittrich, 2020; Henley et al., 2020; Yager et al., 2016), this can lead to a flux of carbon from the atmosphere into the ocean, via a mechanism known as the biological pump.

In areas of calcifying plankton, the biological pump is weakened by the precipitation of calcium carbonate, which generates carbon dioxide as a by-product (Rosso et al., 2017). Hence the community composition of a phytoplankton bloom is directly linked to surface carbon fluxes, with increased dominance of coccolithophores associated with a local weakening to the biological export of carbon (Borowitzka et al., 2016).

The realisation that iron availability might have dictated past shifts in climate via changes in high latitude productivity (Maher et al., 2010; Martin et al., 1991) led researchers to hypothesise that large-scale iron fertilisation could help to offset climate change. Boyd et al. (2007) reviewed some of these efforts in the Southern Ocean, and provided suggestions for future work. However a consensus subsequently emerged against iron fertilisation as a viable form of climate change mitigation (Strong et al., 2009).

Obstruction by sea ice

Where sea ice is present, it is an effective barrier to air-sea exchange of CO_2 and other gases (Gupta et al., 2020). Thus in an outgassing region sea ice cover will lead to more carbon being retained in the ocean, whereas in an uptake region sea ice cover will lead to more carbon being retained in the atmosphere. In addition, the direct contribution of sea ice freezing and melting to surface DIC levels has a non-negligible and highly variable impact on the solubility pump (Hauri et al., 2015; Rosso et al., 2017).

At the same time, sea ice reduces the drag of wind on the sea surface, thereby maintaining stratification, and prevents light reaching phytoplankton, heightening light limitation (Venables et al., 2013). The latter two mechanisms can have confounding influences on phytoplankton growth, and thus on the potential for uptake via the biological pump.

2.2.8 Atmospheric influences

Cloud cover

Cloud cover has been shown to impact coastal phytoplankton communities, particularly *p. antarctica* (Park et al., 2017), both directly due to changes in surface irradiance, and indirectly via changes to sea ice cover and upper ocean stratification.

Atmospheric Dimethyl Sulphide (DMS) concentrations are in turn impacted by blooms of *p. antarctica* (Tortell et al., 2012), and the presence of DMS in the local atmosphere may help to seed the formation of clouds. This linkage between phytoplankton and cloud albedo has been suggested as a climate feedback mechanism (Charlson et al., 1987). In the Amundsen Sea, concentrations of DMS have been shown to correlate with concentrations of chlorophyll (Tortell et al., 2012).

Winds

As well as influencing cloud cover, winds impart stress on the ocean surface and can transport warm air across the Antarctic coastline. Winds dictate Ekman pumping in the marginal sea ice zone, which in turn dictates the access of warm water to the underside of ice shelves (Dutrieux et al., 2014; Kimura et al., 2017; Petty et al., 2013). Meanwhile warmer air intrusions may have an impact on surface melting of ice shelves (Djoumna and Holland, 2021). Warm air tends to cause melting, but also brings increased snowfall.

Wind stress drives the export of sea ice from latent heat polynyas, and thus variability in winds may account for variability in polynya extent and sea ice production (Stammerjohn et al., 2015; Tamura et al., 2016). Wind stress on the ocean surface drives mixed layer deepening, which is a crucial influence on both nutrient limitation and light limitation for phytoplankton (Park et al., 2019; Venables et al., 2013). A combination of mixed layer dynamics and eddies in turn impacts ventilation of carbon dioxide in the Southern Ocean (Dove et al., 2021). Finally, strong winds can impact higher trophic levels in the Southern Ocean ecosystem, such as by improving survival chances for large gliding seabirds (Weimerskirch et al., 2012).

The Southern Annular Mode

The strength of westerly winds in the Southern Ocean is controlled by a meridional air pressure gradient. This Southern Annular Mode (SAM) is defined as the difference in zonally averaged sea level pressure between 40°S and 65°S. Sea ice has a complex sensitivity to SAM, which is the product of two distinct mechanisms on two distinct time scales (Ferreira et al., 2015; Holland et al., 2017). On short time scales sea ice cover increases in response to positive SAM, but on long time scales it decreases. The observations of Jacobs (2006) suggest that this long time scale response, which is caused by increased upwelling of CDW, could also be associated with faster basal melting of ice shelves.

The changes to ocean circulation associated with the positive phase of the SAM in turn have an impact on carbon fluxes (Hauck et al., 2013), with the positive phase being associated with higher biomass and chlorophyll concentrations. This in turn can affect krill and seabird populations (Barbraud et al., 2012). The influence of the SAM on coastal Antarctic polynyas is however difficult to disentangle from other forcings such as the Amundsen Sea Low (ASL) and Southern Oscillation (Jacobs et al., 2012).

2.3 Geographical Variations

2.3.1 Meridional gradients

Sea ice

In general, latent heat polynyas form close to the Antarctic coastline, whereas sensible heat polynyas form off the continental shelf in the open Southern Ocean. Haumann et al. (2020a) found that the cooling of Southern Ocean surface waters is sensitive to the rate at which sea ice is redistributed from the continental shelf, so that the thermodynamics of sensible and latent heat polynyas may be linked. Where more sea ice is imported into the open ocean, its subsequent melting can impede the upwelling of warm waters necessary to generate sensible heat polynyas.

Iron supply

Atmospheric deposition of iron decreases with increasing latitude in the Southern Ocean, but this is outweighed by the increase in iron availability linked to proximity to ice shelves (Alderkamp et al., 2012; Arrigo et al., 2017; Gerringa et al., 2012). Sieber et al. (2021) emphasized the combined importance of recycling, biological uptake and scavenging in controlling the cycling of this coastal iron. Sources on the the continental shelf have been suggested as the drivers of iron supply to the rest of the Southern Ocean, via lateral fluxes (De Jong et al., 2012).

However Sieber et al. (2021) found that, at least near the WAP, strong zonal currents prevent that iron originating on the continental shelf from being transported out into the open Southern Ocean. Instead hydrothermal sources and local topography play a large role in setting iron chemistry for waters moving into the lower latitude basins.

Factors limiting phytoplankton growth

Global modelling by Galbraith et al. (2010) compared two ways in which iron concentrations can limit phytoplankton growth. Firstly, iron limitation reduces the light-saturated photosynthesis rate. Secondly, iron limitation reduces the photosynthetic efficiency, defined as the fraction of incoming light which is converted to chemical energy. In the Southern Ocean, iron limitation of light-saturated photosynthetic rates was seen to dominate over iron limitation of photosynthetic efficiency (Galbraith et al., 2010). This is because, at the very low iron concentrations found across much of the Southern Ocean, growth rates - and thus energy demands - are too low for changes in photosynthetic efficiency to be important. Galbraith et al. (2010) also suggest that the natural tendency for iron limitated systems to favour smaller and thus more energy efficient phytoplankton (as observed by Morel et al. (1991)) may play a part in reducing the impacts from iron limitation of photosynthetic efficiency.

However in those small areas of the Southern Ocean that exhibit very intense primary production, such as coastal polynyas, changes to photosynthetic efficiency may be locally important. Indeed Strzepek and Harrison (2004) found that coastal and open ocean diatoms had evolved different photosynthetic apparatus in response to different levels of iron limitation. This discrepancy appears to be a response to the decrease in iron availability with increasing distance from the coast (Arrigo et al., 2017).

Phytoplankton community composition

Carvalho et al. (2020) found a transition from diatom domination in the southerly part of the WAP to a greater balance between diatoms and cryptophytes in the north. This transition was attributed to gradients in solar angle, wind patterns, and the timing of sea ice retreat.

On a larger scale, the principal feature of Southern Ocean phytoplankton community composition is the transition from diatoms to coccolithophores with decreasing latitude (Freeman et al., 2018; Nissen et al., 2021; Sieber et al., 2021). This coincides with a sharp gradient in ocean biogeochemistry - the silica front - polewards of which silica levels are substantially elevated. Changes in the position of this front may have taken place in response to past changes in the Earth's climate (Cortese and Gersonde, 2007) and may have global effects on ocean biogeochemistry in the future (Nissen et al., 2021).

Phytoplankton in the ecosystem

Grazing of krill by large animals such as penguins is dependent on hotspots of productivity which may in turn be dependent on local bathymetry or topography (Carvalho et al., 2020). On a large scale, the distribution of krill tends to follow latitudinal bands which form grazing territories for various different marine mammals and birds. The distance between breeding grounds and areas of the Southern Ocean with suitable prey is a key factor in determining survival chances for penguins and gliding seabirds (Cristofari et al., 2018; McClymont et al., 2021). Therefore meridional patterns in primary production are closely tied to higher trophic levels in the Southern Ocean (Henley et al., 2020). At the same time, continental shelf systems are vital for wider marine ecosystems in the Southern Ocean (Smith Jr et al., 2012), with the Ross Sea south of 75 °S recently being designated as the largest Marine Protected Area in the world (Brooks et al., 2020).

At the same time, studies of the Ross Sea (Arrigo et al., 2000; Caron et al., 2000) have suggested that rates of primary production and zooplankton grazing are decoupled in some polynyas, implying that grazing may not have a substantial impact on phytoplankton growth in these regions close to ice shelves.

Carbon fluxes

Carbon fluxes in the Southern Ocean can be separated into fluxes of anthropogenic and natural carbon. The latter originates in water masses which have not been in contact with the atmosphere since pre-industrial times (Sarmiento et al., 1998). On a zonally averaged basis, all latitudes of the Southern Ocean are sinks for anthropogenic carbon, whereas there is a transition in natural carbon fluxes from a source south of the polar front to a sink at lower latitudes (Gruber et al., 2019).

Studies of the Drake Passage (Jersild and Ito, 2020) and western Indian Ocean sector of the Southern Ocean (Dove et al., 2021) found high spatial variability in air-sea carbon fluxes in response to eddies across a wide range of scales. In particular Dove et al. (2021) highlighted the importance of standing meanders in the ACC as hotspots of carbon ventilation, while Jersild and Ito (2020) showed that large scale currents and seasonal mixing source carbon to the euphotic zone, with smaller scale eddies combining with biological export to remove carbon to depth. The balance between these import and export processes changes with proximity to the Polar and Subantarctic Fronts.

On the continental shelf carbon fluxes are influenced by coastal polynyas and by ice shelves, as well as by sea ice (Rosso et al., 2017). Mu et al. (2014) found that in a polynya otherwise characterised by strong uptake, the ice shelf outflow itself was a site of carbon release to the atmosphere.

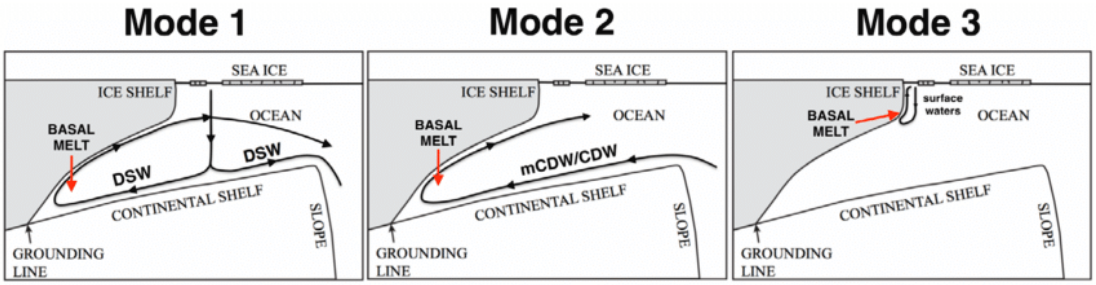

Figure 2.2: The three modes of ice shelf basal melting, from Jacobs et al. (1992) and Silvano et al. (2016). In the first mode, dense shelf water dominates; in the second mode, CDW dominates; in the third mode, surface waters warmed by the sun dominate.

2.3.2 Zonal gradients

Ice-ocean interactions

The large differences between different coastal regions of Antarctica led Jacobs et al. (1992) to introduce the idea of modes of melting to categorise their diverse ice-ocean interactions. This idea was extended by Jenkins et al. (2016) and Silvano et al. (2016). The designation of mode depends on the balance between processes of circumpolar deep water intrusion, dense shelf water formation and solar heating (Figure 2.2). In brief, the three modes are

- Mode I, dominated by the formation of dense shelf water,
- Mode II, dominated by the inflow of circumpolar deep water,
- Mode III, dominated by the influence of solar heating.

Most of West Antarctica, as well as Totten glacier in East Antarctica (Silvano et al., 2016) is classified as Mode II. This is due to intrusions of CDW which in turn are sensitive to bathymetry (Goldberg et al., 2020).

In the Ross Sea, Mode I dominates and there is strong dense shelf water formation (Silvano et al., 2020; Smith Jr et al., 2012). Here, as well as in the Weddell Sea, there is also the potential for supercooling within ice shelf meltwater plumes (Haumann et al., 2020b). At the same time, Stewart et al. (2019) show evidence of strong Mode III melting beneath Ross Ice Shelf. Ice shelves which melt by different modes may also have different sensitivities to increasing concentrations of glacial meltwater on the continental shelf (Moorman et al., 2020).

Sea ice

Sea ice production varies substantially across different coastal polynyas (Tamura et al., 2016) in response to wind and topographical features. In the Ross Sea, which is a site of ABW formation, sea ice dynamics can have a large impact on the sequestration of carbon on millenial timescales (Smith Jr et al., 2012).

Iron supply

The dominant source of iron to each coastal polynya depends in large part on the dominant mode of ice shelf melting. Circumpolar modelling by Dinniman et al. (2020) examined sources including sediments, the meltwater pump, glacial iron, vertical mixing and sea ice. The result of St-Laurent et al. (2017) was affirmed - that the meltwater pump dominates iron supply to the Amundsen Sea, with iron from the meltwater itself a smaller but still important contribution. This explains the correlation between ice shelves and high primary production, though the mechanism is different from that originally proposed by Arrigo et al. (2015).

In the same study Dinniman et al. (2020) found that vertical mixing - independent of and removed from the ice shelf cavity - dominates iron supply in the Ross Sea, with sea ice also forming a larger part of the iron budget compared to the Amundsen Sea. Meanwhile in the Weddell Sea, whilst ice-ocean interactions resemble those in the Ross Sea, there is an additional - non-local - input of meltwater-sourced iron from upstream ice shelves.

Factors limiting phytoplankton growth

Iron deficiency is the key factor limiting primary production across much of the Antarctic continental shelf. However evidence for iron-manganese colimitation of phytoplankton growth rates has been found both in the Drake Passage (Browning et al., 2021) and Weddell Sea (Wu et al., 2019). Meanwhile, Bertrand et al. (2007) found evidence of vitamin B12, as well as iron, limitation in the Ross Sea.

Park et al. (2017) argued that the discrepancy in primary production between the adjacent Amundsen Sea Polynya (ASP) and Pine Island Polynya (PIP) can be ascribed to local variations in cloud cover - and thus light limitation. Meanwhile, within the fjords of the WAP, light limitation may be influenced by meltwater turbidity (Pan et al., 2019).

Carbon fluxes

There is large zonal variability in carbon fluxes and export around the Southern Ocean. Importantly, Lee et al. (2017) found that regions such as the Amundsen Sea displaying very large phytoplankton blooms driven by high basal melt rates might nevertheless exhibit very low efficiency in their export of carbon to depth. This implies that carbon export efficiency, as well as iron supply (Dinniman et al., 2020), may be closely coupled to the mode of ice-shelf melting (Jacobs et al., 1992).

A circumpolar study by Rosso et al. (2017) confirmed variations in the carbon budget across different regions of the Antarctic continental shelf, with a particular contrast in areas exhibiting latent heat polynyas. In areas of intense sea ice production, there is a positive contribution to surface DIC levels, which is then advected away away from the polynya. When sea ice subsequently melts, this excess DIC is once again diluted (Rosso et al., 2017).

2.4 Observations and Data Assimilation

2.4.1 In-situ measurement

Research cruises

In-situ data from the Southern Ocean include both repeat transects (Xu et al., 2020) and one-off expeditions (Yager et al., 2012). The latter is in general the case for studies of coastal polynyas, where heavy sea ice cover makes access difficult and unpredictable. Repeat transects can be used to constrain large-scale data assimilation and to monitor long term changes in Southern Ocean water masses.

Studies of phytoplankton dynamics make use of a combination of biogeochemical tracer measurements and removal of phytoplankton for incubation (Browning et al., 2021). Incubation studies may involve the addition of a micronutrient, such as iron, to examine the response of phytoplankton to relief from micronutrient limitation (Alderkamp et al., 2015). Alternatively variable light conditions during incubation can be used to examine light limitation (Park et al., 2017).

Gliders

The development of unmanned vehicles such as underwater gliders has added new capabilities to ocean observation, complementing those already possible from ships and satellites (Rudnick et al., 2004). The battery power in each glider is used to control buoyancy and thus vertical motion, whilst wings are angled to move the glider laterally (Figure 2.3 a). After being deployed from a ship or platform a glider can collect data continously as it completes cycles of rising and sinking on a sawtooth pattern.

Gliders have proved to be particularly useful in manoeuvring around coastal environments, which in the Southern Ocean makes them ideal for observations of ice shelf cavities (Miles et al., 2016). The maximum speeds achieved by gliders are on the same order of magnitude as ice shelf outflows, so they are well suited to sample meltwater plumes.

Moorings and sediment traps

Moorings can be used to obtain vertical hydrographic and biogeochemical data consistently and at high temporal resolution (Dutrieux et al., 2014). In addition, moorings can be used to deploy sediment traps from which the seasonal evolution of particle export can be tracked, particularly in polynyas. For instance Ducklow et al. (2015) were able to use sediment traps to infer substantial differences in organic matter export between the Amundsen Sea, Ross Sea and WAP. Material from sediment traps can further be compared with that from sediment cores to infer past climate change (Cortese and Gersonde, 2007).

2.4.2 Remote sensing

The basal melting of floating ice shelves leads to a change in surface elevation which can be measured by satellite. In addition, elevation measurements can be used to detect channels under ice shelfs, which may be important for focusing and enhancing basal melting (Gourmelen et al., 2017).

The production of chlorophyll by phytoplankton makes blooms visible from satellite imagery (Arrigo et al., 2008; Arrigo and van Dijken, 2003). However satellite imagery can only measure ocean colour down to one optical depth, D_{opt}, as defined by

$$I(D_{opt}) = \frac{I_0}{e} \tag{2.1}$$

where e is the natural number, I_0 is the irradiance at the surface and $I(D_{opt})$ is the irradiance at one optical depth. This imagery can therefore misrepresent the nature of phytoplankton dynamics throughout the mixed layer, especially if the mixed layer depth is much greater than the optical layer depth. Ground-truthing of algorithms to extract primary production from satellite has traditionally used ship-borne surveys of ocean optics, but floats equipped with optical sensors are now beginning to fulfill this calibration role (Haëntjens et al., 2017; Organelli et al., 2017).

2.4.3 Southern Ocean Carbon and Climate Observations and Modelling (SOCCOM)

Argo floats

The Southern Ocean Carbon and Climate Observations and Modelling project (SOCCOM) has been running since 2014 to integrate data and theory to understand ongoing and future trends in the Southern Ocean. The principal observational component of the SOCCOM project is the deployment of biogeochemical Argo (bgc-Argo) floats across the Southern Ocean (Johnson et al., 2017; Riser et al., 2018). Each bgc-Argo float is equipped with sensors for pH, optical backscatter, nitrate, fluorescence, oxygen and irradiance; the floats transmit data via satellite receivers every time they surface (Figure 2.3 b).

One use of the floats has been in revisiting ocean colour algorithms (Haëntjens et al., 2017) by evaluating relationships between attenuation and chlorophyll concentrations. At the same time, the data being collected on these relationships may lead to better paramterization of self-shading in models (Morel, 1988).

Bgc-argo floats - combined with seal data - have also been used to observe the Weddell Sea Polynya and infer seasonal changes in phytoplankton limitation (von Berg et al., 2020). Briggs et al. (2018) combined float data with a one dimensional model using boundary conditions from the float trajectory to infer NPP. Finally, Carranza et al. (2018) used float data to infer changes in phytoplankton photoacclimation in response to storm events.

Dove et al. (2021) combined float and glider data in order to examine ventilation of carbon and its relation to eddying. In the future float data are likely to become increasingly important as a constraint on the Biological Southern Ocean State Estimate (BSOSE) and on the closure of heat (Tamsitt et al., 2016) and carbon (Rosso et al., 2017) budgets.

The Biological Southern Ocean State Estimate (BSOSE)

The Southern Ocean State Estimation (SOSE) was developed to assimilate ocean and atmosphere data for the entire Southern Ocean over multiple timescales, using the MIT General Circulation Model (MITgcm) (Marshall et al., 1997a). This was evolved into the Biological Southern Ocean State Estimate (BSOSE) with the assimilation of biogeochemical datasets and the incorporation of the Biology Light Iron Nutrients and Gases (BLING) model (Galbraith et al., 2010) into MITgcm (Verdy and Mazloff, 2017).

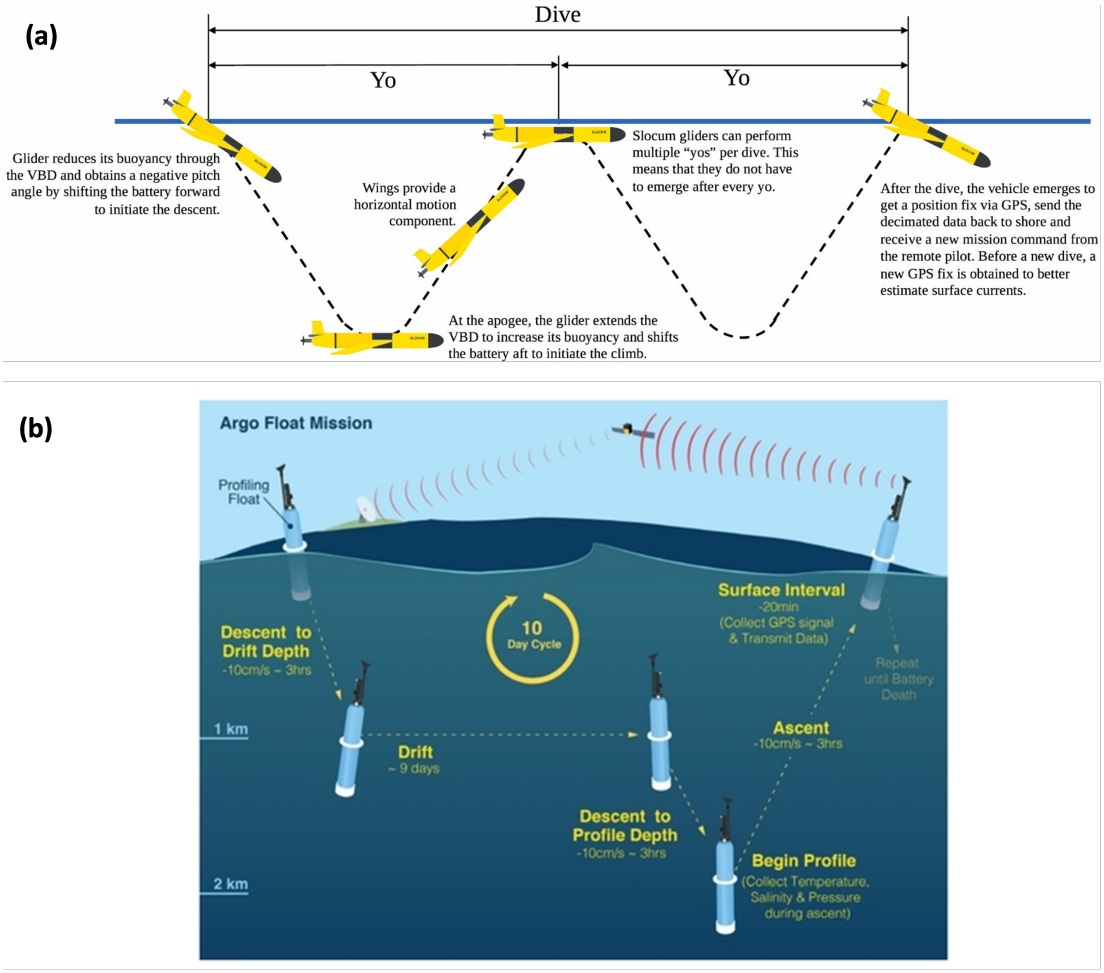

Figure 2.3: (a) The sawtooth diving pattern with which gliders sample the water column (schematic from Anderlini et al. (2021)), with buoyancy regulated by a Variable Buoyancy Device (VBD); (b) the drifting, descent and resurfacing of an Argo float (schematic from Jayne et al. (2017)).

BLING is an intermediate complexity model (Galbraith et al., 2015) which includes three phytoplankton classes, originally intended to represent coccolithiphores, diatoms and diazotrophs. The model is well suited to the Southern Ocean due to its relatively sophisticated representation of iron limitation (Geider et al., 1997). BSOSE has been used to study variability in carbon budgets (Rosso et al., 2017), and also as a source of boundary conditions for regional models of carbon fluxes (Jersild and Ito, 2020). A graphical representation of the BLING model is given in Figure 2.4.

2.5 Past, Current and Future Trends

2.5.1 Past trends

Ice-ocean interactions

With the exception of the Ross Sea (Smith Jr et al., 2012), the continental shelves of Antarctica were all glaciated during the Last Glacial Maximum (LGM). This can be seen in sediment cores using diatoms as proxies; layers of depleted diatom material are more likely to correspond to glacial periods, where biological production is reduced and delivery of non-biogenic sediment from glaciers is increased (Konfirst et al., 2012). Marine sediment cores have also been used to examine past changes to sea ice cover (Cortese and Gersonde, 2007; Lamping et al., 2020).

Modelling suggests that the West Antarctic Ice Sheet (WAIS) collapsed during past interglacial stages, with this collapse accelerated by the the retrograde bed on which the WAIS sits (Pollard and DeConto, 2009). The IPCC Special Report on the Oceans and Cryosphere (SROCC) concluded that "past rapid changes have *likely* been driven by the incursion of Circumpolar Deep Water onto the Antarctic continental shelf" (Portner et al., 2019).

Iron supply

In the modern earth system, there is far greater dust deposition in the northern than in the southern hemisphere, and the Southern Ocean in particular is deficient in aerial sources of iron. What deposition does take place is largely sourced from Patagonia, with this transportation pathway dictated by the strength of westerly wind patterns (Maher et al., 2010).

Ice cores from Antarctica indicate that during the LGM dust fluxes were over an order of magnitude greater than today, largely as a result of greater dust export from Patagonia. Sugden et al. (2009) argue that the sediments exposed by low sea level during the LGM drove this much stronger supply of dust to Antarctica and the Southern Ocean.

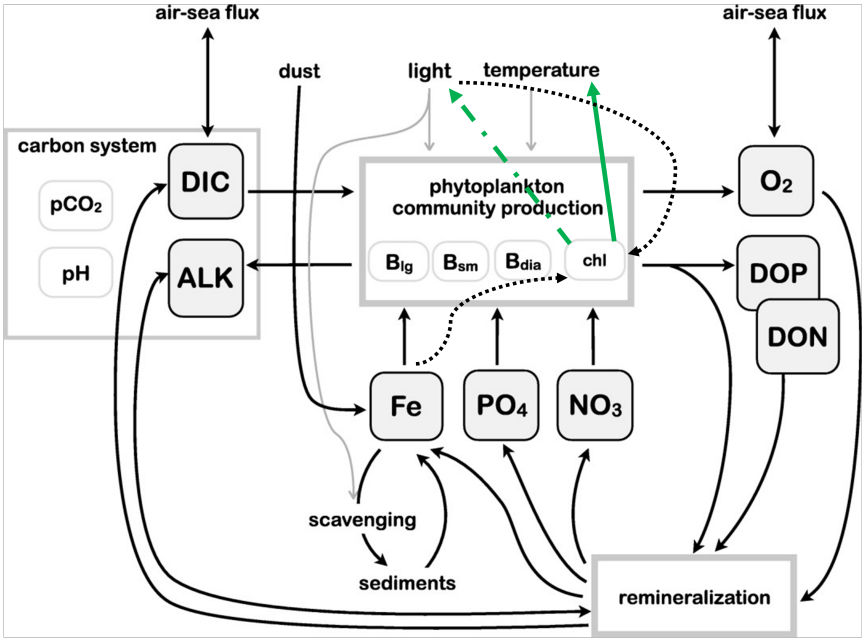

Figure 2.4: Schematic of the Biology Light Iron Nutrients and Gases (BLING) model, adapted from Verdy and Mazloff (2017). Black dotted lines are added to the diagram to explicitly represent the impact of light (via photoacclimation) and iron (as a form of colimitation) on chlorophyll to carbon ratios. Green lines represent modifications to the MITgcm BLING code made in the course of this study. The green dash-dot line represents the self-shading feedback, covered in Chapters 4 and 5, whilst the solid green line represents the feedback of ocean colour onto shortwave heating, covered in Chapter 6.

Factors limiting phytoplankton growth

Metal requirements in phytoplankton do to some extent reflect the availability of these metals in deep seawater (Morel, 2008), but may be far more similar to metal availablity in ancient oceans (Robbins et al., 2016). Evolution of enzymes which utilise metals to aid photosynthesis and other biochemical reactions is very slow (Saito et al., 2003), and thus does not necessarily keep pace with even dramatic changes to ocean chemistry (Robbins et al., 2016). Saito et al. (2003) suggested that - in cyanobacteria - marine trace metal requirements reflected evolution in a sulphidic, rather than oxic ocean. Other studies have argued that metal requirements are driven by cellular function, largely irrespective of availability in the environment (Robbins et al., 2013).

If metal requirements do in fact reflect the conditions under which phytoplankton evolved, then iron limitation is ultimately a product of the shifts in ocean chemistry which have rendered bioavailable iron far less abundant than in the deep past (Robbins et al., 2016). In so far as phytoplankton have evolved to cope with modern – oxygenated – ocean chemistry, it is by using ligands to accelerate iron uptake (Morel, 2008), or by substitution of metals (Saito et al., 2008).

On shorter time scales, changes to trace element sources, such as atmospheric iron deposition (Maher et al., 2010), can lead to changes in community composition. To an extent these changes may buffer the response of carbon fluxes to changes in iron supply (Henley et al., 2020). It has also been suggested that Southern Ocean phytoplankton may have evolved larger photosynthetic antennae than low latitude species in order to harvest more photons under low light, low temperature conditions (Strzepek et al., 2019).

Phytoplankton in the ecosystem

McClymont et al. (2021) used petrel stomach oils as a proxy to infer the presence of coastal polynyas during the LGM. From the chemical make up of stomach oils found in the Weddell Sea sector, the authors were able to identify a transition from a diet dominated by krill to one containing larger amounts of fish. This dietary transition implies a shift in petrel foraging location, from the open ocean to coastal polynyas. Genetic evidence was used by Cristofari et al. (2018) to identify bottlenecks in king penguin populations, ascribed to a polewards shift in krill during warm periods which pushes king penguins to forage further from their breeding grounds on Subantarctic islands.

A large change in top down pressures on Southern Ocean ecosystems occurred with the expansion, then the cessation, of industrial whaling over recent centuries. Maldonado et al. (2016) showed whaling had a measurable impact on the iron budget, particularly on recycling within the euphotic layer.

Carbon fluxes

The Southern Ocean switched from being a source to a sink of carbon due to human activity raising atmospheric CO2 levels to above those observed on average throughout the Southern Ocean (Gupta et al., 2020). On a longer timescale the iron hypothesis of Martin et al. (1991) implies that increased iron supply during past glacial periods increased Southern Ocean primary production, with the subsequent carbon export helping to maintain low levels of carbon dioxide in the atmosphere (Martínez-García et al., 2014).

2.5.2 Ongoing trends

Ice-ocean interactions

Since the mid-twentieth century a weakening of ABW formation in the Ross Sea has been observed. This is partially due to the freshening of the coastal current, which has been transporting increasing concentrations of meltwater from Amundsen and Bellingshausen Seas (Nakayama et al., 2014). In recent years there has been a partial recovery of bottom water formation in the Ross Sea, which Silvano et al. (2020) linked to anomalies in winds and in the SAM.

The speed up of glaciers in the Amundsen Sea sector has been attributed to the same strong basal melting which freshens the coastal current to the Ross Sea (Shepherd et al., 2004). However Joughin et al. (2021) recently suggested that inland dynamics may in fact be driving this change, since in some cases the acceleration precedes increased basal melting.

Sea ice

The anthropologically forced depletion of ozone in the atmosphere has been linked with some of the trends currently observed in sea ice concentrations (Ferreira et al., 2015; Holland et al., 2017). Meanwhile interannual variability and trends in coastal polynyas have likely been driven by winds, though a contribution from sensible heat is also possible (Stammerjohn et al., 2015). Recent years have also seen the reemergence of the (sensible heat-driven) Weddell Sea Polynya, which has been the site of intense phytoplankton blooms (von Berg et al., 2020).

Overall, sea ice trends in the Southern Ocean have not resembled the clear decrease observed in the Arctic. In summary the IPCC SROCC states that "it is *very likely* that Antarctic sea ice cover exhibits no significant trend over the period of satellite observations (1979-2018)" (Portner et al., 2019). However the most recent data – since 2018 – show substantially reduced sea ice cover around some parts of Antarctica (Parkinson, 2019).

Iron supply

The IPCC SROCC concludes, with *medium evidence* and *high agreement*, that "enhanced input of iron from ice shelves, glacial meltwater and icebergs stimulates primary production in polynyas, coastal regions and the wider Southern Ocean" (Portner et al., 2019). On the other hand, it is noted that "there is *low confidence* in predicted zonal changes in phytoplankton biomass due to low confidence regarding future changes in iron supply in the Southern Ocean" (Portner et al., 2019).

Recently remote sensing has been used to track large dust deposition events and their localised impacts on ocean primary production. Wang et al. (2021) and Tang et al. (2021) both found evidence that dust from the large Australian wildfires in early 2020 was transported by westerly winds to regions of the Southern Ocean where they fertilised large phytoplankton blooms.

Phytoplankton community composition

The overall reduction in calcification in the Southern Ocean (Freeman and Lovenduski, 2015) over recent decades has been linked to increased ocean acidification under climate change, corresponding to reduced coccolithophore activity. However Freeman and Lovenduski (2015) find that the polewards movement of the Polar Front may be favouring coccolithophores over diatoms at some latitudes.

Atmospheric influences

The SAM is currently in a more positive state than at any point in the last millenium. Gruber et al. (2019) conclude that this increasing positivity of the SAM drove the weakening of the Southern Ocean sink in the 1990s, with the subsequent reinvigoration of the sink now driven by strengthening of the Amundsen Sea Low (ASL).

Positive SAM is thought to favour an increase in melt rates across much of West Antarctica; however elsewhere on the continent - such as at Shirase Glacier - it may result in a reduction in melting. In general the positive SAM means an intensification of westerly winds and a migration of those winds closer to the coastline (Hirano et al., 2020). Subject to local topography, this can stimulate greater CDW incursions onto the continental shelf.

2.5.3 Future trends

Ice-ocean interactions

The erosion of the WAIS by warm water (Shepherd et al., 2004) is expected to continue and accelerate, although it has been suggested by Djoumna and Holland (2021) that the relative importance of warm air intrusions may increase in the future. In this scenario, ice-ocean interactions would not necessarily be the dominant driver of ice sheet evolution. Wadham et al. (2013) postulate that future melting of the Antarctic ice sheet has the potential to fertilise the Southern Ocean on a large scale, including via subglacial run-off.

Moorman et al. (2020) predict that increased meltwater fluxes can operate as part of two distinct feedbacks - one positive, one negative - on further ice shelf melting around Antarctica. The sign of the predicted feedback depends on the mode of melting. In locations dominated by Mode II melting, increased meltwater speeds up coastal currents and may act to insulate ice shelves from CDW. In locations dominated by Mode I melting a similar process to that in Silvano et al. (2018) is projected, with decreased shelf water formation allowing more CDW onto the continental shelf and thus strengthening melt rates.

Sea ice

Future trends in sea ice will profoundly impact iron supply, light limitation, wind-driven mixing and carbon fluxes. However the IPCC SROCC notes that "there is *limited evidence* and *low agreement* concerning causes of the strong recent decrease (2016-2018) (in sea ice), and *low confidence* in the ability of current-generation climate models to reproduce and explain the observations" (Portner et al., 2019). This makes projections of future trends highly uncertain, including the future response of sea ice to changes in the SAM. In particular, the poor resolution of polynyas in climate models (Mohrmann et al., 2021) makes it very difficult to predict biological consequences of changes in sea ice cover.

Factors limiting phytoplankton growth

There remains a large degree of uncertainty around the impact of temperature both on the speciation of iron and the demand for this iron from phytoplankton (Hutchins and Boyd, 2016). Furthermore the interactions between iron and silica limitation may become increasingly important in dictating diatom growth (Borowitzka et al., 2016). Changes to salinity will also impact toxicity of metals, but laboratory experiments indicate that this will not negatively affect coastal species such as *p. antarctica* (Koppel et al., 2021).

Leung et al. (2015) use 16 CMIP5 models to investigate latitudinal patterns in response of phytoplankton to climate change, including to the increasing positivity of the Southern Annular Mode. Overall, Leung et al. (2015) predicted increased light limitation between 50°S and 65°S due to deeper mixed layer depths and increased cloud cover; south of 65°S it was projected that light limitation will be reduced by decreased sea ice cover, with iron limitation also reduced due to increased supply.

Phytoplankton community composition

Freeman et al. (2018) projected a continued decrease in calcification under current warming scenarios, and Petrou et al. (2019) found a coupling of this acidification with changes to the silica cycle in the Southern Ocean. Nissen et al. (2021) showed that changes to the calcification and thus silica trapping can have impacts on biogeochemistry at a global scale.

However the IPCC Assessment Report 6 (AR6) concluded that "there is low confidence in the sign of the resulting feedback" between changes to community composition and carbon export (Masson-Delmotte et al., 2019). This is due to factors including changes in the microbial loop as well as changes in sinking speed (Henley et al., 2020; Kaufman et al., 2017)

Carbon fluxes

The IPCC SROCC warns that "under RCP8.5, the rate of CO2 uptake by the Southern Ocean is projected to increase from the contemporary 0.91 Pg C yr^{-1} to 2.38 (1.65-2.55) Pg C yr^{-1} by 2100, but the growth in uptake rate will slow and likely stop around 2070 $\pm$ 10 corresponding to cumulative CO2 emissions of 1600 Gt C" (Portner et al., 2019). This slowdown is ascribed to changes in the salinity and temperature of near surface waters, as well as increased supply of DIC from CDW upwelling.

Hauck and Völker (2015) found that the biological pump plays a greater role in uptake of anthropogenic carbon under future climate change scenarios, with the seasonality of Southern Ocean carbon fluxes increasing as a result. However Shadwick et al. (2021) suggested that, at least near the WAP, future reduction in winter sea ice concentrations will enhance winter outgassing. This could partially counteract any increase in biological uptake during summer.

2.6 The Amundsen Sea

2.6.1 Overview

The Amundsen Sea facing sector of West Antarctica is mostly grounded below sea level, and is bounded by large topographical features which separate it from the Weddell Sea and Ross Sea sectors (Nicolas and Bromwich, 2011). Major ice streams include the Pine Island and Thwaites Glaciers, terminating in a series of ice shelves.

The accumulation of snow is influenced by warm air intrusions and by variations in the Amundsen Sea Low (ASL) pressure system (Djoumna and Holland, 2021). Studies show that the ASL migrates annually between the Bellinghausen and Ross Seas (Nicolas and Bromwich, 2011), and that its strength is linked to the El Niño-Southern Oscillation (ENSO) (Turner et al., 2013). The SAM, meanwhile, exhibits large variability on decadal to millenial timescales.

Variations in the ASL have in turn been linked to Antarctic climate both in and beyond the Amundsen Sea, particularly with regards to sea ice concentrations. Palaeoclimate evidence for past changes in the ASL includes diatom records (Konfirst et al., 2012) and ice cores (Raphael et al., 2016). Jacobs et al. (2012) link the ASL and ENSO to recent interannual and decadal variability in melt rates of Amundsen Sea ice shelves.

The changes in diatom assemblage of the Amundsen Sea found by Konfirst et al. (2012) were ascribed by the authors to a historical southwestward shift of the Amundsen Sea Low which strengthened CDW intrusions onto the continental shelf.

The influence of ice shelf meltwater on freshwater balance in the Amundsen Sea has been investigated through observations (Randall-Goodwin et al., 2015) and modelling (Bett et al., 2020). The strength of the contribution from meltwater suggests the possibility for a feedback onto further ice shelf melting (Moorman et al., 2020), and may explain the high primary production observed in the Amundsen Sea (Arrigo et al., 2015). The coastal current along the Amundsen Sea coastline entrains meltwater from the ice shelves it passes but is obstructed by grounded icebergs (Bett et al., 2020; St-Laurent et al., 2017).

The grounded icebergs on Bear Ridge, to the east of Dotson Ice Shelf (DIS) also block the westwards advection of sea ice (Bett et al., 2020). This feature, known as the Thwaites Fast Ice Tongue (TFIT), therefore facilitates the formation of the Amundsen Sea Polynya (ASP). Another latent heat polynya is found further upstream in Pine Island Bay. Both the PIP and ASP exhibit very high levels of annual primary production, the latter up to 105 g C $m^{-2}yr^{-1}$ (Arrigo et al., 2015).

2.6.2 Oceanographic surveys

The Amundsen Sea is characterized by heavy sea ice from around 65°S, which stretches as far as the continent except where there are polynyas. This heavy sea ice cover made exploration of the coastline by sea highly challenging during the twentieth century (see Jacobs et al. (2012) for a history of exploration attempts). The first scientific survey of the Amundsen Sea coastline was not until 1994, but immediately found evidence of CDW intrusions beneath the Pine Island Glacier Ice Shelf (PIGIS), contributing to a paradigm shift in understanding of the West Antarctic Ice Sheet (Shepherd et al., 2004).

In the winter of 2010/2011 the RVIB Nathaniel B Palmer visited the Amundsen Sea for the Amundsen Sea Polynya International Research Expedition (ASPIRE) (Yager et al., 2012). The result of the cruise was an ASPIRE special issue which covered many areas of the physics and biogeochemistry of the polynya (for example freshwater balance (Randall-Goodwin et al., 2015), particle flux (Ducklow et al., 2015)). In particular, the cruise made use of glider technology to measure hydrographic and optical properties of the meltwater outflow from DIS (Miles et al., 2016).

Concurrently, since 2010, a series of expeditions led by the Korean Polar Research Institute (KOPRI) have visited the ASP (Lee et al., 2016), and the combined datasets from these two projects have proved a rich resource for subsequent analysis and modelling. For example, Oliver et al. (2019); St-Laurent et al. (2019) modelled the phytoplankton bloom in the ASP, whilst Lee et al. (2017) concluded that a large part of the primary production from this bloom is not exported to depth.

In early 2014 an expedition to the eastern Amundsen Sea – including Pine Island Bay – revisited some of the measurements of the original 1994 expedition (Heywood et al., 2016). However this expedition was able to make use of new observational techniques, in particular the recruitment of seals to study meltwater properties in Pine Island Bay (Zheng et al., 2021). A combination of further research cruises, moorings and seal data will likely be required in the future – alongside new technologies – to expand monitoring of the critical processes ongoing in the Amundsen Sea (Heywood et al., 2016).

2.6.3 Interannual variability

Interannual variability in the Amundsen Sea has been examined from the perspective of physical oceanography (Dutrieux et al., 2014; Kimura et al., 2017; St-Laurent et al., 2015; Webber et al., 2017) and biogeochemistry (Park et al., 2019).

Studies including Webber et al. (2017) identified a cold period in front of Pine Island Glacier Ice Shelf (PIGIS) from October 2011 to May 2013. Two hypotheses were initially put forward to explain this interannual variability. Dutrieux et al. (2014); Petty et al. (2013) argued that variations in Ekman pumping at the continental shelf break lead to variable CDW intrusions onto the shelf, which in turn leads to lesser melt rates in years with lower CDW intrusions. By contrast, St-Laurent et al. (2015) argued that the heat available to melt PIGIS is modulated by processes at the surface of Pine Island Polynya, specifically an increase in sea ice production and associated winter cooling. Webber et al. (2017) ultimately concluded that a combination of both these mechanisms could be used to explain the observed variability.

Kimura et al. (2017) showed that in addition to interannual variability there is also seasonal variation in the thickness of CDW intrusions, which in turn leads to seasonal variation at the ice shelf fronts. However the different pathways of CDW to the various ice shelves of the Amundsen Sea means that these seasonal cycles are of different phase for different ice shelves.

The greater density of primary production in the ASP compared to the PIP was attributed by Park et al. (2017) to greater cloud cover, and therefore lower surface irradiance of the PIP compared to the ASP. Park et al. (2019) examined the interannual variability of polynyas including the ASP and PIP, and again found an influence of cloud cover, as well as a correlation with wind strengths. The sensitivity of Amundsen Sea oceanography to local atmospheric forcings highlights the value of climate reanalysis products, with Jones et al. (2016) confirming that ERA-Interim provides the best match to the sparse observations of the region.

2.6.4 Outlook

Gourmelen et al. (2017) observed channels below Dotson Ice Shelf which accelerate basal melting and thus contribute to destabilising of glacers in the Amundsen Sea. There is high sensitivity to both local and regional bathymetry (Goldberg et al., 2020), with Rosier et al. (2021) already identifying a set of key tipping points. On a shorter time scale, the ASP is highly sensitive to changes in the configuration of the TFIT (Bett et al., 2020; Stammerjohn et al., 2015). Thus future changes in grounded icebergs could have very large impacts on polynya ecosystems.

Pollard and DeConto (2009) warned of future collapse of the WAIS due to an instability, known as the Marine Ice Shelf Instability, resulting from the retrograde slope of the glacial bed. As an ice shelf retreats along a retrograde slope, the front of the ice shelf grows in thickness and thus the flux of ice across the grounding line increases, triggering further retreat. However Barletta et al. (2018) highlighted rapid bedrock rebound as a mechanism by which such a positive feedback could be averted.

In summary, the IPCC SROCC stated that there "there is growing observational and modelling evidence that accelerated retreat may be underway in several major Amundsen Sea outlets, including Thwaites, Pine Island, Smith, and Kohler glaciers ... supporting the MISI [Marine Ice Sheet Instability] hypothesis, although observed grounding line retreat on retrograde slope is not definitive proof that MISI is underway" (Portner et al., 2019).

2.6.5 Connectivity of the Amundsen Sea to the Southern Ocean

Processes on the Amundsen Sea continental shelf both influence, and are influenced by, regional and global change (Heywood et al., 2016). Moore et al. (2018) and Henley et al. (2020) have highlighted the potential for changes in primary production of the Antarctic coastal polynyas to propagate through to global biogeochemical cycles. The increased uptake of macronutrients in productive areas of the Southern Ocean may be the dominant control on low-latitude productivity trends over the next century (Moore et al., 2018). Meanwhile, Haumann et al. (2020a) have shown that the export of sea ice from the continental shelf can in turn export a surface cooling signal to the open Southern Ocean.

The study of coastal polynyas in general is important for wider Southern Ocean processes for a variety of reasons. Firstly, an understanding of the physics of glacial meltwater spreading and the biogeochemical processes controlling the coastal iron budget are crucial lateral boundary conditions on the Southern Ocean as a whole (De Jong et al., 2012; Moore et al., 2018). Secondly, the intensity of phytoplankton blooms in coastal polynyas mean that they contribute a substantial part of total carbon flux in the Southern Ocean (Arrigo and van Dijken, 2003). Thirdly, coastal polynyas have important similarities — as well as important differences — with the less well-studied (sensible heat) polynyas of the open ocean (von Berg et al., 2020).

2.7 Summary

In this review, an overview has been provided of mechanisms important to biophysical interactions in the Southern Ocean, of the geographical variability which characterises these mechanisms, and of the evolution of these interactions over time.

In particular, this review highlights the high degree of zonal asymmetry between different coastal polynyas, despite the same set of mechanisms being present to some degree in each. Figure 2.5 summarises the way in which some of these forms of asymmetry map onto each other in the Amundsen, Ross and Weddell Seas. For instance, the Amundsen Sea exhibits Mode II melting, ice shelf-driven iron supply and low carbon export efficiency, whereas the Ross Sea exhibits Mode I/III melting, high carbon export efficiency, and an iron supply largely insensitive to the ice shelf.

The focus of this thesis on the Amundsen Sea is justified by the magnitude of phytoplankton blooms in the ASP and PIP, as well as by the the rapid basal melting of adjacent ice shelves. However in later chapters, the results from modelling in this thesis are used to infer possible responses in the Ross Sea and elsewhere.

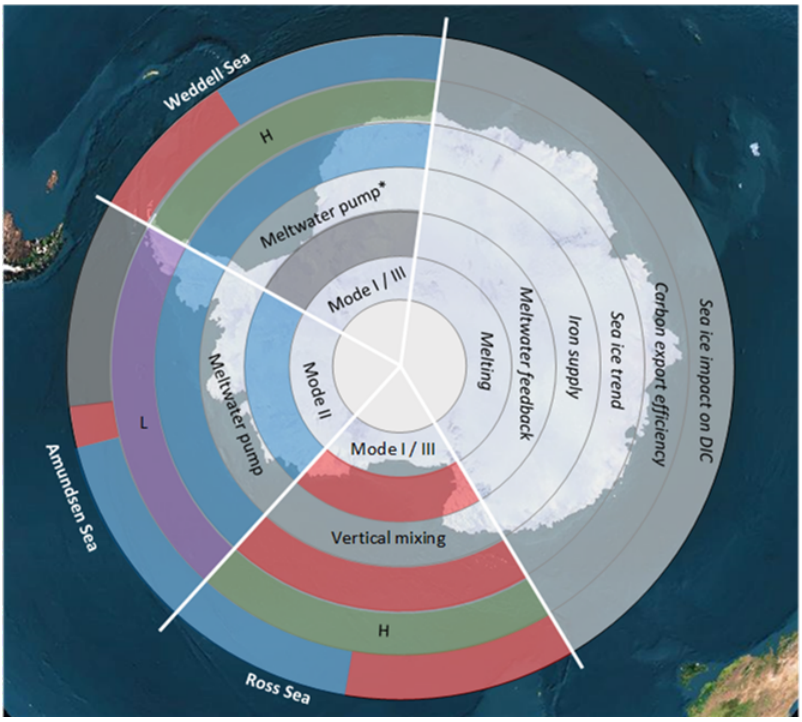

Figure 2.5: Zonal variations in ice-ocean and biogeochemical interactions, showing the Ross, Amundsen and Weddell Seas. From interior to exterior: mode of melting (Silvano et al., 2016), thermal response to increased meltwater over next century (Moorman et al., 2020) - with blue for cooling and red for warming, dominant source of iron supply (Dinniman et al., 2020), trend in sea ice concentration over last decade (Parkinson, 2019) - with blue for decrease and red for increase, carbon export efficiency (Lee et al., 2017) with purple for low and green for high, and local impact of sea ice on surface DIC concentrations (Rosso et al., 2017), with blue for dilution and red for increasing concentration. The asterisk next to the meltwater pump for the Weddell Sea refers to the fact that the most important contribution is from upstream glaciers rather than from local meltwater pump effects.

Chapter 3

Methods

3.1 Introduction

The Southern Ocean has long been poorly observed compared to other ocean basins, making modelling even more crucial in assessing both its current state and its ongoing change. State estimates such as the Biological Southern Ocean State Estimate (BSOSE) provide a best fit to data by using sparse observations from a variety of sources as constraints on a model.

BSOSE uses a combination of Argo floats, seals and Conductivity Temperature Depth (CTD) casts to constrain temperatures and salinities in a Southern Ocean model run in MITgcm. Meanwhile, a different set of observations provides constraints on biogeochemical tracers within the model; for instance, data from bgc-Argo floats are used to constrain oxygen profiles. The biogeochemical component of the model itself is a version of the the Biology Light Iron Nutrients and Gases (BLING) model, originally developed by Galbraith et al. (2010) and then adapted to be compatible with MITgcm (Verdy and Mazloff, 2017).

Recently an MITgcm-based state estimate has been developed for the Amundsen Sea sector (Nakayama et al., 2021), building on the Amundsen Sea models of Holland et al. (2017) and Kimura et al. (2017). However so far these implementations of MITgcm for the Amundsen Sea have dealt only with ocean physics. The only biogeochemical model of the Amundsen Sea thus far was developed by St-Laurent et al. (2019) using the Regional Ocean Modelling System (ROMS).

In this chapter the modelling approach used in this thesis is described in detail, culminating in a comparison of the MITgcm-BLING setup to other biogeochemical models. For the most part, the equations presented here are the same as those used by Verdy and Mazloff (2017), with subsequent modifications described in later chapters.

3.2 Physical model

3.2.1 The MITgcm

The MIT General Circulation Model (MITgcm) is an open source modelling framework composed of a dynamical kernel as well as additional packages, such as those representing vertical mixing, sea ice, ice shelves and biogeochemistry.

Equations of motion

MITgcm was designed to model both atmospheric and ocean circulation by solving the Boussinesq form of the Navier-Stokes equations (Marshall et al., 1997a). All variables in MITgcm are categorised as either bulk quantities or face quantities. Scalars such as salinity and temperature are bulk quantities and are defined at cell centres; meanwhile most vectors such as velocity are defined at cell faces.

MITgcm solves the equations of fluid dynamics in an incompressible regime, meaning that the continuity equation

$$\Delta \cdot \mathbf{v} = 0 \tag{3.1}$$

holds throughout. Here $\mathbf{v}$ is the velocity vector for a small fluid parcel, with horizontal component v_{xy} and vertical component w. The acceleration of the parcel,

$$\frac{\partial v_{xy}}{\partial t} = G_{v_{xy}} - \Delta_{xy} P \tag{3.2}$$

$$\frac{\partial w}{\partial t} = G_w - \frac{\partial P}{\partial z}, \tag{3.3}$$

is determined by the gradient of the pressure P, as well as by the combination of gravitational and Coriolis forces encompassed in $G_{v_{xy}}$ and G_w (Marshall et al., 1997b).

3.2.2 Vertical Mixing

Fluid circulation often encounters boundaries - in this case land, ice shelves, sea ice and bathymetry - which imply the existence of a boundary layer within the fluid itself. Models of macroscopic ocean circulation are unable to fully capture processes occuring within this boundary layer.

Throughout most of this study the K-Profile Parameterization (KPP) (Large et al., 1994) is used as a package within MITgcm to implicitly represent mixing of properties within the boundary layer between ocean and atmosphere. KPP works by first computing the depth of the boundary layer, then stretching a shape function across that depth to arrive at a vertical profile $K_z(z)$ of diffusivity. The diffusion of each tracer is then calculated as a sum of local and non-local terms. For example the KPP term for salt S is

$$KPP_S = K_z(z)\left(\gamma_S - \frac{\partial S}{\partial z}\right) \tag{3.4}$$

where the non-local term γ_S allows for turbulent fluxes even when the gradient $\frac{\partial S}{\partial z}$ is zero (van Roekel et al., 2018).

A range of other methods is used to parameterize vertical mixing in other models, both simpler and more sophisticated than KPP. The Biological Southern Ocean State Estimate (BSOSE), for example, uses the GGL_90 mixing scheme (Gaspar et al., 1990) within MITgcm. This is an example of a scheme where the diffusivity profile is based on turbulent kinetic energy (TKE) closure, and does not consider non-local influences on mixing. The choice of KPP for the investigations in this thesis is based on the previous implementation of KPP within ice-ocean modelling of the Amundsen Sea (Kimura et al., 2017; Nakayama et al., 2017).

3.2.3 Active tracer budgets

Salt budget

Salt is transported by a combination of advection ADV_S, diffusion $DIFF_S$ and paramterized mixing KPP_S, so that the salt budget for each cell is

$$\frac{\partial S}{\partial t} = ADV_S + DIFF_S + KPP_S \tag{3.5}$$

where a number of different advection and diffusion schemes can be set within the MITgcm.

Heat budget

The MITgcm heat budget (Tamsitt et al., 2016) is described by the equation for the time evolution of the temperature tracer $\frac{\partial T}{\partial t}$ in each cell:

$$\frac{\partial T}{\partial t} = ADV_T + DIFF_T + KPP_T + \frac{1}{\rho c_p}\left(\frac{\Delta I}{\Delta z_k} + \frac{F_Q}{\Delta z_1}\right) \tag{3.6}$$

where the water density ρ and the specific heat capacity c_p are used to convert between energy and temperature units. As with the salt tracer, the temperature tracer is transported by advection (ADV_T), diffusion ($DIFF_T$) and the KPP vertical mixing scheme (KPP_T) - each of which is calculated analogously to salt.

In each cell (of thickness Δz_k) there is also a shortwave heating effect proportional to the divergence of the shortwave radiation I. Meanwhile the surface heat flux F_Q represents the sum of longwave, latent and sensible heat fluxes and is equal to zero for sub-surface cells.

Shortwave heating

The default shortwave heating scheme in MITgcm makes use of a constant attenuation profile, which can be adjusted at compile time by choice of water type. The attenuation with respect to depth is

$$\frac{\Delta I}{\Delta z_k} = k_{vis} I_{vis} + k_{ir} I_{ir} \tag{3.7}$$

where

$$I = I_{vis} + I_{ir} \tag{3.8}$$

is the sum of visible light and infrared radiation.

The parameters k_{vis}, k_{ir}, as well as the partitioning between I_{vis} and I_{ir} at the surface, are adjustable at compile time and reflect the choice of water type (Paulson and Simpson, 1977). In Chapter 6 the implementation of an alternative formulation of shortwave heating, taking account of chlorophyll concentrations, is described in detail.

3.2.4 Passive tracer transport

Passive tracers are in general transported around the domain similarly to active tracers, but do not impact the density of the fluid. In several of the investigations detailed here a passive ice shelf meltwater tracer is generated over a field consisting of each cell immediately adjacent to the ice shelf.

Then the meltwater tracer evolves according to the equation

$$\frac{\partial M_w}{\partial t} = ADV_{M_w} + DIFF_{M_w} + KPP_{M_w} + \frac{Q_{M_w}}{\Delta z_1} \tag{3.9}$$

where Q_{M_w} - the flux of meltwater from the ice shelf - is identically zero in all cells not adjacent to the ice shelf.

The biogeochemical tracers used by BLING are also carried through the model as passive tracers, so that for each BLING tracer Ω_i ($i = 1, 2...9$)

$$\frac{\partial \Omega_i}{\partial t} = ADV_{\Omega_i} + DIFF_{\Omega_i} + KPP_{\Omega_i} + BGC_{\Omega_i}. \tag{3.10}$$

Here the term BGC_{Ω_i} encompasses all the biogeochemical processes in BLING that act on Ω_i.

3.2.5 The Shelf-Ice package

Ice shelf thermodynamics is based on the three equation formulation of Holland and Jenkins (1999) for heat and salt fluxes across the ice-ocean boundary. This treatment fixes the ice-ocean interface at the local freezing temperature T_B (°C), which in turn depends on the local salinity S_B (psu) and pressure p_B (Pa)

$$T_B = aS_B + b + cp_B, \tag{3.11}$$

where $a = -0.0575$ °C psu^{-1}, $b = 0.0901$ °C and $c = -7.61 \times 10^{-8}$ °C Pa^{-1} are constants. Then the fluxes of latent heat Q^T_{latent} (W m^{-2}) and salt Q^S_{brine} (psu m s^{-1}) are calculated as the difference between the respective fluxes into the ice (Q^T_I, Q^S_I) and from the ocean boundary layer (Q^T_B, Q^S_B).

$$Q^T_I - Q^T_B = Q^T_{latent} \tag{3.12}$$

$$Q^S_I - Q^S_B = Q^S_{brine} \tag{3.13}$$

where both of these fluxes are influenced by the interface temperature. The flux of salt across the ocean boundary layer is related to the meltwater tracer flux via

$$Q^S_B = -Q_{M_w} S_B. \tag{3.14}$$

where S_B is the salinity within the boundary layer.

3.2.6 The sea ice package

Thermodynamics

The sea ice thermodynamics is based on the assumptions of a zero layer model (Semtner Jr, 1976), namely that the ice has uniform conductivity and zero heat capacity. This means that the one dimensional heat equation

$$\rho c \frac{\partial T}{\partial t} = k \frac{\partial^2 T}{\partial z^2} \tag{3.15}$$

applies, where k is the heat conductivity coefficient. Thus the heat flux is sensitive to the sea ice thickness as well as to the temperature difference between air and ocean.

Dynamics

Sea ice dynamics is driven primarily by a combination of wind and ice-ocean stresses, here denoted as τ_{air} and τ_{ocean} respectively. In addition, there are internal stresses represented by $\mathbf{F}$ and and gravitiational effects due to the gradient of the sea surface height potential $\phi(0)$. The momentum equation for sea ice is thus

$$m \frac{D\mathbf{u}}{Dt} = -mf\mathbf{k} \times \mathbf{u} + \tau_{air} + \tau_{ocean} - m\Delta\phi(0) + \mathbf{F} \tag{3.16}$$

where m is the ice mass per unit area, $\mathbf{u}$ is the ice velocity, k is the unit vector in the z-direction and f is the Coriolis parameter. A full description of the treatment of internal ice stresses is provided in Appendix A. of Losch et al. (2010).

The wind and ice-ocean stresses are given by

$$\tau_{air} = \rho_{air} C_{air} |\mathbf{U}_{air} - \mathbf{u}| R_{air} (\mathbf{U}_{air} - \mathbf{u}) \tag{3.17}$$

and

$$\tau_{ocean} = \rho_{ocean} C_{ocean} |\mathbf{U}_{ocean} - \mathbf{u}| R_{ocean} (\mathbf{U}_{ocean} - \mathbf{u}) \tag{3.18}$$

respectively.

3.3 Biogeochemical model

3.3.1 Development of BLING

Much of the computational cost associated with incorporating biogeochemistry into ocean models is due to the need to include large numbers of additional tracers, all of which must be transported around the model at each time step. The Biology Light Iron Nutrients and Gases (BLING) model minimises computational cost by using a small number of explicit tracers, whilst still resolving a large number of physiological and biogeochemical processes.

BLING was developed by Galbraith et al. (2010) for use within the Geophysical Fluid Dynamics Laboratory (GFDL) Earth System Model (ESM), and was extended in further studies such as Kim et al. (2015). Verdy and Mazloff (2017) evolved BLING into a package within MITgcm (see Figure 2.4), which then went on to form the basis of the Biological Southern Ocean State Estimate (BSOSE). Whereas Verdy and Mazloff (2017) used eight tracers – DIC, Alkalinity, Oxygen, Nitrate, Phosphate, Dissolved Iron, Dissolved Organic Nitrogen (DON) and Dissolved Organic Phosphorus (DOP) – the modelling presented in this thesis includes a ninth tracer which represents phytoplankton biomass. The inclusion of this tracer allows the model to represent the effect of biomass transport on phytoplankton blooms, as well as the effect of nutrient and trace metal transport.

3.3.2 Phytoplankton growth

Nutrient limitation

Phytoplankton growth within BLING is a function of three factors: nutrient availability, temperature, and light intensity. Nutrient limitation is encoded within the dimensionless term n_{lim} and is calculated according to Liebig's law of the minimum applied to nitrate (NO_3), phosphate (PO_4) and dissolved iron (Fe) concentrations:

$$n_{lim} = \min\left(\frac{NO_3}{NO_3 + K_N}, \frac{PO_4}{PO_4 + K_P}, \frac{Fe}{Fe + K_{Fe}}\right). \tag{3.19}$$

The saturation parameters for nitrate ($K_N = 2.05$ mmol N m^{-3}), phosphate ($K_P = 10.25$ μmol P m^{-3}) and iron ($K_{Fe} = 0.16$ μmol Fe m^{-3}) are constants.

As well as impacting growth rate, the iron concentration also modulates the chlorophyll-to-carbon ratio θ (mg Chl (g C)$^{-1}$). Specifically, the chlorophyll-to-carbon ratio for a phytoplankton cell under low light conditions varies as

$$\theta_{dark} = \theta^{min}_{dark} + (\theta^{max}_{dark} - \theta^{min}_{dark})\frac{Fe}{Fe + K_{Fe}}; \tag{3.20}$$

where $\theta^{min}_{dark} = 10$ mg Chl (g C)$^{-1}$ and $\theta^{max}_{dark} = 40$ mg Chl (g C)$^{-1}$.

Temperature

Temperature T affects modelled phytoplankton growth rates via a term $e^{\kappa T}$, where $\kappa = 0.063$ $^{\circ}\text{C}^{-1}$ is a constant (Eppley, 1972). Therefore, the per capita growth rate Pc_{max} for a phytoplankton cell which is nutrient and temperature limited, but which is saturated with regards to light, is

$$Pc_{max} = \mu_{max} e^{\kappa T} n_{lim}. \tag{3.21}$$

Here $\mu_{max} = 1.47$ day^{-1} is the maximum growth rate under light and nutrient replete conditions at 0°C, using the same value as in Verdy and Mazloff (2017).

Light saturation

As phytoplankton cells are exposed to increasing light, they become progressively more saturated. The degree of light saturation, I_k (W m^{-2}), increases in response to increases in the irradiance I_{mem} (W m^{-2}) which the cell is acclimated to, and to increases in Pc_{max}; whilst decreasing in response to increases in θ_{dark}:

$$I_k = \frac{I_{mem}}{2} + \frac{Pc_{max}}{\theta_{dark}\alpha_{chl}}. \tag{3.22}$$

Here α_{chl} has units g C (mg Chl)$^{-1}$ day^{-1} (W m^{-2})$^{-1}$ and represents photosynthetic efficiency, or the fraction of solar energy which is transformed into chemical energy. A full discussion of the I_{mem} term is given in Section 4.3.

As phytoplankton cells become saturated with light and I_k increases, the chlorophyll-to-carbon ratio θ is reduced:

$$\theta = \frac{Pc_{max}}{\alpha_{chl} I_k}. \tag{3.23}$$

Light limitation

The per capita phytoplankton growth rate μ (day^{-1}) is the product of Pc_{max} and a dimensionless light limitation term:

$$\mu = Pc_{max}(1 - e^{-I/I_k}). \tag{3.24}$$

At each time step BLING calculates this growth rate and multiplies it by the phytoplankton biomass B (g C m^{-3}) to calculate the Net Primary Production (NPP),

$$NPP = \mu B, \tag{3.25}$$

which has units of g C m^{-3} day^{-1}.

It follows from Equation 3.22 that, considering a phytoplankton cell acclimated to very low light,

$$\lim_{I_{mem}\to 0} I_k = \frac{Pc_{max}}{\theta_{dark}\alpha_{chl}}. \tag{3.26}$$

If the incident irradiance is then increased from zero, I will at first be much smaller than I_k, so using

$$\lim_{I\to 0} e^{-I/I_k} = 1 - \frac{I}{I_k}. \tag{3.27}$$

it follows that Equation 3.24 becomes

$$\lim_{I\to 0} \mu = \frac{I}{I_k} Pc_{max}. \tag{3.28}$$

Then combining Equations 3.28 and 3.26,

$$\lim_{I\to 0} \lim_{I_{mem}\to 0} \mu = \theta_{dark}\alpha_{chl} I; \tag{3.29}$$

where the quantity

$$\alpha = \theta_{dark}\alpha_{chl} \tag{3.30}$$

can be measured from phytoplankton incubation experiments as the initial slope of the curve of photosynthetic rate against irradiance.

Biomass and primary production

Biomass is partioned between two classes: small phytoplankton B_{sm} and large phytoplankton B_{lg}. In the context of ASP modelling, the large phytoplankton class represents various diatom species and the small phytoplankton class represents the haptophyte *Phaeocystis antarctica*. Verdy and Mazloff (2017) included a third class representing diazotrophs, but this is neglected here due to the rarity of nitrogen fixation at the low temperatures found in Antarctic polynyas.

Increases in biomass due to phytoplankton growth are balanced by depletion due to grazing, which is based on a fixed per capita grazing rate $\lambda = 0.19$ day^{-1}, as in Verdy and Mazloff (2017). Changes in biomass of the different phytoplankton classes are treated separately at each time step. As described in Verdy and Mazloff (2017) and Dunne et al. (2005), the model is designed so that a bloom of large phytoplankton undergoes less severe grazing pressure relative to its developing size than an equivalent bloom of small phytoplankton. The small biomass fraction changes as

$$\left(\frac{\partial B_{sm}}{\partial t}\right)_{BGC} = \left(\mu - \lambda e^{\kappa T}\frac{B_{sm}}{B_0}\right)B_{sm} \tag{3.31}$$

within BLING whilst the large biomass fraction changes as

$$\left(\frac{\partial B_{lg}}{\partial t}\right)_{BGC} = \left(\mu - \lambda e^{\kappa T}\left(\frac{B_{lg}}{B_0}\right)^3\right)B_{lg}; \tag{3.32}$$

with B_0 the same constant in both cases. Whilst the different phytoplankton fractions are treated seperately within BLING, it is only their sum $B = B_{sm} + B_{lg}$ which is transported around the model. Thus Equation 3.10 becomes

$$\frac{\partial B}{\partial t} = ADV_B + DIFF_B + KPP_B + (\mu - \lambda e^{\kappa T}\frac{B_{sm}}{B_0})B_{sm} + (\mu - \lambda e^{\kappa T}(\frac{B_{lg}}{B_0})^3)B_{lg}. \tag{3.33}$$

for the overall change in the biomass tracer by both physical and biogeochemical processes.

3.3.3 Iron cycling

Biological uptake

The rate of biological iron uptake (Fe_{upt}; units of μmol Fe m^{-3} day^{-1}) varies with NPP and with the iron-to-nitrate uptake ratio σ (units of μmol Fe (mmol N)$^{-1}$):

$$Fe_{upt} = \frac{\sigma}{\eta}NPP. \tag{3.34}$$

Here the carbon-to-nitrogen ratio $\eta = 0.081$ g C (mmol N)$^{-1}$ is constant, but σ increases as iron availability increases, with this extra 'luxury' uptake of iron going into intracellular storage. Defining $K_\sigma = 0.82$ μmol Fe m^{-3} (assuming the default value in BLING) as the half saturation constant for iron uptake,

$$\sigma = \sigma_{min} + (\sigma_{max} - \sigma_{min}) \frac{Fe}{Fe + K_\sigma}. \tag{3.35}$$

where $\sigma_{min} = 0.014$ μmol Fe (mmol N)$^{-1}$ and $\sigma_{max} = 0.17$ μmol Fe (mmol N)$^{-1}$ are the minimum and maximum iron-to-nitrate ratios respectively, and both assume the default BLING values. A proportion of the iron uptake is then exported downwards through the water column in detrital form. This proportion is not constant; it is instead a function ϕ_{sink} of temperature, biomass and the ratio of large to small phytoplankton fractions, as derived in Dunne et al. (2005) and adapted for BLING in Galbraith et al. (2010) and Verdy and Mazloff (2017).

Scavenging, sinking and remineralisation

The flux of sinking particulate iron is supplemented further by scavenging, whereby free dissolved iron becomes adsorbed onto particles and sinks in colloidal form. The equations used to parameterize scavenging in BLING are described in full in Galbraith et al. (2010). As this particulate iron sinks through the cell, a portion is remineralised into dissolved iron. Any particulate iron which is not remineralised contributes to a net imbalance between the particulate iron flux pFe^{bot}_{flux} (units of μmol Fe m^{-2} day $^{-1}$) leaving the cell and the particulate iron flux pFe^{top}_{flux} entering the cell:

$$pFe^{top}_{flux} + (\phi_{sink} Fe_{upt} + Fe_{scav})\Delta r = (1 + z_{remin}\Delta r) pFe^{bot}_{flux} \tag{3.36}$$

where Δr (measured in m) is the depth range covered by the cell. The remineralisation length scale z_{remin} (measured in m^{-1}) is a function of oxygen (O_2) saturation:

$$z_{remin} = \frac{\gamma_{POM}}{w_{sink}} \left(r_{min} + \frac{O_2^2}{O_2^2 + K_{O2}^2} (1 - r_{min}) \right) \tag{3.37}$$

where $\gamma_{POM} = 0.12$ day^{-1} is the (BLING default) decay timescale for particulate organic matter, $K_{O2} = 20$ mmol O_2 m^{-3} is the half saturation constant for oxygen and $r_{min} = 0.12$ is a constant. The sinking speed w_{sink} (units of m day^{-1}) is parameterized identically to Galbraith et al. (2010). In acting as a sink of particulate iron, remineralisation is also a source Fe_{remin} (μmol Fe m^{-3} day^{-1}) of dissolved iron:

$$Fe_{remin} = z_{remin} pFe^{bot}_{flux}. \tag{3.38}$$

Recycling

A further source of dissolved iron is recycling, whereby the microbial loop returns a quantity Fe_{rec} (μmol Fe m^{-3} day^{-1}) of the iron taken up by phytoplankton back into the dissolved pool. In BLING this process is assumed to happen instantaneously, so that at each time step the quantity of iron recycled is simply equal to the difference between uptake and particulate export:

$$Fe_{rec} = (1 - \phi_{sink}) Fe_{upt}. \tag{3.39}$$

Iron budget

The total contribution of biogeochemistry to the dissolved iron concentration in a given cell is equal and opposite to the change in particulate iron flux over the depth Δr of that cell. Where more particulate iron sinks into a cell than sinks out of the cell, this means there is a positive contribution to the dissolved iron budget. Hence Equation 3.10 becomes

$$\frac{\partial Fe}{\partial t} = ADV_{Fe} + DIFF_{Fe} + KPP_{Fe} + \frac{pFe^{top}_{flux} - pFe^{bot}_{flux}}{\Delta r} \tag{3.40}$$

where

$$BGC_{Fe} = \frac{pFe^{top}_{flux} - pFe^{bot}_{flux}}{\Delta r} \tag{3.41}$$

is the contribution to the iron budget from BLING alone. Substituting Equations 3.34 to 3.39 into Equation 3.40 and re-arranging, the dissolved iron budget is

$$\frac{\partial Fe}{\partial t} = ADV_{Fe} + DIFF_{Fe} + KPP_{Fe} - Fe_{upt} + Fe_{rec} + Fe_{remin} - Fe_{scav}. \tag{3.42}$$

Throughout this thesis the air-sea flux of iron from dust is neglected, as this is thought to be negligible within the study area. Furthermore, analysis is limited to the upper ocean iron budget, so that burial of iron into sediments and its subsequent release is neglected.

3.3.4 Carbon cycling

Net Community Production

Net Community Production (NCP) is calculated as the portion of organic carbon generated by NPP which is not returned back into the pool of DIC:

$$NCP = NPP - R_{ML} - R_{POM} - r_{DOM}. \tag{3.43}$$

DIC is regenerated by microbial recycling within the mixed layer (R_{ML}) and by remineralisation of particulate (R_{POM}) and dissolved (r_{DOM}) organic matter (Rosso et al., 2017). This DIC is itself composed of carbon in four different forms,

$$DIC = [CO_2] + [H_2CO_3] + [HCO_3^-] + [CO_3^{2-}], \tag{3.44}$$

with a chemical equilibrium emerging from the following - reversible - reactions:

$$CO_2 + H_2O \rightleftharpoons H_2CO_3 \tag{3.45}$$

$$H_2CO_3 \rightleftharpoons HCO_3^- + H^+ \tag{3.46}$$

$$HCO_3^- + H_2O \rightleftharpoons CO_3^{2-} + H^+. \tag{3.47}$$

A new variable CO_2^* can be defined with is the sum of CO_2 and carbonic acid (H_2CO_3) (Follows et al., 2006). Then the partial pressure $pCO2$ is defined by the relation

$$[CO_2^*] = K_0(T,S)pCO_2 \tag{3.48}$$

where $K_0(T,S)$ is the solubility of CO_2 as a function of temperature T and salinity S. It is the difference between partial pressure at the ocean surface and partial pressure in the atmosphere adjacent to the ocean $p_{CO_2}^{atm}$ that then gives rise to a flux of carbon dioxide.

Air-sea carbon fluxes

The air-sea flux is calculated via a numerical scheme in BLING, based on Follows et al. (2006), which accounts for contributions from both the biological pump and solubility pump. The rate of gaseous exchange K_{ex} across the ocean surface has a power-law dependence ε on the wind speed u_w, and is also dependent on the concentration of sea ice a_{ice}:

$$K_{ex} = 0.337(1 - a_{ice})u_w^{\varepsilon}. \tag{3.49}$$

The flux of carbon is

$$Q_{CO_2} = K_{ex}(fug_1 p_{CO_2}^{atm} - fug_2 p_{CO_2}) \tag{3.50}$$

where fug_1 and fug_2 are fugacity factors, also calculated in BLING and dependent on alkalinity and phosphate concentrations (Dutkiewicz et al., 2006).

Study	Domain	Physical model	Biogeochemistry	Limiting nutrients							Optically active water constituents		
				Nitrate	Nitrite	Ammonia	Phosphate	DOP	Iron	Silica	Chlorophyll	CDOM	Detritus
Dutkiewicz et al. 2005	Global	**MITgcm**	DIC				■		■	■	■		
Manizza et al. 2008	Global	ORCA-LIM	PlankTOM5				■		■	■	■		
Follows et al. 2007	Global	**MITgcm** (ECCO)	Darwin	■	■	■	■		■	■	■		
Galbraith et al. 2010	Global	GFDL ESM	**BLING**				■		■				
Moore et al. 2013	Global	CESM1	BEC	■		■	■	■	■	■	■		
Dunne et al. 2013	Global	GFDL ESM	TOPAZ2	■		■	■		■	■			
Dutkiewicz et al. 2015	Global	**MITgcm** (ECCO)	Darwin	■	■	■	■		■	■	■	■	■
Kim et al. 2015	Global	GFDL ESM	**BLING**				■		■		■	■	
Verdy & Mazloff 2017	Southern Ocean	**MITgcm** (BSOSE)	**BLING**	■			■		■				
Nissen et al. 2018	Southern Ocean	ROMS	BEC	■		■	■	■	■	■	■		
St Laurent et al. 2019	**Amundsen Sea**	ROMS	*(NPZD model)*	■					■				
Pefanis et al. 2020	Arctic	**MITgcm**	Darwin	■	■	■	■		■	■	■	■	
*This thesis	**Amundsen Sea**	**MITgcm**	**BLING**	■			■		■		■		

Figure 3.1: Selected biogeochemical models, listed alongside the limiting nutrients and optically active constituents in each model.

Carbon budget

The carbon budget is thus a balance between NCP, air-sea fluxes (Q_{CO_2}) and transport; the latter by a combination of advection (ADV_{DIC}), diffusion ($DIFF_{DIC}$) and KPP vertical mixing (KPP_{DIC}):

$$\frac{\partial DIC}{\partial t} = ADV_{DIC} + DIFF_{DIC} + KPP_{DIC} - NCP + \frac{Q_{CO_2}}{\Delta z_1} \tag{3.51}$$

where $\frac{\partial DIC}{\partial t}$ is the time evolution of DIC in each cell, and Δz_1 is the thickness of the surface cell. The air-sea carbon flux is defined as positive for carbon entering the ocean, and is exactly zero for sub-surface cells.

3.3.5 Comparison to other biogeochemical models

One measure of the complexity of an ocean biogeochemistry model is the number of tracers included as limiting nutrients for phytoplankton growth (Figure 3.1).

Several models include only one macronutrient limiter, either nitrate (St-Laurent et al., 2019) or phosphate (Dutkiewicz et al., 2005; Manizza et al., 2008). Though the original BLING model developed by Galbraith et al. (2010) and used in Kim et al. (2015) was based around a phosphate tracer only, the version developed for incorporation into MITgcm (Verdy and Mazloff, 2017) was extended also to include an independent nitrate tracer.

Higher complexity models such as the Biogeochemical Element Cycling (BEC) model (Moore et al., 2013; Nissen et al., 2018) and Tracers of Ocean Productivity with Allometric Zooplankton (TOPAZ2) (Dunne et al., 2013) also include an ammonia tracer, which is preferentially taken up by most phytoplankton compared to nitrate. Dissolved Organic Phosphorous (DOP) - which is included as a non-limiting nutrient in BLING, TOPAZ2 and DARWIN - is allowed to limit growth in BEC, whilst the Darwin model (Dutkiewicz et al., 2015; Follows et al., 2007; Pefanis et al., 2020) includes an additional (potentially limiting) source of nitrogen in the form of nitrite.

Silica has been included as a limiting micronutrient in several models (Dutkiewicz et al., 2005; Follows et al., 2007; Manizza et al., 2008; Moore et al., 2013), and is particularly important for studying diatom biogeography and the competition between diatoms and coccolithophores (Nissen et al., 2018). Iron is routinely included as a limiting micronutrient due to its dominant influence on Southern Ocean primary production (Martin et al., 1990), and its distinctive export properties compared to nitrate and phosphate. The key advantage of BLING, however, is in its representation of photosynthetic efficiency, which varies according to iron concentration (Galbraith et al., 2010) (also see Figure 2.4). In most other biogeochemistry models, this aspect of colimitation is absent.

Another measure of model complexity is in the number of modelled water constituents which are included in the calculation of light attenuation. The self-shading effect is included by assigning an attenuating coefficient to chlorophyll in several models (Dutkiewicz et al., 2005; Follows et al., 2007; Manizza et al., 2005; Moore et al., 2013; Nissen et al., 2018). A global analysis of model sensitivity to different optically active constituents was undertaken by Dutkiewicz et al. (2015), which included detrital and Colored Dissolved Organic Matter (CDOM) contributions as well as chlorophyll. The original BLING model developed by Galbraith et al. (2010) did not include attenuation other than by water molecules, nor did the original TOPAZ2 model (Dunne et al., 2013). The version of BLING developed by Kim et al. (2015) did include attenuation by both chlorophyll and CDOM, but neither of these were included in the MITgcm version (Verdy and Mazloff, 2017).

A final aspect of biogeochemical model complexity is the ability to simulate competition between competing species. In both BLING (Galbraith et al., 2010) and TOPAZ2 (Dunne et al., 2013) this is possible for three phytoplankton classes - small, large and diazotroph - whilst Nissen et al. (2018) and Nissen and Vogt (2021) use the three classes in the BEC model to represent diatom, coccolithophore and *p. antarctica* abundance around the Southern Ocean. However the disadvantage of these models is that they are sensitive to the initial conditions on community composition, and struggle to represent the qualitative shifts in ecosystems in response

to environmental change. The Darwin model (Dutkiewicz et al., 2015; Follows et al., 2007) was developed to simulate the emergence of community composition from competition between a large number of phytoplankton functional types, each with a stochastically chosen set of physiological parameters.

Galbraith et al. (2015) compared the performance of BLING against the more complex, more computationally expensive TOPAZ2 model and found good agreement in many diagnostics important to climate. However BLING was seen to overestimate substantially the export of carbon in the Southern Ocean compared to TOPAZ2 and compared to observation-based estimates (Galbraith et al., 2015). The NPZD model developed for the Amundsen Sea by Oliver et al. (2019); St-Laurent et al. (2019), though simpler in most respects than BLING, does include a more advanced treatment of particle sinking and export. In this thesis, the BLING-MITgcm coupling developed by Verdy and Mazloff (2017) is extended to include feedbacks present in the GFDL version of BLING (Kim et al., 2015) as well as in more complex models (Nissen et al., 2018; Pefanis et al., 2020).

Chapter 4

Spatio-temporal patterns in iron-light colimitation in front of Dotson Ice Shelf

4.1 Preface

In this chapter, two different modelling approaches are used to examine spatial and temporal variation in phytoplankton growth rates and primary production. The first set of results, from a Lagrangian model, are unpublished, whilst the majority of the second set of results, using MITgcm-BLING on an idealised domain, form part of the work already published in Twelves et al. (2021). Aspects of the introduction, methods, discussion and conclusion also appear in Twelves et al. (2021). The implementation of self-shading in MITgcm-BLING has since been accepted as part of the open-source code, and is available at `https://github.com/MITgcm/MITgcm/tree/master/pkg/bling`. Meanwhile the Lagrangian model, written in MATLAB, is available from the personal gitHub repository at `https://github.com/atwelves/phyto_gedanken/blob/master/irr_mem.m`.

4.2 Introduction

4.2.1 The Critical Depth Hypothesis

A phytoplankton bloom is light-limited when the flux of downwelling irradiance I reaching cells within the bloom is lower than that needed to maximize the rate of photosynthesis. At low irradiances the response of photosynthetic rate to increases in irradiance is approximately linear, with proportionality constant α (Equation 3.29). At higher irradiances this response becomes progressively less sensitive, as the photosynthetic reaction centres become saturated with photons (Equation 3.22).

The surface irradiance I_0 at a given location is a product of solar angle, overlying cloud cover and, in the high latitudes, sea ice cover. Both the albedo and attenuation coefficients of sea ice are far larger than those of seawater, so the presence of sea ice greatly reduces the irradiance actually penetrating into the water column. Sea ice also has a strong influence on the seasonal cycle of mixed layer depth; an effect demonstrated in the Southern Ocean using a combination of seal, float and ship data (Pellichero et al., 2017). Brine rejection from newly formed sea ice destabilizes the water column, whilst sea ice melting provides a stabilizing layer of freshwater at the ocean surface. Where present, ice shelves are an additional source of freshwater to the water column. The mixed layer depth D is then a function of these salinity forcings as well as wind-driven mixing and heat fluxes.

Attenuation by water molecules and other optically active constituents of the mixed layer means that the light available for phytoplankton varies significantly within a single phytoplankton community. There may be sufficient light for photosynthesis near the surface; however the greater the depth D over which phytoplankton are mixed, the less light is available on average for cells throughout the bloom. Hence there is a theoretical upper bound on the mixed layer depth, beyond which it cannot sustain a phytoplankton bloom. This critical depth D_{cr} is the solution to the equation

$$\frac{D_{cr}}{1 - e^{-k_{vis}D_{cr}}} = \frac{\alpha I_0}{k_{vis}\lambda} \tag{4.1}$$

derived by Sverdrup (1953). Here it is assumed that the surface irradiance I_0 is low enough that the photosynthetic response is linear over the entire water column, and that light attenuation can be represented by a single attenuation constant k_{vis}. This approach also assumes that wind-driven mixing removes any vertical gradients in biomass, and that the phytoplankton loss rate λ is constant. In this context, light limitation arises due to a deep mixed layer($D > D_{cr}$) and/or turbid waters (high k_{vis}) and/or weak surface irradiance (low I_0).

4.2.2 Self-shading and photoacclimation

One aspect of phytoplankton blooms that the critical depth hypothesis neglects is the impact of the bloom itself on light availability. When chlorophyll contributes significantly to overall light attenuation in the mixed layer via self-shading, k_{vis} can no longer be regarded as a constant. Instead k_{vis} will increase with increasing chlorophyll, leading to a self-shading feedback by which biomass near the surface limits the light available for deeper phytoplankton to photosynthesize (Vernet et al., 2008).

Another complication is due to phytoplankton motion through the water column. This may be either active or passive, and plays a major role in regulating carbon fluxes and marine ecosystems (Wirtz and Smith, 2020). As phytoplankton cells move through the water column they sample a range of light environments, and they adapt their physiology accordingly (Geider

et al., 1997). Assuming passive motion, each phytoplankton cell can be modelled as a Lagrangian particle subject to vertical mixing (Kida and Ito, 2017). For each particle there is generally a mismatch between the instantaneous irradiance to which it has access and the irradiance to which it is adapted. The former is a function of current conditions, whilst the latter is a Lagrangian property, dependent on the previous light history to which the cell has been exposed. This light history is known as the irradiance memory.

4.2.3 The Carrying Capacity Hypothesis

A phytoplankton bloom is iron-limited when the demand from photosynthesizing cells for bioavailable iron exceeds the supply. Numerical models have been used to construct iron budgets that show how physical and biogeochemical processes control iron supply to the polynya over the course of a growing season (St-Laurent et al., 2019).

In general, iron availability in the upper ocean is expected to be at a maximum during winter when there is strong vertical mixing from deeper waters; the availability of iron then progressively declines as the bloom develops in summer. This gives rise to the carrying capacity hypothesis (Hopkinson et al., 2013), whereby the inventory of iron just before bloom onset places a limit on the NPP which a given location can ultimately support.

4.2.4 Iron supply to the Amundsen Sea Polynya

Dotson Ice Shelf (DIS) is an ice shelf on the coast of Marie Byrd Land, West Antarctica, just west of the Amundsen Sea Embayment into which flow Pine Island and Thwaites Glaciers. Sea ice is advected from east to west in front of the Amundsen Sea Embayment by a strong coastal current, but Thwaites Fast-Ice Tongue (TFIT) (St-Laurent et al., 2017) prevents much of the sea ice formed upstream from entering the Amundsen Sea Polynya (ASP). Thus in summer the ASP is consistently free of sea ice (Stammerjohn et al., 2015). Furthermore, mixed layers are generally shallow in summer, rarely exceeding 70 m (Alderkamp et al., 2015; Park et al., 2017), suggesting that it is instead water column turbidity which leads to light limitation in the ASP (Schofield et al., 2015).

St-Laurent et al. (2017) used a summertime drawdown of iron in order to mimic biological uptake, and assessed the different contributions to the replenishment of the iron inventory over the winter. Possible sources of iron to the ASP include sea ice, sediments, Circumpolar Deep Water (CDW), icebergs, atmospheric dust, and glacial meltwater. Shipboard measurements in the ASP show a gradient of increasing iron concentration with increasing proximity to DIS, suggesting a source within the ice shelf cavity (Alderkamp et al., 2015; Gerringa et al., 2012). Accordingly St-Laurent et al. (2017) identified both sediments and glacial iron as important contributors to the wintertime iron inventory, with the contribution from the former mediated by the meltwater pump effect. This mechanism entrains iron-rich deep water into the buoyancy-

driven overturning beneath the ice shelf, resulting in a redistribution of iron from depth to the upper ocean. A meltwater pump effect has already been identified as a key driver of high NPP around Greenland, where it serves to bring limiting macronutrients to the surface (Cape et al., 2019).

Further modelling of the ASP (Oliver et al., 2019; St-Laurent et al., 2019) has resolved the principal biogeochemical components of the dissolved iron budget: uptake, scavenging and remineralisation. The westwards flowing coastal current in the Amundsen Sea was shown to be an important driver of seasonal iron cycles. Oliver et al. (2019) undertook extensive optimization of biogeochemical parameters, making use of datasets from the ASPIRE research cruise (Yager et al., 2012) (see values listed in Table 1). The resulting one dimensional model was able to provide a good fit to data for multiple stations. Furthermore, it reproduced many key features of the 2010/2011 bloom in the ASP, most importantly a transition from light limitation to iron limitation was observed over the course of the season.

4.2.5 Colimitation of phytoplankton blooms in the Amundsen Sea Polynya

In the ASP there is strong evidence for colimitation of productivity, whereby the relative importance of iron versus light varies with:

- Time: As in Oliver et al. (2019), depletion of iron stocks over the growing season may lead to a temporal succession from light to iron limitation. This is difficult to verify in the ASP due to the narrow time window for which it is accessible to research cruises. However Arrigo et al. (2017) do observe this succession from light to iron limitation near the West Antarctic Peninsula (WAP).
- Depth: Light availability decays exponentially with depth, whilst the iron concentration will often show a near-surface minimum. Hence iron limitation may dominate near the surface even whilst light limitation dominates deeper in the mixed layer.
- Location: Large horizontal gradients in sea ice cover, mixed layer depth and external iron supply may lead to differences in limitation between different regions of the polynya. Alderkamp et al. (2015) measured greater iron limitation in the central ASP, despite its higher productivity compared to coastal waters.

In addition, the demands of phytoplankton for iron and light are codependent. Phytoplankton cells demand iron in part to maintain their photosynthetic apparatus (Strzepek and Harrison, 2004). When ambient iron concentrations are below those needed for efficient photosynthesis, and cells are thus in a state of iron stress, light limitation can become more severe (Geider et al., 1997). An important marker of iron stress in phytoplankton is the ratio of variable fluorescence to maximum fluorescence (Fv/Fm), as used in the ASP by Alderkamp et al. (2015) and Park et al. (2017). More generally, the various light and nutrient requirements of phytoplankton communities are often intricately coupled rather than being independent of each other (Saito et al., 2008).

Within the consensus that the phytoplankton bloom in the ASP is co-limited by both iron and light, it remains important to study whether the overall productivity of the polynya - and therefore its capacity to sequester carbon (Yager et al., 2016) - is in fact more sensitive to one variable than the other. Park et al. (2017) conducted an intercomparison of two polynyas: the ASP and nearby Pine Island Polynya (PIP). Results showed that compared to the PIP, the ASP exhibits both more severe iron stress and higher productivity. This apparent paradox can be resolved if the Amundsen Sea is primarily light-limited, since reanalysis data show lower cloud cover above the ASP, leading to surface irradiances up to 15% greater than in the PIP (Park et al., 2017). Conversely Arrigo et al. (2015) completed a continental scale survey of coastal polynyas and identified basal melting as the key driver of NPP, by supplying iron to phytoplankton communities where it is strongly limiting.

4.2.6 Motivation for Lagrangian and Eulerian Modelling

Following the deployment of autonomous gliders during the ASPIRE expedition to the ASP, Schofield et al. (2015) identified water column turbidity, iron supply, vertical mixing and photoacclimation as key factors which influence the changing biogeochemistry of the Amundsen Sea. Modelling provides opportunities to understand how these different drivers each affect the polynya.

Interactions between vertical mixing and photoacclimation are difficult to capture within a Eulerian model, as each cell adapts its photosynthetic apparatus based on its individual light history, rather than based on the bulk properties of the bloom. Instead, the first section of this chapter shows how a one-dimensional Lagrangian model can be used to examine the ways in which external (vertical mixing) and internal (adaptation of photosynthetic apparatus) timescales dictate the bio-optical properties of each cell within the bloom.

In the second section of this chapter, the MITgcm-BLING model described in Chapter 3 is applied to an idealised domain covering DIS and the ASP. A series of experiments is used to quantify the relative importance of light and iron limitation, and to identify a transition from the former to the latter over the course of the phytoplankton bloom in the ASP.

4.3 A Lagrangian Model of Photoacclimation

Lagrangian ocean models allow for tracking of individual fluid parcels and of individual particles within the fluid. On a global scale, Lagrangian modelling has been used to investigate microplastic accumulation (Sterl et al., 2020); whilst combined with the Southern Ocean State Estimate (SOSE) Lagrangian tracking has been used to follow the trajectories of Argo floats (Chamberlain et al., 2018) and to study the connectivity of Antarctic Bottom Water (ABW) with the Atlantic, Pacific, and Indian Oceans (van Sebille et al., 2013).

On a smaller scale, Kida and Ito (2017) used Lagrangian modelling to study the conditions necessary for the sustenance of phytoplankton blooms. In this section a one-dimensional Lagrangian particle-tracking model similar to that of Kida and Ito (2017) is combined with the definition of irradiance memory used in the Biology Light Iron Nutrients and Gases (BLING) model, in order to investigate the interplay between vertical mixing and photoacclimation within a phytoplankton bloom representative of that in the ASP.

4.3.1 Model setup

An ensemble of phytoplankton cells is considered, in which each cell is assumed to move by diffusion through the water column as a passive particle (Figure 4.1). At every time step each phytoplankton cell moves from depth z_{n-1} (m) to a new depth z_n (m) according to

$$z_n = z_{n-1} + v_n \Delta t \tag{4.2}$$

where $\Delta t = 60$ s is the length of the time step. The stochastic velocity v_n (ms^{-1}) is generated using a random number R_{norm} drawn from a normal distribution $P(v_n)$ with mean zero and unit standard deviation,

$$v_n = R_{norm} \sqrt{2 \frac{K_z}{\Delta t}}, \tag{4.3}$$

where K_z (m^{2}s^{-1}) is the vertical diffusivity. Combining Equations 4.2 and 4.3 it is apparent that, for $n > 1$, z_n is drawn from a normal distribution $P(z_n)$ centred on z_{n-1} and with width $\sqrt{2K_z \Delta t}$:

$$z_n = z_{n-1} + R_{norm} \sqrt{2K_z \Delta t}. \tag{4.4}$$

The initial depth z_1 (m) of each phytoplankton cell is generated using a random number R_{uni} drawn from a uniform distribution over the unit interval,

$$z_1 = R_{uni} D, \tag{4.5}$$

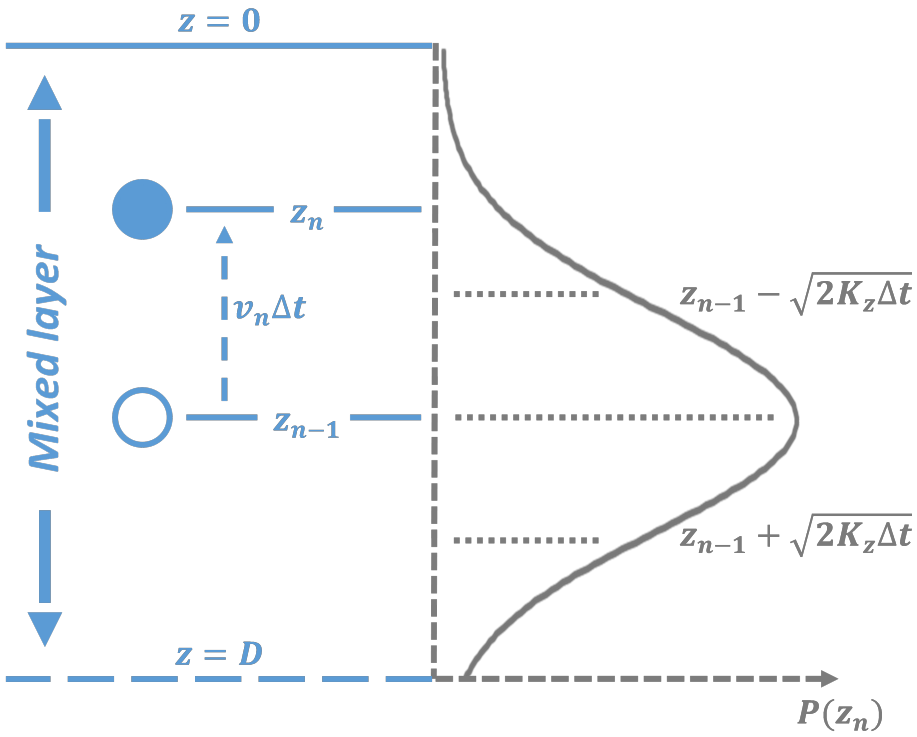

Figure 4.1: Schematic showing movement of a phytoplankton cell from position z_{n-1} to position z_n in time Δt according to the Lagrangian model. The position z_n is drawn from a normal distribution $P(z_n)$ centred on z_{n-1} and with width $\sqrt{2K_z \Delta t}$; the velocity of the particle is v_n.

where $D = 20$ m is the mixed layer depth. Reflective boundary conditions keep the phytoplankton cell within the mixed layer, so that a cell translated by Equation 4.4 to a position z_n which is above the sea surface is instead reflected down to $-z_n$, whilst a cell translated by Equation 4.4 to a position z_n which is deeper than the mixed layer D is instead reflected back up to $2D - z_n$. Thus the boundary conditions are

$$z_n = \begin{cases} -z_n \text{ if } z_n < 0 \\ z_n \text{ if } 0 < z_n < D \\ 2D - z_n \text{ if } z_n > D. \end{cases} \tag{4.6}$$

At each time step, the depth of the phytoplankton cell is used to calculate the instantaneous irradiance I (W m^{-2}) to which it is subjected:

$$I(z_n) = I_0 e^{-kz_n}. \tag{4.7}$$

Table 4.1: The four experiments conducted on the Lagrangian model, defined by values of vertical diffusivity K_z anf photoacclimation timescale τ_{acc}.

		τ_{acc} (hours)	
		1	24
K_z (m^2 s^{-1})	0.01	$turb\_fast$	$turb\_slow$
	0.001	$strat\_fast$	$strat\_slow$

Here $I_0 = 100$ W m^{-2} is the surface irradiance and $k_{vis} = 0.04$ m^{-1} is the visible light attenuation coefficient in the mixed layer, which is assumed here to be constant. Finally the irradiance memory I_{mem} (W m^{-2}) is calculated via

$$I_{mem}(z_n, z_{n-1}, ...z_1) = (1 - \frac{\Delta t}{\tau_{acc}})I_{mem}(z_{n-1}, z_{n-2}, ...z_1) + \frac{\Delta t}{\tau_{acc}}I(z_n), \tag{4.8}$$

analogous to the calculation of irradiance memory within BLING. Here the photo-adaptation timescale τ_{acc} decides the relative importance of the irradiance memory at the previous time step and the instantaneous irradiance at the current time step, in determining the new value for irradiance memory.

4.3.2 Model experiments

This model setup leaves two free parameters which can be adjusted: the photo-adaptation time scale τ_{acc} and the vertical diffusivity K_z. The impact of these parameters on irradiance memory is not predictable analytically, but here is investigated numerically by running the model with four different choices of parameters. These four experiments - $turb\_slow$, $turb\_fast$, $strat\_slow$, $strat\_fast$ - are defined in Table 4.1.

The model is iterated through 5000 time steps, for each of 1000 independent phytoplankton cells. The trajectories of the cells are then examined as well as the final states of instantaneous irradiance $I(z_{5000})$ and irradiance memory $I_{mem}(z_{5000}, z_{4999}, ...z_1)$.

4.3.3 Results

The distribution of final states for each model experiment is shown in Figure 4.2, relative to the depth averaged irradiance over the mixed layer, I_{mld}. This latter quantity can be calculated analytically as

$$I_{mld} = \frac{I_0}{k_{vis}D}(1 - e^{-k_{vis}D}), \tag{4.9}$$

giving a value $I_{mld} = 68.8$ W m^{-2} for $k_{vis} = 0.04$ m^{-1}, $D = 20$ m. Each of the plots in Figure 4.2 also includes a least squares linear fit for the distribution of final states (I,I_{mem}).

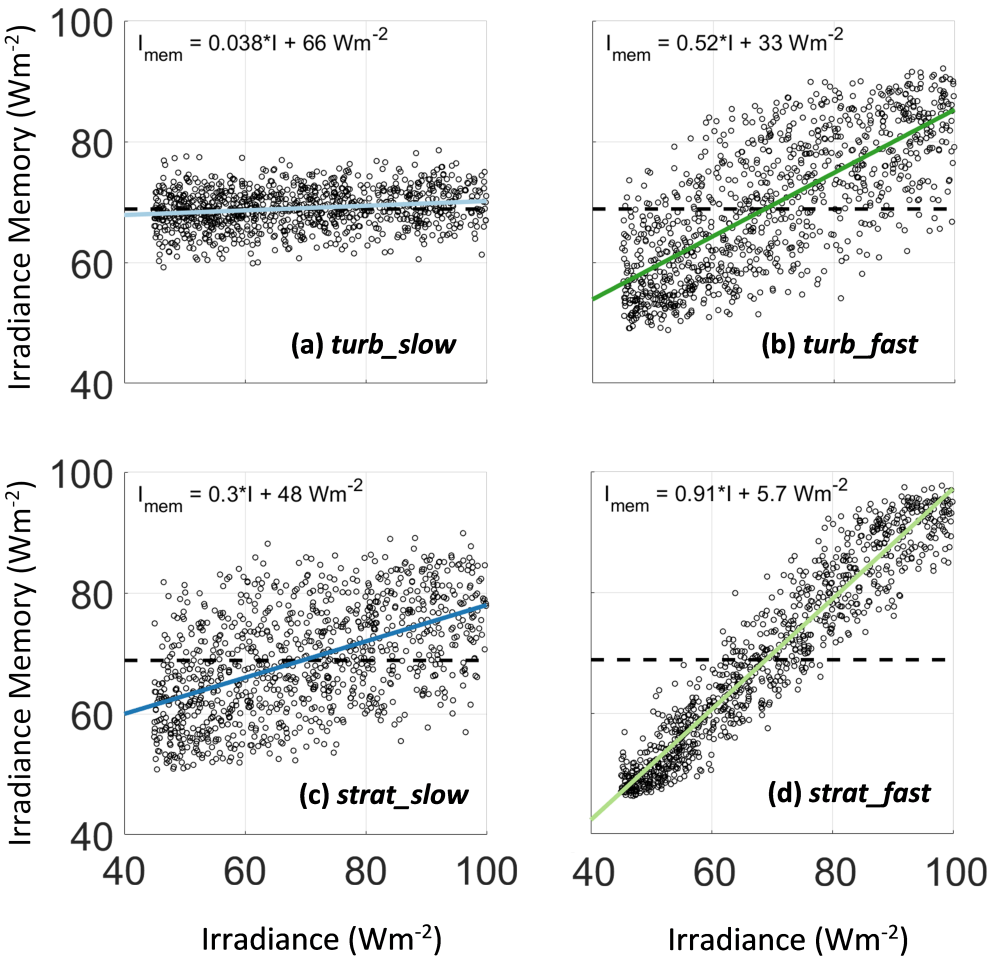

Figure 4.2: Distribution of final states (I, I_{mem}) for each of the four experiments. Each circle represents the final state (I, I_{mem}) of a phytoplankton cell at the end of 5000 iterations of the Lagrangian model.

For the $turb\_slow$ experiment, which has intense mixing and slow photoacclimation, there is a narrow distribution of final states with I_{mem} close to I_{mld} for all values of I. For the $strat\_fast$ experiment, which has weak mixing and fast photoacclimation, there is a narrow distribution of final states with values of I_{mem} situated along a line close to $I_{mem} = I$.

For the $turb\_fast$ and $strat\_slow$ experiments, the distributions of final states are wider, reflecting a greater spread in the degree of acclimation along different particle trajectories. The slope of the trend in each case is intermediate between the $turb\_slow$ and $strat\_fast$ results.

This distribution of final states is investigated further in Figure 4.3, where a sub-set of particle trajectories is plotted for each of the four experiments. The spreads of trajectories in $turb\_slow$ and $turb\_fast$ are qualitatively equivalent. However whilst in $turb\_slow$ the intense mixing leads to a progressive homogenisation of irradiance memory, in $turb\_fast$ the fast photoacclimation is such that the vertical structure in irradiance memory is partially retained. Similarly, in $strat\_slow$ and $strat\_fast$, the spreads of trajectories are qualitatively equivalent, but vertical structure in irradiance memory is retained to a much greater degree in $strat\_fast$ compared to $strat\_slow$.

4.3.4 Towards a parameterization of photoacclimation

These numerical results can be used to motivate a parameterization for use in Eulerian models, by first defining the mixing timescale

$$\tau_{mix} = D^2/K_z \tag{4.10}$$

as in Kida and Ito (2017). Then the ratio between mixing and photoacclimation timescales can be defined as

$$\zeta = \frac{D^2}{K_Z \tau_{acc}}. \tag{4.11}$$

This dimensionless parameter ζ is calculated for each of the four experiments in Table 4.2.

Next, a heuristic approach can be employed to arrive at a parameterization for I_{mem}, and thus for the photoacclimation process itself. Logic dictates that when mixing is much faster than photoacclimation, each phytoplankton cell should be entirely adapted to the average mixed layer irradiance I_{mld}, and thus

$$\lim_{\tau_{mix} << \tau_{acc}} I_{mem} = I_{mld}. \tag{4.12}$$

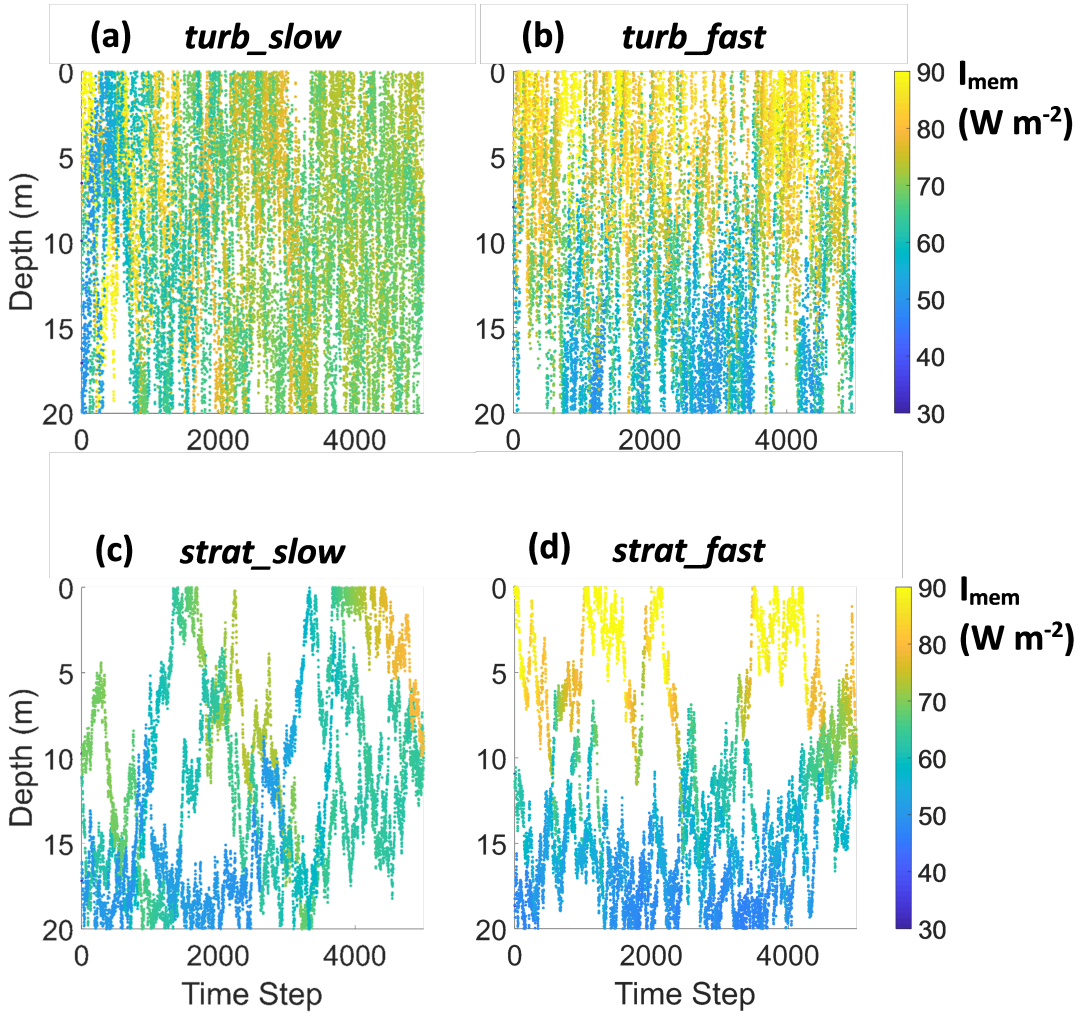

Figure 4.3: Representative trajectories for phytoplankton cells in each of the four experiments, with the colourmap denoting irradiance memory.

Table 4.2: Values of ζ calculated for the four experiments, with $D = 20$ m.

		τ_{acc} (hours)	
		1	24
K_z (m^2 s^{-1})	0.01	11.1	0.463
	0.001	111	4.63

Conversely, when photoacclimation is much faster than mixing, the irradiance memory should be independent of the average mixed layer irradiance, and instead each phytoplankton cell should be entirely adapted to the instantaneous irradiance I:

$$\lim_{\tau_{mix} >> \tau_{acc}} I_{mem} = I. \tag{4.13}$$

The simplest formulation for I_{mem} which can fulfill these requirements is a sum of two terms, one featuring I and another featuring I_{mem}. The weighting of the terms should be dictated only by the value of $zeta$; more especially, the multiplier of I should increase from zero to a maximum of one as the value of $zeta$ increases, whilst the multiplier of I_{mld} should increase from zero to a maximum of one as the value of $zeta$ decreases. The simplest formulation meeting all of these tests is

$$I_{mem} = \frac{1}{1+\zeta} I_{mld} + \frac{\zeta}{1+\zeta} I, \tag{4.14}$$

which using Equation 4.9 can be restated as

$$I_{mem} = \frac{I_0}{1+\zeta} \left(\frac{1 - e^{-k_{vis} D}}{k_{vis} D} + \zeta e^{-k_{vis} z} \right). \tag{4.15}$$

In Figure 4.4 the analytically derived values of I_{mem} are plotted alongside the lines of best fit obtained from the numerical simulations. The analytically derived slope is consistently steeper than that produced from the numerical simulations, for each of the different values of ζ. However the ordering of the analytical functions by increasing gradient matches that obtained in the numerical simulations; namely $turb\_slow$, $strat\_slow$, $turb\_fast$, $strat\_fast$.

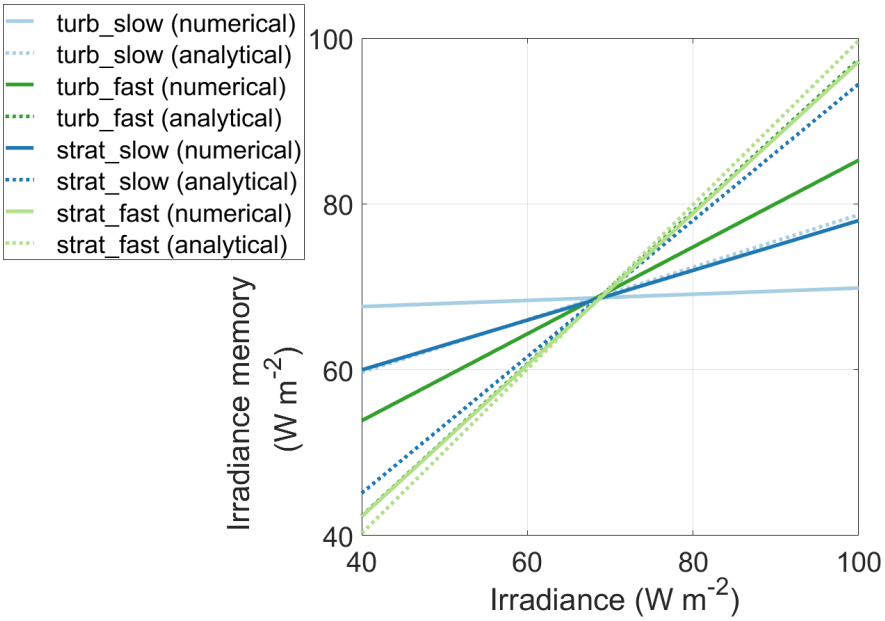

Figure 4.4: Comparison of analytically and numerically derived relationships between irradiance and irradiance memory, for each of the four experiments.

4.4 An idealised representation of the Amundsen Sea Polynya

4.4.1 Model setup

From hereon in, this thesis makes use of the MITgcm-BLING model as introduced in Chapter 3. For this section in particular, the model is implemented on an idealised domain representing the ASP. However some key modifications are made to the BLING setup which distinguish it from the version described in Verdy and Mazloff (2017). These modifications are outlined in the following.

Phytoplankton irradiance memory

Firstly, the relatively high vertical resolution of the model setup compared to that used in the Biological Southern Ocean State Estimate (BSOSE) necessitates a more careful consideration of irradiance memory. At this stage it might be possible to implement a "ζ-parameterization" similar to that described above. However, this modelling also makes use of a vertical mixing scheme based on a depth-varying diffusivity coefficient (Equation 3.4), so that the mixing timescale cannot be derived as simply as in Equation 4.10.

Therefore in this model setup a ζ-parameterization is not introduced; instead it is simply assumed that within the mixed layer

$$\tau_{mix} << \tau_{acc}, \tag{4.16}$$

whilst below the mixed layer

$$\tau_{mix} >> \tau_{acc}; \tag{4.17}$$

whereas before τ_{mix} and τ_{acc} are the mixing and photoacclimation timescales respectively.

This corresponds to a mixed layer where between time $t - \tau_{acc}$ and time t each phytoplankton cell has been transported over the full depth of the mixed layer multiple times; below the mixed layer each cell remains at approximately the same depth between time $t - \tau_{acc}$ and time t. Therefore the irradiance memory becomes a bulk property within the mixed layer, and I_{mem} evolves according to the equation

$$\frac{dI_{mem}}{dt} = \begin{cases} (I_{mld} - I_{mem})/\tau_{acc} \text{ within the mixed layer} \\ (I - I_{mem})/\tau_{acc} \text{ below the mixed layer.} \end{cases} \tag{4.18}$$

The instantaneous irradiance remains unmodified both within and outside the mixed layer. This is in contrast to Galbraith et al. (2010), where both instantaneous irradiance and irradiance memory are homogenised throughout the mixed layer, and Verdy and Mazloff (2017), where neither are homogenised.

Phytoplankton self-shading

This new implementation of phytoplankton self-shading in MITgcm makes use of the bio-optical model of Manizza et al. (2005) as in previous earth system modelling (Kim et al., 2015; Manizza et al., 2008). Photosynthetically available radiation (PAR) is split into two bands of approximately equal power following Foujols et al. (2000). Attenuation coefficients k_{red} (m^{-1}) and k_{bg} (m^{-1}) for the red and blue-green components respectively are calculated as

$$k_{red} = k^0_{red} + \chi_{red}[Chl]^{e_{red}}, \tag{4.19}$$

and

$$k_{bg} = k^0_{bg} + \chi_{bg}[Chl]^{e_{bg}} \tag{4.20}$$

where $[Chl]$ (units of mg Chl m^{-3}) is the local concentration of chlorophyll. The parameters $\chi_{red} = 0.037$ m^{-1} ((mg Chl $m^{-3})^{e_{red}})^{-1}$, $\chi_{bg} = 0.074$ m^{-1} ((mg Chl $m^{-3})^{e_{bg}})^{-1}$, $e_{red} = 0.629$, $e_{bg} = 0.674$, $k^0_{red} = 0.225$ m^{-1} and $k^0_{bg} = 0.0232$ m^{-1} are the same as in Manizza et al. (2005) and are based on the study of Morel (1988). This treatment does not resolve individual scattering or absorption processes, but assumes that the number of photons actually used in photosynthesis is small compared to those otherwise attenuated by chlorophyll.

Thermodynamically, this implies that self-shading should contribute significantly to the heat budget in ocean cells close to the ocean surface - the implementation of this feedback is covered in Chapter 6. The approach in this chapter of not implementing the biophysical feedback allows different versions of the biogeochemical model to be tested whilst maintaining a fixed set of physical properties for the water column.

Choice of biogeochemical parameters

In the original BLING model (Galbraith et al., 2010), the chlorophyll-specific quantum yield α_{chl} of the phytoplankton photosystem depends on the degree of iron limitation. This response,

$$\alpha_{chl} = \alpha_{chl}^{min} + \left(\alpha_{chl}^{max} - \alpha_{chl}^{min}\right) \frac{Fe}{Fe + K_{Fe}}, \tag{4.21}$$

was removed in the BSOSE version of BLING (Verdy and Mazloff, 2017) and replaced with a constant value of α_{chl}. This was based on the fact that, for the Southern Ocean as a whole, photosynthesis rates are not high enough for changes in photosynthetic efficiency to be important (Galbraith et al., 2010). However as the present study is concerned with very intense localised blooms with high growth rates, this iron dependence is reinstated, so that Equation 3.30 becomes

$$\alpha = \left(\alpha_{chl}^{min} + \left(\alpha_{chl}^{max} - \alpha_{chl}^{min}\right) \frac{Fe}{Fe + K_{Fe}}\right) \left(\theta_{dark}^{min} + \left(\theta_{dark}^{max} - \theta_{dark}^{min}\right) \frac{Fe}{Fe + K_{Fe}}\right). \tag{4.22}$$

The values of α_{chl}^{min}, α_{chl}^{max}, θ_{dark}^{min}, θ_{dark}^{max}, taken from Galbraith et al. (2010), and K_{Fe}, taken from Verdy and Mazloff (2017), are listed in Table 4.3 - alongside other key values of parameters in BLING. Where possible the equivalent parameters used by Oliver et al. (2019) are also given. Sensitivity tests are not carried out for these parameters; to do such tests for all the BLING default parameters would require an order of magnitude more computing resources.

Physical Model

The ice shelf model is as described in Section 3.2. Following Schodlok et al. (2012), friction velocities are kept constant, so that ice shelf melt is only dictated by temperature and not by ocean velocities at the interface. The sea ice model is also as described in Section 3.2. Since precipitation is not included in model forcings, the layer of snow with different conductivity and albedo as modelled in Zhang et al. (1998) is absent.

Vertical mixing using the K-Profile Parameterization (KPP) (Large et al., 1994) acts on temperature, salinity and biogeochemical variables, in common with other models of the Amundsen Sea (Kimura et al., 2017; Nakayama et al., 2017). The mixed layer depth is defined using the second derivative of density with depth, and is used both as a diagnostic and in the calculation of irradiance memory homogenization.

Table 4.3: Optical and biogeochemical model parameters for the model, where possible shown alongside optimized values from Oliver et al. (2019); *parfrac* refers to the fraction of total downwelling shortwave irradiance which is deemed to be photosynthetically available.

Parameter Category	Parameter		Value used in *gmw_iron*	Value used in Oliver et al, 2019	Units
Phytoplankton Growth	α_{chl}	min	0.058	-	(mg Chl)$^{-1}$ (W m^{-2})$^{-1}$ day^{-1}
		max	0.346		
	α		$\alpha_{chl}\theta_{dark}$	0.12	(W m^{-2})$^{-1}$ day^{-1}
	θ_{dark}	min	10	-	mg Chl (g C)$^{-1}$
		max	40		
	μ_{max}		1.47	0.82	day^{-1}
	κ		0.063	-	$^{\circ}$C^{-1}
	λ		0.19	0.3	day^{-1}
	K_N		2.05	2.5	mmol N m^{-3}
	K_P		10.25	-	μmol P m^{-3}
	K_{Fe}		0.16	0.26	μmol Fe m^{-3}
Iron Budget	η		0.081	-	g C (mmol N)$^{-1}$
	σ	min	0.17	0.013	μmol Fe (mmol N)$^{-1}$
		max	0.014		
	K_σ		0.82	-	μmol Fe m^{-3}
	γ_{POM}		0.12	-	day^{-1}
	r_{min}		0.15	-	-
	K_{O2}		20	-	mmol O_2 m^{-3}
Irradiance	$parfrac$		0.40	0.64	-
	τ_{acc}		1	-	days
	k_0	red	0.225	0.04	m^{-1}
		bg	0.0232		
	χ	red	0.037	-	m^{-1} ((mg Chl m^{-3})$^{e_{red}}$)$^{-1}$
		bg	0.074		m^{-1} ((mg Chl m^{-3})$^{e_{bg}}$)$^{-1}$
	e	red	0.629	-	-
		bg	0.674		

4.4.2 Model domain

MITgcm is used to model ocean physics, with a domain forming an idealised version of Dotson Ice Shelf (DIS) and the Amundsen Sea Polynya (ASP) (Figure 4.5). A Cartesian grid of 1 km horizontal resolution is employed across the domain, extending 150 km in the zonal and meridional directions. DIS is represented with a static ice shelf bordered to the west and east by blocks of land representing Martin Peninsula and Bear Peninsula respectively. The vertical resolution is variable, ranging from 1 m at the surface to 64 m at the bottom of Dotson Trough. The trough extends from the north west corner of the domain to the southern boundary under the ice shelf. It has a base depth of 950 m, with sides sloping up to the 400 m sill outside the trough. There is an open northern boundary, whilst the zonal boundaries are kept periodic. This means that the model outputs represent the result of a series of adjacent ice shelves, analogous to Pine Island Glacier, Crosson Ice Shelf, Thwaites Glacier and DIS, which run from east to west along the coastline of the ASP (Figure 4.5). Such an approximation is justified by the fact that all these ice shelves share the same fundamental driver - the inflow of warm CDW through troughs from the continental shelf break.

The ice shelf is represented in an idealized fashion, specifically as a wedge with thickness increasing from 100 m at the cavity front to a maximum of 800 m at the southern boundary. The ice is grounded where it meets the sloping sides of the trough, but overlying the deepest part of the trough (where the bathymetry is at 950 m) the grounding line lies beyond the southern edge of the domain.

The freshening tendency at the top of each water column underneath the ice shelf acts as a source for meltwater tracers, two of which are used in the following investigations. These are sourced identically at the ice shelf, but only one of them (the “global” tracer) is allowed to pass through the periodic ocean boundaries, reentering the domain from the east. The other, “local” tracer, is relaxed to zero at periodic boundaries and thus allows us to isolate meltwater from DIS without the influence of upstream sources in the Amundsen Sea.

Work by Stammerjohn et al. (2015) and Bett et al. (2020) suggests that polynya formation in the Amundsen Sea depends on the presence of the Thwaites Fast-Ice Tongue, and the same behaviour was found here in preliminary investigations (not shown). Without any obstruction to westwards moving sea ice, the polynya fails to open in spring. Hence in all subsequent model runs a 2 m thick portion of ice shelf (outlined in red in Figure 4.5) is added at the western boundary, serving as an obstacle to sea ice reentering the domain from the east. This ice tongue is a negligible source of meltwater, but it succeeds in maintaining a small region of open water adjacent to the ice shelf from which the polynya can develop in spring.

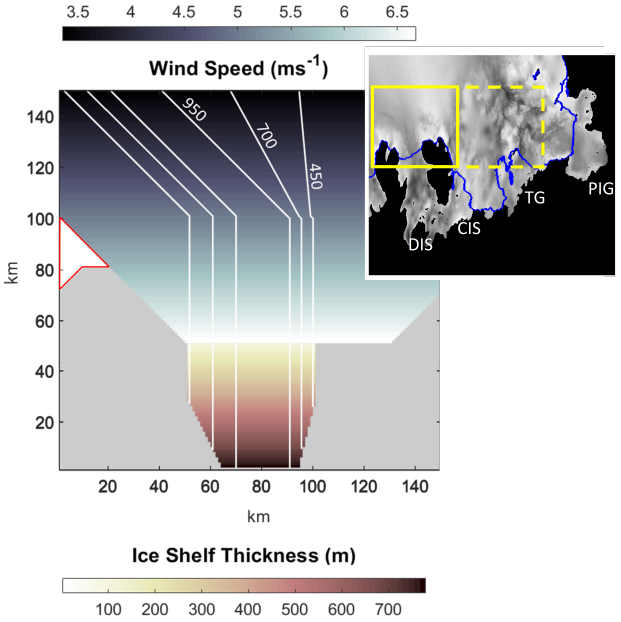

Figure 4.5: Main figure: model domain – viewed from above – including bathymetry, ice shelf topography and wind forcing. The wind speed (blowing from the southeast at 45°) over the ocean domain is shown in the blue colourmap and the ice shelf thickness is shown in the red colourmap. The portion of ice shelf enclosed in a solid red line serves to prevent sea ice re-entering the domain from the east, as a substitute for Thwaites Fast-Ice Tongue. White contours show the bathymetry. Inset: map of Amundsen Sea from BedMachine data (Morlighem et al., 2020), including DIS, Crosson Ice Shelf (CIS), Thwaites Glacier (TG) and Pine Island Glacier (PIG). Blue lines show the position of ice shelf fronts; the grey colourmap shows bathymetry. The box enclosed by a solid yellow line indicates the area modelled in the domain. Since zonal boundaries are set to be periodic, the inputs at the eastern edge of this domain are equivalent to the outputs from an identical domain located to the east. This is represented by the box enclosed by dashed yellow lines.

At the northern boundary the temperature and salinity are relaxed towards prescribed values at a one week timescale. These values are informed by profile outputs from Kimura et al. (2017) on a transect approximately 100 km from the front of DIS, but are kept constant over the course of the year. Therefore the seasonal fluctuations in onshore CDW transport, thought to influence cycles in basal melt rate (Kimura et al., 2017), are not resolved. Surface forcing of the model is via monthly fields for 2 m air temperature and humidity, 10 m winds, longwave and shortwave downwelling radiation. Monthly fields for temperature, humidity and radiation are based on the climatological forcings used in Petty et al. (2013), which in turn derive from NCEP-CFSv1 reanalysis data (Saha et al., 2006). In contrast, winds are treated as constant over time. This is in order to simplify the analysis of couplings between thermocline depth, melt rate and sea ice cover. Constant winds imply that there is no seasonal variation in upwelling and downwelling across the domain (apart from that variability associated with overlying sea ice cover). The winds are south-easterly, with magnitude zonally constant but decreasing with meridional distance from the ice shelf (Kim et al., 2017).

To obtain biogeochemistry boundary conditions, BSOSE outputs are averaged over the period 2008 - 2012 on a monthly basis, for the region covered by 72.9°to 74.8°S, 110°to 115°W. These fields are then transposed onto the higher resolution vertical grid used in the present study. A mask is then applied to the ten cells nearest the northern boundary, and here BLING tracers are relaxed towards their respective boundary conditions, on a timescale of one week. The exception is iron, which is not prescribed on the boundary above 600 m in order to prevent artificial relief from limitation in the iron-depleted waters of the domain interior.

The physical model is first spun up for 18 months to reach quasi-equilibrium with external forcings before BLING is enabled. The eight core BLING tracers (ie. dissolved inorganic carbon, alkalinity, nitrate, phosphate, oxygen, iron, dissolved organic nitrogen and dissolved organic phosphorous) are initialized based on 2008-2012 BSOSE outputs for the month of June. Starting from midwinter allows the biomass tracer to be initialised close to zero. With biogeochemistry enabled, the full model is spun up for a further year, with results taken from the year beginning 30 months after model initialisation. The model spin-up was verified using time series in ocean heat flux, ice shelf melt rate and iron budget (not shown), which were approximately equal in the period with months 31 to 42 as in the period with months 19 to 30. A longer spinup would not be expected to impact substantially on results and would make it excessively costly to run the full suite of experiments presented in this chapter and in the next.

4.4.3 Model experiments

The model experiments are summarised in Table 4.4.

gmw_iron

The *gmw_iron* experiment serves as the base case, with an iron source in glacial meltwater (endmember concentration 20 μmol m^{-3}). The *melt_pump*, *flat_iron*, *fixed_zeu* and *max_yield* experiments all have strictly identical physics to *gmw_iron*, but implement different versions of the biogeochemical code.

melt_pump

The *melt_pump* experiment is identical to *gmw_iron* except for the fact that the source of iron in glacial meltwater is removed. As a result the only impact of the ice shelf on the polynya is via changes in the circulation of the physical model.

fixed_zeu

The impact of using the Manizza et al. (2005) self-shading scheme is investigated by comparison against an experiment (*fixed_zeu*) which employs the constant light extinction profiles used in Verdy and Mazloff (2017). Specifically the chlorophyll-dependent k_{red} and k_{bg} coefficients used in *gmw_iron* are replaced in *fixed_zeu* with a single, chlorophyll independent attenuation constant k_{vis}. A spatially and temporally constant light extinction profile implies a constant euphotic depth (the depth at which PAR is 1% of its surface value). For the *fixed_zeu* experiment a value of $k_{vis} = 0.04$ m^{-1} is chosen, giving a euphotic depth of 111 m. The difference in irradiance profiles and euphotic depths from *gmw_iron* as compared to *fixed_zeu* shows the effect of the modelled chlorophyll concentrations on the polynya light environment. Thus the different NPP observed in *gmw_iron* as compared to *fixed_zeu* is the result of increased light limitation arising from phytoplankton self-shading.

flat_iron

For the *flat_iron* experiment σ from Equation 3.34 is set to zero, so that phytoplankton uptake no longer serves as a sink of dissolved iron in the model. Since recycling is calculated as a fraction of uptake, this is also fixed at zero. As a consequence, the upper ocean iron budget in *flat_iron* represents a balance between remineralisation, scavenging and physical transport processes only. The different NPP observed in *gmw_iron* as compared to *flat_iron* is interpreted to be the result of increased iron limitation arising from phytoplankton uptake.

Table 4.4: List of experiments conducted in this section, showing differences in setup of biogeochemical model.

Experiment name	Self-shading?	Iron depletion?	Iron in meltwater?
gmw_iron	yes	yes	yes
melt_pump	yes	yes	no
fixed_zeu	no	yes	yes
flat_iron	yes	no	yes
max_yield	no	no	yes

max_yield

This experiment considers a hypothetical phytoplankton bloom which is neither strongly iron-limited nor strongly light-limited. For this max_yield experiment both $\sigma = 0$ μmol Fe (mmol N)$^{-1}$ as in $flat\_iron$ and $k_{vis} = 0.04$ m^{-1} as in $fixed\_zeu$ are used. The result is expected to be a much more productive bloom than in gmw_iron. In summary, these three experiments ($flat\_iron$, $fixed\_zeu$ and max_yield) allow iron and light sinks to be switched on and off, helping to demonstrate the relative importance of iron and light limitation at different locations and timings within the bloom.

4.4.4 Results

Impact of self-shading

The inclusion of the Manizza et al. (2005) formulation for self-shading in the model leads to reduced summertime light penetration. However there is an overall deepening in the annual- and spatially-averaged euphotic depth from 111 m to 118 m (Figure 4.6). This is due to lower light attenuation in winter, months when the water column is free of chlorophyll. The spatially averaged euphotic depth calculated in gmw_iron shoals from a maximum of 135 m in winter to a minimum of 95 m in summer. Therefore in $fixed\_zeu$ the euphotic depth is underestimated by as much as 18% in winter and overestimated by up to 17% in summer. There is also significant variation in summertime euphotic depth across the domain when self-shading is enabled, with a range of over 100 m between different locations. There are no differences in mixed layer depth between gmw_iron and $fixed\_zeu$ due to the identical physics of these experiments, and mixed layer is consistently shallower than the euphotic depth.

The reduced summertime light availability due to self-shading causes a reduction in December phytoplankton growth rate throughout most of the water column in gmw_iron as compared to $fixed\_zeu$ (Figure 4.7a). In addition, self-shading leads to a shoaling of the December Deep Chlorophyll Maximum (DCM) (Figure 4.7b) from 70 m in $fixed\_zeu$ to 30 m in gmw_iron. In both experiments the large phytoplankton fraction dominates biomass in at and above the DCM with the smaller fraction dominating below (Figure 4.7c).

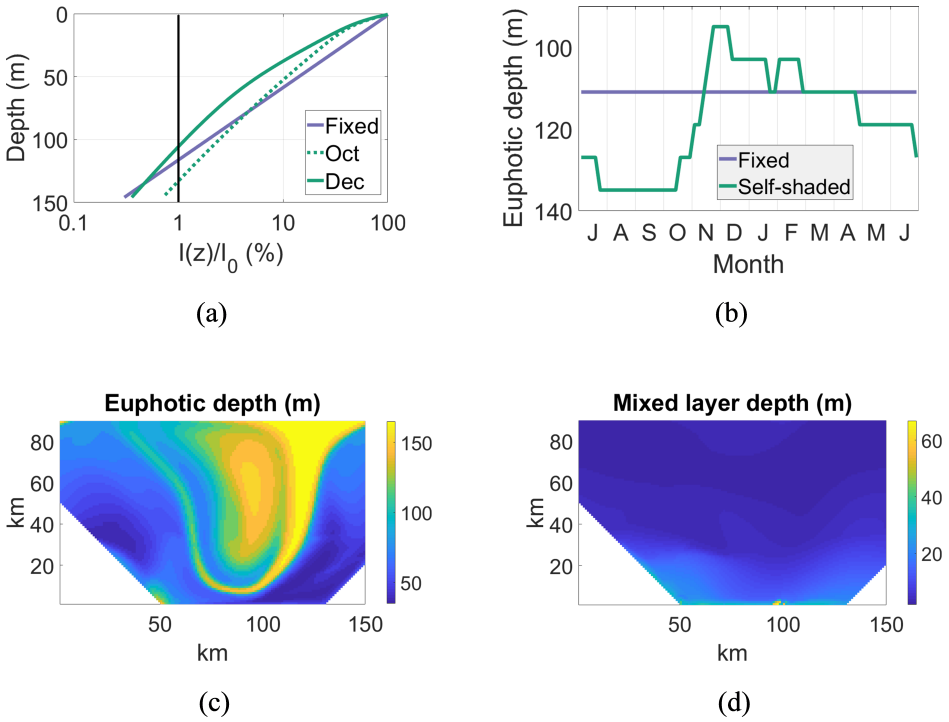

Figure 4.6: Impact of attenuation by chlorophyll on sub-surface light levels. In (a) the ratio of irradiance $I(z)$ at depth z to the irradiance I_0 at the surface is plotted on a logarithmic scale. The purple line shows the constant attenuation in the $fixed\_zeu$ experiment; the dotted green and solid green lines show self-shaded profiles (from gmw_iron) in October and December respectively. The euphotic depth for each profile is defined as the depth at which it intersects the vertical line marking 1% of surface irradiance. In (b) the time series in horizontally averaged euphotic depth are compared for the $fixed\_zeu$ and (self-shaded) gmw_iron experiments. The map in (c) shows spatial variation in the self-shaded euphotic depth for December gmw_iron outputs. The December distribution of mixed layer depths (d) remains the same across both gmw_iron and $fixed\_zeu$ as self-shading is not allowed to impact ocean physics.

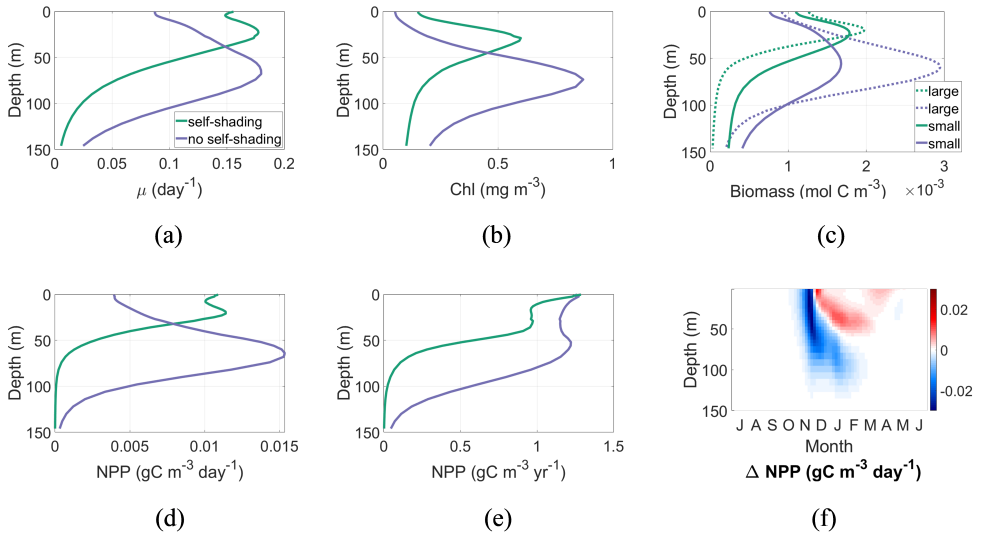

Figure 4.7: Impact of self-shading on averaged December depth profiles for per capita growth rate (a), chlorophyll (b) and biomass (c). Purple lines show results from $fixed\_zeu$, whilst green lines show results from gmw_iron. In (c) the solid line represents small phytoplankton biomass and the dashed line represents large phytoplankton biomass. The December averaged and annually integrated depth profiles of NPP are shown in (d) and (e) respectively. The anomaly in NPP due to self-shading is calculated by subtracting $fixed\_zeu$ results from gmw_iron and is shown in a Hovmoller plot (f).

Strikingly, above approximately 40 m self-shading in fact leads to an increase in both December phytoplankton growth rate December and NPP (Figure 4.7d) near to the surface (above 40m). However a profile of annual integrated NPP (Figure 4.7e) shows that on a yearly basis self-shading leads to a reduction in NPP throughout the entire water column. The anomaly in NPP between gmw_iron and $fixed\_zeu$ is represented in a Hovmoller plot (Figure 4.7f), which confirms the emergence of a positive surface anomaly following a strong negative anomaly earlier in the season. From this it can be inferred that the higher growth rates (and higher NPP) in $fixed\_zeu$ early in the season lead to greater depletion of iron near the surface, with this greater depletion in turn leading - later in the season - to greater surface iron limitation and thus lower surface growth rates (and lower NPP).

Figure 4.8 demonstrates the impact that self-shading has on the vertical distribution of biogeochemical tracers and on their seasonal cycles. The reduced uptake of nutrients in the upper ocean in gmw_iron leads to elevated nitrate and reduced oxygen close to the surface, with contrasting patterns at depth. The relative scarcity of iron means that iron concentrations are more sensitive to the degree of uptake in the system, so that the anomalies in iron concentration between $fixed\_zeu$ and gmw_iron can be greater than an order of magnitude near the surface. Furthermore, whilst anomalies in nitrate and oxygen are limited to the upper ocean, the anomaly in iron extends to the seafloor.

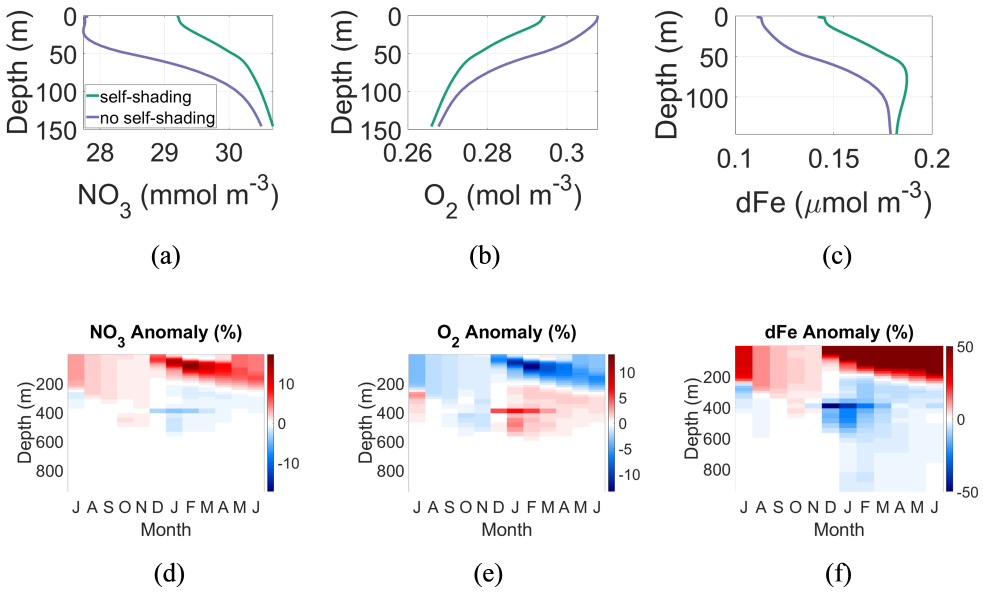

Figure 4.8: Changes in distribution of biogeochemical tracers due to inclusion of light attenuation by chlorophyll. Horizontally averaged December profiles are plotted for nitrate (a), oxygen (b) and iron (c) for the $fixed\_zeu$ and gmw_iron experiments. The Hovmoller plots show the anomaly in tracer concentration due to self-shading, calculated by subtracting the $fixed\_zeu$ fields from gmw_iron for nitrate (d), oxygen (e) and iron (f). In (f) the colourbar is saturated at 50% where severe depletion of iron in the $fixed\_zeu$ experiment leads to a drop in concentrations of several orders of magnitude.

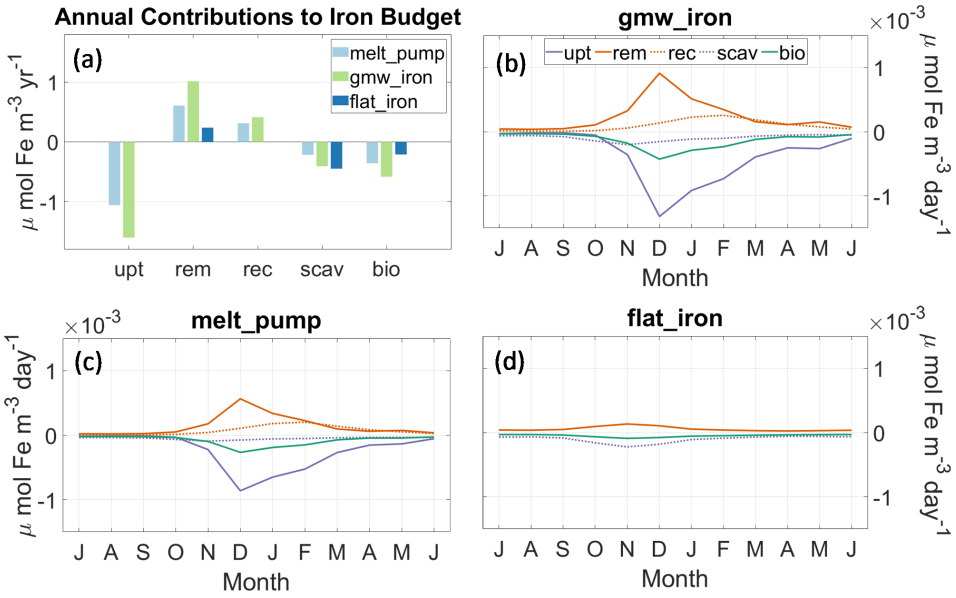

Figure 4.9: Biogeochemical sources and sinks of iron in the top 200 m of the ocean: plotted as annual contributions to the iron budget (a), and as time series for the *melt_pump* (b), *gmw_iron* (c) and *flat_iron* (d) experiments. The overall biological tendency "*bio*" is counteracted by physical processes within MITgcm.

Impact of biological iron uptake

In order to understand the seasonal cycling of iron, and how this impacts iron-light colimitation, the four key processes which BLING calculates in the upper ocean are considered: uptake (Fe_{upt}), remineralisation Fe_{remin}, scavenging Fe_{scav} and recycling Fe_{rec} (Equation 4.23). Thus only the biogeochemical component of Equation 3.42 are retained, namely

$$BGC_{Fe} = -Fe_{upt} + Fe_{rec} + Fe_{remin} - Fe_{scav}. \tag{4.23}$$

This means that the budgets in Figure 4.9 do not include the advection and diffusion processes that are calculated in the physical core of the MITgcm or the vertical mixing calculated using KPP.

In the *melt_pump* and *gmw_iron* cases the primary influences on the biological tendency of iron are the removal of dissolved iron by phytoplankton uptake and the addition of dissolved iron via remineralisation of organic material. Both uptake and remineralisation peak during December. Contributions from scavenging and recycling are smaller, with the latter showing

a peak around February, after the peak of the bloom. Uptake is 51% higher in gmw_iron as compared to $melt\_pump$, in line with the increased supply of iron from the ice shelf. For the $flat\_iron$ experiment iron uptake and recycling are suppressed as expected, but there is still a small biological tendency due to scavenging and remineralisation processes.

Iron-light colimitation

In Figure 4.10a the relative importance of iron and light in dictating NPP is examined using time series from gmw_iron, $fixed\_zeu$, $flat\_iron$ and max_yield. The last shows annual NPP an order of magnitude greater than that for gmw_iron, illustrating the large combined impact of iron uptake and phytoplankton self-shading in reducing the magnitude of the spring bloom. For all four experiments NPP remains close to zero until mid-October due to low light levels characteristic of Antarctic winter. At this point the time series diverge, with both max_yield and $fixed\_zeu$ beginning to show an increase in productivity. The spring bloom does not commence until approximately one month later for $flat\_iron$ and gmw_iron, both of these being experiments where self-shading is enabled.

As the bloom progresses, depletion of the initial iron pool due to phytoplankton uptake becomes cumulatively more severe. Hence NPP in the $flat\_iron$ case first exceeds that in gmw_iron, then eventually surpasses that for $fixed\_zeu$. The time at which $flat\_iron$ becomes more productive than $fixed\_zeu$ is identified as a transition from light to iron limitation. As the bloom declines the $flat\_iron$ experiment remains more productive than gmw_iron due to ongoing iron depletion in the latter.

Figure 4.10b shows how the relative importance of iron and light limitation varies across the domain, by subtracting the NPP in the $fixed\_zeu$ experiment from that in $flat\_iron$. Three distinct regions can be identified on the domain. In parts of the coastal current immediately adjacent to the peninsula, light limitation is strongly dominant. Immediately in front of the ice shelf, and in the outer reaches of the coastal current, iron limitation due to phytoplankton uptake is dominant. In the centre of the polynya, outside of the coastal current, neither the relief from self-shading nor the relief from iron uptake is sufficient to drive substantial productivity. Instead, phytoplankton growth appears to be inhibited from the outset by low ambient levels of dissolved iron.

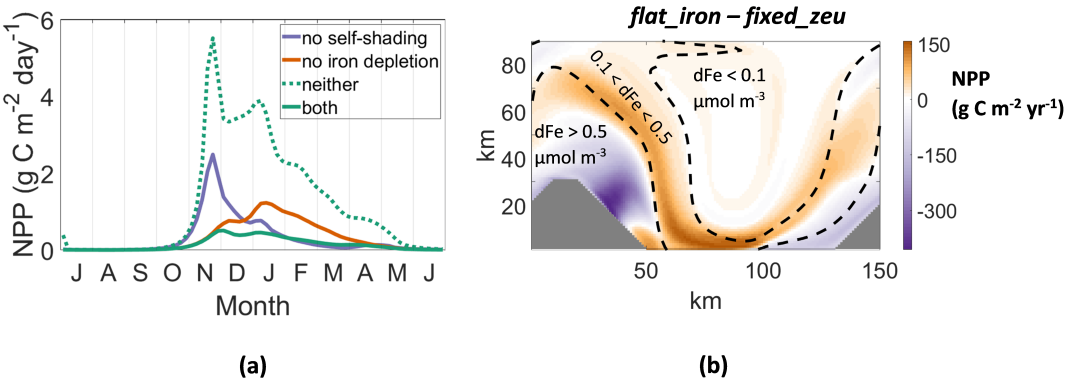

Figure 4.10: (a) Impact of iron-light colimitation on time series of NPP. Shown are the gmw_iron (green solid line), $fixed\_zeu$ (purple line), $flat\_iron$ (orange line) and max_yield (green dotted line) experiments. The relative importance of iron limitation compared to light limitation is shown in (b), calculated by subtracting the annual NPP modelled in $fixed\_zeu$ from that in $flat\_iron$. Wherever in the domain $flat\_iron - fixed\_zeu > 0$ iron limitation is dominant; wherever $flat\_iron - fixed\_zeu < 0$ light limitation is dominant. The dashed contour lines separate the domain into three section depending on the October (prior to bloom) concentration of dissolved iron, with highest concentrations closest to the coast.

4.5 Discussion

4.5.1 Vertical mixing

In this study the K-Profile Parameterization (KPP) is used to conduct vertical mixing. This follows previous modelling in the ASP (Kimura et al., 2017) but diverges from BSOSE, which uses the GGL_90 mixing scheme (Gaspar et al., 1990). Mixed layer depths of less than 20 m are observed throughout the domain except adjacent to the ice shelf front where there is a strong meltwater outflow from below 100 m. These depths were calculated using the second derivative of the density profile with depth, and were used as diagnostics as well as for homogenizing the irradiance memory. Modelled mixed layer depths are shallow compared to Alderkamp et al. (2015) and Park et al. (2017), who find mixed layers of up to 70 m and 50 m respectively in the ASP. This may in part be due to the fact that these observations use a density threshold to calculate mixed layer depth rather than the second derivative of density. If instead the mismatch is due to an underestimate of wind-driven mixing in the model, then this may result either from the choice of mixing scheme or from the choice of wind forcing.

The distribution of biomass shows that the dominant phytoplankton type varies with depth (Figure 4.7c) . This is a result of the differential treatment of loss rate between small (*P. antarctica*) and large (diatom) phytoplankton classes in BLING; furthermore it is likely that the differences in community composition with depth are underestimated. Biomass is mixed through the water column as a single tracer, so that variability in community composition tends to be smoothed out by the physical model.

Vertical mixing is also important in determining how well adapted phytoplankton are to their light environment. As outlined in Section 2.2.3, the assumption made is that that the irradiance memory is a function of the average light throughout the mixed layer. This implies that near-surface phytoplankton are acclimated to efficiently utilize light levels lower than those to which they are presently exposed. Thus their already high photosynthesis rates are enhanced (Schofield et al., 2015). Conversely, phytoplankton at the bottom of the mixed layer are exposed to light levels lower than those to which they have acclimated, so here the already low rate of photosynthesis is suppressed further. The contrary assumption would remove this enhancement/suppression of photosynthesis at the surface/base of the mixed layer, and thus likely give a flatter profile of productivity with depth.

Data from Argo floats in the Southern Ocean indicate that it may not be possible to define a constant time-scale for mixing of bio-optical properties (Carranza et al., 2018). Instead they are mixed episodically following storms, becoming restratified in the days that follow. These observations indicate that a parameterization similar to that in Equation 4.13 might improve the representation of phytoplankton blooms in models. However the use of a single photoacclimation timescale in ζ might not be appropriate given the observed differences in photo-acclimation between different phytoplankton species. For instance shipboard measurements from the Amundsen Sea show that diatoms are better able to make use of variable light conditions than *P. antarctica* (Alderkamp et al., 2012). This indicates that the degree of photoacclimation may be species-dependent as well as time-dependent over the course of the bloom.

Implementation of a ζ-parameterization in a Eulerian model such as MITgcm would also be complicated by the choice of vertical mixing parameterization. Mixing schemes such as KPP generate a range of values for K_z, so these would likely have to be averaged over the mixed layer at each time step before calculating ζ. In summary, substantially more work is needed to develop a parameterization of irradiance memory which accurately captures the competing effects of turbulent mixing and phytoplankton acclimation; more especially if this parameterization is going to be applicable in global earth system models.

4.5.2 Self-shading

By using the Manizza et al. (2005) formulation the results in this chapter demonstrate that phytoplankton self-shading has a large impact on light penetration and consequently on the euphotic depth (Figure 4.6). Furthermore, there is large spatial and temporal variability in the self-shaded euphotic depth, a phenomenon which cannot be captured using a single attenuation constant throughout the model. Self-shading leads to a shoaling of the December mean DCM by 40 m (Figure 4.7b) and a reduction in annual NPP from 115 g C $m^{-2}yr^{-1}$ to 55g C $m^{-2}yr^{-1}$, compared to the model run with constant euphotic depth. Self-shading also leads to a delay in bloom onset, which in turn results in enhanced late-season surface NPP for gmw_iron compared to the $fixed\_zeu$ experiment (discussed in section 4.3). Moreover, these changes in productivity impact the distribution of nitrate and oxygen within the model. Changes in nitrate export due to self-shading were identified in Manizza et al. (2005) and Kim et al. (2015) as impacting on productivity in the macronutrient-limited lower latitudes. Meanwhile the reduced oxygen concentrations above 200 m and increased concentrations below illustrate how changes in light environment may impact the wider polynya ecosystem.

Conversely, the model produces euphotic depths in excess of those measured by Park et al. (2017), even when the impact of self-shading is included. A more accurate light field for the ASP might be obtained by tuning coefficients in the bio-optical model to better represent local conditions. The combination of shallow mixed layers and deeper euphotic zones would be expected to reduce light limitation, yet the model does not overestimate productivity. Instead the modelled annual NPP is in the range 50 - 150 g C $m^{-2}yr^{-1}$ depending on location within the domain, which is in line with Yager et al. (2012) (their Figure 3) as well as most stations modelled in Oliver et al. (2019). However, depending on boundary conditions, the pattern of NPP often differs substantially from previous observations and modelling (see Chapter 5).

While attenuation due to phytoplankton can potentially impact the upper ocean heat budget (Manizza et al., 2005), this feedback is not yet implemented in BLING within MITgcm. Instead, the total shortwave irradiance used for heating and the PAR relevant for biology are treated independently in the ocean interior. This means that the mixed layer depth is allowed to impact the euphotic depth via changes in chlorophyll distribution, but the euphotic depth cannot in turn feedback onto the mixed layer depth. Allowing BLING to impact onto shortwave heating within BLING may provide a more accurate picture of polynya dynamics (see Chapter 6).

4.5.3 Iron-light colimitation

The balance between iron and light limitation in the ASP varies with location and with time. In all experiments, the phytoplankton bloom can not initiate until the sea ice cover has largely retreated. This accords with observations, with low humidity and strong katabatic winds preventing the formation of the melt ponds which permit under-ice blooms in the Arctic (Horvat et al., 2017). However, a comparison of experiments with identical sea ice cycles in Figure 4.10 shows that the sea ice cover is not the only control on the timing of bloom initiation. The inclusion of self-shading delays the onset of the bloom in gmw_iron by around a month compared to $fixed\_zeu$. This implies that after sea-ice begins to retreat, the early growth of the bloom is slowed by the negative feedback between biomass and light penetration. The peak NPP reached in gmw_iron of 0.51 g C $m^{-2}day^{-1}$ is 80% lower than the 2.47 g C $m^{-2}day^{-1}$ reached in $fixed\_zeu$. Up to this point, $flat\_iron$ does not diverge significantly from gmw_iron. This demonstrates that light limitation is the primary control in the early part of the bloom leading to the initial peak.

The timing of the initial gmw_iron peak is around a month earlier than the peak generally observed in the ASP. It is followed by a second peak at the start of January, by which point $flat\_iron$ has surpassed $fixed\_zeu$, indicating a transition from a predominantly light-limited to a predominantly iron-limited system. Nonetheless, for the entirety of December and January both $fixed\_zeu$ and $flat\_iron$ are more productive than gmw_iron, so that the bloom can be regarded as co-limited by iron and light. The severe iron limitation that occurs in gmw_iron as compared to $flat\_iron$ is a cumulative result of uptake by phytoplankton. Moreover, by December the bloom in $fixed\_zeu$ has been substantially more productive than gmw_iron and has thus exacerbated the depletion of the iron pool. Nearest the surface where light limitation is least severe, this allows for higher growth rates and greater productivity in the self-shaded experiment gmw_iron despite being exposed to less intense light than in $fixed\_zeu$ (Figure 4.7d) – this demonstrates that colimitation is depth dependent within the euphotic zone.

The seasonal succession from light to iron limitation reflects previous modelling results in the ASP (Oliver et al., 2019), as well as observations from the West Antarctic Peninsula (Arrigo et al., 2017) and the Weddell Sea (von Berg et al., 2020). However this study moves beyond Oliver et al. (2019) by identifying the factors which regulate this transition, namely the attenuating power of chlorophyll and the variable iron quota of phytoplankton cells. In addition, the results shown in Figure 4.10b recall some of the spatial variability observed by Alderkamp et al. (2015), with light limitation outweighing iron limitation in the DIS meltwater outflow. However, these model results challenge the application of the carrying capacity hypothesis (Hopkinson et al., 2013) to the ASP, on two different fronts.

The carrying capacity hypothesis assumes an initial reservoir of upper ocean iron which is sufficient to support a spring phytoplankton bloom; it also assumes the absence of any resupply, so that the bloom goes into decline when this initial reservoir is exhausted. Conversely, the model results presented here show that within the coastal current summertime resupply of iron from the meltwater pump is substantial, and cannot be neglected as being small in comparison to the initial wintertime inventory. At the same time, the model results also demonstrate that outside of the coastal current even the the *initial* springtime concentrations of iron are insufficient to support a substantial phytoplankton bloom. Ultimately the carrying capacity hypothesis of Hopkinson et al. (2013) is valid solely along the boundary of these two regions, where there is enough iron for a bloom to start, but only a weak resupply over the growing season.

An important distinction between the model setup described here and that used in Oliver et al. (2019) and St-Laurent et al. (2019) is in the use here of an iron-to-nitrate uptake ratio which increases with iron concentration. As a result the 51% higher annual iron uptake in gmw_iron compared to $melt\_pump$ (Figure 4.9d) is only associated with a 34% increase in productivity (see Chapter 5). Overall, uptake by phytoplankton is the most important sink for dissolved iron in the polynya, substantially larger than scavenging. When the phytoplankton iron sink is removed as in $flat\_iron$, this is equivalent to the addition of a continuous flux compensating for phytoplankton uptake. The result is a large increase in the annual production of the ASP, from 54 g C $m^{-2}yr^{-1}$ to 116 g C $m^{-2}yr^{-1}$. This is consistent with the conclusion of Alderkamp et al. (2015), that a continuous resupply of iron is necessary to increase annual NPP.

4.6 Conclusion

Results from an idealised model of the ASP show that both iron and light availability impact productivity, and that it is their combined effect which controls annual NPP. However there is strong spatial and temporal variability in iron-light colimitation. As in Oliver et al. (2019), the phytoplankton bloom is primarily light-limited in its early stages, with a large part of this light limitation attributable to the self-shading feedback which arises due to chlorophyll in the water column. The inclusion of the chlorophyll dependent light penetration formula from Manizza et al. (2005) reduces peak NPP by 80%, and likely produces a better representation of phytoplankton dynamics. Further improvements in this representation could result from the use of a parameterization which considers mixing and photoacclimation time-scales, particularly in models with high vertical resolution.

Later in the season iron limitation becomes the primary control on growth rates and primary production, as phytoplankton uptake depletes iron concentrations faster than they are replenished. However in some parts of the polynya even the initial iron concentration, before phytoplankton uptake, is insufficient to support a phytoplankton bloom. Hence whilst the spatial pattern of NPP is dictated by the wintertime iron supply from the ice shelf, the termination of the bloom is controlled by the balance between resupply during summer and depletion by phytoplankton.

Chapter 5

Sensitivity of Net Primary Production to thermocline depth and surface irradiance

5.1 Preface

In this chapter, the model presented in Chapter 4 is extended by running a suite of sensitivity experiments; as in Chapter 4 parts of this chapter appear in Twelves et al. (2021). Unpublished results are presented in subsection 5.3.2 on ice shelf morphology and at the end of subsection 5.4.2 on changes to phytoplankton community composition.

5.2 Introduction

The rapid basal melting of Dotson Ice Shelf (DIS) is driven by intrusions of warm, saline Circumpolar Deep Water (CDW) onto the continental shelf via Dotson Trough (Jacobs et al., 2012). These intrusions are in turn coupled to the wind and sea ice conditions at the shelf break, with variability at the shelf break thus leading to variation in basal melt rate (Kim et al., 2017). However for the melting which takes place beneath the ice shelf to have an impact on biological processes in the adjacent Amundsen Sea Polynya (ASP), meltwater must first undergo horizontal spreading away from the shelf (Schofield et al., 2015). Modelling is required to elucidate the link between melt rate and meltwater pathways, with recent results from Kimura et al. (2017) indicating that greater melting does not necessarily lead to higher meltwater concentrations away from the continent.

In this chapter a range of boundary conditions, both at the surface and at depth, is applied to the model described in Chapter 4. The results of this suite of experiments are used to infer the sensitivity of the polynya – and the phytoplankton bloom hosted within it – to variability in CDW intrusions and cloud cover.

Table 5.1: List of experiments conducted in this section, showing their setup with regard to ice-ocean interactions.

Experiment name	Ice shelf melt?	Iron in meltwater?	Maximum depth of ice shelf (m)
gmw_iron	yes	yes	800
melt_pump	yes	no	800
no_melt	no	no	800
thin_shelf	yes	yes	600

5.3 Quantifying the impact of the meltwater pump and glacial iron on primary productivity

5.3.1 Model experiments

The model experiments are summarised in Table 5.1.

gmw_iron

As in Chapter 4, the *gmw_iron* experiment serves as the base case. Iron content in glacial meltwater is specified as 20 μmol m^{-3}. In some later results this experiment is renamed *base_med*.

melt_pump

As in Chapter 4, the *melt_pump* is identical to *gmw_iron* except for the fact that the source of iron in glacial meltwater is removed. As a result the only impact of the ice shelf on the polynya is via changes in the circulation of the physical model.

no_melt

In the *no_melt* experiment, ice shelf melt is suppressed by setting the heat flux into the ice equal to zero. Thus in this experiment both impacts of the ice shelf on biogeochemistry - glacial iron and meltwater pump - are removed.

thin_shelf

An additional experiment *thin_shelf* with a less steep ice shelf slope (extending down to 600m rather than 800m) is run to examine the impact of grounding line depth on meltwater plume buoyancy and therefore dynamics.

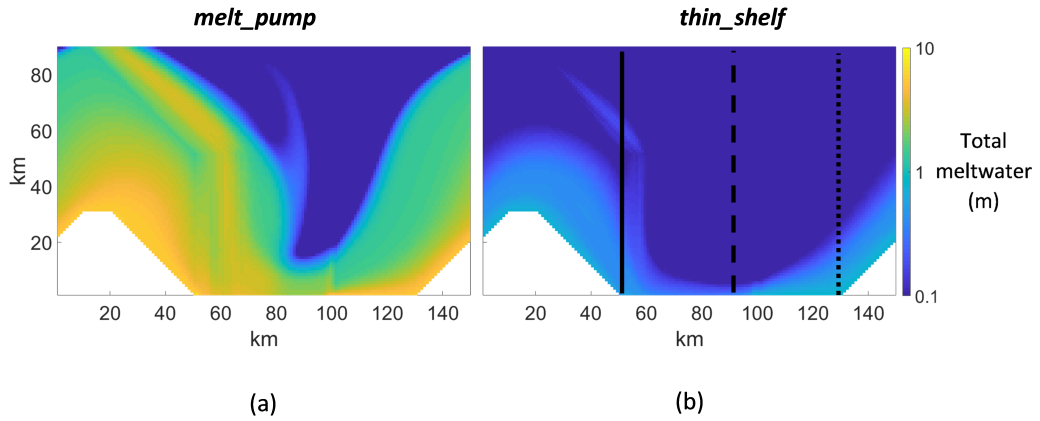

Figure 5.1: Comparison of vertically integrated meltwater content in the experiments between (a) the $melt\_pump$ experiment and (b) the $thin\_shelf$ experiment. Solid, dashed and dotted lines in (b) represent the western, central and eastern transects respectively - see Figure 5.2.

5.3.2 Results

Importance of ice shelf morphology

In both the gmw_iron and $thin\_shelf$ experiments the iron-laden meltwater outflow from the ice shelf is strongly focused in a narrow coastal current, as discussed previously in Chapter 4 (Figure 4.10). However in the $thin\_shelf$ experiment the concentrations of meltwater within this current are an order of magnitude lower compared to $melt\_pump$ (Figure 5.1).

To examine the dynamics of meltwater outflow further, the $thin\_shelf$ experiment is repeated with the single meltwater tracer replaced with two independent tracers, each seeded over a narrow range of depths. The near-surface tracer is seeded between 350m and 400m whilst the deep tracer is seeded between 550m and 600m.

Figure 5.2 shows that the near-surface meltwater tracer is positively buoyant and emerges at the surface. The deep meltwater tracer is split between a positively buoyant plume and another portion which achieves neutral buoyancy at depth and spreads along close to the bathymetry at the western edge of the trough. Thus ice shelf topography impacts not only the overall flux of meltwater from the ice shelf but also its vertical distribution, as discussed previously by Bett (2021).

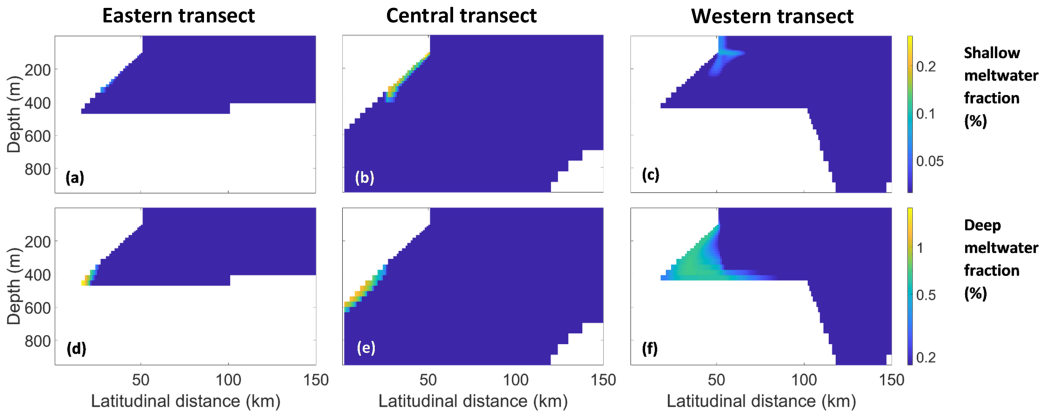

Figure 5.2: Comparison of meltwater pathways from close to the grounding line and close to the ice shelf front, using the transects shown in Figure 5.1b. In (a) to (c) the pathway of the near-surface tracer is shown along the eastern (dotted line in Figure 5.1b), central (dashed line) and western (solid line) transects respectively. Similarly in (d) to (f) for the deep tracer.

Validation against observations

In order to compare $melt\_pump$ results with observations, a transect along the front of the ice shelf in January is examined (Miles et al., 2016; Randall-Goodwin et al., 2015). Figure 5.3a shows the temperatures measured by Miles et al. (2016) during January 2014, with a warm and saline CDW layer below approximately 750 m. The modelled thermocline (Figure 5.3b), by contrast, lies at around 600m, mirroring the condition imposed on the model at the northern boundary. In both observations and modelling there is a weak summertime warming effect visible close to the surface. The surface layer is more clearly distinguished as a strong freshening in the salinity fields, both in observations (Figure 5.3c) and from the model output (Figure 5.3d).

Figure 5.3e shows the (south-to-north) outflow velocities measured across the front of DIS by Randall-Goodwin et al. (2015) in January 2011. Basal melting drives an inflow of water into the ice shelf cavity at its eastern edge, with a stronger, more focused outflow at the western edge. This is reproduced in the model outputs, except that inflow velocities are enhanced relative to observations whilst outflow velocities are slightly suppressed (Figure 5.3f). Randall-Goodwin et al. (2015) also examined temperatures in front of the cavity, this time as anomalies subtracted from the mean temperature at that depth (Figure 5.3g). This metric is reproduced for the model results in Figure 5.3h. Both observations and modelling reveal a clear warm anomaly at the western edge of DIS, although this anomaly is located slightly deeper in the water column in the model. The origin of the warm anomaly is likely to be the same warm CDW which drives basal melting.

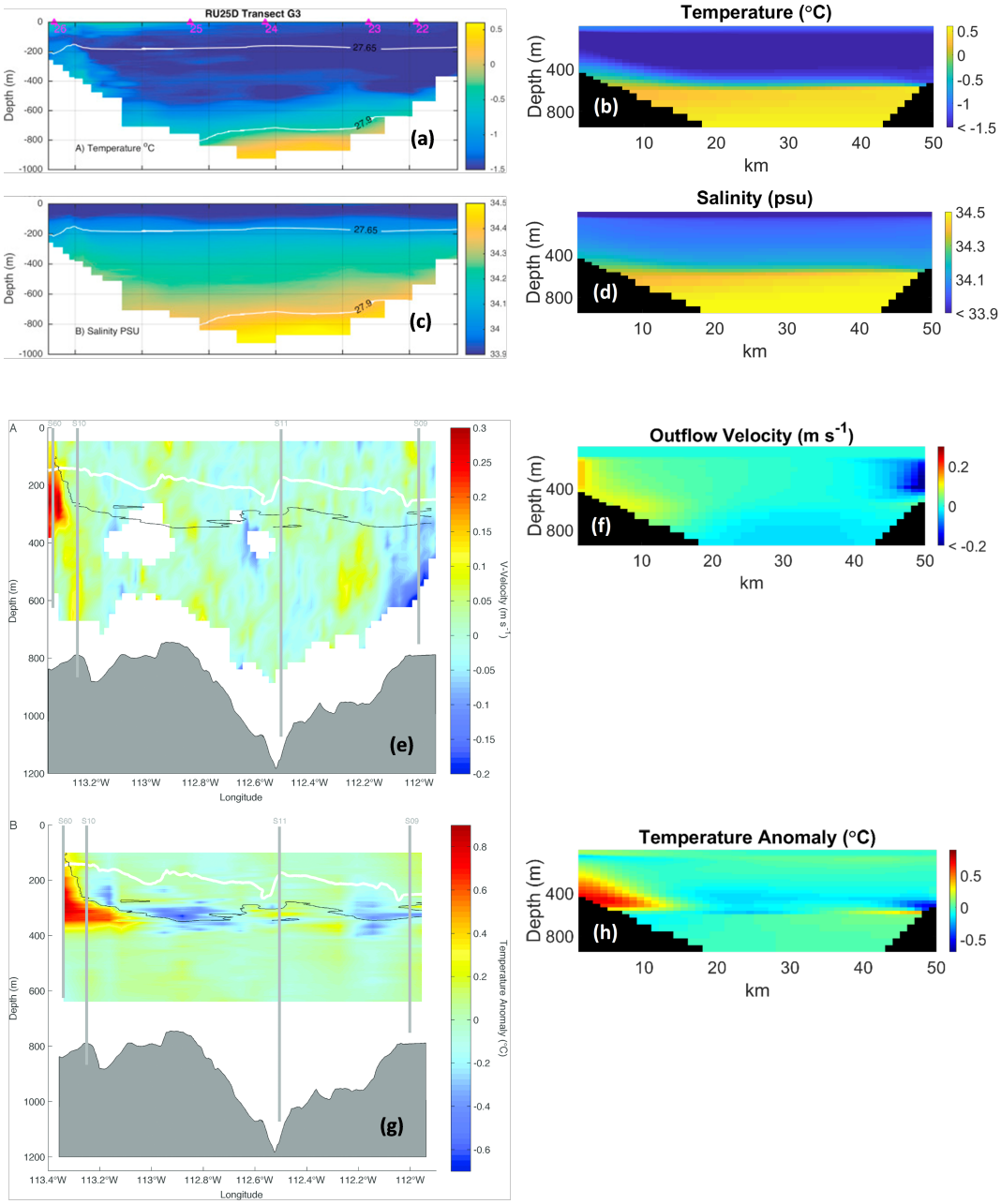

Figure 5.3: Temperature in front of DIS, (a) from observations of Miles et al. (2016) and (b) from model outputs; similarly salinity observations from Miles et al. (2016) (c) alongside model outputs (d). Also outflow velocities, with positive defined northwards, (e) from observations of Randall-Goodwin et al. (2015) and (f) from the model. Finally, in (g) and (h), for observations (Randall-Goodwin et al., 2015) and model output respectively, the temperature anomaly is calculated by subtracting the depth averaged temperature at each location across the front of the cavity.

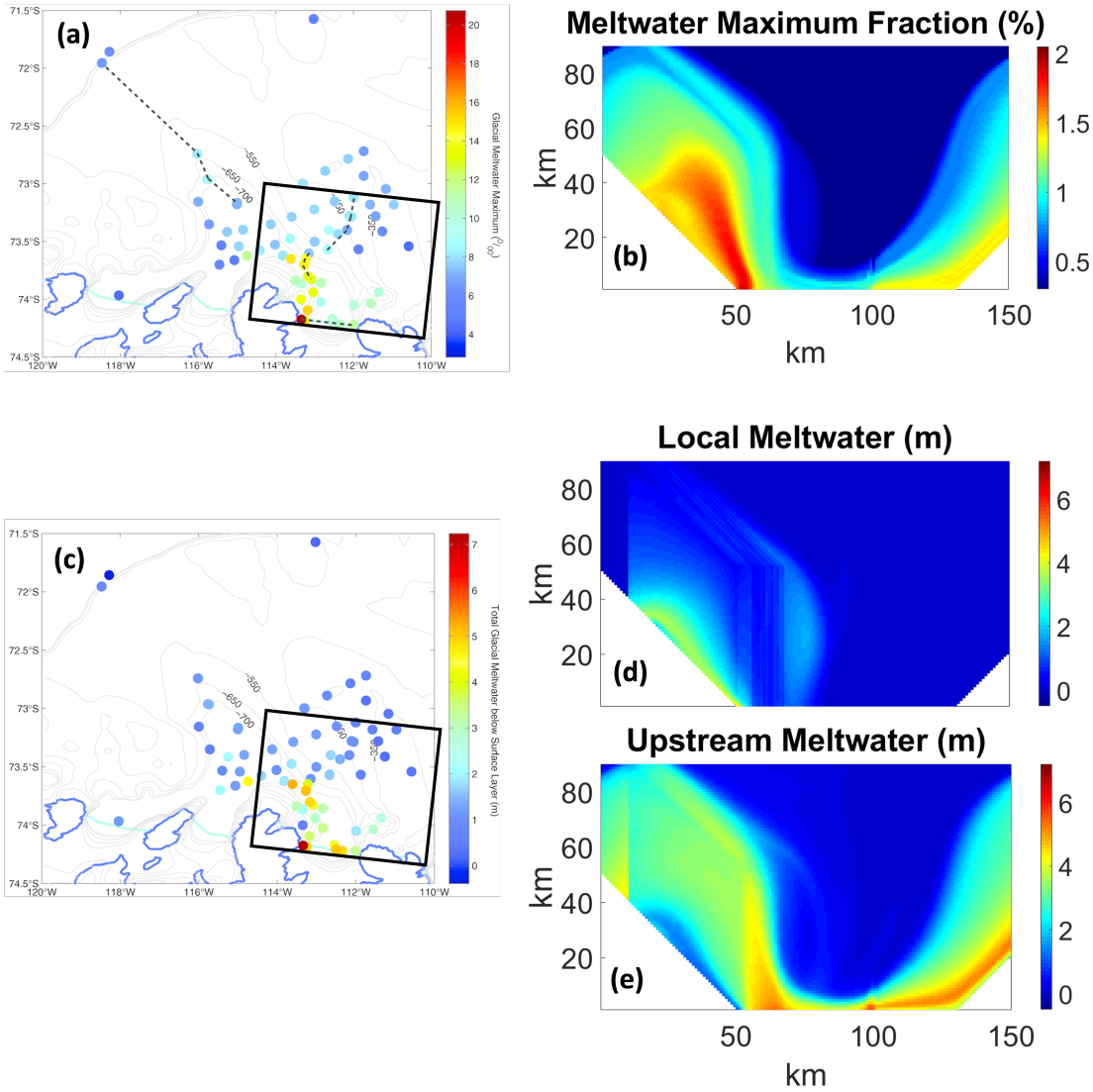

Figure 5.4: Maximum meltwater concentrations from observations (a, Randall-Goodwin et al. (2015)) and from the model (b), defined as fraction of total seawater volume. In (c) Randall-Goodwin et al. (2015) calculated the total depth of meltwater at different locations by integrating the meltwater fraction over the depth of the water column. This is replicated with the model results in (d) and (e), showing locally-sourced and upstream-sourced meltwater respectively.

Buoyant meltwater exiting the cavity rises through the water column and is pulled to the west by the strong boundary current. Figures 5.4a and 5.4b show the maximum fraction of meltwater found over the depth of the water column, at different locations across the domain, from observations (Randall-Goodwin et al., 2015) and the model respectively. In both, the highest concentration of meltwater is found at the western edge of the ice shelf front, with meltwater making up around 2% of seawater volume at this location.

By integrating the meltwater fraction over the depth of the water column, Randall-Goodwin et al. (2015) arrived at another way to track the meltwater pathway in Figure 5.4c. Again, the meltwater is most concentrated at the western edge of the ice shelf front and then spreads to the north and west. This pattern is broadly replicated in the model outputs (Figures 5.4d and 5.4e). These latter two figures differ in that 5.4d is calculated from the local meltwater tracer, thus representing meltwater directly sourced from DIS; meanwhile Figure 5.4e is calculated as the difference between the global and local tracers, thus representing meltwater sourced from ice shelves upstream of DIS.

It is clear from this analysis that the majority of the meltwater present in the model domain is the result of recirculation via the periodic zonal boundaries, and also that the inclusion of these upstream sources can provide a better fit to observed meltwater concentrations. However the ability of the upstream meltwater to continue circulating zonally indefinitely – without being depleted – prevents it from reaching a steady state. Thus in the remaining investigations using this domain only the local meltwater tracer is used to compare quantitatively against data from the ASP.

The Meltwater Pump

In order to assess the impact of ice shelf melting on the physical state of the ASP, the $melt\_pump$ and no_melt experiments are compared. Figure 5.5a shows that sea surface temperature (SST) peaks in February in both experiments, with only a small (0.1°C) decrease in maximum SST due to melting. The April peak in melt rate two months later suggests that the downwelling of warmed surface waters is responsible for melting at the front of the ice shelf, a mechanism previously observed at the Ross Ice Shelf (Stewart et al., 2019). The cycles in sea ice coverage and spatially averaged mixed layer depth with and without melt are shown in Figure 5.5b. The presence of a melt-driven circulation reduces maximum wintertime sea ice coverage from 88% to 79% of the ocean domain. The impact of ice shelf melt on horizontally averaged mixed layer depth is most visible at the start and end of summer, where it is likely due in part to the aforementioned differences in sea ice distribution between no_melt and $melt\_pump$.

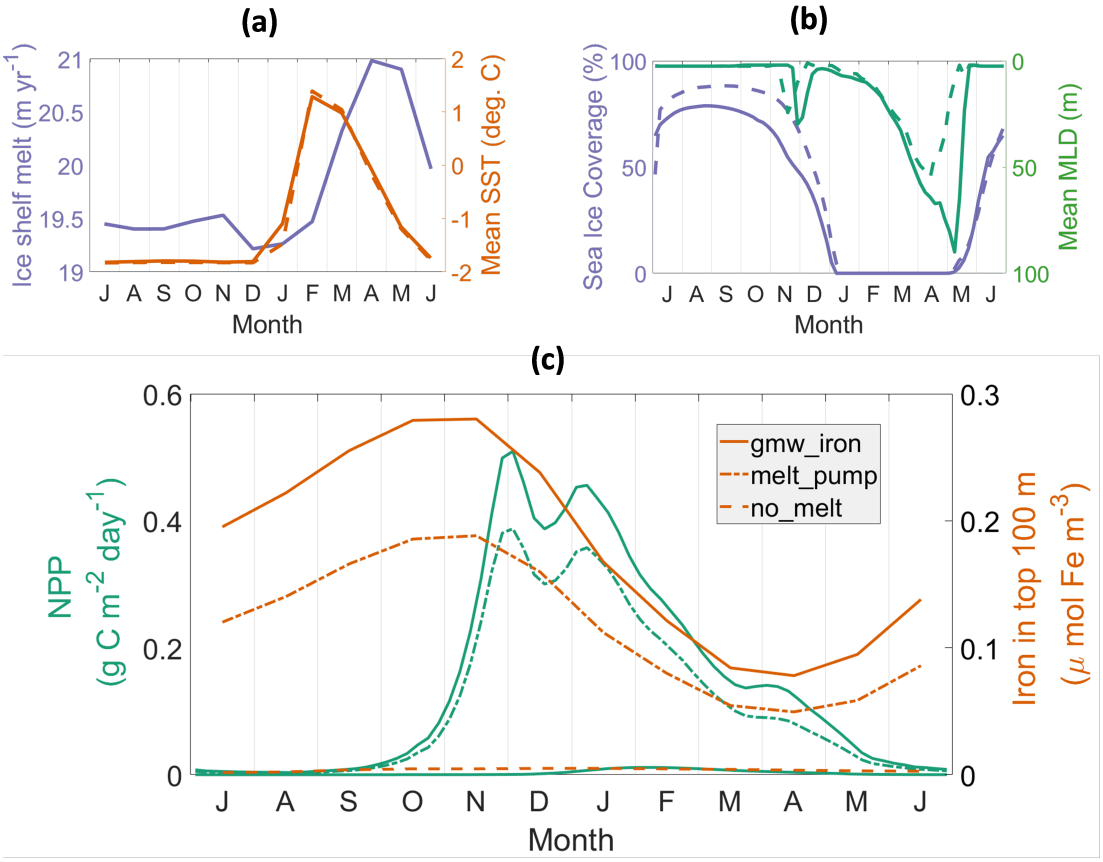

Figure 5.5: The spatially averaged ice shelf melt rate (purple line in (a)) and its impact on spatially averaged SST (orange lines in (a)); also the impact of melting on (b) sea ice coverage (purple lines) and horizontally averaged mixed layer depth (green lines). Results are shown for experiments with ($melt\_pump$, solid lines) and without (no_melt, dashed lines) ice shelf melt. In (c) time series in NPP (green lines) and iron concentration (averaged over upper 100m, orange lines) are used to examine the impact of the meltwater pump and glacial iron on biogeochemistry. Results are shown for the no_melt (dashed lines), $melt\_pump$ (dash-dot lines) and gmw_iron (solid lines) experiments.

Unlike the meltwater tracer, the iron tracer is periodically depleted on a seasonal basis due to biogeochemical processes, and thus does not accumulate over successive years. Therefore iron sourced from upstream ice shelves is still included in integrating the global iron tracer to produce the time series in Figure 5.5c. The importance of iron supplied from upstream ice shelves visible from Figure 5.10 reflects previous modelling studies (St-Laurent et al., 2019). The near-surface iron pool follows a strong seasonal cycle in the $melt\_pump$ case, with a peak in November. The wintertime iron inventory is depleted by 74% over the course of the bloom, reaching a minimum in April. With gmw_iron there is an additional (glacial) source of iron, resulting in a 49% increase in wintertime iron inventory. Similar to $melt\_pump$, this is then depleted by 72% to a minimum in April.

The annually integrated NPP reaches 41 g C $m^{-2}yr^{-1}$ in the $melt\_pump$ case, peaking at 0.39 gC $m^{-2}day^{-1}$ in early December (Figure 5.5). This compares to annual and peak NPP values of 1 g C $m^{-2}yr^{-1}$ and 0.01 gC $m^{-2}day^{-1}$ in the no_melt case, with the peak occurring in February. Thus the meltwater pump brings forward the spring bloom by around 2 months and causes a 40-fold increase in productivity. This is attributable to a similarly large increase in the pool of dissolved iron available within the top 100 m. Time series of NPP for $melt\_pump$ and gmw_iron show similar patterns with the initial December peak followed by a secondary peak in January. The additional iron available in gmw_iron causes peak NPP to increase by 28% to 0.51 g C $m^{-2}day^{-1}$ and annual NPP by 34% to 55 g C $m^{-2}yr^{-1}$.

5.4 Variations in external forcing

5.4.1 Model experiments

In this section a suite of sensitivity experiments is used to investigate how the ocean, ice shelf and phytoplankton bloom respond to changes in environmental conditions (see Table 5.2). Different external forcings at the boundaries of the model domain (Figure 5.6) are used to perform eight sensitivity experiments in addition to gmw_iron, which serves as the base case. The relevant boundary conditions, plus their values in gmw_iron (and all other experiments named thus far) are as follows:

1. At the northern (open) boundary a thermocline is imposed between 400 m and 600 m depth. Above the thermocline there is a layer of (cold and fresh) winter water with temperature increasing from -1.8 °C at the top of the thermocline to -1.6 °C at the surface. Salinity decreases from 34.1 psu at the top of the thermocline to 33.9 psu at the surface. Below the thermocline there is a layer of modified CDW, which is warm (0.6 °C), highly saline (34.5 psu) and homogeneous. Water properties are interpolated linearly over the depth of the thermocline between the two layers.

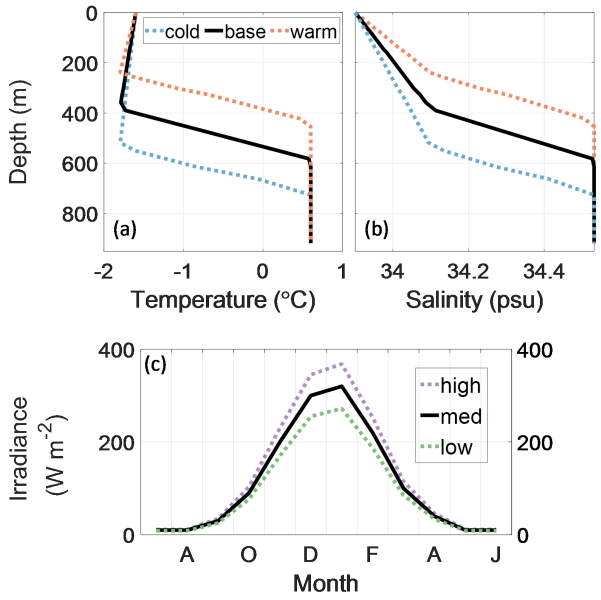

Figure 5.6: In sensitivity experiments the temperature (a) and salinity (b) profiles at the northern boundary are varied, as well as (c) the downwelling shortwave irradiance at the ocean surface.

2. At the ocean surface a seasonal cycle of downwelling shortwave irradiance is imposed, 40 % of which is deemed to be photosynthetically available radiation (PAR). Based on the NCEP-CFSv1 re-analysis (Petty et al., 2013; Saha et al., 2006) the peak irradiance, applied in January, is 320 Wm^{-2}. Irradiance falls to a minimum of 10 Wm^{-2} in polar winter.

Observations from the Amundsen Sea (Dutrieux et al., 2014; Randall-Goodwin et al., 2015; Sherrell et al., 2015) indicate the magnitude of interannual variability in CDW intrusions onto the continental shelf. Based on these studies experiments (named with the prefix $warm-$) are performed where the thermocline at the northern boundary is situated between 250 m and 450 m depth, to approximate years with larger than average intrusion of CDW. Similarly experiments (prefixed $cold-$) are performed where the thermocline (and the halocline) is situated between 550 m and 750 m to approximate years with smaller than average intrusion of CDW onto the continental shelf. The prefix $base-$ refers to experiments conducted with the "base case" CDW condition ie. a thermocline (and a halocline) between 400 m and 600 m. A positive correlation between the quantity of heat transported onshore by CDW and the rate of basal melting from DIS is expected, based on Bett et al. (2020).

Recent work by Park et al. (2017) attributed large differences in NPP between the ASP and PIP to differences in surface irradiance on the order of 15%. To examine whether changes in surface irradiance of this magnitude can have large impacts on productivity in the ASP, experiments are performed where the amplitude of the seasonal cycle in downwelling short-

Table 5.2: List of sensitivity experiments conducted in this section, where $base\_med$ is equivalent to gmw_iron, showing variation in applied boundary conditions.

Experiment name	Depth at top of thermocline (m)	Depth at base of thermocline (m)	Peak shortwave irradiance (W m^{-2})
cold_low	550	750	272
cold_med	550	750	320
cold_high	550	750	368
base_low	400	600	272
base_med	400	600	320
base_high	400	600	368
warm_low	250	450	272
warm_med	250	450	320
warm_high	250	450	368

wave radiation was either increased or decreased by 15%. In the low irradiance experiments (suffixed $-low$) the surface irradiance peaks in January at 272 W m^{-2}; in the high irradiance cases (suffixed $-high$) it peaks at 368 W m^{-2}. The suffix $-med$ then refers to experiments with the original irradiance forcing. With these three different regimes for surface irradiance, in combination with the three different regimes for the northern thermocline, there are nine different iterations of the model (including the base case gmw_iron). The annual productivity which results from each of these different setups will indicate whether the known variability in surface or deep ocean conditions has a greater impact on biology in the ASP. Further the results will indicate whether the hypothesized relationships between NPP and cloud cover (Park et al., 2017) and between NPP and basal melt rate (Arrigo et al., 2015) are reproduced in this model.

5.4.2 Results

Sensitivity of ice shelf to boundary conditions

The depth of the thermocline and the strength of surface irradiance both impact ice shelf melt rates. Figures 5.7 a – c show profiles of melt rate with depth for each of the nine different sensitivity experiments. In this section, to enhance clarity, the base case gmw_iron experiment is referred to as $base\_med$. Lowering the thermocline leads to a reduction in melt rate across the entire shelf, with annual melt reduced by 14% from 22.9 m yr^{-1} in $base\_med$ to 19.7 m yr^{-1} in $cold\_med$. Meanwhile raising the thermocline leads to an increase in melt in the range 200 - 400 m, but a reduction outside these limits, with overall average melt reduced by 4% to 22.0 m yr^{-1} in $warm\_med$. This distribution of melting may be in part be dictated by Ekman downwelling.

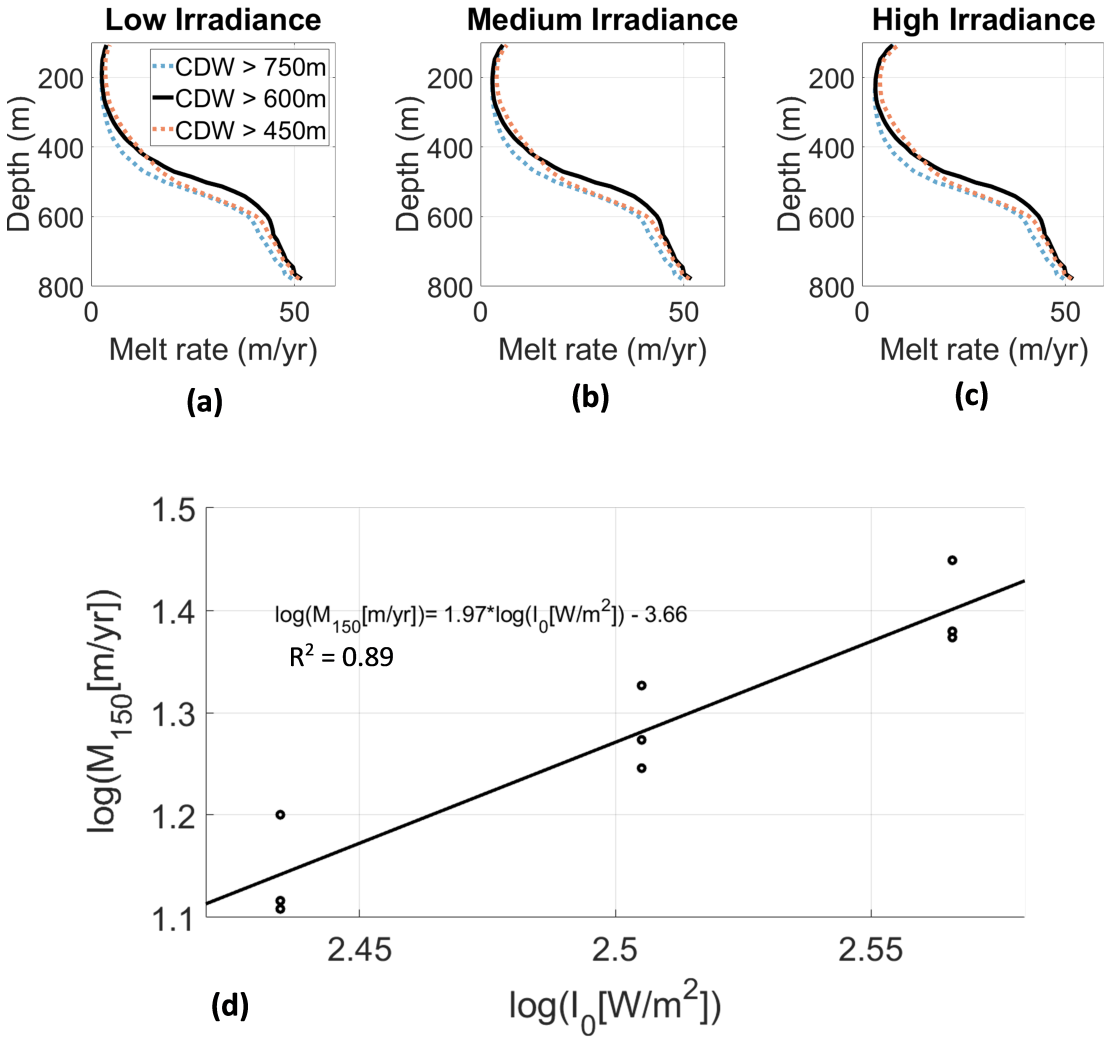

Figure 5.7: Impact of thermocline depth and surface irradiance on depth profiles of annual ice shelf melt: shown are the $-low$ (a), $-med$ (b) and $-high$ (c) irradiance cases. In each figure results are shown for the $cold-$ (dotted blue line), $base-$ (solid black line) and $warm-$ (dotted red line) ocean cases. In (d) the response of near-surface melt to changes in surface irradiance is shown, with the trendline showing a least-squares regression on the logarithmic ratio. Melt rate is integrated from 100m to 150m depth on the ice shelf, with peak irradiances coming in January.

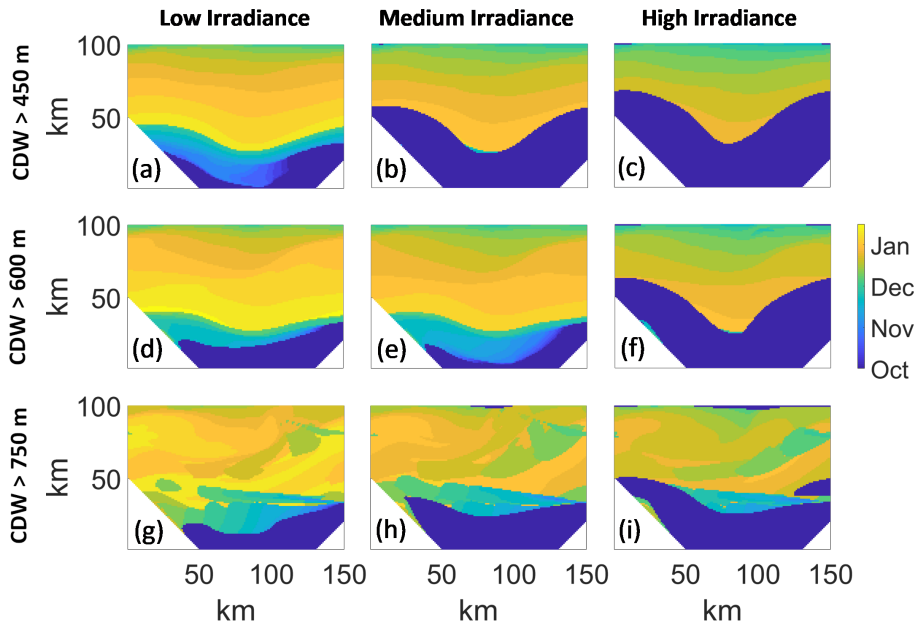

Figure 5.8: Impact of thermocline depth and surface irradiance on polynya opening date across the ocean domain ie. the date at which the sea ice cover at each location falls below 15%.

As expected the surface irradiance does not impact melt rate at depth. However under the shallowest part of the ice shelf the melt rate is reduced from 5.8 m yr^{-1} in $base\_med$ to 3.9 m yr^{-1} in the low irradiance case $base\_low$, and increased to 7.5 m yr^{-1} in the high irradiance case $base\_high$. In Figure 5.7d the melt rate is integrated down from 100m to 150m for each of the nine experiments, and plotted against the peak irradiance. There appears to be an approximately quadratic relationship between the peak irradiance and near-surface melting, although this is sensitive to the choice of depths over which the near-surface melt is integrated.

Sensitivity of sea ice cover to boundary conditions

The maps in Figure 5.8 show spatio-temporal patterns in the timing of spring sea-ice retreat for each of the nine sensitivity experiments. For the $base-$ and $warm-$ cases, the sea ice cover retreats from both the north and south, with a band through the centre of the ocean domain the last to retain ice cover greater than 15%.

This pattern is different in the $cold-$ experiments subject to a deepened thermocline, with a more heterogeneous distribution of retreat date. Across all CDW scenarios the result of increased surface irradiance is earlier sea-ice melt and thus earlier opening of the polynya at the start of summer.

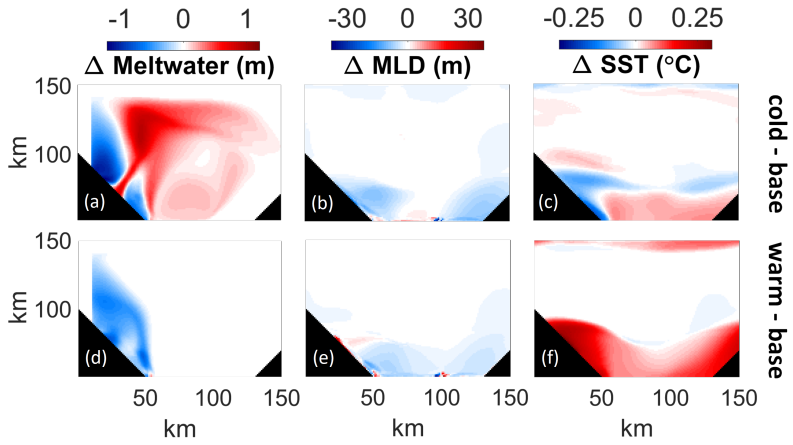

Figure 5.9: Changes in the October distribution of meltwater in the top 100 m of the ocean (a), the December mixed layer depth (b) and December SST (c) due to the lowering of the thermocline from 600 m to 750 m. Plots in (d-f) show the corresponding changes due to the raising of the thermocline from 600 m to 450 m.

Sensitivity of primary production to boundary conditions

The impact of variations in thermocline depth on physical variables relevant to phytoplankton growth is examined in Figure 5.9. Most significantly, meltwater concentrations increase in the central portion of the ASP, whilst decreasing close to the coast, in $cold\_med$ as compared to $base\_med$. Mixed layer depth responds most strongly near the coastline, with a slight shallowing visible in both the $cold\_med$ and $warm\_med$ cases, as compared to the $base\_med$ experiment. Reduced melt rate in $cold\_med$ produces a weak sea surface warming close to the shelf, probably due to the reduced inputs of freshwater; meanwhile in the $warm\_med$ case the strong warming is likely due in part to changes in upwelling.

The effects of variations in thermocline depth on horizontally averaged upper ocean iron and NPP are shown in Figure 5.10 with maps of their respective distributions. In $base\_med$ and $warm\_med$ (Figures 5.10 b & c), iron levels in October (before the bloom) are highest close to the coast and in front of the peninsulas. In contrast, the $cold\_med$ experiment (Figure 5.10a) shows significant levels of iron in front of the ice shelf in the center of the domain. In Figures 5.10 d – f the distribution is plotted for the local iron tracer only, so as to remove the impact of upstream meltwater via the zonal periodic boundaries. In these figures the different pathway of iron from the ice shelf cavity in the $cold\_med$ case can be seen clearly. These same plots also show a gradual strengthening of the modelled gyre as the thickness of the CDW layer is decreased. The maps of annually integrated NPP in Figures 5.10 g – i show that a shallowing

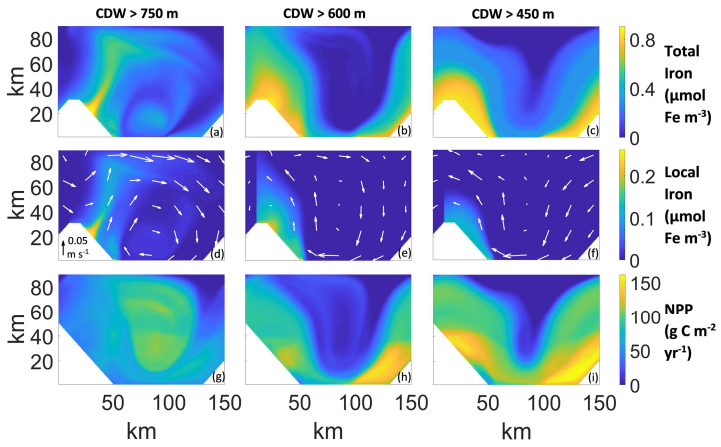

Figure 5.10: Different melt rates leading to different distributions of wintertime (October) iron concentration in the upper 100 m in $cold\_med$ case (a) as compared to the $base\_med$ (b) and $warm\_med$ (c) experiments. Similarly in (d-f) for the local iron tracer with white arrows indicating mean flow in the upper 100 m. Finally, plots of the annual NPP for the three experiments in (g-i) show a qualitative difference in the spatial distribution of NPP for the (deepened thermocline, low melt rate) $cold\_med$ experiment as compared to $base\_med$ and $warm\_med$.

of the thermocline (and thickening of the CDW layer) in $warm\_med$ strengthens productivity in the coastal current, but does not radically change the distribution of the bloom. However the deepening of the thermocline (and thinning of the CDW layer) in $cold\_med$ leads to a qualitative change in NPP distribution as compared to $base\_med$, with the bloom now focused in the centre of the domain rather than in front of the peninsulas.

Both peak and annual NPP show a sub-linear response to surface irradiance, with a stronger sensitivity to thermocline depth (Figure 5.11). In the (lowered melt rate) $cold-$ cases there is a single peak in NPP, as opposed to the double peak observed in $base-$ and $warm-$ experiments, with the $cold-$ peak up to 20% higher than the $base-$ peak. This elevated NPP from $cold-$ boundary conditions is in spite of a reduction in horizontally averaged iron concentration across the near-surface (<100 m) waters of the domain. In particular, the annual productivity of the polynya increases from 55 g C $m^{-2}yr^{-1}$ in $base\_med$ to 66 g C $m^{-2}yr^{-1}$ in the $cold\_med$ experiment. In the $warm-$ cases, where the thermocline is shallow compared to $base-$ experiments, NPP is again increased by around 20%, though this time in conjunction with an increase in iron content. For all three ocean conditions, increased irradiance causes small increases in NPP and small reductions in upper ocean iron concentration (due to increased phytoplankton uptake).

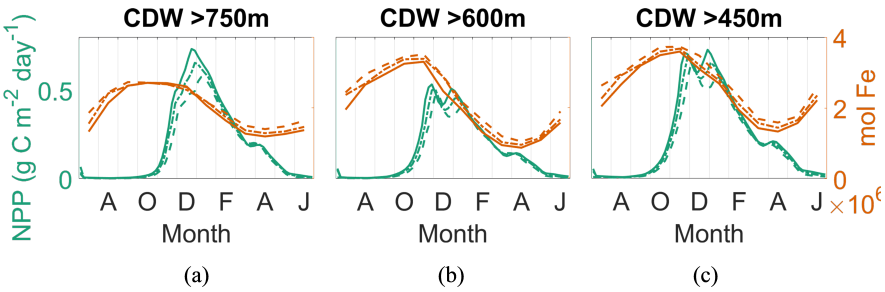

Figure 5.11: Impact of boundary conditions on time series of NPP (green lines) and iron inventory in the top 100 m (orange lines) for the $cold-$ (a), $base-$ (b) and $warm-$ (c) cases. In each figure results are shown for the $-low$ (dashed lines), $-med$ (dash-dot lines) and $-high$ (solid lines) irradiance cases.

Sensitivity of phytoplankton community composition to boundary conditions

Finally, the impact of environmental forcings on phytoplankton community composition is examined. Figures 5.12 a & b show the sensitivity of the small and large phytoplankton fractions respectively, relative to the same changes in boundary conditions detailed above. The large fraction is seen to be more sensitive, with peak large biomass almost doubling in the $cold\_high$ case compared to $base\_med$, whilst peak small biomass increases by only 33% for the same change in boundary conditions.

As a result of this difference in sensitivity, there is also a shift in community composition. In the $base\_med$ case, the peak large phytoplankton biomass is around 60% of the peak in small phytoplankton biomass. Apart from the $base\_low$ experiment, all other cases see an increase in the ratio of large to small phytoplankton peaks. In the $cold\_high$ case, the peak large biomass is nearly equal in magnitude to the peak in small biomass.

5.5 Discussion

5.5.1 Impact of the ice-shelf on primary production

Results from this study indicate that the high primary productivity observed in the ASP would be highly improbable without the basal melting of adjacent ice shelves. Annual NPP is increased from 1 g C $m^{-2}yr^{-1}$ to 41 g C $m^{-2}yr^{-1}$ based on the meltwater pump alone. Previously, modelling of the meltwater pump in the Amundsen Sea had already pointed to an important role for ice shelves in driving NPP (St-Laurent et al., 2017), whilst Dinniman et al. (2020) had examined how this mechanism translates to other polynyas around the Antarctic coastline. Significantly, this study reaches agreement on the importance of the meltwater pump by explicitly preventing ice shelf melt in the base case, rather than by merely setting iron

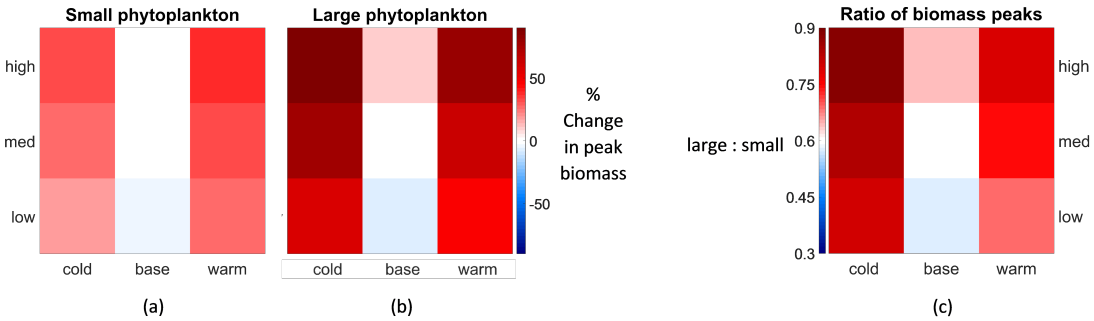

Figure 5.12: Impact of changing thermocline depth and surface irradiance on phytoplankton biomass. The blue to red colormap is centred on white at the value for the *gmw_iron* experiment.

concentrations to zero at the ice shelf front as in St-Laurent et al. (2019). The agreement of two different hydrodynamic models, applying different biogeochemical packages on different domains and with different approaches to the base case, substantially increases confidence in the assertion that the meltwater pump drives high NPP in the ASP.

The set of experiments presented here does not distinguish between iron originating off the continental shelf in CDW and iron sourced from sediments on the continental shelf. There remain large uncertainties in specifying the end-member concentration of dissolved iron in glacial meltwater, compounded by the uncertainty surrounding the partial bio-availability of the particulate iron pool (Gerringa et al., 2012). In this study the example of St-Laurent et al. (2019) is followed in using a 20 μmol m^{-3} concentration for iron in meltwater, and a 49% increase in maximum wintertime iron inventory is observed as a result. This in turn drives a 51% increase in iron uptake, indicating the near-linear response expected for an iron-limited system where $Fe << K_{Fe}$ (c.f. Equation 3.19). The accompanying increase in NPP is smaller - only 34% - due to the variable iron-to-nitrate uptake ratio.

Using a small domain covering only the region of the Amundsen Sea in front of Dotson Ice Shelf, but with periodic zonal boundaries, helps to confirm the influence of upstream ice shelves suggested by St-Laurent et al. (2019). A comparison of the total and local meltwater tracers demonstrates that a large proportion of the meltwater present in the domain is sourced from the eastern periodic boundary, corresponding to an upstream source. This is reflected in the relative values of local and global iron tracers. The presence of a deep meltwater maximum in Dotson Trough (Figure 5.4) raises the possibility that some of the iron which is melted out from the ice shelf may become re-entrained in the inflow of modified CDW into the ice shelf cavity. Thus a portion of the iron pulled up from depth by the meltwater pump may

itself be glacial in origin. Meanwhile, the comparison against an experiment with shallower ice shelf slope (the $thin\_shelf$ experiment) highlights the importance of bathymetry and ice shelf topography in dictating the transport of large quantities of both meltwater and iron from depth to the surface.

In these model results, melting of the ice shelf is shown to be an important driver not only of iron distribution but also of upper ocean circulation, sea ice cover, and vertical mixing. Sensitivity experiments, conducted with no change in wind forcing, show that melt rate dictates the strength of the coastal current which counters the wind driven gyre. This, in combination with surface irradiance, largely sets the timing of the sea-ice retreat in spring. Furthermore, the mixed layer depth shows sensitivity to melt rate, though this sensitivity is mostly confined to the region where the coastal current is strong.

Overall, and including the results presented in Chapter 4, the model shows a tight coupling between ice shelf melting, dissolved iron dynamics and phytoplankton growth. Warm CDW drives strong Mode II basal melting (Jacobs et al., 1992) which brings a mixture of glacial meltwater and modified CDW to the surface. This water mass, enriched in iron from both glacial and CDW sources, then drives substantial, though not complete, relief from iron limitation. This allows for the formation of a large phytoplankton bloom in the ASP. When ice shelf topography changes there is a large reduction in Mode II melting and in meltwater supply, the latter due to reduced buoyancy in the glacial outflow (see also Bett (2021)). Furthermore, the response of the ice shelf to variations in surface irradiance indicates a contribution of Mode III melting to the overall ice-ocean dynamics, a contribution which increases in significance as cloud cover decreases.

5.5.2 Impact of varying thermocline depth and cloud cover on the Amundsen Sea Polynya

In the sensitivity experiments, the perturbation of downwelling short-wave irradiance is an idealised representation of the variation in cloud cover over the ASP and PIP as reported in Park et al. (2017), whilst the raising and lowering of the thermocline depth at the northern boundary is an attempt to represent interannual variability in the amount of CDW observed on the Amundsen Sea shelf (Dutrieux et al., 2014; Jenkins et al., 2018). It is clear that both sets of forcing impact on productivity, but there are important qualitative differences in the response. The response of peak and annual NPP to perturbations in irradiance is sub-linear and symmetric with respect to the sign of the perturbation, i.e. NPP increases or decreases with the irradiance change with roughly similar magnitudes, regardless of thermocline depth. It is worth noting that this response is not solely due to a change in PAR, but represents a convolution of signals from PAR, modified sea ice retreat and advance, surface stratification due to heat input, and modified late-season melt input due to downwelling of solar-heated water.

Raising and lowering of the thermocline yields changes in peak and annual NPP which are highly nonlinear and greater in magnitude than changes driven by surface irradiance. This is in part due to the fact that the melt response to thermocline change is asymmetric, due both to the complexity of sub-ice shelf circulation and to Ekman downwelling at the ice-shelf front (discussed below; see also Kim et al. (2017)). However, this is not sufficient to explain the NPP response, as wintertime iron inventory does increase monotonically with the shoaling of the thermocline.

The response to elevated iron levels when the thermocline is raised to 450 m is a modest increase in peak and annual NPP, attributable at least in part to a strengthening of observed patterns of iron concentration and sea-ice opening (Figures 5.8 & 5.10). A lowering of the thermocline to 750 m yields lower iron levels on a spatially integrated basis, and yet here too productivity is enhanced. This response is likely due to a large-scale change in the mode of circulation - a transition from a strong, westward-flowing, coastally-intensified current to a circulating gyre, transporting iron to the centre of the polynya (Figure 16). This change in the strength of the coastal current can be attributed at least in part to the reduced melt rate.

In all experiments, ice-shelf melting leads to a meridional density gradient at the ice-shelf front due to the rising, buoyant, melt-laden waters, and this gradient induces a boundary current. This boundary current is weakened when melt rate is lowered, allowing transport of melt water, and therefore iron, away from the coast. A similar coupling between coastal current and meltwater distribution is seen in the studies of Nakayama et al. (2014) and Kimura et al. (2017) (their Figure 13). It can be concluded that the weakening of the coastal current in years with reduced CDW intrusion allows iron to spread into the region of the domain where it is most limiting. Thus whilst in the $warm$ case, the stronger supply of iron helps only to (partially) offset uptake by phytoplankton, in the $cold$ case it serves to expand the region where initial iron levels are high enough to fuel phytoplankton growth.

It is important to note that in the experiments shown the *ferricline* - i.e. the point above which zero concentration of iron was imposed at the northern boundary - is held constant, even when the thermocline was modified. This approach helps to isolate the effect of the melt pump on productivity. Thus the $warm-$ experiment results likely give a lower bound on the effect of increased ocean heat flux. However, an additional $cold\_med$ experiment was run with a lowered ferricline (results not shown); it showed qualitatively the same pattern of productivity as the results described above.

In addition to changes in overall primary production, there are alterations to phytoplankton community composition resulting from changes in iron and light supply. In all experiments where primary production increases relative to $base\_med$ there is an increase in the ratio of peak large biomass to peak small biomass; in the single experiment where productivity decreases there is a reduction in this ratio. Hence conditions more favourable to phytoplankton growth are also more favourable to a bloom consisting predominantly of diatoms, rather than *p. antarctica*.

In the model setup as described here, the two phytoplankton classes are situated along a gleaner-opportunist axis (Burson et al., 2019; Litchman and Klausmeier, 2001) which follows entirely from their different loss rates (see Equations 3.32 and 3.31 and discussion in Chapter 3). The large fraction - corresponding to diatoms - are opportunists whose biomass responds more strongly to change in growth rate than the small gleaner fraction(*p. antarctica*). However this model setup does not account for for the influence of silica limitation on diatoms, nor for their different iron requirement as compared to *p. antarctica*. Neither does the preceding analysis account for changes in zooplankton populations which may in turn impact phytoplankton community composition.

One factor that does not feature in the sensitivity experiments is the impact of the imposed wind forcing. In all experiments there is a southeasterly wind stress forcing, zonally constant but decreasing northward. Such a wind stress pattern leads to Ekman upwelling over most of the domain (Kim et al., 2017). As such upwelling can lead to an input of cyclonic vorticity (Hughes, 2005); this may explain the gyre-like circulation which develops in the absence of a strongly buoyancy-forced boundary current. The strength of this upwelling (along with details of the background stratification) may then quantitatively affect the transition from a boundary current regime to a gyre circulation regime, and thus impact the nonlinear response of NPP to thermocline depth.

It is not currently known whether the mechanism identified above – lowered melting due to a deeper thermocline leading to increased transport of iron to more iron-limited regions – is important for productivity in coastal polynyas in the Amundsen Sea. Melt variability is not as well known as that of bloom strength or sea ice cover due to the need for *in situ* measurements (Jenkins et al., 2018). Moreover, the results of Arrigo et al. (2012) suggest that productivity is strongly determined by the mean open water area in the polynya, which is strongly modulated by wind variability, as well as other factors such as the presence of grounded icebergs (Bett et al., 2020; Stammerjohn et al., 2015). In this study a set of independent sensitivity experiments is used to study the consequences of different regimes of CDW intrusion on the continental shelf. In the future a multi-year model with interannual variability may be necessary to disentangle these signals from those arising due to wind forcing at the surface (Jacobs et al., 2012).

5.6 Conclusion

The ASP is one of several highly productive polynyas around West Antarctica, most of which are close to fast melting ice shelves. This study demonstrates that (1) ice shelves play a crucial role in driving high NPP, and (2) there is strong connectivity between the polynya and ice shelves further upstream, due to the presence of a strong coastal current. Using a novel methodology, the same behavior as in St-Laurent et al. (2017) is reproduced: the melting of the ice shelf increases iron availability in the polynya both due to a meltwater pump effect and due to release of iron entrained at the glacier bed. However the strong westwards transport of iron in the coastal current (St-Laurent et al., 2019) suggests that changes to ice shelves immediately to the east of DIS may have as large an impact on biology in the ASP as changes to the DIS itself.

This study shows that ice shelf melt rate dictates meltwater dispersal, and that this in turn exerts the dominant control on the spatial distribution of the phytoplankton bloom. When less buoyant meltwater is able to spread into more iron-limited regions of the domain (Figure 5.13, the iron contained within it is more efficiently taken up and the polynya becomes a stronger sink for carbon and nutrients. Primary production in the lower latitudes, and the ecosystems that this production supports, are likely to be sensitive to such changes in Southern Ocean polynyas (Henley et al., 2020; Moore et al., 2018).

Recent modelling (Moorman et al., 2020) has shown that over longer timescales a strengthening of coastal currents around Antarctica may suppress ice shelf melting; the present study suggests a separate mechanism by which these strong coastal currents could impact the global climate system, by suppressing the iron supply to phytoplankton. In conclusion, the future viability of Antarctic polynyas as biological carbon sinks may be subject to a trade-off between increased iron leaving the ice shelf cavity and stronger coastal currents preventing this iron from reaching the phytoplankton communities where it is most limiting.

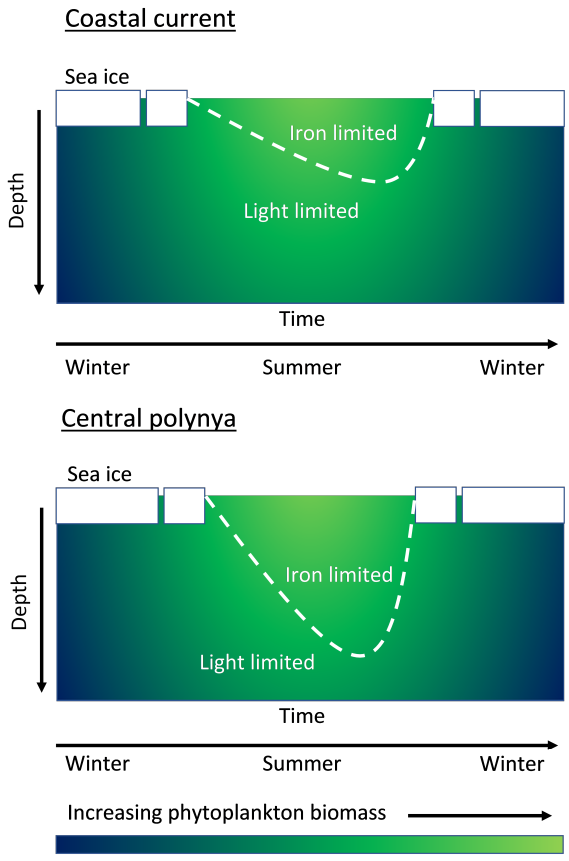

Figure 5.13: Schematic diagram to demonstrate spatial variability in iron and light limitation. In large parts of the coastal current light limitation is more severe than iron limitation. In the central polynya, there is less iron available from the meltwater pump and therefore iron limitation is more severe, extending to greater depths in the water column.

Chapter 6

Impact of Pine Island Bay phytoplankton blooms on carbon fluxes and basal melting

6.1 Preface

In this chapter the feedback of biology onto physics via ocean colour is implemented in MITgcm-BLING, and tested on three different model domains: a global low resolution domain, the idealised domain from Chapters 4 and 5, and a new realistic domain for the entire Amundsen Sea and adjoining ice shelves. This biophysical feedback is not yet included as part of the MITgcm-BLING, but is available via the personal branched gitHub repository `https://github.com/atwelves/MITgcm/tree/blingLight/pkg/bling`.

6.2 Introduction

Antarctic coastal polynyas are unique marine environments due to their high seasonality, which results from their high latitude, and their high climate sensitivity, which results from their proximity to ice shelves. At the same time, an understanding of these coastal polynyas can be instructive for other marine environments elsewhere in, and beyond, the Southern Ocean. In particular, the intense primary productivity which occurs at locations such as the Amundsen Sea Polynya (ASP) and Pine Island Polynya (PIP) can be used to examine the strong seasonal imprint which phytoplankton blooms leave on both ocean chemistry and ocean physics.

The seasonal depletion of DIC by phytoplankton Net Primary Production (NPP) forms an important part of the global ocean carbon budget, inducing a flux of CO_2 from the atmosphere across the air-sea interface. Modelling suggests that, as anthropogenic climate change progresses, this biological pump mechanism will become increasingly important relative to other drivers of air-sea carbon flux, especially in the Southern Ocean (Hauck et al., 2013).

In the highly productive Amundsen Sea, observations suggest a spatially inhomogenous pattern of carbon fluxes (Mu et al., 2014), but modelling of the ASP (Oliver et al., 2019; St-Laurent et al., 2019) has so far not resolved this contribution to the carbon budget. Thus the interplay between the biological pump and the solubility pump in driving carbon fluxes in the Amundsen Sea remains poorly constrained.

Meanwhile, the production of chlorophyll within phytoplankton blooms changes near-surface ocean colour. This effect, which allows phytoplankton blooms to be observed and monitored from satellites (Arrigo and van Dijken, 2003), tends to increase the rate at which seawater absorbs energy from solar radiation. Hence there are changes both to the light available for deeper phytoplankton (via the self-shading feedback, see Chapter 4) and to the distribution of solar heating over the upper layers of the ocean (Morel, 1988). Previous modelling has shown that impacts of ocean colour on ocean physics include cooling in tropical upwelling systems (Hernandez et al., 2017), steering of tropical cyclones (Gnanadesikan et al., 2010) and strengthening of marine heatwaves (Gnanadesikan et al., 2019). Meanwhile these changes to ocean physics in turn impact phytoplankton growth, with changes to global ocean biogeochemistry arising via a bio-optical feedback (Manizza et al., 2008).

Allowing phytoplankton blooms to impact solar heating within a coupled physical and biogeochemical model of the Arctic led to substantial reductions in sea ice cover (Pefanis et al., 2020). Similar effects have been seen for the Southern Ocean within a global model (Manizza et al., 2005). However regional modelling of the Antarctic coastline has either neglected biologically-forced changes in ocean colour entirely or has limited its impact to the self-shading feedback (see Chapter 4, and Twelves et al. (2021)). Furthermore, state estimates such as BSOSE do not in general consider this two-way coupling between physics and biology, potentially leading to biases in data assimilation.

The work in this chapter builds upon the modelling approach from Chapters 4 & 5, both by using the existing utility within BLING to examine air-sea carbon fluxes, and by substantially reworking the MITgcm solar heating framework to account for biologically-forced changes in ocean colour. This modified framework is first implemented within a low resolution global domain, then within the idealised domain described in earlier chapters, and finally within a realistic domain covering the entire Amundsen Sea sector (Figure 6.1). Results from the latter domain, requiring just two independent model experiments, allow for simultaneous quantification of the biological impact on air-sea carbon fluxes and on upper ocean thermodynamics. This study represents the first time that both these mechanisms have been studied within a realistic ice-ocean model.

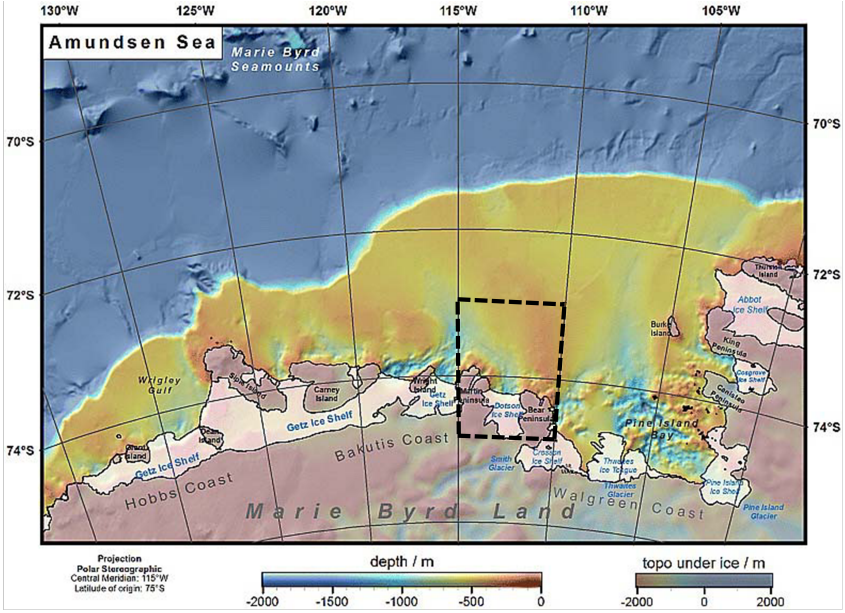

Figure 6.1: Bathymetry in the Amundsen Sea sector, reproduced from Nitsche et al. (2007) with dashed box added to indicate location of idealised domain used in Chapters 4 & 5 and then again in the early part of this chapter. The realistic model domain used in the latter part of this chapter covers the entire sector.

6.3 Development of the bio-optical feedback within a global biogeochemical model

6.3.1 Model setup

In the original MITgcm framework, the subroutine $swfrac$ uses a constant attenuation profile to compute the distribution of (solar) shortwave absorption with depth over the water column. This subroutine is in turn called from the routine $apply\_forcing$, thus contributing to the overall heat budget.

For the purposes of the following investigations, a new subroutine $bling\_swfrac$ is constructed, and called instead of $swfrac$ from the MITgcm kernel. This computes the distribution of shortwave absorption with depth using the same optical parameterization previously described - within the context of phytoplankton self-shading - in Chapter 4.4. Hence the change ΔI in total (red rd, blue-green bg and infrared ir) shortwave intensity $I = I_{red} + I_{bg} + I_{ir}$ over a change Δz_k in depth,

$$\frac{\Delta I}{\Delta z_k} = k_{red}(z) I_{red}(z) + k_{bg}(z) I_{bg}(z) + k_{ir} I_{ir}(z), \tag{6.1}$$

becomes a function not only of the constant infrared attenuation k_{ir} but also of the chlorophyll dependent attenuation variables k_{red} and k_{bg} - as described in Chapter 4. Thus the heat budget $\frac{\partial T}{\partial t}$ from Chapter 3 (Equation 3.6) becomes

$$\frac{\partial T}{\partial t} = ADV_T + DIFF_T + \frac{1}{\rho c_p}\left(k_{RED}(z)I_{red}(z) + k_{bg}(z)I_{bg}(z) + k_{ir}I_{ir}(z) + \frac{F_Q}{\Delta z_1}\right) \tag{6.2}$$

where ADV_T and $DIFF_T$ represent advection and diffusion respectively; once again the surface heat flux F_Q is equal to zero below the surface layer. In this simplified global domain (Figure 6.2) KPP is not used and therefore does not appear in the heat budget.

6.3.2 Model domain

The following global model is developed from the previous BLING verification experiment $global\_oce\_biogeo\_bling$, which is based on a Cartesian grid of $\sim$ 3 degree resolution. This experiment is modified to include the sea ice and external forcing packages. The latter is necessary to provide a seasonally and spatially varying field of shortwave radiation.

As in $global\_oce\_biogeo\_bling$, the model is run over 15 vertical levels with a timestep of one day. However the vertical levels are modified to cover only the upper 400m of the ocean, so that interactions between the surface and deeper water masses are neglected. This choice allows the new shortwave heating scheme to be efficiently tested, at the cost of realism. Studies such as Manizza et al. (2005) offer global results from a full-depth domain, but the focus here is on preparing the setup for use in regional ice-ocean modelling. The initial concentrations of nutrient tracers are compressed to fit the new shallow domain.

6.3.3 Model experiments

Two experiments – "bio" and "$clear$" – are run on this global upper-ocean model. In each, the model is initially spun up for a year, with results taken from the second year. Both use the new $bling\_swfrac$ routine to calculate shortwave heating, but in the $clear$ experiment the coefficients k_{red} and k_{bg} are deliberately held fixed at k^0_{red} and k^0_{bg} respectively, to mimic conditions of zero chlorophyll concentration.

6.3.4 Results

The model domain can be seen in Figure 6.2a, with December concentrations of sea-surface chlorophyll from the bio experiment. The highest concentrations of chlorophyll (around 6 mg m^{-3}) are visible in the ACC, with the model resolution too coarse to capture coastal polynyas such as the ASP. As expected, there are differences in Sea Surface Temperature (SST) between the bio and $clear$ experiments, due to the change in shortwave attenuation (Figure 6.2b). Though this change in attenuating power of seawater is the result of chlorophyll

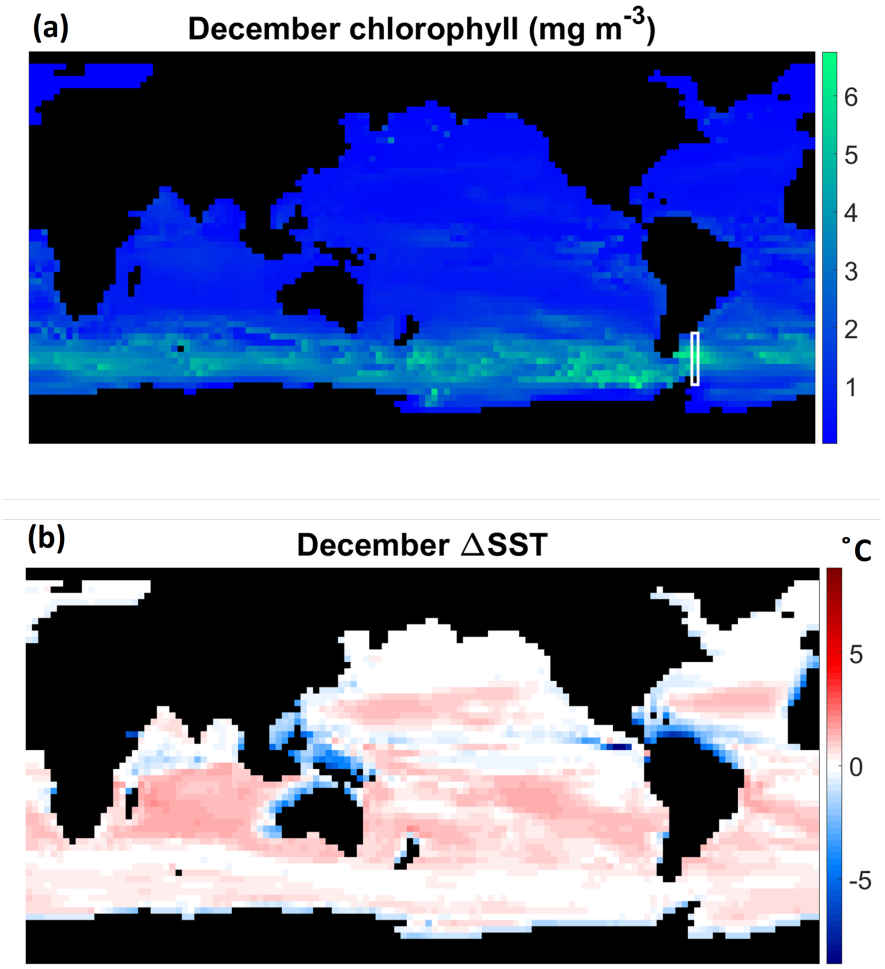

Figure 6.2: (a) Distribution of surface chlorophyll across the entire domain in December. Also (b) the global distribution of sea surface temperature anomaly resulting from the inclusion of shortwave attenuation by chlorophyll. Positive anomalies indicate warming due to inclusion of chlorophyll, negative anomalies indicate cooling; the latter results from changes to ocean circulation, primarily upwelling.

concentrations generated within BLING, the pattern of changes in SST is also a function of spatial variations in the external radiative forcing. These variations in external forcing in turn reflect variations in cloud cover, via the surface irradiance imposed as an external forcing. Hence the changes in December SST do not directly map onto the December distributions of chlorophyll. In particular, the ACC shows large phytoplankton blooms with little impact on local SST, whilst there are strong cooling anomalies – greater than 5°C – visible around continental low-latitude continental margins, even in the absence of phytoplankton. An increase in SST is seen across most of the domain, with widespread warming of 1°C or more.

In order to understand better how changes to shortwave attenuation lead to changes in temperature, the MITgcm heat budget can be examined. In Figure 6.3 the Southern Ocean (south of 30 $^{\circ}$) heat budget is expressed as a set of time series for the surface (0-10m) sub-surface (10-50m) and deeper waters (50-350m). In both the $clear$ and bio experiments there is a strong, almost sinusoidal, cycle in contributions to the surface heat budget. The mid-summer peak in shortwave heating is higher in the bio experiment, driving a mid-summer warming anomaly in the overall temperature trend. However in both experiments shortwave heating is outweighed by the diffusive gain of heat from below and by losses at the surface (a combination of longwave, sensible and latent heat fluxes). The contribution of advection to the surface heat budget is negligible. Advection is again insignificant in the sub-surface layers between 10m and 50m, whilst diffusion switches from being a net source to a net sink of heat for most of the year. However in bio there is strong diffusive heating in mid-summer as the chlorophyll-forced warming anomaly diffuses downwards. This is balanced by a reduction in direct shortwave heating below 10m, so that the overall temperature trends in $clear$ and bio remain similar. Finally, in the deeper waters below 50m, the contribution of shortwave heating to the heat budget becomes neglible for both the $clear$ and bio experiments. The temperature trend is dominated by a near-sinusoidal cycle in diffusive cooling, whilst advection provides a small source of heat to this depth range of the Southern Ocean.

Finally, a transect across the Drake Passage (as marked by the white rectangle in Figure 6.2a) is used to investigate changes in temperature and biogeochemistry concurrently. Biologically-forced changes to ocean colour lead to a positive anomaly in SST across most of the transect, with cooling in deeper layers (Figure 6.4). Notably, the positive anomaly in SST does not extend to the Antarctic continent, where instead there is a strong cooling signal over the full depth of the water column. This strong cooling signal is accompanied by a strong freshening over most of the water column, though there is a sharp increase in salinity in the uppermost layers. The coarse resolution of the model run, plus the absence of sea ice and ice shelves makes it difficult to interpret the cooling signal seen near Antarctica. Previously, chlorophyll has been shown by Hernandez et al. (2017) to cause surface cooling along continental boundaries in the tropics, by inhibiting upwelling.

The same transect is used in Figure 6.5 to compare oxygen fields from the bio and $clear$ experiments with the BSOSE solution detailed in Verdy and Mazloff (2017). The $clear$ experiment (Figure 6.5 d) tends to overestimate oxygen concentrations in the upper ocean, particularly to the north of the transect, whereas the bio experiment (Figure 6.5 d) tends to underestimate them by a substantial margin compared to BSOSE. To some extent this difference in oxygen concentrations between the two model runs seems to reflect the heightened stratification in bio, but may also be affected by a realignment of the large scale circulation

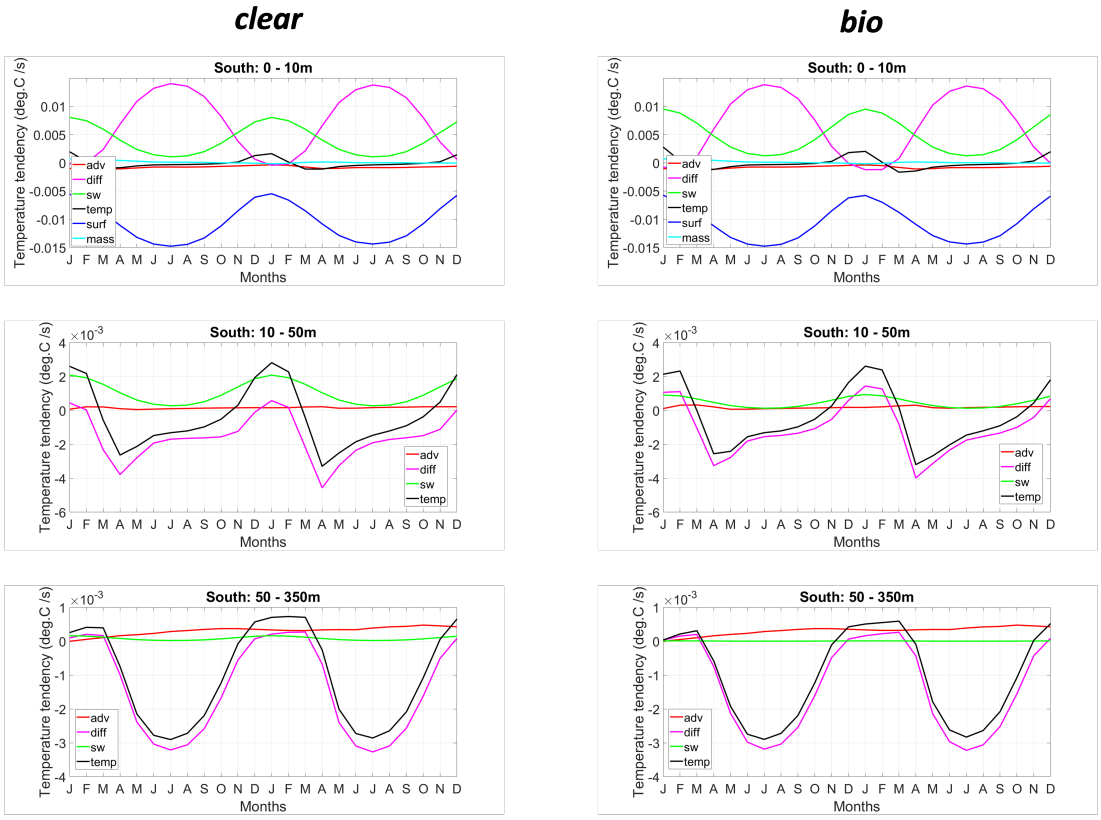

Figure 6.3: Heat budget time series in the Southern Hemisphere, shown at three depth intervals and for both the experiments with (bio) and without ($clear$) the effects of heating by chlorophyll. Contributions are included from advection, diffusion, shortwave heating, surface fluxes, and mass correction.

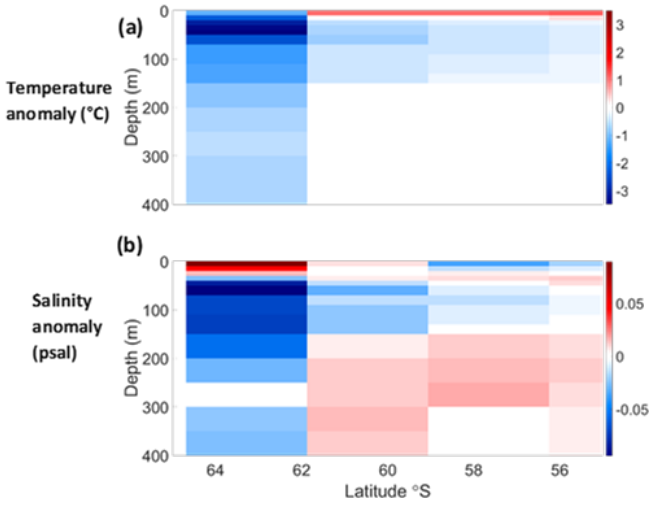

Figure 6.4: Comparison of Drake Passage temperature and salinity for the two experiments, taken from the same section as in Figure 6.5 c. In (a), the temperature anomaly is calculated by subtracting $clear$ results from bio. Similarly in (b) for salinity.

In addition, a portion of the oxygen anomaly between bio and $clear$ results from differences in primary production. Figure 6.5 f shows that the inclusion of heating from chlorophyll in the bio experiment enhances productivity in the upper 20m of the Drake Passage, whilst diminishing productivity below.

6.4 Implementing the biophysical feedback in the idealised domain

6.4.1 Model setup

Next the $bling\_swfrac$ subroutine is implemented within the same idealised ASP domain covered in Chapters 4 & 5. Again, experiments are conducted where chlorophyll contributes to light attenuation (bio) and where this contribution is artificially set to zero ($clear$). As in Chapters 4 & 5 the model is spun up for 30 months before results are analysed.

The heat budget consists of the same terms as described for the low-resolution global model except that a KPP term is now included as in the original heat budget (Equation 3.6) described in Section 3.2. This term takes the form

$$KPP_T = K_z(z)\left(\gamma_T - \frac{\partial T}{\partial z}\right). \tag{6.3}$$

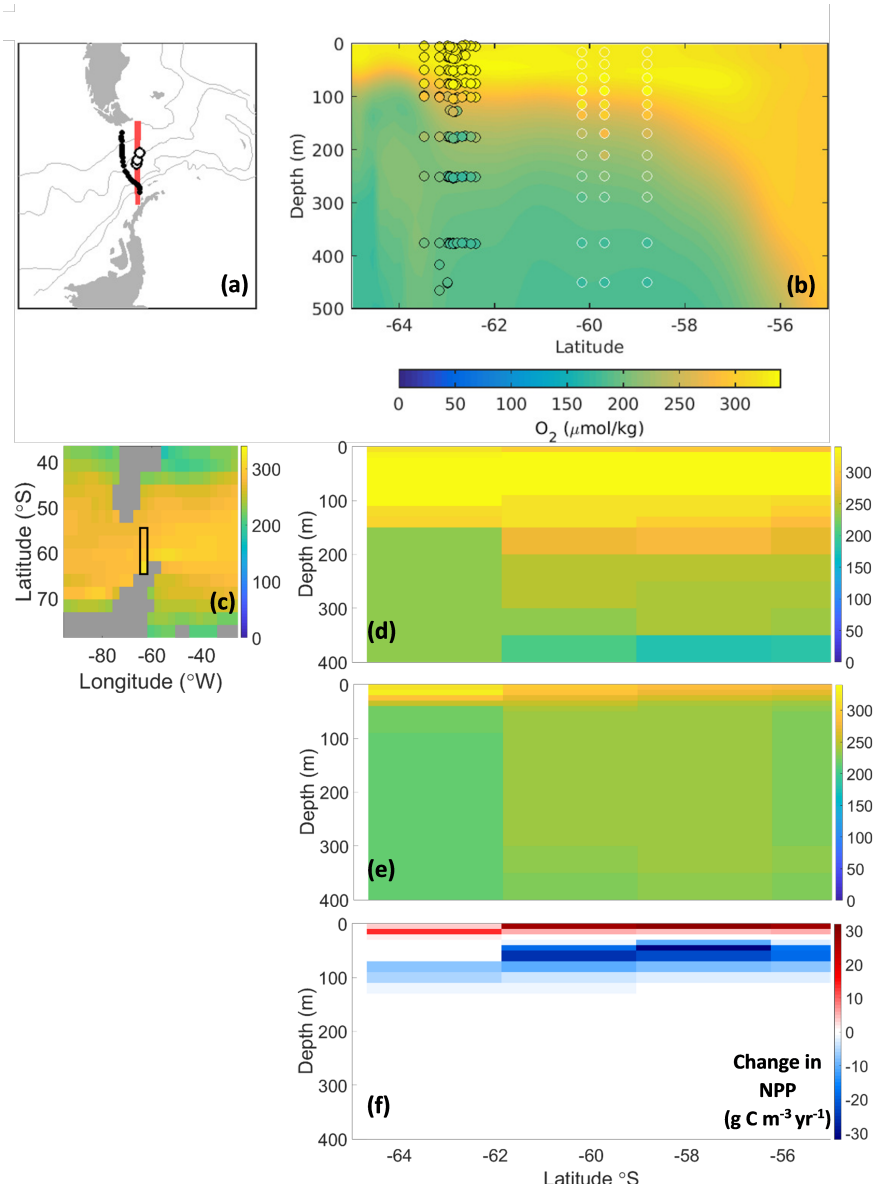

Figure 6.5: Comparison of model results for the Drake Passage with BSOSE and observations. Figures (a) and (b) are taken from Verdy and Mazloff (2017) (their Figure 7 c & d), with background shading showing BSOSE oxygen fields, black contoured bubbles showing the GLODAPv2 estimate and white contoured bubbles showing bgc-Argo profiles - all from February 2009. A similar transect, shown in (c) is used for the model experiments, with (d) and (e) showing oxygen concentrations for the *clear* and *bio* runs respectively. The anomaly in NPP between the two experiments is shown in (f).

Importantly, the calculation of the KPP boundary layer depth reverts back to use of the $swfrac$ routine. This means that the profile of heat diffusivity $K_z(z)$ is calculated independently of chlorophyll, with biology only contributing to the KPP term directly through the gradient in temperature $\frac{\partial T}{\partial z}$.

6.4.2 Results

A comparison of the bio and $clear$ experiments reveals the impact that biologically forced changes to ocean colour have on ice-ocean interactions in the idealised model of the ASP and Dotson Ice Shelf. Figure 6.6 shows the melt rate anomaly in February, March and April, alongside the contribution which chlorophyll makes to the upper ocean (0-50m) heat budget for each of the same months.

As in previous experiments using this model domain (see Chapters 4 & 5 and Twelves et al. (2021)), ice-ocean interactions are dominated by a strong signal from Mode II (CDW-driven) melting at depth, but with a weaker Mode III (solar-driven) signal visible at the front of the ice shelf towards the end of summer. Shortwave attenuation by chlorophyll contributes up to 0.5 $^{\circ}$C enhanced solar heating in February, compared to attenuation by water alone. This contribution of chlorophyll to the heat budget decreases in magnitude as the bloom declines (Figure 6.6).

Over this same three month period the bio experiment shows a reduction in Mode III melting compared to $clear$. This reduction is greatest in March - the month following the peak in shortwave heating anomaly.

There is a clear separation visible between this chlorophyll-sensitive Mode III melting at the front of the ice shelf and the Mode II melting at depth, the latter almost entirely unaffected by changes in ocean colour. This is as expected, since Mode II melting is by definition driven by the intrusion of Circumpolar Deep Water rather than by surface processes. However a more realistic ice shelf topography is needed to assess whether this clear separation between Mode II and Mode III melting is itself realistic.

6.5 A realistic model of the Amundsen Sea sector

As well as simplifying ice shelf topography, the idealised domain described above and in Chapters 4 & 5 also has simplified ocean bathymetry. Whilst this is suitable for investigating mechanisms such as Mode II and Mode III melting, it makes it difficult to assess their relative importance. By extension, the idealised domain is also inadequate to quantify the impact of biologically-forced changes in ocean colour on sea ice and ice shelves. In the following a more realistic setup is described, building on the work of Kimura et al. (2017) and Holland et al. (2017).

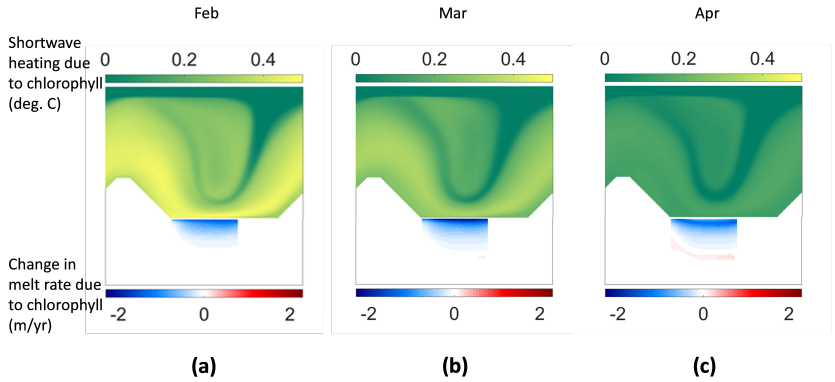

Figure 6.6: Impact of the bio-optical feedback on Dotson Ice Shelf in three months: February, March and April. The green to yellow colourbar shows the contribution, in °C, of chlorophyll to the heat budget in that month. The blue to red colourbar shows the anomaly in melt rate resulting from this increase in shortwave heating.

6.5.1 Model setup

The sea ice model remains as described in Chapter 3, and as implemented in Chapters 4 & 5, except that a layer of snow is now included on top of the sea ice floe as in Zhang et al. (1998). KPP is again used for vertical mixing, and the ice shelf model is as described previously, except that ocean velocity is now allowed to impact melt rate (as well as ocean temperature).

Once again BLING is used to model biogeochemistry. Of the eight BLING tracers described in Verdy and Mazloff (2017), a glacial meltwater value is only prescribed for dissolved iron, again choosing a value of 20 μmolm^{-3} as in earlier chapters and Twelves et al. (2021). The remaining tracers - dissolved inorganic carbon (DIC), alkalinity, nitrate, phosphate, oxygen, dissolved organic nitrogen and dissolved organic phosphorus - are not diluted by glacial meltwater in the model. Neither are values prescribed for iron in dust, or for any of the tracers in sea ice melt. This is an approximation: it is acknowledged that dilution of DIC by sea ice meltwater plays a role in the pattern of air-sea carbon fluxes across the Southern Ocean (see Chapter 3 as well as Hauri et al. (2015) and Rosso et al. (2017)).

Unlike in the modelling conducted on the idealised domain, the growth rates of small and large phytoplankton fractions are treated separately, by introducing size-specific iron requirements. Thus the growth rate μ is replaced by μ_{sm} and μ_{lg} for the small and large fractions respectively. Equations 3.31 and 3.32 for changes in biomass now become

$$\frac{\partial B_{sm}}{\partial t} = \left(\mu_{sm} - \lambda e^{\kappa T} \frac{B_{sm}}{B_0}\right) B_{sm} \tag{6.4}$$

and

$$\frac{\partial B_{lg}}{\partial t} = \left(\mu_{lg} - \lambda e^{\kappa T} \left(\frac{B_{lg}}{B_0} \right)^3 \right) B_{lg}. \tag{6.5}$$

Similarly Equation 3.25 describing NPP now becomes

$$NPP = \mu_{sm} B_{sm} + \mu_{lg} B_{lg}. \tag{6.6}$$

In order that the small and large fractions most closely represent *p. antarctica* and diatoms respectively, values of $k_{Fe}^{sm} = 0.2\ \mu\text{molm}^{-3}$ and $k_{Fe}^{lg} = 0.15\ \mu\text{molm}^{-3}$, are chosen, as in Nissen and Vogt (2021). The value of μ_{max} remains the same for both size fractions as in the original BLING setup.

Due to the coarser vertical resolution in this setup compared to the idealised domain - the surface cell is 10m thick rather than 1m thick - the summertime mixed layer depth can often not be resolved sufficiently to make it a meaningful quantity. Therefore the irradiance memory is not homogenised in the mixed layer, and instead is calculated as

$$\frac{dI_{mem}}{dt} = \frac{I - I_{mem}}{\tau_{acc}} \tag{6.7}$$

over the full depth of the water column.

In addition, the iron-dependent α_{chl} described in Equation 4.21 is replaced by a constant α_{chl} as in Verdy and Mazloff (2017) as it is assumed, in line with the results of Galbraith et al. (2010), that changes to photosynthetic efficiency due to iron limitation are negligible compared to other effects of iron limitation on growth rate.

6.5.2 Model domain

The regional domain is that of Kimura et al. (2017), with resolution varying from $\sim$2.8 km near the Amundsen Sea coastline to $\sim$5.2 km at the northern boundary. The model has 50 vertical levels, with resolution varying from 10m at the surface to 200m at depth.

Boundary conditions for temperature and salinity are derived from the World Ocean Atlas climatology (Locarnini et al., 2018; Zweng et al., 2019). Boundary conditions for ocean velocity, as well as for sea-ice thickness, concentration, snow depth and velocity, are from the BSOSE state estimate (Verdy and Mazloff, 2017). Bathymetry and ice-shelf draft are from BedMachine Version 1 (Morlighem et al., 2020), and atmospheric forcing is from ERA5, 1979-

2018 (Hersbach et al., 2020). As in Bett et al. (2020), a grounded iceberg "wall" extends from Bear Island, which blocks westward advection of sea ice and thus permits the ASP to form in the model. Meanwhile iceberg fluxes are represented by addition of a freshwater flux over the upper 300 m close to the coast.

This model setup is similar to that described in Naughten et al. (2022), and differs in the following ways: the authors used a more recent checkpoint of the MITgcm code base (67s instead of 67c) and a more recent version of BedMachine Antarctica (v2 instead of v1); additionally, Naughten et al. (2022) calculated the wind stress from the relative wind speed rather than absolute.

At the boundaries of the domain vertical profiles are applied to the eight original BLING tracers, generated as the seasonal climatology of BSOSE (Verdy and Mazloff, 2017) outputs from the 2008-2012 solution. Based on the high spatial homogeneity of atmospheric CO_2 around Antarctica, an atmospheric CO_2 value of 381.46 ppm taken from the January 2008 measurement at Palmer station is used in the calculation of air-sea carbon fluxes. Phytoplankton biomass is set to zero at the domain boundaries.

6.5.3 Model experiments

The following analysis covers two independent experiments. These represent the Amundsen Sea with (the $GREEN$ experiment) and without (the $BLUE$ experiment) summertime phytoplankton blooms. The latter experiment is carried out by artificially setting both μ_{sm} and μ_{lg} to zero, thereby preventing a phytoplankton bloom from developing. There remains only a small residual NCP contributing to the carbon budget; this is a product of remineralisation and recycling of residual organic carbon within the model. The source for this residual organic carbon is the minimum phytoplankton biomass concentration which must be applied to maintain numerical stability in the model. Thus whilst the base case ($clear$) described previously eliminated only the impact of phytoplankton on heating, the base case ($BLUE$) used in the following effectively eliminates the impact of phytoplankton both on heating *and* on carbon fluxes.

In both cases the physical model is spun up from 1 January 1979 (with initial condition seeded from a preliminary 24-year run), then passive tracers are circulated from 1 January 1995, before BLING is enabled on 1 January 2003 – with initial conditions taken from BSOSE. After a further five year spinup, the outputs from each experiment are analysed over the five year period covering 1 January 2008 to 31 December 2012.

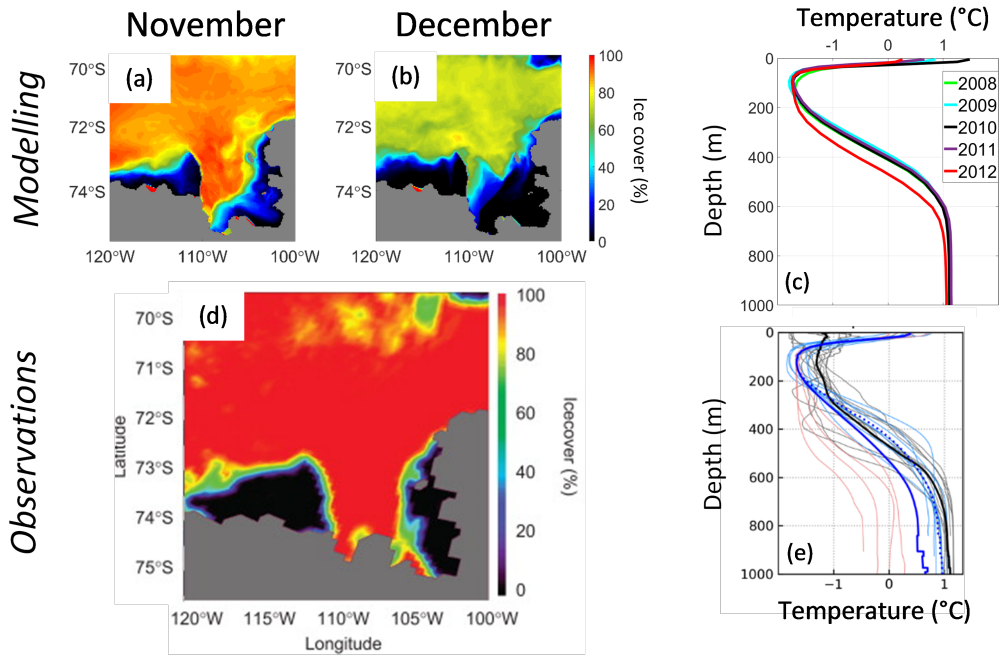

Figure 6.7: Sea ice retreat and summertime temperature structure in Pine Island Polynya. Modelled sea ice concentrations in November (a) and December (b) are shown for 2008; vertical temperature profiles are shown in (c) for each year of the 2008 - 2012 run, averaged over January and February in each case. The sea ice concentration detected using satellite on 1st December 2008 is shown in (d), reproduced from Alderkamp et al. (2012) (their Figure 7 f). The observed temperature profiles for 1997 - 2013 are shown as grey lines in (e), reproduced from Naughten et al. (2022) (their Supplementary Figure 2 b).

6.5.4 Results: Validation of the *GREEN* experiment against observations

Temperatures and sea ice

A combination of satellite data and in-situ measurements is used in Figure 6.7 to assess the accuracy of the *GREEN* model run in the 2008/2009 summer, for the region of the domain covering the two polynyas (ASP and PIP). The maximum sea ice cover is underestimated in the model outputs, reaching only around 85% in November rather than the near 100% cover observed by satellite. The position of the sea ice edge, however, is similar between observations and modelling. By December the maximum modelled sea ice cover is reduced to around 70%, and the edge of the ice floe has migrated substantially to the northwest.

The modelled (January-to-February averaged) PIB temperature profiles from *GREEN* (Figure 6.7 c) lie within the envelope of the observations shown as thin grey lines in Figure 6.7 e, reproduced from Naughten et al. (2022). The 2012 profile shown in red in Figure 6.7 c is indicative of the anomalously cool conditions in that year (St-Laurent et al., 2015; Webber et al., 2017).

In front of Dotson Ice Shelf, meanwhile, the model output after 2008 starts showing signs of convection (Bett et al., 2020), so that stratification in the ASP diverges considerably from observations (Figure 6.8). Therefore the following analysis is focused on the PIP (sub-domain indicated in Figure 6.11), which does not undergo convection during the study period and instead remains well-aligned with observations. Furthermore, the PIP is upstream of the ASP and therefore should not be affected strongly by processes in the former.

Chlorophyll and light attenuation

Figure 6.9 offers a comparison of February 2012 model results against in-situ observations from the same month. This shows that the model underestimates surface chlorophyll concentrations, especially in the centre of PIB, by as much as an order of magnitude. As a result of underestimating surface chlorophyll, the model overestimates the transmission of light through the surface layers and thus overestimates the euphotic depth. Elsewhere in PIB, the observed and modelled chlorophyll estimates are closer, and therefore so are the euphotic depths.

6.5.5 Results: Comparison with the $BLUE$ experiment

Air-sea carbon fluxes

In both experiments there is a pronounced meridional gradient in wintertime air-sea carbon fluxes, with strong outgassing near the northernmost boundary of the domain at 62°S, where surface temperatures are highest and sea ice is absent year-round (Figure 6.10 a). Between 64°S and 68°S there is carbon uptake in winter, likely due to the colder surface temperatures here which increase solubility of CO_2. Between 68°S and 72°S there is negligible wintertime exchange across the air-sea interface, due to large sea ice coverage. Further south, around the continental margins, there is weak carbon outgassing.

In the summertime (Figure 6.10 b), the carbon fluxes calculated in the $BLUE$ and $GREEN$ experiments diverge considerably. In $BLUE$ the zonally averaged flux is negative at all latitudes, indicating outgassing, whilst in $GREEN$ there is a transition from strong outgassing north of 69°S to strong uptake south of this latitude.

The annually averaged carbon fluxes (Figure 6.10 c) are dominated by the summertime fluxes, with a marked difference between the $GREEN$ and $BLUE$ experiments. This anomaly is entirely driven by the presence of phytoplankton in $GREEN$, through impacts on sea ice and ocean temperature structure, as well as the drawdown of DIC.

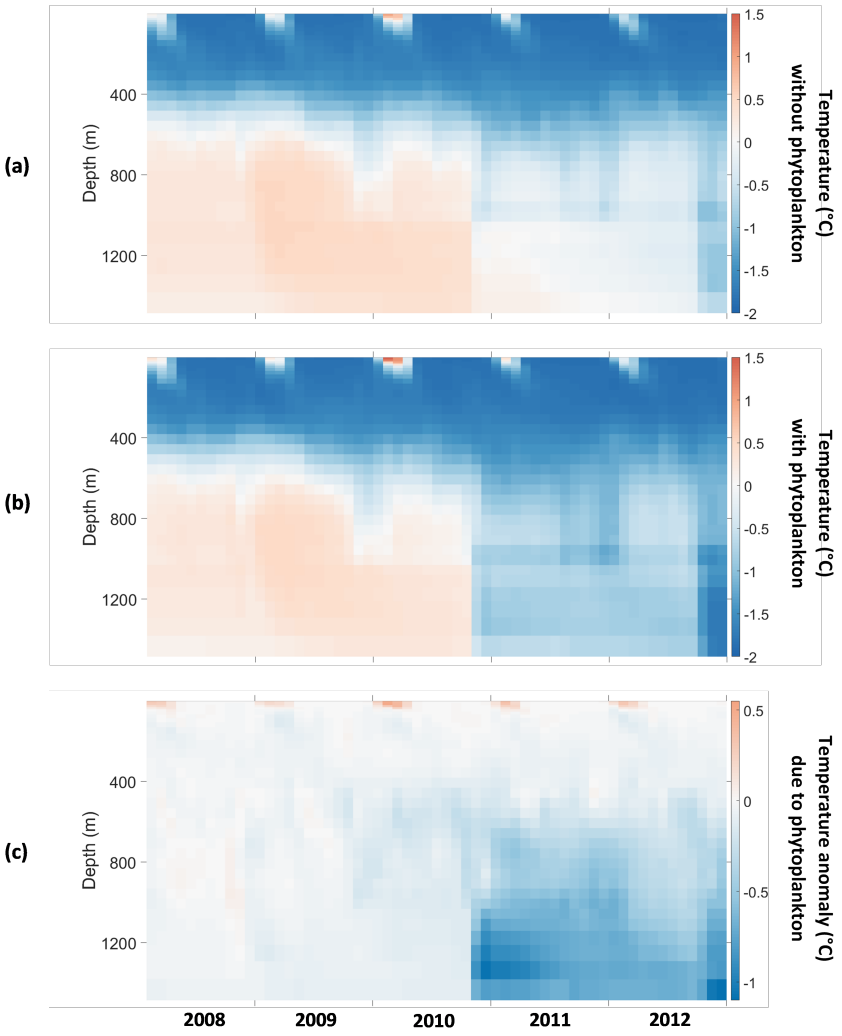

Figure 6.8: Depth structure and seasonal cycle of temperature in front of Dotson Ice Shelf, showing the onset of convection in late 2010; both without (a) and with (b) phytoplankton. The onset of convection then exaggerates the influence of the sub-surface cooling caused by surface chlorophyll, as shown in the anomaly plot (c).

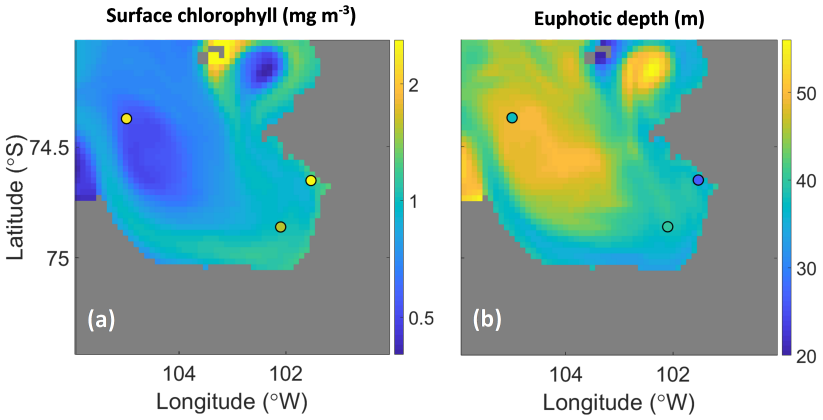

Figure 6.9: Comparison of February 2012 conditions between the model and in-situ observations from three of the stations featured in Park et al. (2017), with the latter shown in the colour scale within the black-outlined circles. In (a) the surface concentrations of chlorophyll are plotted in mg m^{-3} using a logarithmic scale. In (b) the euphotic depth in m is plotted, defined as the depth where light drops to 1% of its intensity at the surface.

Surface heat fluxes

The distribution of phytoplankton in the $GREEN$ experiment (Figure 6.11 a) enhances near-surface absorption of shortwave radiation, most substantially in the productive waters close to the coastline (Figure 6.11 b). Here almost 100% of energy from shortwave radiation is dissipated in the upper 30m of the ocean, as opposed to 90% in the $BLUE$ experiment.

This increased heating of the surface ocean in $GREEN$ means there is more heat available to melt sea ice in summer, so that January sea ice cover is reduced across much of the domain (Figure 6.11 c). However a substantial portion of the additional energy absorbed from shortwave radiation at the surface is instead released back to the atmosphere as part of the surface heat flux F_Q (Figure 6.11 d).

Within the polynyas (ASP and PIP), the ocean surface is already free of sea ice by the time the bloom is at its peak, and the impact of biology on remaining sea ice cover is negligible. In contrast, the negative anomaly in F_Q is clearly visible in both the ASP and PIP. Averaged over the PIP sub-domain indicated in Figure 6.11 d, the heat emitted at the ocean surface during January increases by 5%, from 188 Wm^{-2} in $BLUE$ to 198 Wm^{-2} in $GREEN$.

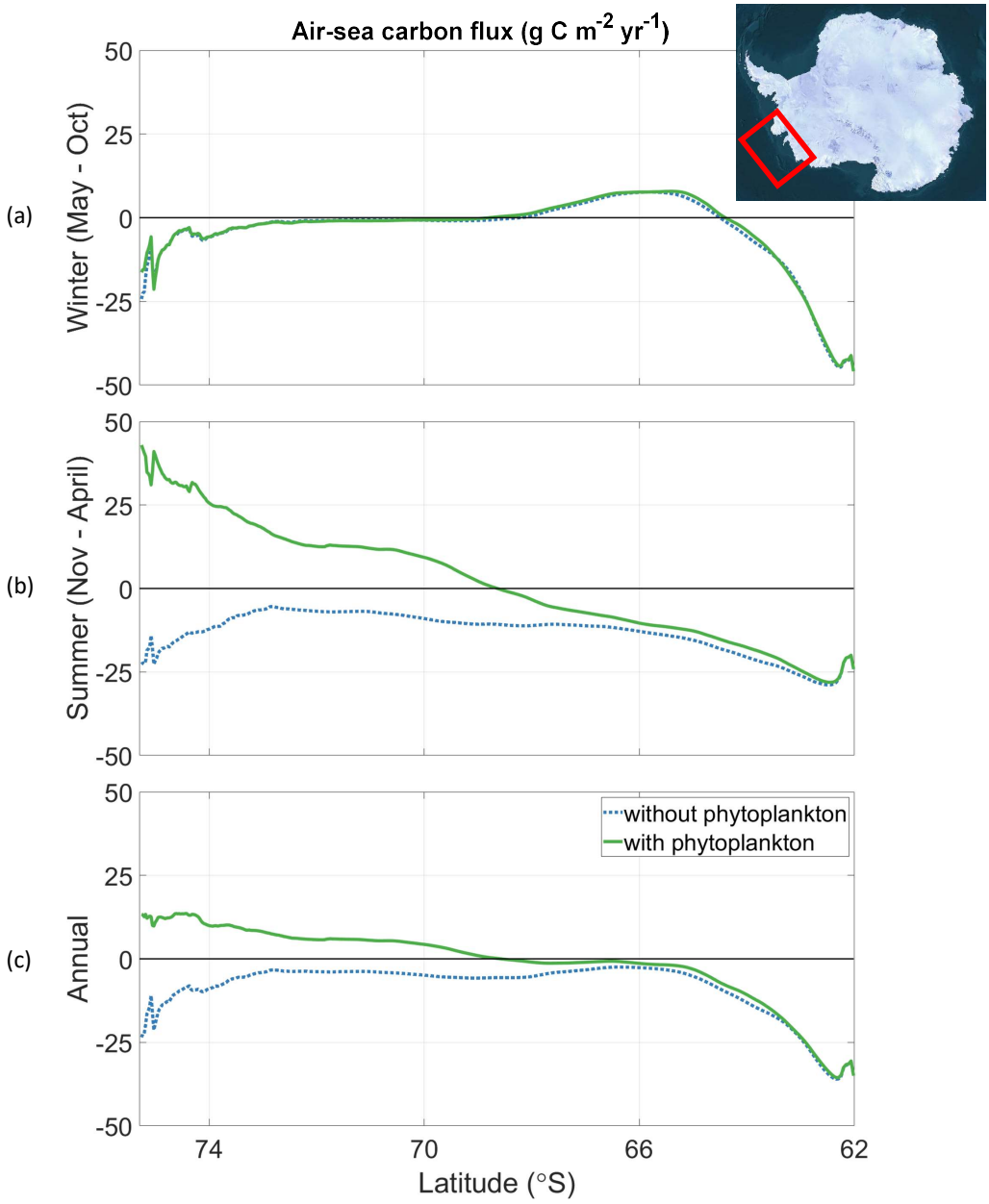

Figure 6.10: Impact of biological production on air-sea carbon fluxes over the study period, with positive defined as a flux into the ocean. Zonally averaged fluxes without the phytoplankton bloom (blue dotted line) and with phytoplankton bloom (green solid line) are plotted against latitude in winter (a), summer (b) and on an annual basis (c). The inset figure shows the location of the domain on the Antarctic coastline.

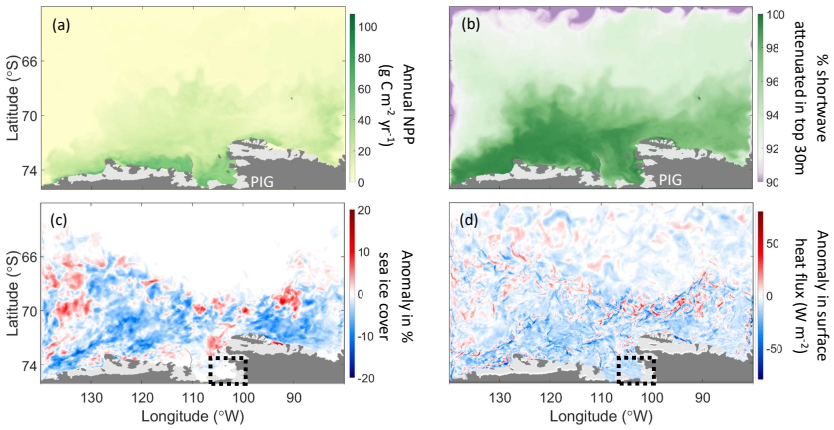

Figure 6.11: Impact of phytoplankton on ocean biogeochemistry and physics in the Amundsen Sea. Annual NPP integrated over the water column is shown for the whole domain in (a), with the location of Pine Island Glacier Ice Shelf (PIGIS) marked. In (b), the percentage of shortwave radiation attenuated in the upper 30m of the ocean in January is plotted for the $GREEN$ experiment. The colourmap is chosen so that purple (90% attenuation) represents cells without phytoplankton - as found throughout the domain in the $BLUE$ experiment - whilst white (91.5% attenuation) represents the Jerlov water type 2 approximation (Paulson and Simpson, 1977). The maps in (c) and (d) show the impact of these changes in ocean colour on January sea ice and surface heat flux distributions respectively. Surface heat flux is defined as positive for a flux into the ocean, so a negative anomaly in flux corresponds to heat lost from the ocean to the atmosphere. In both cases the anomaly is calcuated by subtracting the $BLUE$ output from the $GREEN$ output, with the black dashed box marking the location of Pine Island Polynya (PIP).

Basal melting

In both experiments, there is a warm layer of Circumpolar Deep Water (CDW) at depth (below 600m) in the PIP, with cooler waters above (Figure 6.12 a). Superimposed onto this structure is a seasonal cycle in the temperature of the upper ocean, driven by solar heating. Some interannual variability is present in both experiments, though this is relatively weak compared to the observed variability in CDW properties on longer (decadal) timescales. Interannual variability in upper ocean temperature, salinity, and mixed layer depth - both wintertime and summertime - is qualitatively the same in both experiments, and also for a model run which retained the original $swfrac$ formulation (Figure 6.13), which was based on Jerlov water type (Paulson and Simpson, 1977).

A trend of decreasing temperature at depth may be seen in Figure 6.12 a, but this does not represent a total breakdown of stratification as is observed in the modelled convection of the ASP. Importantly, this trend appears to precede the trend in the ASP, making it unlikely that convection in the ASP is adversely affecting the accuracy of the model in the PIP.

Subtracting the $BLUE$ from the $GREEN$ model output shows the anomaly in temperature due to the presence of the phytoplankton bloom (Figure 6.12 b). From the surface down to around 30m there is a positive anomaly of up to 0.5°C in the summer months (November-March), whilst in the winter months the two experiments are near-identical. From 30m to 150m there is a similar seasonality but with opposite sign: the maximum negative anomaly in summertime is around -0.35°C. With increasing depth, the sub-surface cooling becomes smaller in magnitude but longer-lived. Below around 150m, this cooling persists year-round with low seasonality. Below 600m the cooling is substantially weaker, although it strengthens over the course of the study period.

There is good agreement between modelled ice shelf melt rates and the observational record, with both showing substantially lower melting in 2012 than other years (Figures 6.12 c & d). The sub-surface cooling anomaly in $GREEN$ leads to reduced melting across the extent of the ice shelf and throughout the study period. In 2012, this reduction in melt is particularly noticeable in the deepest part of the ice shelf (Figure 6.9 d e), with the integrated meltwater flux in 2012 reduced by 9% from 62 $km^3 yr^{-1}$ in $BLUE$ to 56 $km^3 yr^{-1}$ in $GREEN$.

Decoupling of meltwater and DIC distributions

The biologically-forced reduction in ice shelf melt rate in turn leads to reduced meltwater concentrations at the surface of the PIP. This negative anomaly in surface meltwater is substantially larger in April (Figure 6.14 d) than in October (Figure 6.14 a).

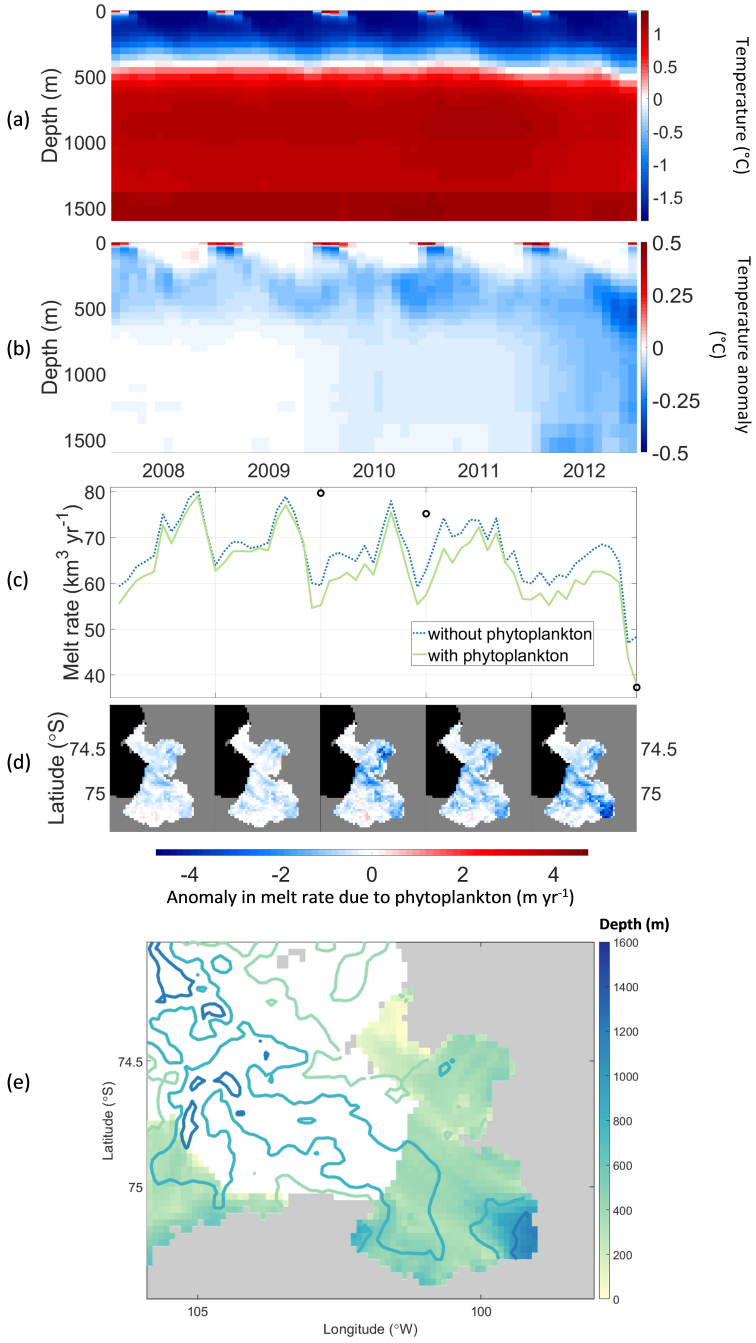

Figure 6.12: Impact of chlorophyll on ocean temperature structure and on ice shelf melt rates. The Hovmoller diagram in (a) shows horizontally averaged temperatures within the sub-domain marked in Figures 3 c & d for the $BLUE$ experiment. In (b) the anomaly in temperature due to phytoplankton is calculated by subtracting the $BLUE$ output from the $GREEN$ output. The time series in (c) shows the total volume of meltwater from PIGIS without (blue dotted line) and with (green solid line) the phytoplankton bloom. Black circles on the time series indicate the observed meltwater fluxes for 2009, 2010 and 2012 as listed in Dutrieux et al. (2014). In (d) the distribution of the anomaly in basal melting is plotted for each of the five study years, again calculated by subtracting $BLUE$ from $GREEN$. Finally in (e), contours show bathymetry in Pine Island Bay whilst colourmap shows depth at base of Thwaites and Pine Island ice shelves.

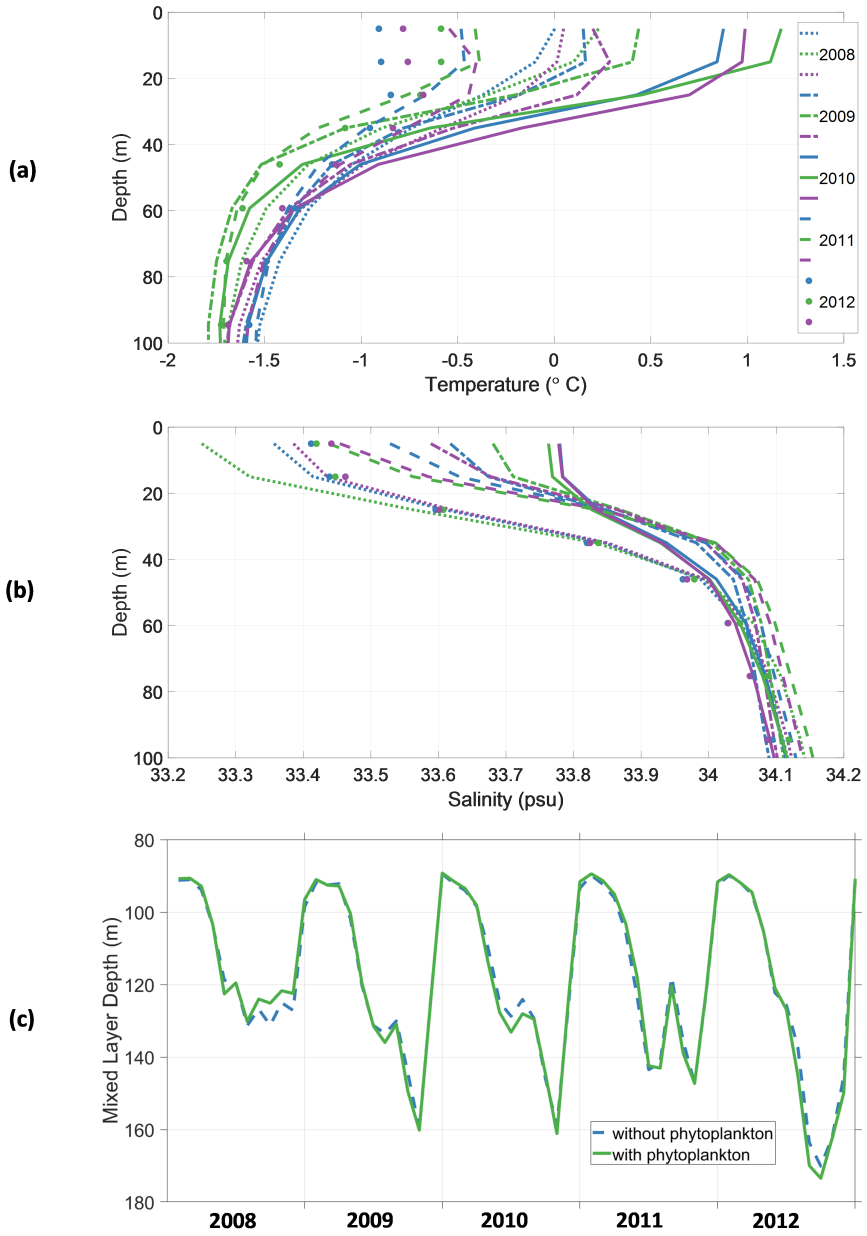

Figure 6.13: Interannual variability in February upper ocean temperature (a) and salinity (b) within Pine Island Bay; plotted for the experiments without (blue) and with (green) phytoplankton as well as for the default MITgcm shortwave heating scheme (purple). Also the seasonal cycle in mixed layer depth (c), averaged across Pine Island Bay.

In the $GREEN$ experiment, October concentrations of DIC are slightly higher than in $BLUE$ (Figure 6.14 b). This positive anomaly is comprised of DIC remineralised from biological carbon export in the previous summer, which is then returned to the surface over the winter (Figure 6.15). In April (Figure 6.14 e), following the phytoplankton bloom, DIC concentrations remain slightly enhanced in $GREEN$ compared to $BLUE$ in the central part of the polynya. However DIC concentrations are substantially reduced closer to the coastline.

Figures 6.14 c & f, representing October and April respectively, show meltwater and DIC concentrations along a transect in Pine Island Bay. In October, meltwater and DIC are well-correlated in both the $BLUE$ and $GREEN$ experiments. In April, DIC and meltwater remain well-correlated in $BLUE$, though the equalising effect of summertime outgassing means the DIC distribution is more homogenous compared to that in October.

However in the $GREEN$ experiment, meltwater and DIC become decoupled close to the ice shelf, with DIC concentrations decreasing as meltwater concentrations increase. This result demonstrates that the negative anomaly in DIC is not merely a function of the negative anomaly in meltwater, and is in fact largely due to biological uptake and export near the ice shelf.

6.5.6 Results: Trends and Inter-annual Variability in Pine Island Bay

Dissolved iron and DIC

Figure 6.8 clearly demonstrates the onset of convection in the model close to DIS – contrary to observations – whilst Figure 6.12 suggests that even close to PIGIS there may be a drift in the physical model. To examine whether this also implies a drift within BLING, dissolved iron and DIC concentrations are plotted in time-depth coordinates for PIB in Figure 6.16. In each case the monthly average for the period 2008 – 2012 is subtracted, so that the trend over the five years can be seen and compared in magnitude to the interannual variability.

There is a clear trend of increasing dissolved iron which dominates over interannual variability at most depths. By comparison, the drift in DIC concentrations is substantially less over most of the water column. For both DIC and iron there appears to be an especially strong increasing trend in near-surface concentrations during springtime. However there is no clear trend in phytoplankton community production, nor in air-sea carbon fluxes.

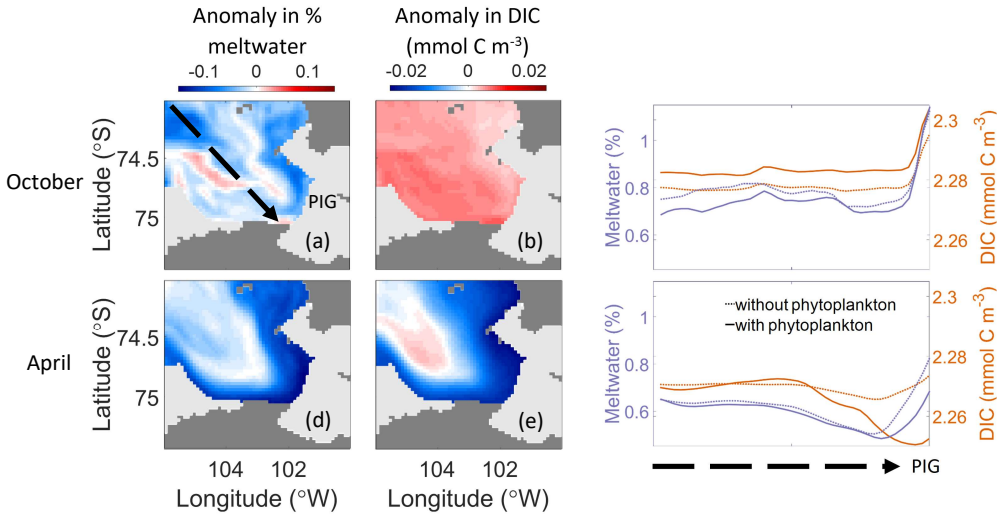

Figure 6.14: Impact of phytoplankton on meltwater and DIC distributions. By subtracting $BLUE$ results from $GREEN$ results the anomalies in meltwater (a) and DIC (b) distributions are plotted for the month of October, averaged over 2008-2012. In (c), meltwater and DIC concentrations are plotted for each of the two experiments, using the transect marked in the black dashed line in (a). Purple solid and dotted lines show October meltwater fractions for the $GREEN$ and $BLUE$ experiments respectively. Orange solid and dashed lines show October DIC concentrations for the $GREEN$ and $BLUE$ experiments respectively. The panels (d) to (f) show the equivalent plots for the month of April.

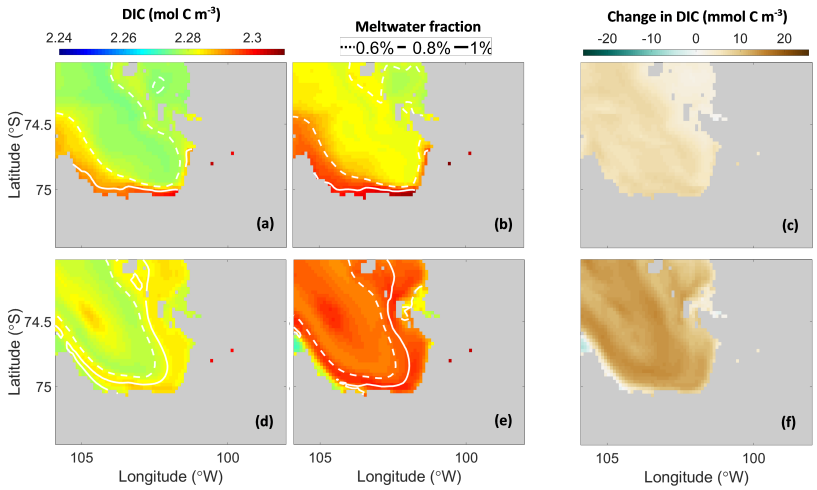

Figure 6.15: Impact of phytoplankton on October concentrations of DIC (colourmap) and meltwater (contours) at a depth of 145m, shown via the results without (a) and with (b) phytoplankton, as well as the anomaly in DIC (c). October represents conditions before the onset of the phytoplankton bloom, whilst (d) to (f) show conditions after the phytoplankton bloom, in April.

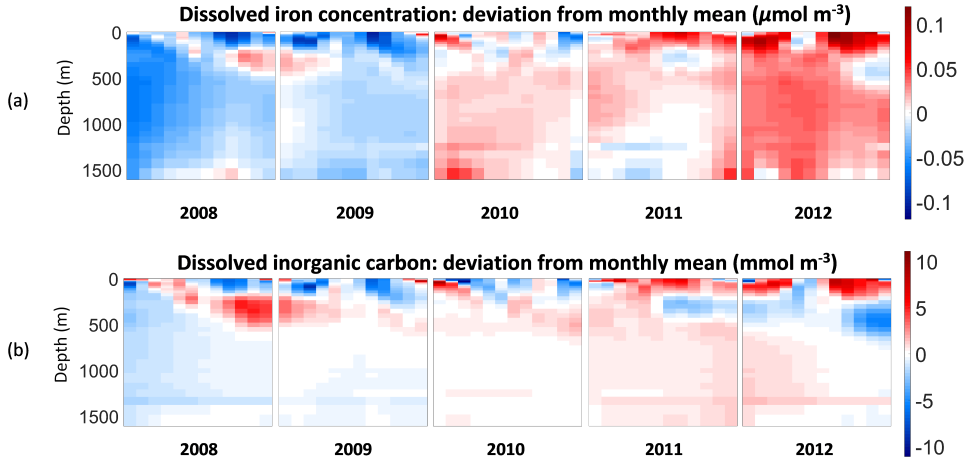

Figure 6.16: Trend in biogeochemical model output for the PIP over the period 2008 – 2012, calculated by subtracting monthly mean from each of the years. In (a) the drift is shown for the dissolved iron concentration; in (b) the drift is plotted for DIC concentration.

Sea ice and Carbon Fluxes

As stated previously, atmospheric carbon levels are held constant throughout the model run. Therefore inter-annual variability in carbon fluxes is entirely driven by trends and inter-annual variability in sea ice and in the ocean. This variability is examined in the following, alongside the variability in surface NCP and sea ice cover (Figure 6.17).

The dominant mode of variability is clearly the seasonal cycle, with sea ice cover gradually increasing in autumn, before retreating quickly in spring. The maximum in sea ice cover (minimum open-water area) shows some interannual variability, occurring as early as July in 2010 and 2012, but not until September in 2008.

Substantial NCP is generally initiated in November, giving rise to a rapid switch in the sign of the carbon flux, from the polyna being a strong source in November to a strong sink in December. There is particularly strong spring outgassing in October 2010, associated with an early retreat of sea ice. As sea ice slowly re-enters the polynya from April onwards, fluxes are slowly dampened until they are negligible in midwinter.

Overall, attribution of variability in the air-sea flux to variability in environmental drivers is difficult. For instance, the anomalously high October outgassing in 2010 may be due to the unusually large open water area or to the relatively prolonged uptake of carbon in the preceding summer. The latter may in turn have been influenced by the unusually large open water area in April. In the following summer (November 2010 – February 2011), NCP is reduced, perhaps indicating that early sea ice cover reduces the effectiveness of the biological pump.

6.6 Discussion

6.6.1 Influence of ice shelves on carbon fluxes

The model results demonstrate the opposing effects of ice shelf melting on carbon fluxes in the Amundsen Sea. When the meltwater pump entrains DIC from depth and pulls it to the surface, this tends to promote carbon outgassing in the meltwater-rich coastal waters. However, at the same time, the meltwater pump also draws iron towards the surface, as shown in Chapters 4 & 5. In summer this additional input of iron tends to promote phytoplankton growth and strong productivity, thereby promoting carbon uptake (Figure 6.18).

The modelled meltwater distribution in Pine Island Bay is similar to observations (Thurnherr et al., 2014; Zheng et al., 2021) and models (Bett et al., 2020; Kimura et al., 2017; Nakayama et al., 2014) in that concentrations are at a minimum in the centre of the bay, due to a gyre transporting meltwater in a cyclonic circulation in front of the ice shelves. As well as meltwater, this circulation can also transport DIC and iron (Dinniman et al., 2020; St-Laurent et al., 2017;

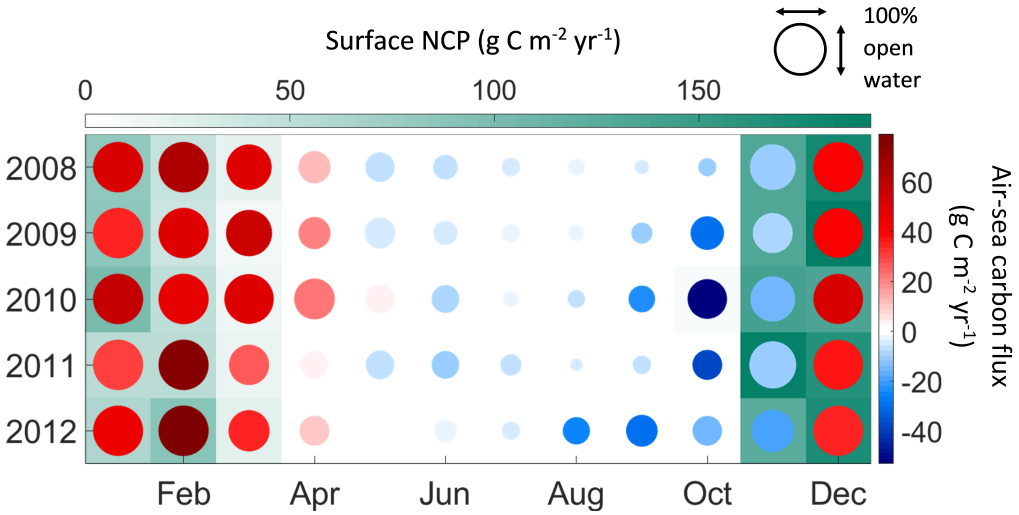

Figure 6.17: Variability in sea ice, Net Community Production (NCP) and air-sea carbon flux in the PIP between 2008-2012, for the $GREEN$ experiment. The white to green colourmap shows NCP in the surface layer (0 – 10m), whilst the size of each circle overlay represents the size of the open water area in each month, calculated as the sum of the open water areas across all cells in the polynya. The blue to red colourmap within each circle shows the magnitude and sign of the air-sea carbon flux.

Twelves et al., 2021). The reduced melting due to surface chlorophyll appears to change only the magnitude of surface meltwater concentrations, but not their lateral distribution. This indicates that the circulation within PIB is relatively insensitive to changes in surface ocean colour.

One constraint of this study is that, due to insufficient storage space, diagnostics for each component of the iron and carbon budgets could not be saved. Future studies which include such full budgets should seek to answer whether the observed increasing trend of iron at depth is a result of changes to internal biogeochemical cycling or of changes to mixing and advection of the tracers.

6.6.2 Influence of ocean colour on the heat budget

All three model setups (global, idealised and realistic) demonstrate that the chlorophyll concentrations calculated in BLING tend to increase near-surface attenuation of shortwave radiation - although in the global run, there are also some cooling anomalies in upwelling regions similar to those seen in Hernandez et al. (2017). In the realistic Amundsen Sea model this increased shortwave heating is in part compensated by an increase in heat lost to the atmosphere by longwave, sensible and latent heat fluxes. A larger change to the heat budget comes in the sub-surface, which is substantially insulated from solar heating in all model setups. In the global model, changes to the heat budget, and associated changes to ocean

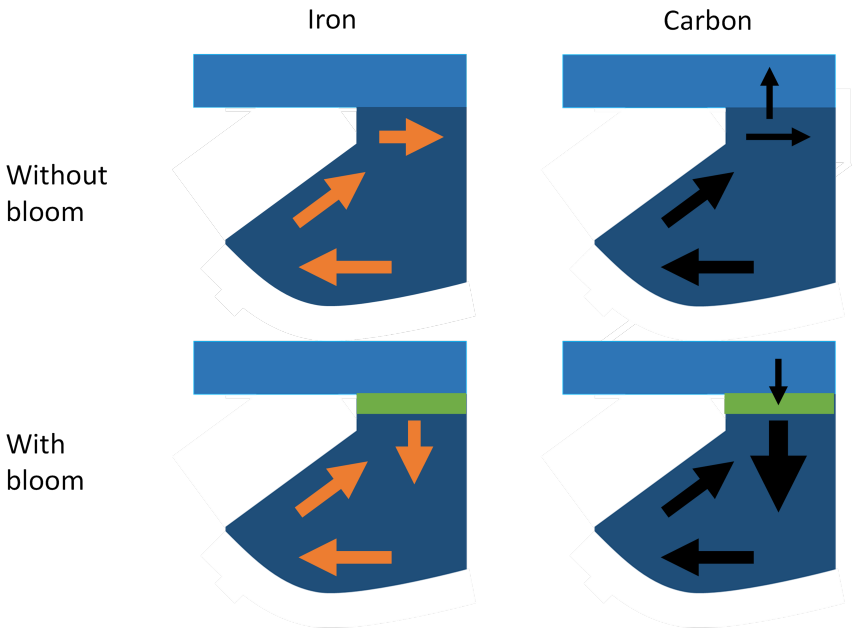

Figure 6.18: Schematic representation showing impact of Pine Island Glacier on iron and carbon cycling in Pine Island Bay. The meltwater pump pulls both dissolved iron and dissolved inorganic carbon from depth to the surface of the polynya. In the absence of a phytoplankton bloom, iron is advected away from the ice shelf as it reaches the surface, before it is eventually scavenged onto sinking particles. Carbon is also advected away, whilst at the surface some carbon is lost to the atmosphere. When a phytoplankton bloom is present, it makes use of iron for growth, and thus produces a sink of dissolved iron. This iron-fuelled growth drives depletion of dissolved carbon, which in turn drives a reversal in the air-sea carbon flux.

circulation and NPP, due to shortwave attenuation by chlorophyll, in turn lead to large changes in Drake Passage biogeochemistry. This suggests that the bio-optical feedback could be an important mechanism to include in future circumpolar modelling and in state estimates such as BSOSE.

6.6.3 Influence of ocean colour on sea ice

Modelling by Pefanis et al. (2020) found a large impact of biologically sourced changes in ocean colour onto sea ice coverage in the Arctic. The results from this study also show reduced sea ice cover due to chlorophyll across much of the domain, but not in the ASP or PIP. This follows from the fact that both the ASP and PIP are examples of latent heat polynyas, which are formed by the presence of an upstream barrier that blocks wind driven advection of sea ice. Thus unless the Thwaites Fast-Ice Tongue (TFIT) is itself affected by ocean colour - a possibility which this study cannot exclude - the sea ice coverage in the ASP and PIP is likely insensitive to chlorophyll.

In contrast, sensible heat polynyas are formed thermodynamically as the result of upwelling warm water. Therefore, given the impacts on surface temperature and heat fluxes shown in this study, it is to be expected that biology could play a non-negligible role in the thermodynamics of sensible heat polynyas.

6.6.4 Influence of ocean colour on basal melting

The increased surface heating due to chlorophyll leads to sub-surface cooling of the PIP and thus partially insulates PIGIS from solar heating, reducing melt rates. This insulating effect is the direct result of high chlorophyll concentrations occurring in midsummer at the same time as solar heating is at its peak. Hence this mechanism is sensitive to a change in the timing of the spring phytoplankton bloom; this could occur as a consequence of climate-driven changes underway around Antarctica. If the peak of the bloom were to shift to earlier in the season, this could leave ice shelves more exposed to solar heating in midsummer.

In the idealised domain model runs, there is a clear separation between Mode II and Mode III melting at DIS, with the latter reduced by the presence of chlorophyll in the phytoplankton bloom. In the realistic model results, it is more difficult to disentangle these different modes at PIGIS, and the effect of changes to ocean colour is seen over much of the water column. Further work is needed to ascertain whether this represents distinct responses between the two ice shelves, or is merely an artefact of the different model setups.

The results obtained for DIS as part of the larger domain do not appear to be realistic, and instead show the onset of convection in the model, possibly caused by errors in the re-analysis products used as surface forcings. This convection, however, does offer an approximation of Mode I ice-ocean interactions, and indicates that ocean colour could substantially impact the formation and associate temperatures of dense shelf water within such systems.

6.7 Conclusion

The exchange of carbon between the atmosphere and ocean represents a balance between uptake via the solubility and biological pumps and outgassing of oceanic CO_2. Modelling suggests that phytoplankton in a highly productive polynya can influence both of these mechanisms, including by inhibiting the basal melting of adjacent ice shelves. In summary, phytoplankton can affect carbon fluxes in coastal polynyas:

- directly via primary production (the biological pump),
- indirectly via changes to summertime sea surface temperature (influencing the solubility pump), and
- indirectly via changes to basal melting and thus the supply of meltwater and iron (impacting both biological and solubility pumps).

This chapter has demonstrated a two-way coupling between the physical and biogeochemical properties of the Amundsen Sea. Hence in future improved parameterizations of upper ocean light attenuation will be needed to improve estimates of ice shelf melt rates, meltwater transport, and carbon fluxes on the Antarctic continental shelf.

Chapter 7

Synthesis

7.1 Evaluation and development of modelling strategies

7.1.1 Idealised and realistic representations of the Amundsen Sea

The idealised domain used in Chapters 4 and 5 has the advantage of low computational cost, allowing multiple sensitivity experiments to be run on the same basic setup. This in turn enables analyses which isolate specific mechanisms - in this case surface irradiance and thermocline depth, as well as different iron sources - and their impacts on the state of the phytoplankton bloom. It also provided a useful first test of the impact of chlorophyll on ice-ocean interactions in Chapter 6. However this setup did not accurately capture the impacts of winds, either over the polynya or at the continental shelf break.

The more realistic domain introduced in Chapter 6 more accurately captures the important components of the system, and is derived from a physics-only model which matches observations well over the past half century. However the model fails in its representation of ocean conditions in the immediate vicinity of Dotson Ice Shelf, possibly due to errors in the re-analysis product used as external forcing.

7.1.2 Modelling phytoplankton blooms with BLING

Previously, BLING has been used on global and Southern Ocean scales, including in state estimates. The work presented in this thesis represents the first time that BLING has been used extensively to model individual phytoplankton blooms. Several lessons can be drawn from this work which may inform the use of BLING in BSOSE or in future applications to regional domains.

Attenuation of shortwave radiation within phytoplankton blooms

The modelling carried out in this thesis demonstrates the importance of light attenuation in driving both ocean physics and biogeochemistry. The use of a fixed light attenuation profile in the default version of MITgcm-BLING proves inadequate to reproduce realistic profiles of phytoplankton blooms. The formulation implemented in its place, derived from the work of Manizza et al. (2005), offers substantial improvements in this area, with euphotic depths far closer to those recorded in observations. Whether there is a similar improvement in the representation of polynya physics remains unclear, as it is difficult to isolate the impact of ocean colour within physical oceanography observations. In addition, the realistic model employed in Chapter 6 had already been tuned to observations of ice shelf melt (Holland et al., 2017; Kimura et al., 2017), so that an improvement in representation of melt rates will not be obtained by simply introducing chlorophyll to the heat budget. Nevertheless Chapter 6 shows that, at least in principle, biologically-forced upper ocean heating can make a non-negligible contribution to ice-ocean interactions.

As in Manizza et al. (2005) and Kim et al. (2015), the chosen parameterization of self-shading was informed by bio-optical data from lower latitudes, rather than data specific to the region of interest (Morel, 1988). Previously, efforts to quantify the attenuation of light by chlorophyll in Antarctic polynyas have been more focused on constructing algorithms to extract NPP from satellite ocean colour data (Arrigo et al., 2008) than on constraining large-scale models. In the future there is set to be a large increase in the availability of in-situ data from the Amundsen Sea, including from autonomous platforms (Meredith et al., 2016). Meanwhile at greater distances from the coastline, including in sensible heat polynyas, there may be opportunities to incorporate light attenuation data from bgc-Argo floats (Haëntjens et al., 2017). Thus there will be a significant opportunity to improve the characterization of bio-optical feedbacks in this important region of the Southern Ocean, leading to better estimates of NPP both from satellite data and from models.

Dissolved iron dynamics

In this thesis a novel methodology is used to study iron limitation within a polynya. By comparing against an experiment where phytoplankton growth is not allowed to deplete iron, it is demonstrated that phytoplankton uptake is the dominant sink of dissolved iron within the polynya and thus plays a large role in the decline of the bloom. This in turn emphasizes the importance of the iron-to-nitrate uptake ratio early in the bloom development. The greater this ratio in the early (iron-replete) stages of the bloom, the more severe will be the iron limitation in the later stages of the bloom. Therefore an accurate representation of iron uptake is crucial to reproduce successfully the dynamics of phytoplankton blooms in polynyas such as the ASP.

Advection of meltwater and upwelled water from upstream is found to be vital in supplying iron to the ASP, although it remains difficult to isolate different sources (CDW, glacial, benthic) within a single model experiment, especially when different sources may exhibit differing degrees of bio-availability. Future modelling using MITgcm-BLING could make use of multiple passive tracers for iron (similar to the “local” iron tracer described in Chapters 4 & 5), as has been done for various sources in the ROMS simulations by St-Laurent et al. (2019) and Dinniman et al. (2020). A more sophisticated understanding of how phytoplankton blooms respond to different iron sources might be gained by switching to an adjoint modelling approach (Dutkiewicz et al., 2006; Song et al., 2016).

Competition between phytoplankton species

The progression of this thesis coincides with an advancement in how BLING treats different phytoplankton classes. In Chapters 4 & 5, the only distinction between large and small classes is in their sensitivity to grazing pressure, whereas the version of BLING subsequently developed, and implemented here in Chapter 6, includes differential iron requirements.

A new version of BLING - "siBLING" - has recently been developed which incorporates silica limitation of growth for the large (diatom) fraction. This could help to improve both representations of diatom – coccolithophore competition (in the open Southern Ocean) and diatom – *p. antarctica* competition (in coastal polynyas).

Carbon fluxes

For the first time, this thesis uses BLING to ask what Southern Ocean carbon fluxes would remain in the absence of the biological pump (ie. the $BLUE$ experiment in Chapter 6). With the phytoplankton bloom suppressed, ocean circulation and temperature alone dictate the pattern of fluxes. Future studies using BLING may also benefit from running additional experiments with the phytoplankton growth rate set to zero.

7.2 Scenarios for the future of Amundsen Sea biogeochemical cycles

Based on the modelling presented in this thesis, six scenarios are identified for the future evolution of the Amundsen Sea coastal polynyas. These scenarios are neither exhaustive nor mutually exclusive, but are intended to show how the findings of this thesis can be integrated into, and challenge, existing understanding of the region. The six scenarios are:

1. Increased basal melting leads to more intense iron supply and thus more intense phytoplankton blooms

2. Increased basal melting leads to stronger coastal current and less efficient biological uptake of iron
3. Increased basal melting and reduced sea ice cover leads to more intense springtime ventilation of carbon
4. Earlier sea ice retreat leads to earlier bloom peak and lower integrated production
5. Earlier sea ice retreat leads to shift in phytoplankton community composition
6. Local atmospheric forcing dictates biological response of Amundsen Sea Polynya

In the following, each scenario is described using evidence from the modelling presented in this thesis, as well as challenged based on other lines of evidence in the existing literature. The uncertainty inherent in each of these scenarios illustrates the need for continued work on coastal polynya processes, incorporating both new modelling developments and new observational technologies.

7.2.1 Scenario I: Increased basal melting leads to more intense iron supply and thus more intense phytoplankton blooms

If Circumpolar Deep Water continues to warm, and prevailing conditions at the continental shelf break continue to favour strong Ekman pumping, then basal melt rates around the Amundsen Sea can be expected to continue their increasing trend. In this case, the enhanced supply of iron to the coastal current, driven by the meltwater pump (Section 5.4, see also St-Laurent et al. (2019)) would further offset losses of iron over the development of the bloom. This in turn could drive an increase in annual primary production in the ASP and PIP, potentially strengthening the biological carbon sink in the Amundsen Sea (Section 6.5).

However the results of Lee et al. (2017) demonstrate that the same CDW-driven basal melting which supplies iron to the polynya via the meltwater pump also acts to weaken the export efficiency of Amundsen Sea phytoplankton blooms. Thus it is conceivable that increases in chlorophyll, which would be observable by satellite, might not imply increases in carbon sequestration. Furthermore, Park et al. (2019) show that there is in fact a (weak) decreasing trend in Amundsen Sea surface chlorophyll over recent years, despite the concurrent observations of rapid ice shelf thinning.

In the longer term, significant uncertainties remain over the potential for collapse of ice shelves in the Amundsen Sea sector, which could impact the overturning capacity of the meltwater pump. The results presented in Section 5.3 indicate that ice shelf morphology, and thus the position of the grounding line, play a dominant role in controlling the strength of the meltwater pump (Bett, 2021; Oliver et al., 2020). A deeper-grounded ice shelf could be expected to drive a stronger buoyancy overturning circulation in the short term, though such a deepening in the future may anyway herald the start of wider ice sheet collapse (Pollard and DeConto, 2009), with more dramatic and unpredictable impacts on coastal polynyas.

7.2.2 Scenario II: Increased basal melting leads to stronger coastal current and less efficient biological uptake of iron

If an increase in CDW-driven melt is associated with a more buoyant and faster flowing meltwater outflow, then this could result in a strengthening of the coastal current (Section 5.4, see also Kimura et al. (2017); Moorman et al. (2020). This stronger coastal current, with high concentrations of iron, would likely see a local increase in primary production. However, since this coastal current is already strongly light-limited (Section 4.4), this local increase in primary production would be unlikely to compensate for the reduced dispersal of iron to the centre of the polynya, where iron is most limiting.

The investigations detailed here indicate that self-shading by chlorophyll can be the major driver of phytoplankton light limitation in the Amundsen Sea. However if the coastal current becomes sufficiently concentrated with glacial and sediment particles, then this matter may in turn have a non-negligible impact on light attenuation, thus further weakening the capacity of phytoplankton to utilise iron.

Numerous modelling studies (Moorman et al., 2020; Silvano et al., 2020) indicate that the coastal current from the Amundsen Sea transports freshwater into the Ross Sea. Evidence suggests a similar coastal current drives iron supply in the Weddell Sea (Dinniman et al., 2020). However, given the relatively short residence time scale of dissolved iron (Sieber et al., 2021), it is unclear whether unused iron from the Amundsen Sea could become an important driver of NPP in the Ross Sea.

7.2.3 Scenario III: Increased basal melting and reduced sea ice cover lead to more intense springtime ventilation of carbon

If the current decreasing trend in Amundsen Sea sea ice cover continues then this will allow for increased air-sea gas exchange in the future. At the same time, an increase in the strength of the meltwater pump will bring more DIC to the surface (Mu et al., 2014), especially in the coastal current where sea ice retreats earliest. This could drive an increase in springtime (October) outgassing close to ice shelves (Section 6.5).

Large scale modelling projects an increasingly large role for the biological pump in driving carbon fluxes as anthropogenic climate change progresses (Hauck and Völker, 2015). However Shadwick et al. (2021) found that, along the WAP, this increased outgassing, outside of the phytoplankton growth season, can outweigh the uptake from increased biological production.

A further complication, not included in this thesis, is the contribution of sea ice meltwater to the near-surface carbon budget (Hauri et al., 2015; Rosso et al., 2017). Dilution by sea ice meltwater could serve to slow springtime outgassing, although the strong sea ice export in productive polynyas suggests that this will be a smaller effect than the enhancement of DIC concentrations at the start of winter when sea ice advances.

7.2.4 Scenario IV: Earlier sea ice retreat leads to earlier bloom peak and lower integrated production

If sea ice retreats earlier, this will also provide an earlier alleviation of light limitation for phytoplankton. Since light limitation is the dominant control on early bloom development (Section 4.4, see also Arrigo et al. (2017) in the Peninsula region), this could lead to an earlier bloom peak. Although in the idealised domain this leads to an overall increase in primary production, other studies have indicated that earlier blooms can lead to a decrease in overall bloom production by lowering the peak intensity of the bloom (Schultz et al., 2021). Furthermore, a reduction in wintertime sea ice cover could have a negative effect on entrainment of nutrients into the mixed layer to fuel spring growth (Venables et al., 2013). In Section 6.5, the realistic model seems to show weaker biological export of carbon in summer months which follow an anomalously early sea ice retreat.

A large change in bloom phenology could also leave the ice shelf more exposed to solar heating in midsummer, with earlier sea ice retreat thus tending to promote stronger Mode III basal melting (see Section 6.4). At the same time, a less chlorophyll-saturated, and therefore cooler, midsummer sea surface would promote greater solubility of CO_2 and thus increased midsummer carbon uptake.

However Alderkamp et al. (2015) question the applicability of the carrying capacity hypothesis to the Amundsen Sea. Similarly in Chapter 4 of this thesis it is demonstrated that the carrying capacity hypothesis is likely invalid outside of a narrow border region between the iron-rich meltwater plume and the iron-poor centre of the polynya. Within the plume, where there is a sufficiently high rate of iron re-supply to the euphotic zone, a longer growing season could support an increase in overall primary production. Potentially, this could be in the form of multiple distinct blooms, limited by different factors, as reported within a sensible heat polynya in the Weddell Sea (von Berg et al., 2020).

7.2.5 Scenario V: Earlier sea ice retreat leads to shift in phytoplankton community composition

Aside from impacts on bulk bloom production and ocean colour, increased melt rate and earlier sea ice retreat could change the balance of competition between different phytoplankton species in the Amundsen Sea. From Section 5.4, it seems that diatoms are likely to be better placed to take advantage of these altered conditions compared to *p. antarctica*, as the former are more responsive to increases in light and iron supply. Therefore in the future diatoms could be expected to be increasingly dominant, which in turn would imply greater silica utilisation in coastal waters.

This increase in silica uptake and export in coastal polynyas would reduce the silica content of northwards flowing intermediate waters, increasing the potential for silica limitation in the open Southern Ocean. This in turn would reduce the ability of diatoms to compete with coccolithophores at lower latitudes in the Southern ocean.

Burson et al. (2019) demonstrated that, regardless of iron limitation, different phytoplankton species can occupy different niches in a fluctuating light environment. In Section 4.3 it was shown that a balance between mixing time scales and photo-adaptation time scales controls the vertical bio-optical structure within the bloom. Therefore it is possible that differences in photo-adaptation time scales could play a role in the competition between diatoms and *p. antarctica*. However, as emphasized in Lee et al. (2021), the Amundsen Sea hosts a diverse assemblage of diatoms with different bio-optical and physiological properties, with competition between different diatom species potentially as important as that with *p. antarctica*.

7.2.6 Scenario VI: Local atmospheric forcing dictates biological response of Amundsen Sea Polynya

In the future, changes in local atmospheric circulation could impact the ASP and PIP in at least three distinct ways. Firstly, Park et al. (2017) suggested that cloud cover is a first-order control on primary production by phytoplankton. Secondly, as shown in Section 5.4 the (sub-dominant) Mode III melting which takes place under Dotson Ice Shelf may respond quadratically to changes in shortwave irradiance (and therefore cloud cover). Thirdly, Djoumna and Holland (2021) argued that localised atmospheric warming events may become increasingly significant drivers of ice shelf melting in the future, potentially exceeding oceanic drivers.

Based on all these factors, future changes in Amundsen Sea biogeochemistry could be decoupled from the CDW-forced basal melting which is hitherto assumed to control NPP. The modelling of Leung et al. (2015) predicted that changes to cloud cover would be a major driver of changes to primary production only at lower latitudes in the Southern Ocean, though their analysis did not consider the potential impact of shortwave radiation on ice shelf melt rates.

Overall, the most immediate control on both the physics and biology of the Amundsen Sea coastline is the Thwaites Fast Ice Tongue (TFIT). As discussed by Stammerjohn et al. (2015), there is variability and unpredictability inherent in TFIT. It is not fully understood what drives changes in the TFIT, but it is likely that the collapse of this feature would mean the disappearance of the ASP - certainly, it would then require a far greater sensible heat component in order to compensate for the influx of advected sea ice. In this case, both oceanic and atmospheric drivers become irrelevant in driving the ASP phytoplankton bloom, even if the bloom is light-limited, since sea ice is the primary control on light limitation. Similar considerations must be applied when modelling other latent heat polynyas that are dependent on an unstable topographic feature for their formation.

7.3 Wider Implications for Antarctica, the Southern Ocean and beyond

Strong seasonal blooms are observed in front of ice shelves of all melting modes (Arrigo and van Dijken, 2003). However the scenarios outlined above for the Amundsen Sea cannot be mapped directly onto other locations along the Antarctic coastline. This is due to the high levels of zonal asymmetry in the high-latitude Southern Ocean (see Chapter 3). Whereas in the present-day Amundsen Sea the dominance of Mode II melting makes CDW a strong control on ice shelf melt rates, this is not the case for many other Antarctic ice shelves (Jacobs et al., 1992, 2012; Silvano et al., 2016). Whilst changes to CDW are likely to drive increased basal melting in the Amundsen Sea, it is uncertain that they will drive such responses elsewhere. Furthermore, results pertaining to latent heat polynyas in this thesis raise important questions about the dynamics of sensible heat polynyas, and about the future of nutrient export from the Southern Ocean to lower latitudes.

7.3.1 Mode I melting

Mode I melting is not directly sensitive to CDW intrusions, as it relies instead on the downwards mixing of cold, saline surface waters to depths where they are above the local freezing temperature. At the same time, ice shelves such as Ross Ice Shelf that are characterised by deep convection and Mode I melting are not in general large factors in the supply of iron to phytoplankton (Dinniman et al., 2020). For both these reasons, Scenario I, whereby changes to CDW drive increased basal melt rate and thus greater productivity, is unlikely to be applicable to Mode I-dominated ice shelves.

Meanwhile, the meltwater-driven strengthening of coastal currents described in Scenario II has different impacts on Mode I and Mode II ice shelves (Moorman et al., 2020). Whereas in the Amundsen Sea, there may be a negative feedback on further melting, in the Ross Sea this feedback is likely to be positive. Greater concentrations of low salinity, meltwater-enriched waters on the continental shelf have the potential to reduce dense shelf water formation, and thus enhance intrusions of CDW. What such a shift would mean for overall iron supply is highly uncertain, but the argument in Scenario II around lower uptake efficiency does not necessarily apply beyond Mode II-dominated systems.

Scenarios III - V are contingent on a trend of decreasing sea ice, as has recently been observed in the Amundsen, Bellingshausen and Weddell Seas. However an increasing trend of sea ice has been reported in the Ross Sea, so that the pressures on phytoplankton bloom timing, carbon fluxes and community composition are likely different to those in the Mode II-dominated Amundsen Sea.

Finally, though the modelling in this thesis does not explicitly represent Mode I melting, Section 6.5 does indicate that where convection occurs, the impact of ocean colour on deep ocean conditions - including under ice shelves - is enhanced. Much more work, both observations and modelling, is required to investigate how ocean colour impacts ice shelves such as Ross Ice Shelf.

7.3.2 Mode III melting

During Mode III melting, seasonally-warmed surface waters are transported under-shelf and lead to melting of ice-shelf fronts (Silvano et al., 2016). As with Mode I, the direct influence of CDW intrusions is reduced compared to Mode II. The role of Mode III melting in supplying iron to coastal polynyas has not been studied extensively; however there is some evidence of Mode III melting playing a role in iron fertilisation adjacent to the Amery Ice Shelf in East Antarctica (Herraiz-Borreguero et al., 2016).

As shown in Chapter 6, particularly for the idealised ASP domain in 6.3, Mode III melting is substantially more sensitive to changes in ocean colour compared to Mode II. Where summertime solar heating causes substantial near-surface melting, as in the Ross Sea (Stewart et al., 2019), it is likely that phytoplankton blooms are an important control on the flux of heat available for melting. A substantial decrease in chlorophyll production close to the front of Ross Ice Shelf would be expected to lead to substantially increased near-surface melting. If this enhanced melting occurs in a location important for ice-shelf buttressing, it may also be an important driver of ice sheet loss (Reese et al., 2018; Stewart et al., 2019). Thus more work on the coupling between biology and Mode III melting is critically important.

7.3.3 Sensible heat polynyas

As discussed in Chapter 6, latent heat polynyas are relatively insensitive to variability in ocean temperature, since the impetus for their formation comes from the combination of strong winds driving sea ice export and topographic features blocking sea ice import. In contrast, the formation of sensible heat polynyas is predominantly a function of thermodynamics.

Phytoplankton blooms can substantially alter ocean colour within sensible heat polynyas (Jena and Pillai, 2020), and, as for productive latent heat polynyas, modify the upper ocean heat budget. Unlike latent heat polynyas, changes to the heat budget would likely impact the sea ice budget. An increase in sea surface temperature due to chlorophyll could promote greater expansion of the polynya in summer, as well as delaying the contraction of the polynya in winter. However it is also possible that this same increase in surface temperature could increase stratification in such a way as to reduce both the upwelling of heat and the supply of nutrients (for instance iron and silica) from below to the euphotic zone (Prend et al., 2019).

Trends in sensible heat polynyas are in general harder to observe compared to latent heat polynyas, and both are difficult to model (Mohrmann et al., 2021). Although von Berg et al. (2020) find that a longer growing season can give rise to distinct light and iron limited phytoplankton blooms, it remains uncertain what effect this has on community composition and on air-sea carbon fluxes.

7.3.4 Lower latitudes

Highly productive Antarctic polynyas, including those in the Amundsen Sea, are sinks for macronutrients - nitrate and phosphate - as well as micronutrients - iron and silica. These nutrients are brought from the ACC onto the continental shelf via CDW, and then are brought to the surface via the meltwater pump.

The extent to which nitrate, phosphate and silicic acid are depleted in the ASP and PIP is largely a function of the limits which iron and light put on phytoplankton growth. The analysis presented in Section 4.4 of this thesis demonstrates that changes to euphotic depth, mediated by phytoplankton self-shading, have impacts on macronutrient concentrations deeper in the water column. Where high concentrations of chlorophyll - or any other optically active water constituent - lead to shallower euphotic depths, the size of the sink is reduced, both for macronutrients and micronutrients.

In the iron-limited Amundsen Sea, summertime primary production always leaves an excess of nitrate, phosphate and silicic acid, which then gets transported northwards along the thermocline (Gruber et al., 2019; Sarmiento et al., 1998). In the Ross Sea, these excess nutrients may instead be sequestered in Antarctic Bottom Water (Marinov et al., 2006). Therefore the size of phytoplankton blooms in coastal polynyas has an impact on nutrient availability at lower latitudes. In particular, any increase in Amundsen Sea primary production - such as in Scenario I - could contribute to reduced phytoplankton growth at lower latitudes. Conversely, a decrease in Amundsen Sea primary production - such as in Scenarios II & IV - could contribute to enhanced phytoplankton growth at lower latitudes. If such changes were to occur only in the Amundsen Sea, then the global impact might be small, but if replicated elsewhere around Antarctica the combined impact could be substantial.

7.4 Priorities for future research

It is increasingly clear that the Antarctic coastline is highly asymmetric in many respects, including response to climate. Thus there is an ongoing role for regional models which focus on specific areas of the continental shelf, with boundary conditions taken from larger low resolution models. At the same time, there is an increasing quantity of high resolution palaeoenvironmental data coming from the Amundsen Sea and other coastal polynya-forming re-

gions of the Southern Ocean. One aim for future regional modelling should be to run over long enough time scales that results can be verified not just against sediment traps but against sediment cores as well. Projecting forwards to the future, there is a need to model phytoplankton blooms under the conditions of ice sheet retreat predicted in IPCC reports.

This thesis has proved that BLING can be used to model primary production at a multitude of spatial scales. It would be instructive also to run a higher complexity model such as DARWIN in the Amundsen Sea, in particular to examine how changes in the cryosphere drive changes in phytoplankton community composition. Furthermore, there are new questions emerging as to the role of marine viruses in phytoplankton bloom termination (Biggs et al., 2021). These should be investigated in future observations of the Amundsen Sea and, if possible, parameterized as drivers of phytoplankton loss in models.

Since Martin et al. (1990), iron limitation has been implicated as a key control on Southern Ocean productivity, and thus on the overall partitioning of carbon dioxide between the atmosphere and oceans. Quantifying the current degree of iron limitation, and representing it in models, requires three factors to be considered: external sources of iron, bio-availability of that iron, and the requirement for iron from phytoplankton communities. This is represented in Figure 7.1.

This thesis has demonstrated the key role that ice shelves play in bringing iron to the surface of Amundsen Sea polynyas, and has shown that, where meltwater-enriched waters reach the surface, the steady resupply of iron substantially delays the onset of iron limitation in phytoplankton blooms. Both the extent of this iron limitation, and where it occurs, has been shown to be highly sensitive to the flux of heat arriving at the ice shelf. On a macroscopic scale, this is a function of the depth of the thermocline which separates CDW from cooler waters above, and it is important to investigate further the observed variability in thermocline depth. On a microscopic scale, heat fluxes depends on boundary-layer processes, which are parameterized in models via heat exchange coefficients. This thesis suggests that continued tuning of these coefficients is necessary not only to represent changes in the cryosphere, but also to capture biogeochemical responses.

Another factor which may play both a direct and indirect role in driving iron supply to phytoplankton is subglacial hydrology. Wadham et al. (2013) proposed that subglacial run-off could be a large source of iron, potentially outweighing that from basal melting. However the chemistry of this iron source remains largely undetermined and thus difficult to include in models. At the same time, subglacial plumes can impact the meltwater pump by enhancing buoyancy forcing, and thus have an indirect impact on iron supply. The bio-availability of particulate iron, including from subglacial sources, remains highly uncertain, whilst the bio-availability of dissolved iron is known to depend on speciation through redox chemistry. The balance between Fe^{2+} and Fe^{3+} is a function of temperature and of pH, and thus is sensitive to ongoing climate change (Hutchins and Boyd, 2016).

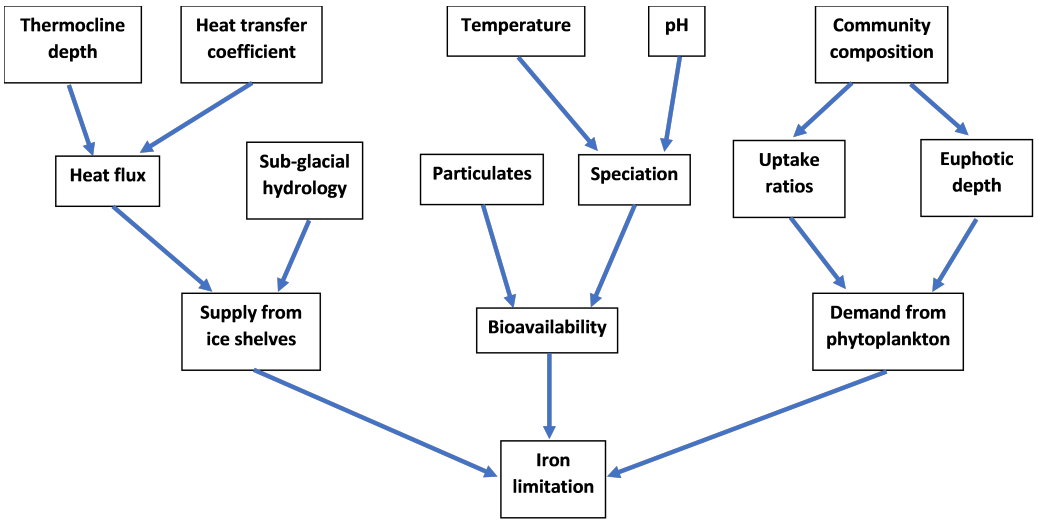

Figure 7.1: Factors dictating the degree of iron limitation in the ASP and other similar coastal polynyas around Antarctica.

As shown in this thesis, the phytoplankton demand for iron changes according to the vertical extent of the bloom - dictated by the euphotic depth - and according to the rate at which cells take up iron early in the bloom development. The balance of species in the phytoplankton bloom influences both these factors. A shift in the community composition can alter shortwave attenuation, thus changing the euphotic depth, as well as changing the ratio of nitrogen to iron uptake. The original use of BLING by Galbraith et al. (2010) was to compare direct and indirect forms of iron-light colimitation. In the future, BLING, and other biogeochemical models, should be used to investigate comprehensively the relative importance of iron supply, bioavailability and demand in dictating the size of the Southern Ocean carbon sink. Similarly, whilst Galbraith et al. (2015) compared the performance of biogeochemical models on a global domain, a similar analysis is required for meltwater-influenced coastal polynyas. Such an intercomparison project should include BLING as well as models less complex, such as the DIC package, and more complex, such as DARWIN.

Finally, if the role of phytoplankton blooms within the earth system is to be fully understood, then more work is required to quantify their contribution to polynya heat budgets. Currently there remains large uncertainty both in the size to the chlorophyll contribution and in its importance relative to other water constituents, including the glacial sediment sourced from ice shelves. It is critically important to understand if, and how, biologically forced changes to ocean colour impact on ice shelf melting, water mass formation and sea ice cover.

Chapter 8

Conclusion

Since Martin et al. (1991) first identified iron as a key driver of Southern Ocean carbon fluxes, broader scientific understanding of ocean and climate has increased immeasurably. With anthropogenic climate change set to continue and accelerate, it has never been more important to investigate the delicate interplay between marine physics, chemistry and biology, especially in the polar oceans.

To that end, this thesis has set out to model some of the largest and most climate-sensitive phytoplankton blooms seen in the Southern Ocean. This modelling was expected to demonstrate the important role that ice shelves play in generating the conditions necessary for phytoplankton growth in the Amundsen Sea. However this thesis has shown the connections between ice shelves and phytoplankton blooms to be richer and more intricate than previously assumed.

Throughout this thesis, modelling demonstrated that ice shelves act to pull iron and carbon enriched water from depth to the surface. Wherever this water meets a gap in the sea ice – a polynya – strong phytoplankton blooms can occur. This meltwater pump mechanism dictates the lateral distribution of phytoplankton, and where the bloom is focused; whilst the iron-to-nitrogen uptake ratio dictates the level of depletion within the bloom, and thus the timing of bloom decline. Iron limitation also varies with depth, and this depth-dependence in turn changes in response to changes in light attenuation due to chlorophyll. Meanwhile the onset of the bloom is dictated not by iron availability but by the retreat of sea ice and the subsequent increase in light reaching the upper ocean. Importantly, model results revealed that the complex interplay between iron and light limitation could in some cases prevent stronger ice shelf melt rates from leading to stronger NPP, thereby casting doubt on projections that high latitude productivity will increase in the future due to accelerated basal melting.

The primary methodological advances in the course of this thesis have been in modelling the relationship between light and chlorophyll. Though not yet included in BLING, the parameterization of phytoplankton photoacclimation shown early in this thesis offers a potential route for Eulerian modelling to incorporate results from Lagrangian experiments; the importance of photoacclimation in community structure and carbon export within phytoplankton blooms

remains to be examined in future studies. Conversely, this thesis successfully took an existing parameterization of the phytoplankton self-shading effect, and implemented it for the first time within MITgcm-BLING. The outcome was a more accurate representation of coastal phytoplankton blooms, and of their impacts on nutrient drawdown.

These results in turn suggested the next avenue of investigation, regarding the impact of ocean colour on ocean physics. The same self-shading parameterization was extended to impact the heat budget as well as the light environment; the first time this effect had been examined in the context of Southern Ocean phytoplankton blooms. Surprisingly, results showed a small impact of chlorophyll-induced heating on sea ice cover, but a substantial impact on basal melting, with phytoplankton blooms acting to partially insulate ice shelves from solar heating.

Currently the Southern Ocean Carbon and Climate Observations and Modelling (SOCCOM) project is deepening understanding of large scale heat and carbon fluxes within the Southern Ocean, whilst projects such as the International Thwaites Glacier Collaboration (ITGC) are revealing the rapid change underway around the Antarctic margin. In the future, continued and expanded cooperation between these two fields of research will be vital in making an accurate assessment of how coastal polynyas both affect, and are affected by, regional and global climate change.

Bibliography

Alderkamp, A.-C., Mills, M. M., van Dijken, G. L., Laan, P., Thuróczy, C.-E., Gerringa, L. J., de Baar, H. J., Payne, C. D., Visser, R. J., Buma, A. G., et al. (2012). Iron from melting glaciers fuels phytoplankton blooms in the amundsen sea (southern ocean): Phytoplankton characteristics and productivity. *Deep Sea Research Part II: Topical Studies in Oceanography*, 71:32–48.

Alderkamp, A.-C., van Dijken, G. L., Lowry, K. E., Connelly, T. L., Lagerström, M., Sherrell, R. M., Haskins, C., Rogalsky, E., Schofield, O., Stammerjohn, S. E., et al. (2015). Fe availability drives phytoplankton photosynthesis rates during spring bloom in the amundsen sea polynya, antarctica. *Elem Sci Anth*, 3.

Anderlini, E., Salavasidis, G., Harris, C. A., Wu, P., Lorenzo, A., Phillips, A. B., and Thomas, G. (2021). A remote anomaly detection system for slocum underwater gliders. *Ocean Engineering*, 236:109531.

Arrigo, K. R., DiTullio, G. R., Dunbar, R. B., Robinson, D. H., VanWoert, M., Worthen, D. L., and Lizotte, M. P. (2000). Phytoplankton taxonomic variability in nutrient utilization and primary production in the ross sea. *Journal of Geophysical Research: Oceans*, 105(C4):8827–8846.

Arrigo, K. R., Lowry, K. E., and van Dijken, G. L. (2012). Annual changes in sea ice and phytoplankton in polynyas of the amundsen sea, antarctica. *Deep Sea Research Part II: Topical Studies in Oceanography*, 71:5–15.

Arrigo, K. R., van Dijken, G., and Long, M. (2008). Coastal southern ocean: A strong anthropogenic co2 sink. *Geophysical Research Letters*, 35(21).

Arrigo, K. R. and van Dijken, G. L. (2003). Phytoplankton dynamics within 37 antarctic coastal polynya systems. *Journal of Geophysical Research: Oceans*, 108(C8).

Arrigo, K. R., van Dijken, G. L., Alderkamp, A.-C., Erickson, Z. K., Lewis, K. M., Lowry, K. E., Joy-Warren, H. L., Middag, R., Nash-Arrigo, J. E., Selz, V., et al. (2017). Early spring phytoplankton dynamics in the western antarctic peninsula. *Journal of Geophysical Research: Oceans*, 122(12):9350–9369.

Arrigo, K. R., van Dijken, G. L., and Strong, A. L. (2015). Environmental controls of marine productivity hot spots around antarctica. *Journal of Geophysical Research: Oceans*, 120(8):5545–5565.

Barbraud, C., Rolland, V., Jenouvrier, S., Nevoux, M., Delord, K., and Weimerskirch, H. (2012). Effects of climate change and fisheries bycatch on southern ocean seabirds: a review. *Marine Ecology Progress Series*, 454:285–307.

Barletta, V. R., Bevis, M., Smith, B. E., Wilson, T., Brown, A., Bordoni, A., Willis, M., Khan, S. A., Rovira-Navarro, M., Dalziel, I., et al. (2018). Observed rapid bedrock uplift in amundsen sea embayment promotes ice-sheet stability. *Science*, 360(6395):1335–1339.

Beaird, N. L., Straneo, F., and Jenkins, W. (2018). Export of strongly diluted greenland meltwater from a major glacial fjord. *Geophysical Research Letters*, 45(9):4163–4170.

Bernardello, R., Marinov, I., Palter, J. B., Galbraith, E. D., and Sarmiento, J. L. (2014). Impact of weddell sea deep convection on natural and anthropogenic carbon in a climate model. *Geophysical Research Letters*, 41(20):7262–7269.

Bertrand, E. M., Saito, M. A., Rose, J. M., Riesselman, C. R., Lohan, M. C., Noble, A. E., Lee, P. A., and DiTullio, G. R. (2007). Vitamin b12 and iron colimitation of phytoplankton growth in the ross sea. *Limnology and Oceanography*, 52(3):1079–1093.

Bett, D. (2021). *Modelling the freshwater balance and influence of icebergs in the Amundsen Sea, Antarctica*. PhD thesis, University of Southampton.

Bett, D. T., Holland, P. R., Naveira Garabato, A. C., Jenkins, A., Dutrieux, P., Kimura, S., and Fleming, A. (2020). The impact of the amundsen sea freshwater balance on ocean melting of the west antarctic ice sheet. *Journal of Geophysical Research: Oceans*, 125(9):e2020JC016305.

Biggs, T. E., Huisman, J., and Brussaard, C. P. (2021). Viral lysis modifies seasonal phytoplankton dynamics and carbon flow in the southern ocean. *The ISME Journal*, pages 1–8.

Borowitzka, M. A., Beardall, J., Raven, J. A., et al. (2016). *The physiology of microalgae*, volume 6. Springer.

Boyd, P. W., Jickells, T., Law, C., Blain, S., Boyle, E., Buesseler, K., Coale, K., Cullen, J., De Baar, H. J., Follows, M., et al. (2007). Mesoscale iron enrichment experiments 1993-2005: synthesis and future directions. *science*, 315(5812):612–617.

Briggs, E. M., Martz, T. R., Talley, L. D., Mazloff, M. R., and Johnson, K. S. (2018). Physical and biological drivers of biogeochemical tracers within the seasonal sea ice zone of the southern ocean from profiling floats. *Journal of Geophysical Research: Oceans*, 123(2):746–758.

Brooks, C. M., Crowder, L. B., Österblom, H., and Strong, A. L. (2020). Reaching consensus for conserving the global commons: The case of the ross sea, antarctica. *Conservation Letters*, 13(1):e12676.

Browning, T. J., Achterberg, E. P., Engel, A., and Mawji, E. (2021). Manganese co-limitation of phytoplankton growth and major nutrient drawdown in the southern ocean. *Nature communications*, 12(1):1–9.

Burson, A., Stomp, M., Mekkes, L., and Huisman, J. (2019). Stable coexistence of equivalent nutrient competitors through niche differentiation in the light spectrum. *Ecology*, 100(12):e02873.

Cape, M. R., Straneo, F., Beaird, N., Bundy, R. M., and Charette, M. A. (2019). Nutrient release to oceans from buoyancy-driven upwelling at greenland tidewater glaciers. *Nature Geoscience*, 12(1):34–39.

Caron, D. A., Dennett, M. R., Lonsdale, D. J., Moran, D. M., and Shalapyonok, L. (2000). Microzooplankton herbivory in the ross sea, antarctica. *Deep Sea Research Part II: Topical Studies in Oceanography*, 47(15-16):3249–3272.

Carranza, M. M., Gille, S. T., Franks, P. J., Johnson, K. S., Pinkel, R., and Girton, J. B. (2018). When mixed layers are not mixed. storm-driven mixing and bio-optical vertical gradients in mixed layers of the southern ocean. *Journal of Geophysical Research: Oceans*, 123(10):7264–7289.

Carvalho, F., Fitzsimmons, J. N., Couto, N., Waite, N., Gorbunov, M., Kohut, J., Oliver, M. J., Sherrell, R. M., and Schofield, O. (2020). Testing the canyon hypothesis: evaluating light and nutrient controls of phytoplankton growth in penguin foraging hotspots along the west antarctic peninsula. *Limnology and Oceanography*, 65(3):455–470.

Chamberlain, P. M., Talley, L. D., Mazloff, M. R., Riser, S. C., Speer, K., Gray, A. R., and Schwartzman, A. (2018). Observing the ice-covered weddell gyre with profiling floats: Position uncertainties and correlation statistics. *Journal of Geophysical Research: Oceans*, 123(11):8383–8410.

Charlson, R. J., Lovelock, J. E., Andreae, M. O., and Warren, S. G. (1987). Oceanic phytoplankton, atmospheric sulphur, cloud albedo and climate. *Nature*, 326(6114):655–661.

Cortese, G. and Gersonde, R. (2007). Morphometric variability in the diatom fragilariopsis kerguelensis: Implications for southern ocean paleoceanography. *Earth and Planetary Science Letters*, 257(3-4):526–544.

Cristofari, R., Liu, X., Bonadonna, F., Cherel, Y., Pistorius, P., Le Maho, Y., Raybaud, V., Stenseth, N. C., Le Bohec, C., and Trucchi, E. (2018). Climate-driven range shifts of the king penguin in a fragmented ecosystem. *Nature Climate Change*, 8(3):245–251.

De Jong, J., Schoemann, V., Lannuzel, D., Croot, P., de Baar, H., and Tison, J.-L. (2012). Natural iron fertilization of the atlantic sector of the southern ocean by continental shelf sources of the antarctic peninsula. *Journal of Geophysical Research: Biogeosciences*, 117(G1).

Dinniman, M. S., St-Laurent, P., Arrigo, K. R., Hofmann, E. E., and van Dijken, G. L. (2020). Analysis of iron sources in antarctic continental shelf waters. *Journal of Geophysical Research: Oceans*, 125(5):e2019JC015736.

Dittrich, R. (2020). *Cycling of dissolved and particulate organic matter in the ocean west of the Antarctic Peninsula*. PhD thesis, University of Edinburgh.

Djoumna, G. and Holland, D. (2021). Atmospheric rivers, warm air intrusions, and surface radiation balance in the amundsen sea embayment. *Journal of Geophysical Research: Atmospheres*, page e2020JD034119.

Dove, L. A., Thompson, A. F., Balwada, D., and Gray, A. R. (2021). Observational evidence of ventilation hotspots in the southern ocean. *Journal of Geophysical Research: Oceans*, 126(7):e2021JC017178.

Ducklow, H. W., Yager, P. L., Sherrell, R. M., Lowry, K. E., Lee, S. H., Erickson, M., Stammerjohn, S. E., Post, A. F., and Wilson, S. E. (2015). Particle flux on the continental shelf in the amundsen sea polynya and western antarctic peninsula.

Dunne, J. P., Armstrong, R. A., Gnanadesikan, A., and Sarmiento, J. L. (2005). Empirical and mechanistic models for the particle export ratio. *Global Biogeochemical Cycles*, 19(4).

Dunne, J. P., John, J. G., Shevliakova, E., Stouffer, R. J., Krasting, J. P., Malyshev, S. L., Milly, P., Sentman, L. T., Adcroft, A. J., Cooke, W., et al. (2013). Gfdl's esm2 global coupled climate–carbon earth system models. part ii: carbon system formulation and baseline simulation characteristics. *Journal of Climate*, 26(7):2247–2267.

Dutkiewicz, S., Follows, M. J., Heimbach, P., and Marshall, J. (2006). Controls on ocean productivity and air-sea carbon flux: An adjoint model sensitivity study. *Geophysical Research Letters*, 33(2).

Dutkiewicz, S., Follows, M. J., and Parekh, P. (2005). Interactions of the iron and phosphorus cycles: A three-dimensional model study. *Global Biogeochemical Cycles*, 19(1).

Dutkiewicz, S., Hickman, A., Jahn, O., Gregg, W., Mouw, C., and Follows, M. (2015). Capturing optically important constituents and properties in a marine biogeochemical and ecosystem model. *Biogeosciences*, 12(14):4447–4481.

Dutrieux, P., De Rydt, J., Jenkins, A., Holland, P. R., Ha, H. K., Lee, S. H., Steig, E. J., Ding, Q., Abrahamsen, E. P., and Schröder, M. (2014). Strong sensitivity of pine island ice-shelf melting to climatic variability. *Science*, 343(6167):174–178.

Eppley, R. W. (1972). Temperature and phytoplankton growth in the sea. *Fish. bull*, 70(4):1063–1085.

Evans, C., Brandsma, J., Meredith, M. P., Thomas, D. N., Venables, H. J., Pond, D. W., and Brussaard, C. P. (2021). Shift from carbon flow through the microbial loop to the viral shunt in coastal antarctic waters during austral summer. *Microorganisms*, 9(2):460.

Ferreira, D., Marshall, J., Bitz, C. M., Solomon, S., and Plumb, A. (2015). Antarctic ocean and sea ice response to ozone depletion: A two-time-scale problem. *Journal of Climate*, 28(3):1206–1226.

Follows, M. J., Dutkiewicz, S., Grant, S., and Chisholm, S. W. (2007). Emergent biogeography of microbial communities in a model ocean. *science*, 315(5820):1843–1846.

Follows, M. J., Ito, T., and Dutkiewicz, S. (2006). On the solution of the carbonate chemistry system in ocean biogeochemistry models. *Ocean Modelling*, 12(3-4):290–301.

Foujols, M.-A., Lévy, M., Aumont, O., and Madec, G. (2000). Opa 8.1 tracer model reference manual. *Institut Pierre Simon Laplace*, page 39.

Freeman, N. M. and Lovenduski, N. S. (2015). Decreased calcification in the southern ocean over the satellite record. *Geophysical Research Letters*, 42(6):1834–1840.

Freeman, N. M., Lovenduski, N. S., Munro, D. R., Krumhardt, K. M., Lindsay, K., Long, M. C., and Maclennan, M. (2018). The variable and changing southern ocean silicate front: insights from the cesm large ensemble. *Global Biogeochemical Cycles*, 32(5):752–768.

Galbraith, E. D., Dunne, J. P., Gnanadesikan, A., Slater, R. D., Sarmiento, J. L., Dufour, C. O., De Souza, G. F., Bianchi, D., Claret, M., Rodgers, K. B., et al. (2015). Complex functionality with minimal computation: Promise and pitfalls of reduced-tracer ocean biogeochemistry models. *Journal of Advances in Modeling Earth Systems*, 7(4):2012–2028.

Galbraith, E. D., Gnanadesikan, A., Dunne, J. P., and Hiscock, M. R. (2010). Regional impacts of iron-light colimitation in a global biogeochemical model. *Biogeosciences*, 7(3):1043–1064.

Gaspar, P., Grégoris, Y., and Lefevre, J.-M. (1990). A simple eddy kinetic energy model for simulations of the oceanic vertical mixing: Tests at station papa and long-term upper ocean study site. *Journal of Geophysical Research: Oceans*, 95(C9):16179–16193.

Geider, R., MacIntyre, H., and Kana, T. (1997). Dynamic model of phytoplankton growth and acclimation: responses of the balanced growth rate and the chlorophyll a: carbon ratio to light, nutrient-limitation and temperature. *Marine Ecology Progress Series*, 148:187–200.

Gerringa, L. J., Alderkamp, A.-C., Laan, P., Thuroczy, C.-E., De Baar, H. J., Mills, M. M., van Dijken, G. L., van Haren, H., and Arrigo, K. R. (2012). Iron from melting glaciers fuels the phytoplankton blooms in amundsen sea (southern ocean): Iron biogeochemistry. *Deep Sea Research Part II: Topical Studies in Oceanography*, 71:16–31.

Gnanadesikan, A., Emanuel, K., Vecchi, G. A., Anderson, W. G., and Hallberg, R. (2010). How ocean color can steer pacific tropical cyclones. *Geophysical Research Letters*, 37(18).

Gnanadesikan, A., Kim, G. E., and Pradal, M.-A. S. (2019). Impact of colored dissolved materials on the annual cycle of sea surface temperature: Potential implications for extreme ocean temperatures. *Geophysical Research Letters*, 46(2):861–869.

Goldberg, D. N., Smith, T. A., Narayanan, S. H., Heimbach, P., and Morlighem, M. (2020). Bathymetric influences on antarctic ice-shelf melt rates. *Journal of Geophysical Research: Oceans*, 125(11):e2020JC016370.

Gourmelen, N., Goldberg, D. N., Snow, K., Henley, S. F., Bingham, R. G., Kimura, S., Hogg, A. E., Shepherd, A., Mouginot, J., Lenaerts, J. T., et al. (2017). Channelized melting drives thinning under a rapidly melting antarctic ice shelf. *Geophysical Research Letters*, 44(19):9796–9804.

Gruber, N., Landschützer, P., and Lovenduski, N. S. (2019). The variable southern ocean carbon sink. *Annual review of marine science*, 11:159–186.

Gupta, M., Follows, M. J., and Lauderdale, J. M. (2020). The effect of antarctic sea ice on southern ocean carbon outgassing: Capping versus light attenuation. *Global Biogeochemical Cycles*, 34(8):e2019GB006489.

Haeberli, W. and Weingartner, R. (2020). In full transition: Key impacts of vanishing mountain ice on water-security at local to global scales. *Water Security*, 11:100074.

Haëntjens, N., Boss, E., and Talley, L. D. (2017). Revisiting o cean c olor algorithms for chlorophyll a and particulate organic carbon in the s outhern o cean using biogeochemical floats. *Journal of Geophysical Research: Oceans*, 122(8):6583–6593.

Hauck, J. and Völker, C. (2015). Rising atmospheric co2 leads to large impact of biology on southern ocean co2 uptake via changes of the revelle factor. *Geophysical Research Letters*, 42(5):1459–1464.

Hauck, J., Völker, C., Wang, T., Hoppema, M., Losch, M., and Wolf-Gladrow, D. A. (2013). Seasonally different carbon flux changes in the southern ocean in response to the southern annular mode. *Global Biogeochemical Cycles*, 27(4):1236–1245.

Haumann, F. A., Gruber, N., and Münnich, M. (2020a). Sea-ice induced southern ocean subsurface warming and surface cooling in a warming climate. *AGU Advances*, 1(2):e2019AV000132.

Haumann, F. A., Moorman, R., Riser, S. C., Smedsrud, L. H., Maksym, T., Wong, A. P., Wilson, E. A., Drucker, R., Talley, L. D., Johnson, K. S., et al. (2020b). Supercooled southern ocean waters. *Geophysical Research Letters*, 47(20):e2020GL090242.

Hauri, C., Doney, S. C., Takahashi, T., Erickson, M., Jiang, G., and Ducklow, H. W. (2015). Two decades of inorganic carbon dynamics along the western antarctic peninsula. *Biogeosciences Discuss*, 12:6929–6969.

Henley, S. F., Cavan, E. L., Fawcett, S. E., Kerr, R., Monteiro, T., Sherrell, R. M., Bowie, A. R., Boyd, P. W., Barnes, D. K., Schloss, I. R., et al. (2020). Changing biogeochemistry of the southern ocean and its ecosystem implications. *Frontiers in Marine Science*, 7:581.

Hernandez, O., Jouanno, J., Echevin, V., and Aumont, O. (2017). Modification of sea surface temperature by chlorophyll concentration in the atlantic upwelling systems. *Journal of Geophysical Research: Oceans*, 122(7):5367–5389.

Herraiz-Borreguero, L., Lannuzel, D., van Der Merwe, P., Treverrow, A., and Pedro, J. (2016). Large flux of iron from the amery ice shelf marine ice to prydz bay, east antarctica. *Journal of Geophysical Research: Oceans*, 121(8):6009–6020.

Hersbach, H., Bell, B., Berrisford, P., Hirahara, S., Horányi, A., Muñoz-Sabater, J., Nicolas, J., Peubey, C., Radu, R., Schepers, D., et al. (2020). The era5 global reanalysis. *Quarterly Journal of the Royal Meteorological Society*, 146(730):1999–2049.

Heywood, K. J., Biddle, L. C., Boehme, L., Dutrieux, P., Fedak, M., Jenkins, A., Jones, R. W., Kaiser, J., Mallett, H., Garabato, A. C. N., et al. (2016). Between the devil and the deep blue sea: The role of the amundsen sea continental shelf in exchanges between ocean and ice shelves. *Oceanography*, 29(4):118–129.

Hirano, D., Tamura, T., Kusahara, K., Ohshima, K. I., Nicholls, K. W., Ushio, S., Simizu, D., Ono, K., Fujii, M., Nogi, Y., et al. (2020). Strong ice-ocean interaction beneath shirase glacier tongue in east antarctica. *Nature communications*, 11(1):1–12.

Holland, D. M. and Jenkins, A. (1999). Modeling thermodynamic ice–ocean interactions at the base of an ice shelf. *Journal of Physical Oceanography*, 29(8):1787–1800.

Holland, M. M., Landrum, L., Kostov, Y., and Marshall, J. (2017). Sensitivity of antarctic sea ice to the southern annular mode in coupled climate models. *Climate Dynamics*, 49(5):1813–1831.

Hopkinson, B. M., Seegers, B., Hatta, M., Measures, C. I., Mitchell, B. G., and Barbeau, K. A. (2013). Planktonic c: Fe ratios and carrying capacity in the southern drake passage. *Deep Sea Research Part II: Topical Studies in Oceanography*, 90:102–111.

Hopwood, M. J., Carroll, D., Browning, T., Meire, L., Mortensen, J., Krisch, S., and Achterberg, E. P. (2018). Non-linear response of summertime marine productivity to increased meltwater discharge around greenland. *Nature Communications*, 9(1):1–9.

Horvat, C., Jones, D. R., Iams, S., Schroeder, D., Flocco, D., and Feltham, D. (2017). The frequency and extent of sub-ice phytoplankton blooms in the arctic ocean. *Science advances*, 3(3):e1601191.

Hughes, C. W. (2005). Nonlinear vorticity balance of the antarctic circumpolar current. *Journal of Geophysical Research: Oceans*, 110(C11).

Hutchins, D. and Boyd, P. (2016). Marine phytoplankton and the changing ocean iron cycle. *Nature Climate Change*, 6(12):1072–1079.

Jacobs, S. (2006). Observations of change in the southern ocean. *Philosophical Transactions of the Royal Society A: Mathematical, Physical and Engineering Sciences*, 364(1844):1657–1681.

Jacobs, S., Helmer, H., Doake, C., Jenkins, A., and Frolich, R. (1992). Melting of ice shelves and the mass balance of antarctica. *Journal of Glaciology*, 38(130):375–387.

Jacobs, S., Jenkins, A., Hellmer, H., Giulivi, C., Nitsche, F., Huber, B., and Guerrero, R. (2012). The amundsen sea and the antarctic ice sheet. *Oceanography*, 25(3):154–163.

Jayne, S. R., Roemmich, D., Zilberman, N., Riser, S. C., Johnson, K. S., Johnson, G. C., and Piotrowicz, S. R. (2017). The argo program: present and future. *Oceanography*, 30(2):18–28.

Jena, B. and Pillai, A. N. (2020). Satellite observations of unprecedented phytoplankton blooms in the maud rise polynya, southern ocean. *The Cryosphere*, 14(4):1385–1398.

Jenkins, A., Dutrieux, P., Jacobs, S., Steig, E. J., Gudmundsson, H., Smith, J., and Heywood, K. (2016). Decadal ocean forcing and antarctic ice sheet response: Lessons from the amundsen sea. *Oceanography*, 29.

Jenkins, A., Shoosmith, D., Dutrieux, P., Jacobs, S., Kim, T. W., Le, S. H., Ha, H. K., and Stammerjohn, S. (2018). West antarctic ice sheet retreat in the amundsen sea driven by decadal oceanic variability. *Nat. Geoscience*, 11:733–738.

Jersild, A. and Ito, T. (2020). Physical and biological controls of the drake passage pco 2 variability. *Global Biogeochemical Cycles*, 34(9):e2020GB006644.

Johnson, K. S., Plant, J. N., Coletti, L. J., Jannasch, H. W., Sakamoto, C. M., Riser, S. C., Swift, D. D., Williams, N. L., Boss, E., Haëntjens, N., et al. (2017). Biogeochemical sensor performance in the soccom profiling float array. *Journal of Geophysical Research: Oceans*, 122(8):6416–6436.

Jones, R., Renfrew, I., Orr, A., Webber, B., Holland, D., and Lazzara, M. (2016). Evaluation of four global reanalysis products using in situ observations in the amundsen sea embayment, antarctica. *Journal of Geophysical Research: Atmospheres*, 121(11):6240–6257.

Joughin, I., Shapero, D., Dutrieux, P., and Smith, B. (2021). Ocean-induced melt volume directly paces ice loss from pine island glacier. *Science Advances*, 7(43):eabi5738.

Kaufman, D. E., Friedrichs, M. A., Smith Jr, W. O., Hofmann, E. E., Dinniman, M. S., and Hemmings, J. C. (2017). Climate change impacts on southern r oss s ea phytoplankton composition, productivity, and export. *Journal of Geophysical Research: Oceans*, 122(3):2339–2359.

Kauko, H. M., Hattermann, T., Ryan-Keogh, T., Singh, A., de Steur, L., Fransson, A., Chierici, M., Falkenhaug, T., Hallfredsson, E. H., Bratbak, G., et al. (2021). Phenology and environmental control of phytoplankton blooms in the kong håkon vii hav in the southern ocean. *Frontiers in Marine Science*, 8:287.

Kida, S. and Ito, T. (2017). A lagrangian view of spring phytoplankton blooms. *Journal of Geophysical Research: Oceans*, 122(11):9160–9175.

Kim, G., Pradal, M.-A., and Gnanadesikan, A. (2015). Quantifying the biological impact of surface ocean light attenuation by colored detrital matter in an esm using a new optical parameterization. *Biogeosciences*, 12(16):5119–5132.

Kim, T.-W., Ha, H. K., Wåhlin, A., Lee, S., Kim, C.-S., Lee, J. H., and Cho, Y.-K. (2017). Is ekman pumping responsible for the seasonal variation of warm circumpolar deep water in the amundsen sea? *Continental Shelf Research*, 132:38–48.

Kimura, S., Jenkins, A., Regan, H., Holland, P. R., Assmann, K. M., Whitt, D. B., van Wessem, M., van de Berg, W. J., Reijmer, C. H., and Dutrieux, P. (2017). Oceanographic controls on the variability of ice-shelf basal melting and circulation of glacial meltwater in the amundsen sea embayment, antarctica. *Journal of Geophysical Research: Oceans*, 122(12):10131–10155.

Konfirst, M. A., Scherer, R. P., Hillenbrand, C.-D., and Kuhn, G. (2012). A marine diatom record from the amundsen sea—insights into oceanographic and climatic response to the mid-pleistocene transition in the west antarctic sector of the southern ocean. *Marine Micropaleontology*, 92:40–51.

Koppel, D. J., Whitelaw, N., Adams, M. S., King, C. K., and Jolley, D. F. (2021). The microalga phaeocystis antarctica is tolerant to salinity and metal mixture toxicity interactions. *Environmental Science: Processes & Impacts*, 23(9):1362–1375.

Kranzler, C. F., Brzezinski, M. A., Cohen, N. R., Lampe, R. H., Maniscalco, M., Till, C. P., Mack, J., Latham, J. R., Bruland, K. W., Twining, B. S., et al. (2021). Impaired viral infection and reduced mortality of diatoms in iron-limited oceanic regions. *Nature Geoscience*, 14(4):231–237.

Lamping, N., Müller, J., Esper, O., Hillenbrand, C.-D., Smith, J. A., and Kuhn, G. (2020). Highly branched isoprenoids reveal onset of deglaciation followed by dynamic sea-ice conditions in the western amundsen sea, antarctica. *Quaternary Science Reviews*, 228:106103.

Lannuzel, D., Bowie, A. R., van der Merwe, P. C., Townsend, A. T., and Schoemann, V. (2011). Distribution of dissolved and particulate metals in antarctic sea ice. *Marine Chemistry*, 124(1-4):134–146.

Lannuzel, D., Schoemann, V., De Jong, J., Pasquer, B., van der Merwe, P., Masson, F., Tison, J.-L., and Bowie, A. (2010). Distribution of dissolved iron in antarctic sea ice: Spatial, seasonal, and inter-annual variability. *Journal of Geophysical Research: Biogeosciences*, 115(G3).

Large, W. G., McWilliams, J. C., and Doney, S. C. (1994). Oceanic vertical mixing: A review and a model with a nonlocal boundary layer parameterization. *Reviews of Geophysics*, 32(4):363–403.

Lee, S., Ducklow, H. W., Schofield, O., Wahlin, A., and Meredith, M. P. (2016). International efforts to understanding of the changing antarctic climate: The kopri expedition to the amundsen sea. *Deep Sea Research II*, 123:1–144.

Lee, S., Hwang, J., Ducklow, H. W., Hahm, D., Lee, S. H., Kim, D., Hyun, J.-H., Park, J., Ha, H. K., Kim, T.-W., et al. (2017). Evidence of minimal carbon sequestration in the productive amundsen sea polynya. *Geophysical Research Letters*, 44(15):7892–7899.

Lee, Y., Jung, J., Kim, T. W., Yang, E. J., and Park, J. (2021). Phytoplankton growth rates in the amundsen sea (antarctica) during summer: The role of light. *Environmental Research*, page 112165.

Leung, S., Cabré, A., and Marinov, I. (2015). A latitudinally banded phytoplankton response to 21st century climate change in the southern ocean across the cmip5 model suite. *Biogeosciences*, 12(19):5715–5734.

Litchman, E. and Klausmeier, C. A. (2001). Competition of phytoplankton under fluctuating light. *The American Naturalist*, 157(2):170–187.

Locarnini, M., Mishonov, A., Baranova, O., Boyer, T., Zweng, M., Garcia, H., Seidov, D., Weathers, K., Paver, C., Smolyar, I., et al. (2018). World ocean atlas 2018, volume 1: Temperature.

Losch, M., Menemenlis, D., Campin, J.-M., Heimbach, P., and Hill, C. (2010). On the formulation of sea-ice models. part 1: Effects of different solver implementations and parameterizations. *Ocean Modelling*, 33(1-2):129–144.

Maher, B., Prospero, J., Mackie, D., Gaiero, D., Hesse, P. P., and Balkanski, Y. (2010). Global connections between aeolian dust, climate and ocean biogeochemistry at the present day and at the last glacial maximum. *Earth-Science Reviews*, 99(1-2):61–97.

Maldonado, M. T., Surma, S., and Pakhomov, E. A. (2016). Southern ocean biological iron cycling in the pre-whaling and present ecosystems. *Philosophical Transactions of the Royal Society A: Mathematical, Physical and Engineering Sciences*, 374(2081):20150292.

Manizza, M., Le Quéré, C., Watson, A. J., and Buitenhuis, E. T. (2005). Bio-optical feedbacks among phytoplankton, upper ocean physics and sea-ice in a global model. *Geophysical Research Letters*, 32(5).

Manizza, M., Le Quéré, C., Watson, A. J., and Buitenhuis, E. T. (2008). Ocean biogeochemical response to phytoplankton-light feedback in a global model. *Journal of Geophysical Research: Oceans*, 113(C10).

Marinov, I., Gnanadesikan, A., Toggweiler, J., and Sarmiento, J. L. (2006). The southern ocean biogeochemical divide. *Nature*, 441(7096):964–967.

Marshall, J., Adcroft, A., Hill, C., Perelman, L., and Heisey, C. (1997a). A finite-volume, incompressible navier stokes model for studies of the ocean on parallel computers. *Journal of Geophysical Research: Oceans*, 102(C3):5753–5766.

Marshall, J., Hill, C., Perelman, L., and Adcroft, A. (1997b). Hydrostatic, quasi-hydrostatic, and nonhydrostatic ocean modeling. *Journal of Geophysical Research: Oceans*, 102(C3):5733–5752.

Martin, J. H., Gordon, M., and Fitzwater, S. E. (1991). The case for iron. *Limnology and Oceanography*, 36(8):1793–1802.

Martin, J. H., Gordon, R. M., and Fitzwater, S. E. (1990). Iron in antarctic waters. *Nature*, 345(6271):156–158.

Martínez-García, A., Sigman, D. M., Ren, H., Anderson, R. F., Straub, M., Hodell, D. A., Jaccard, S. L., Eglinton, T. I., and Haug, G. H. (2014). Iron fertilization of the subantarctic ocean during the last ice age. *Science*, 343(6177):1347–1350.

Masson-Delmotte, V., Zhai, P., Pirani, A., Connors, S., Péan, C., Berger, S., Caud, N., Chen, Y., Goldfarb, L., Gomis, M., Huang, M., Leitzell, K., Lonnoy, E., Matthews, J., Maycock, T., Waterfield, T., Yelekçi, O., Yu, R., and (eds.), B. Z. (2019). Climate change 2021: The physical science basis. contribution of working group i to the sixth assessment report of the intergovernmental panel on climate change.

McClymont, E. L., Bentley, M. J., Hodgson, D. A., Spencer-Jones, C. L., Wardley, T., West, M. D., Croudace, I. W., Berg, S., Gröcke, D. R., Kuhn, G., et al. (2021). Summer sea-ice variability on the antarctic margin during the last glacial period reconstructed from snow petrel (pagodroma nivea) stomach-oil deposits. *Climate of the Past Discussions*, pages 1–39.

Meredith, M. P., Ducklow, H. W., Schofield, O., Wahlin, A., Newman, L., and Lee, S. (2016). The interdisciplinary marine system of the amundsen sea, southern ocean: Recent advances and the need for sustained observations. *Deep Sea Research II*, 123:1–6.

Middag, R., de Baar, H. J., Klunder, M. B., and Laan, P. (2013). Fluxes of dissolved aluminum and manganese to the weddell sea and indications for manganese co-limitation. *Limnology and oceanography*, 58(1):287–300.

Miles, T., Lee, S. H., Wåhlin, A., Ha, H. K., Kim, T. W., Assmann, K. M., and Schofield, O. (2016). Glider observations of the dotson ice shelf outflow. *Deep Sea Research Part II: Topical Studies in Oceanography*, 123:16 – 29. International efforts to understanding of the changing Antarctic climate: The KOPRI expedition to the Amundsen Sea.

Mohrmann, M., Heuzé, C., and Swart, S. (2021). Southern ocean polynyas in cmip6 models. *The Cryosphere Discussions*, pages 1–43.

Moore, J. K., Fu, W., Primeau, F., Britten, G. L., Lindsay, K., Long, M., Doney, S. C., Mahowald, N., Hoffman, F., and Randerson, J. T. (2018). Sustained climate warming drives declining marine biological productivity. *Science*, 359(6380):1139–1143.

Moore, J. K., Lindsay, K., Doney, S. C., Long, M. C., and Misumi, K. (2013). Marine ecosystem dynamics and biogeochemical cycling in the community earth system model [cesm1 (bgc)]: Comparison of the 1990s with the 2090s under the rcp4. 5 and rcp8. 5 scenarios. *Journal of Climate*, 26(23):9291–9312.

Moorman, R., Morrison, A. K., and McC. Hogg, A. (2020). Thermal responses to antarctic ice shelf melt in an eddy-rich global ocean–sea ice model. *Journal of Climate*, 33(15):6599–6620.

Morel, A. (1988). Optical modeling of the upper ocean in relation to its biogenous matter content (case i waters). *Journal of geophysical research: oceans*, 93(C9):10749–10768.

Morel, F. M. (2008). The co-evolution of phytoplankton and trace element cycles in the oceans. *Geobiology*, 6(3):318–324.

Morel, F. M., Hudson, R. J., and Price, N. M. (1991). Limitation of productivity by trace metals in the sea. *Limnology and oceanography*, 36(8):1742–1755.

Morlighem, M., Rignot, E., Binder, T., Blankenship, D., Drews, R., Eagles, G., Eisen, O., Ferraccioli, F., Forsberg, R., Fretwell, P., et al. (2020). Deep glacial troughs and stabilizing ridges unveiled beneath the margins of the antarctic ice sheet. *Nature Geoscience*, 13(2):132–137.

Mu, L., Stammerjohn, S., Lowry, K., and Yager, P. (2014). Spatial variability of surface pco 2 and air-sea co 2 flux in the amundsen sea polynya, antarctica. *Elem Sci Anth*, 3.

Nakayama, Y., Menemenlis, D., Schodlok, M., and Rignot, E. (2017). Amundsen and b ellingshausen s eas simulation with optimized ocean, sea ice, and thermodynamic ice shelf model parameters. *Journal of Geophysical Research: Oceans*, 122(8):6180–6195.

Nakayama, Y., Menemenlis, D., Wang, O., Zhang, H., Fenty, I., and Nguyen, A. T. (2021). Development of adjoint-based ocean state estimation for the amundsen and bellingshausen seas and ice shelf cavities using mitgcm–ecco (66j). *Geoscientific Model Development*, 14(8):4909–4924.

Nakayama, Y., Timmermann, R., Rodehacke, C. B., Schröder, M., and Hellmer, H. H. (2014). Modeling the spreading of glacial meltwater from the amundsen and bellingshausen seas. *Geophysical Research Letters*, 41(22):7942–7949.

Naughten, K. A., Holland, P. R., Dutrieux, P., Kimura, S., Bett, D. T., and Jenkins, A. (2022). Simulated twentieth-century ocean warming in the amundsen sea, west antarctica. *Geophysical Research Letters*, 49(5):e2021GL094566.

Nicolas, J. P. and Bromwich, D. H. (2011). Climate of west antarctica and influence of marine air intrusions. *Journal of Climate*, 24(1):49–67.

Nissen, C., Gruber, N., Münnich, M., and Vogt, M. (2021). Southern ocean phytoplankton community structure as a gatekeeper for global nutrient biogeochemistry. *Global Biogeochemical Cycles*, 35(8):e2021GB006991.

Nissen, C. and Vogt, M. (2021). Factors controlling the competition between *Phaeocystis* and diatoms in the southern ocean and implications for carbon export fluxes. *Biogeosciences*, 18(1):251–283.

Nissen, C., Vogt, M., Münnich, M., Gruber, N., and Haumann, F. A. (2018). Factors controlling coccolithophore biogeography in the southern ocean. *Biogeosciences*, 15(22):6997–7024.

Nitsche, F., Jacobs, S., Larter, R., and Gohl, K. (2007). Bathymetry of the amundsen sea continental shelf: Implications for geology, oceanography, and glaciology. *Geochemistry, Geophysics, Geosystems*, 8(10).

Oliver, H., Castelao, R. M., Wang, C., and Yager, P. L. (2020). Meltwater-enhanced nutrient export from greenland's glacial fjords: A sensitivity analysis. *Journal of Geophysical Research: Oceans*, 125(7):e2020JC016185.

Oliver, H., St-Laurent, P., Sherrell, R. M., and Yager, P. L. (2019). Modeling iron and light controls on the summer phaeocystis antarctica bloom in the amundsen sea polynya. *Global Biogeochemical Cycles*, 33(5):570–596.

Organelli, E., Claustre, H., Bricaud, A., Barbieux, M., Uitz, J., d'Ortenzio, F., and Dall'Olmo, G. (2017). Bio-optical anomalies in the world's oceans: An investigation on the diffuse attenuation coefficients for downward irradiance derived from biogeochemical argo float measurements. *Journal of Geophysical Research: Oceans*, 122(5):3543–3564.

Pan, B. J., Vernet, M., Reynolds, R. A., and Mitchell, B. G. (2019). The optical and biological properties of glacial meltwater in an antarctic fjord. *Plos one*, 14(2):e0211107.

Park, J., Kuzminov, F. I., Bailleul, B., Yang, E. J., Lee, S., Falkowski, P. G., and Gorbunov, M. Y. (2017). Light availability rather than fe controls the magnitude of massive phytoplankton bloom in the amundsen sea polynyas, antarctica. *Limnology and Oceanography*, 62(5):2260–2276.

Park, J., Shin, E. K., Ko, E., and Park, T. (2019). Atmospheric factors influencing biological productivity in the antarctic polynyas, derived from satellite and reanalysis data. *Remote Sensing Letters*, 10(11):1113–1122.

Parkinson, C. L. (2019). A 40-y record reveals gradual antarctic sea ice increases followed by decreases at rates far exceeding the rates seen in the arctic. *Proceedings of the National Academy of Sciences*, 116(29):14414–14423.

Paulson, C. A. and Simpson, J. J. (1977). Irradiance measurements in the upper ocean. *Journal of Physical Oceanography*, 7(6):952–956.

Pefanis, V., Losa, S. N., Losch, M., Janout, M. A., and Bracher, A. (2020). Amplified arctic surface warming and sea ice loss due to phytoplankton and colored dissolved material. *Geophysical Research Letters*, 47(21):e2020GL088795.

Pellichero, V., Sallée, J.-B., Schmidtko, S., Roquet, F., and Charrassin, J.-B. (2017). The ocean mixed layer under southern ocean sea-ice: Seasonal cycle and forcing. *Journal of Geophysical Research: Oceans*, 122(2):1608–1633.

Petrou, K., Baker, K. G., Nielsen, D. A., Hancock, A. M., Schulz, K. G., and Davidson, A. T. (2019). Acidification diminishes diatom silica production in the southern ocean. *Nature Climate Change*, 9(10):781–786.

Petty, A. A., Feltham, D. L., and Holland, P. R. (2013). Impact of atmospheric forcing on antarctic continental shelf water masses. *Journal of Physical Oceanography*, 43(5):920–940.

Petty, A. A., Holland, P. R., and Feltham, D. L. (2014). Sea ice and the ocean mixed layer over the antarctic shelf seas. *The Cryosphere*, 8(2):761–783.

Pollard, D. and DeConto, R. M. (2009). Modelling west antarctic ice sheet growth and collapse through the past five million years. *Nature*, 458(7236):329–332.

Pondaven, P., Gallinari, M., Chollet, S., Bucciarelli, E., Sarthou, G., Schultes, S., and Jean, F. (2007). Grazing-induced changes in cell wall silicification in a marine diatom. *Protist*, 158(1):21–28.

Portner, H.-O., Roberts, D., Masson-Delmotte, V., Zhai, P., Tignor, M., Poloczanska, E., Mintenbeck, K., Alegria, A., Nicolai, M., Okem, A., Petzold, J., Rama, B., and (eds.), N. W. (2019). Ipcc special report on the ocean and cryosphere in a changing climate.

Prend, C. J., Gille, S. T., Talley, L. D., Mitchell, B. G., Rosso, I., and Mazloff, M. R. (2019). Physical drivers of phytoplankton bloom initiation in the southern ocean's scotia sea. *Journal of Geophysical Research: Oceans*, 124(8):5811–5826.

Randall-Goodwin, E., Meredith, M., Jenkins, A., Yager, P., Sherrell, R., Abrahamsen, E., Guerrero, R., Yuan, X., Mortlock, R., Gavahan, K., et al. (2015). Freshwater distributions and water mass structure in the amundsen sea polynya region, antarctica. *Elementa: Science of the Anthropocene*, 3.

Raphael, M. N., Marshall, G., Turner, J., Fogt, R., Schneider, D., Dixon, D., Hosking, J., Jones, J., and Hobbs, W. R. (2016). The amundsen sea low: Variability, change, and impact on antarctic climate. *Bulletin of the American Meteorological Society*, 97(1):111–121.

Raven, J. and Waite, A. (2004). The evolution of silicification in diatoms: inescapable sinking and sinking as escape? *New phytologist*, 162(1):45–61.

Reese, R., Gudmundsson, G. H., Levermann, A., and Winkelmann, R. (2018). The far reach of ice-shelf thinning in antarctica. *Nature Climate Change*, 8(1):53–57.

Riser, S. C., Swift, D., and Drucker, R. (2018). Profiling floats in soccom: Technical capabilities for studying the southern ocean. *Journal of Geophysical Research: Oceans*, 123(6):4055–4073.

Robbins, L., Lalonde, S., Saito, M. A., Planavsky, N., Mloszewska, A., Pecoits, E., Scott, C., Dupont, C., Kappler, A., and Konhauser, K. (2013). Authigenic iron oxide proxies for marine zinc over geological time and implications for eukaryotic metallome evolution. *Geobiology*, 11(4):295–306.

Robbins, L. J., Lalonde, S. V., Planavsky, N. J., Partin, C. A., Reinhard, C. T., Kendall, B., Scott, C., Hardisty, D. S., Gill, B. C., Alessi, D. S., et al. (2016). Trace elements at the intersection of marine biological and geochemical evolution. *Earth-Science Reviews*, 163:323–348.

Rosier, S. H., Reese, R., Donges, J. F., De Rydt, J., Gudmundsson, G. H., and Winkelmann, R. (2021). The tipping points and early warning indicators for pine island glacier, west antarctica. *The Cryosphere*, 15(3):1501–1516.

Rosso, I., Mazloff, M. R., Verdy, A., and Talley, L. D. (2017). Space and time variability of the southern ocean carbon budget. *Journal of Geophysical Research: Oceans*, 122(9):7407–7432.

Rudnick, D. L., Davis, R. E., Eriksen, C. C., Fratantoni, D. M., and Perry, M. J. (2004). Underwater gliders for ocean research. *Marine Technology Society Journal*, 38(2):73–84.

Saha, S., Nadiga, S., Thiaw, C., Wang, J., Wang, W., Zhang, Q., van den Dool, H., Pan, H.-L., Moorthi, S., Behringer, D., et al. (2006). The ncep climate forecast system. *Journal of Climate*, 19(15):3483–3517.

Saito, M. A., Goepfert, T. J., and Ritt, J. T. (2008). Some thoughts on the concept of colimitation: three definitions and the importance of bioavailability. *Limnology and Oceanography*, 53(1):276–290.

Saito, M. A., Sigman, D. M., and Morel, F. M. (2003). The bioinorganic chemistry of the ancient ocean: the co-evolution of cyanobacterial metal requirements and biogeochemical cycles at the archean–proterozoic boundary? *Inorganica Chimica Acta*, 356:308–318.

Sarmiento, J. L., Hughes, T. M., Stouffer, R. J., and Manabe, S. (1998). Simulated response of the ocean carbon cycle to anthropogenic climate warming. *Nature*, 393(6682):245–249.

Sarmiento, J. L., Slater, R., Barber, R., Bopp, L., Doney, S., Hirst, A., Kleypas, J., Matear, R., Mikolajewicz, U., Monfray, P., et al. (2004). Response of ocean ecosystems to climate warming. *Global Biogeochemical Cycles*, 18(3).

Schodlok, M. P., Menemenlis, D., Rignot, E., and Studinger, M. (2012). Sensitivity of the ice-shelf/ocean system to the sub-ice-shelf cavity shape measured by nasa icebridge in pine island glacier, west antarctica. *Annals of Glaciology*, 53(60):156–162.

Schofield, O., Miles, T., Alderkamp, A.-C., Lee, S., Haskins, C., Rogalsky, E., Sipler, R., Sherrell, R. M., and Yager, P. L. (2015). In situ phytoplankton distributions in the amundsen sea polynya measured by autonomous gliders. *Elementa-Science Of The Anthropocene*, 3:1.

Schultz, C., Doney, S. C., Hauck, J., Kavanaugh, M., and Schofield, O. (2021). Modeling phytoplankton blooms and inorganic carbon responses to sea-ice variability in the west antarctic peninsula. *Journal of Geophysical Research: Biogeosciences*, 126(4):e2020JG006227.

Semtner Jr, A. J. (1976). A model for the thermodynamic growth of sea ice in numerical investigations of climate. *Journal of Physical Oceanography*, 6(3):379–389.

Shadwick, E., De Meo, O., Schroeter, S., Arroyo, M., Martinson, D., and Ducklow, H. (2021). Sea ice suppression of co2 outgassing in the west antarctic peninsula: Implications for the evolving southern ocean carbon sink. *Geophysical Research Letters*, 48(11):e2020GL091835.

Shepherd, A., Wingham, D., and Rignot, E. (2004). Warm ocean is eroding west antarctic ice sheet. *Geophysical Research Letters*, 31(23).

Sherrell, R., Lagerström, M., Forsch, K., Stammerjohn, S., and Yager, P. (2015). Dynamics of dissolved iron and other bioactive trace metals (mn, ni, cu, zn) in the amundsen sea polynya, antarctica. *Elem Sci Anth*, 3.

Sieber, M., Conway, T. M., de Souza, G., Hassler, C. S., Ellwood, M. J., and Vance, D. (2021). Isotopic fingerprinting of biogeochemical processes and iron sources in the iron-limited surface southern ocean. *Earth and Planetary Science Letters*, 567:116967.

Silvano, A., Foppert, A., Rintoul, S. R., Holland, P. R., Tamura, T., Kimura, N., Castagno, P., Falco, P., Budillon, G., Haumann, F. A., et al. (2020). Recent recovery of antarctic bottom water formation in the ross sea driven by climate anomalies. *Nature Geoscience*, 13(12):780–786.

Silvano, A., Rintoul, S. R., and Herraiz-Borreguero, L. (2016). Ocean-ice shelf interaction in east antarctica. *Oceanography*, 29(4):130–143.

Silvano, A., Rintoul, S. R., Peña-Molino, B., Hobbs, W. R., van Wijk, E., Aoki, S., Tamura, T., and Williams, G. D. (2018). Freshening by glacial meltwater enhances melting of ice shelves and reduces formation of antarctic bottom water. *Science advances*, 4(4):eaap9467.

Smetacek, V. (1985). Role of sinking in diatom life-history cycles: ecological, evolutionary and geological significance. *Marine biology*, 84(3):239–251.

Smith Jr, W. O., Sedwick, P. N., Arrigo, K. R., Ainley, D. G., and Orsi, A. H. (2012). The ross sea in a sea of change. *Oceanography*, 25(3):90–103.

Song, H., Marshall, J., Follows, M. J., Dutkiewicz, S., and Forget, G. (2016). Source waters for the highly productive patagonian shelf in the southwestern atlantic. *Journal of Marine Systems*, 158:120–128.

St-Laurent, P., Klinck, J., and Dinniman, M. (2015). Impact of local winter cooling on the melt of pine island glacier, antarctica. *Journal of Geophysical Research: Oceans*, 120(10):6718–6732.

St-Laurent, P., Yager, P. L., Sherrell, R. M., Oliver, H., Dinniman, M. S., and Stammerjohn, S. E. (2019). Modelling the seasonal cycle of iron and carbon fluxes in the amundsen sea polynya, antarctica. *Journal of Geophysical Research: Oceans*, 124(3):1544–1565.

St-Laurent, P., Yager, P. L., Sherrell, R. M., Stammerjohn, S. E., and Dinniman, M. S. (2017). Pathways and supply of dissolved iron in the amundsen sea (antarctica). *Journal of Geophysical Research: Oceans*, 122(9):7135–7162.

Stammerjohn, S., Maksym, T., Massom, R., Lowry, K., Arrigo, K., Yuan, X., Raphael, M., Randall-Goodwin, E., Sherrell, R., and Yager, P. (2015). Seasonal sea ice changes in the amundsen sea, antarctica, over the period of 1979–2014. *Elem Sci Anth*, 3.

Sterl, M. F., Delandmeter, P., and van Sebille, E. (2020). Influence of barotropic tidal currents on transport and accumulation of floating microplastics in the global open ocean. *Journal of Geophysical Research: Oceans*, 125(2):e2019JC015583.

Stewart, C. L., Christoffersen, P., Nicholls, K. W., Williams, M. J., and Dowdeswell, J. A. (2019). Basal melting of ross ice shelf from solar heat absorption in an ice-front polynya. *Nature Geoscience*, 12(6):435.

Strong, A., Chisholm, S., Miller, C., and Cullen, J. (2009). Ocean fertilization: time to move on. *Nature*, 461(7262):347–348.

Strzepek, R. F., Boyd, P. W., and Sunda, W. G. (2019). Photosynthetic adaptation to low iron, light, and temperature in southern ocean phytoplankton. *Proceedings of the National Academy of Sciences*, 116(10):4388–4393.

Strzepek, R. F. and Harrison, P. J. (2004). Photosynthetic architecture differs in coastal and oceanic diatoms. *Nature*, 431(7009):689.

Sugden, D. E., McCulloch, R. D., Bory, A. J.-M., and Hein, A. S. (2009). Influence of patagonian glaciers on antarctic dust deposition during the last glacial period. *Nature Geoscience*, 2(4):281–285.

Sverdrup, H. (1953). On conditions for the vernal blooming of phytoplankton. *J. Cons. Int. Explor. Mer*, 18(3):287–295.

Tamsitt, V., Talley, L. D., Mazloff, M. R., and Cerovečki, I. (2016). Zonal variations in the southern ocean heat budget. *Journal of Climate*, 29(18):6563–6579.

Tamura, T., Ohshima, K. I., Fraser, A. D., and Williams, G. D. (2016). Sea ice production variability in antarctic coastal polynyas. *Journal of Geophysical Research: Oceans*, 121(5):2967–2979.

Tang, W., Llort, J., Weis, J., Perron, M. M., Basart, S., Li, Z., Sathyendranath, S., Jackson, T., Sanz Rodriguez, E., Proemse, B. C., et al. (2021). Widespread phytoplankton blooms triggered by 2019–2020 australian wildfires. *Nature*, 597(7876):370–375.

Thurnherr, A. M., Jacobs, S., Dutrieux, P., and Giulivi, C. (2014). Export and circulation of ice cavity water in pine island bay, west antarctica. *Journal of Geophysical Research: Oceans*, 119(3):1754–1764.

Tortell, P. D., Long, M. C., Payne, C. D., Alderkamp, A.-C., Dutrieux, P., and Arrigo, K. R. (2012). Spatial distribution of pco2, δo2/ar and dimethylsulfide (dms) in polynya waters and the sea ice zone of the amundsen sea, antarctica. *Deep Sea Research Part II: Topical Studies in Oceanography*, 71:77–93.

Turner, J., Phillips, T., Hosking, J. S., Marshall, G. J., and Orr, A. (2013). The amundsen sea low. *International Journal of Climatology*, 33(7):1818–1829.

Twelves, A. G., Goldberg, D. N., Henley, S. F., Mazloff, M. R., and Jones, D. C. (2021). Self-shading and meltwater spreading control the transition from light to iron limitation in an antarctic coastal polynya. *Journal of Geophysical Research: Oceans*, 126(2):e2020JC016636.

van Roekel, L., Adcroft, A. J., Danabasoglu, G., Griffies, S. M., Kauffman, B., Large, W., Levy, M., Reichl, B. G., Ringler, T., and Schmidt, M. (2018). The kpp boundary layer scheme for the ocean: Revisiting its formulation and benchmarking one-dimensional simulations relative to les. *Journal of Advances in Modeling Earth Systems*, 10(11):2647–2685.

van Sebille, E., Spence, P., Mazloff, M. R., England, M. H., Rintoul, S. R., and Saenko, O. A. (2013). Abyssal connections of antarctic bottom water in a southern ocean state estimate. *Geophysical Research Letters*, 40(10):2177–2182.

Venables, H. J., Clarke, A., and Meredith, M. P. (2013). Wintertime controls on summer stratification and productivity at the western antarctic peninsula. *Limnology and Oceanography*, 58(3):1035–1047.

Verdy, A. and Mazloff, M. R. (2017). A data assimilating model for estimating southern ocean biogeochemistry. *Journal of Geophysical Research: Oceans*, 122(9):6968–6988.

Vernet, M., Martinson, D., Iannuzzi, R., Stammerjohn, S., Kozlowski, W., Sines, K., Smith, R., and Garibotti, I. (2008). Primary production within the sea-ice zone west of the antarctic peninsula: I—sea ice, summer mixed layer, and irradiance. *Deep Sea Research Part II: Topical Studies in Oceanography*, 55(18-19):2068–2085.

von Berg, L., Prend, C. J., Campbell, E. C., Mazloff, M. R., Talley, L. D., and Gille, S. T. (2020). Weddell sea phytoplankton blooms modulated by sea ice variability and polynya formation. *Geophysical Research Letters*, page e2020GL087954.

Wadham, J., De'Ath, R., Monteiro, F., Tranter, M., Ridgwell, A., Raiswell, R., and Tulaczyk, S. (2013). The potential role of the antarctic ice sheet in global biogeochemical cycles. *Earth and Environmental Science Transactions of the Royal Society of Edinburgh*, 104(1):55–67.

Wang, Y., Chen, H.-H., Tang, R., He, D., Lee, Z., Xue, H., Wells, M., Boss, E., and Chai, F. (2021). Australian fire nourishes ocean phytoplankton bloom. *Science of the Total Environment*, page 150775.

Webber, B. G., Heywood, K. J., Stevens, D. P., Dutrieux, P., Abrahamsen, E. P., Jenkins, A., Jacobs, S. S., Ha, H. K., Lee, S. H., and Kim, T. W. (2017). Mechanisms driving variability in the ocean forcing of pine island glacier. *Nature communications*, 8(1):1–8.

Weimerskirch, H., Louzao, M., de Grissac, S., and Delord, K. (2012). Changes in wind pattern alter albatross distribution and life-history traits. *science*, 335(6065):211–214.

Williams, C., Dupont, A., Loevenich, J., Post, A., Dinasquet, J., and Yager, P. (2016). Pelagic microbial heterotrophy in response to a highly productive bloom of phaeocystis antarctica in the amundsen sea polynya, antarcticamicrobial heterotrophy in amundsen sea polynya. *Elementa: Science of the Anthropocene*, 4.

Wilson, S. E., Swalethorp, R., Kjellerup, S., Wolverton, M. A., Ducklow, H. W., and Yager, P. L. (2015). Meso-and macro-zooplankton community structure of the amundsen sea polynya, antarctica (summer 2010–2011) zooplankton community structure of the amundsen sea polynya, antarctica. *Elementa: Science of the Anthropocene*, 3.

Wirtz, K. and Smith, S. L. (2020). Vertical migration by bulk phytoplankton sustains biodiversity and nutrient input to the surface ocean. *Scientific reports*, 10(1):1–12.

Wu, M., McCain, J. S. P., Rowland, E., Middag, R., Sandgren, M., Allen, A. E., and Bertrand, E. M. (2019). Manganese and iron deficiency in southern ocean phaeocystis antarctica populations revealed through taxon-specific protein indicators. *Nature communications*, 10(1):1–10.

Xu, X., Chassignet, E. P., Firing, Y. L., and Donohue, K. (2020). Antarctic circumpolar current transport through drake passage: What can we learn from comparing high-resolution model results to observations? *Journal of Geophysical Research: Oceans*, 125(7):e2020JC016365.

Yager, P. L., Sherrell, R., Sipler, R., et al. (2016). A carbon budget for the amundsen sea polynya, antarctica: Estimating net community production and export in a highly productive polar ecosystem. *Elementa-Science Of The Anthropocene*, 4(140).

Yager, P. L., Sherrell, R. M., Stammerjohn, S. E., Alderkamp, A.-C., Schofield, O., Abrahamsen, E. P., Arrigo, K. R., Bertilsson, S., Garay, D. L., Guerrero, R., et al. (2012). Aspire: the amundsen sea polynya international research expedition. *Oceanography*, 25(3):40–53.

Zhang, J., Hibler III, W., Steele, M., and Rothrock, D. (1998). Arctic ice–ocean modeling with and without climate restoring. *Journal of Physical Oceanography*, 28(2):191–217.

Zheng, Y., Heywood, K. J., Webber, B. G., Stevens, D. P., Biddle, L. C., Boehme, L., and Loose, B. (2021). Winter seal-based observations reveal glacial meltwater surfacing in the southeastern amundsen sea. *Communications Earth & Environment*, 2(1):1–9.

Zweng, M., Seidov, D., Boyer, T., Locarnini, M., Garcia, H., Mishonov, A., Baranova, O., Weathers, K., Paver, C., Smolyar, I., et al. (2019). World ocean atlas 2018, volume 2: Salinity.